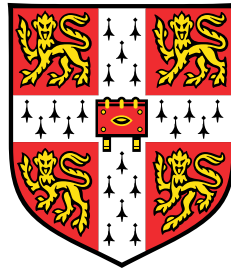


Distribution and regulation of ion channels in neurons

**Quantitative studies of global ion channel
transport and homeostatic synaptic scaling**



Adriano Alexandro Bellotti

Department of Engineering
University of Cambridge

This dissertation is submitted for the degree of
Doctor of Philosophy

Declaration

I hereby declare that except where specific reference is made to the work of others, the contents of this dissertation are original and have not been submitted in whole or in part for consideration for any other degree or qualification in this, or any other university. This dissertation is my own work and contains nothing which is the outcome of work done in collaboration with others, except as specified in the text and Acknowledgments. This dissertation does not exceed the prescribed word limit for the relevant Degree Committee.

Adriano Alexandro Bellotti

December 2020

Distribution and regulation of ion channels in neurons

Quantitative studies of global ion channel
transport and homeostatic synaptic scaling

Adriano Alexandro Bellotti

Abstract

A healthy neuron must continually produce millions of proteins and distribute them to function-specific regions of the cell. Among these proteins are ion channels that modulate neuronal excitability, allowing neurons to fulfill their primary role of information transfer. Neurons are unique among cells in their morphology, with projections that extend hundreds to thousands of microns. Neuron size and asymmetry pose a challenge for autoregulation of properties that require cargo transport across the cell. Homeostasis of ion channel localization has strong implications for neural excitability. This thesis concerns the intracellular distribution of ion channels in the context of longitudinal transport and global neuron regulation.

The principal contributions are experimental measurements, data analysis, and modeling in the study of longitudinal neurite transport. Empirical investigations focus on the distribution and trafficking kinetics of ion channel Kv4.2, including quantitative measurements of both passive diffusion and active microtubule-based transport in both axons and dendrites (Chapters 3 and 5). Mass action models reveal that measured transport profiles corroborate discrepancies in Kv4.2 localization both between neurite types and along the somatodendritic axis (Chapter 4). Exchange between mobile and immobile fractions, inferred from analysis of repeated photobleaching, shapes intracellular distribution of Kv4.2 (Chapter 5). Further, the ensuing theoretical study surveys global regulation of ion channels, specifically for synaptic scaling, which requires cell-wide modulation of AMPA receptors for normalization of neural excitability. A unified model of synaptic potentiation, transport, and feedback reveals limitations imposed on synaptic scaling by neuron morphology. A neuron balances the stability, accuracy, and efficiency of synaptic scaling (Chapter 6).

Acknowledgements

Four years ago, I reached out to Tim O’Leary as a medical student interested in a joint theoretical-experimental neuroscience project. Together, we approached Dax Hoffman with a proposal on ion channel trafficking and regulation. Since then, both supervisors have provided incredible support for this course of study. My supervisors were curious and open-minded when initially formulating early research goals. They were encouraging and committed when experiments or analyses returned unexpected results. They were quick and collected when our objectives had to change or pivot. They were patient and accommodating with the challenges of an overseas collaboration. I am very grateful for their time and help over the past four years. Without their thoughtful considerations and efforts, these studies would not have been successful.

During my studies, I have made numerous contacts and connections from a broad range of scientists across experimental and computational neuroscience. My preliminary studies during my first year began with the Control Group in the Department of Engineering at the University of Cambridge. I want to acknowledge everyone in the Control Group. Some helped directly—thank you to Tim O’Leary, Fulvio Forni, Rodolphe Sepulchre, Dhruva Ramen, Michael Rule, Monika Jozsa, Andy Stoyechev, and Saeed Aljaberi. All helped with guidance, insight, and inspiration with modeling and analyses. We’d spend long afternoons talking about our latest ideas. We’d have lunchtime meetings, presenting our latest updates. We’d go to pubs in the evenings to continue the discussion. I learned more that first year than any other year in academia, largely because of the kind, welcoming, collaborative environment of the Control Group.

I want to specifically thank Tim, Fulvio, and Saeed for what I think culminated in an elegant study of synaptic scaling. This was a very enjoyable project, even (especially) during the late nights and many revisions. I enjoy reminiscing about how this project started at a conference three years ago and matured over time. I appreciate all your patience, teaching, and mentorship over the years.

The next two years were in the experimental laboratory of Hoffman’s group in the Section on Neurophysiology at the National Institute of Child Health and Human Development at NIH. I am grateful for the time, help, and mentorship of all members of Dax’s group.

Thank you to Jon Murphy who always shared his advice, guidance, and experience with experimental studies. Thank you to Dax Hoffman, who provided direction, ideas, and new leads for the project. Thank you to Lin Lin, who was always there for technical support with techniques as well as personal support and encouragement. Thanks also to Vincent Schram and the NICHD Microscopy and Imaging Core for continued help with microscopy and image analysis.

I want to acknowledge the Gates Cambridge program for guidance, support, and funding during the course of my graduate studies. Thank you also to the National Institutes of Health Oxford-Cambridge Scholars program for organizing, funding, and supporting the collaboration between institutions. Thank you personally to Katie Soucy and Katie Stagliano for their kind help, advice, and managing stubborn students during my time in the program. I want to acknowledge the University of North Carolina (MD-PhD) Medical Scientist Training Program. Thank you especially to Mohanish Deshmukh and Alison Regan who personally supported me in pursuing this course of study.

I lastly want to acknowledge my friends and family who have provided consistent support throughout my graduate studies and personal development. Thank you to my brothers, Amadeo and Aurelio, who constantly challenge and compete with me. Thank you to my loving parents, Aldo and Mireille, who have sacrificed everything for my brothers and me. Thank you to my childhood friend Robert and girlfriend Alyssa who know me better than I do. Thanks to the many friends I've made throughout my graduate studies—Alex, John, Mario, Lawrence, Liz, Steve, and Kris. Thanks also to those who encouraged me from medical school—Clark, Cam, and Wesley.

It is difficult to overstate the benefits of collaboration and mentorship in any scientific endeavor. This project is no exception—it would not have been possible without the help of many people and organizations. I want to express my deepest appreciation to my supervisors, peers, coworkers, friends, and family for sharing your valuable insight and providing unwavering support. Thank you.

Table of contents

List of figures	xiii
List of tables	xvii
1 Introduction	1
1.1 Background	1
1.1.1 Perspective	2
1.1.2 Organization of the thesis	2
1.2 Historical introduction	3
1.2.1 Early history	4
1.2.2 Microscopy	4
1.2.3 The neuron doctrine	6
1.2.4 Intracellular organization and transport	6
1.2.5 Neuron excitability and ion channels	7
1.2.6 Computational neuroscience and control theory	8
1.3 Overview of ion channels	10
1.3.1 Ion channel transport	11
1.3.2 Candidate cargo Kv4.2	13
1.3.3 Kv4.2 function	13
1.3.4 Kv4.2 trafficking	14
1.3.5 Relation to drift-diffusion	15
1.4 Overview of neuroplasticity and regulation	15
1.4.1 Intrinsic excitability	16
1.4.2 Spike-timing-dependent plasticity	17
1.4.3 Other synaptic plasticity	18
1.5 Research questions	19
1.5.1 Empirical investigation	19
1.5.2 Analytical inquiries	20

1.5.3	Theoretical study	20
1.6	Recapitulation	20
2	Methods and experimental validation	23
2.1	Chapter summary and key findings	23
2.2	Introduction	24
2.3	Animals and cell culture	25
2.3.1	Hippocampal dissection and dispersed cultures	25
2.3.2	Construct	26
2.3.3	Transfection	26
2.3.4	Immunostaining	26
2.4	Cell and neurite morphology	27
2.4.1	Differentiating cell types	27
2.4.2	Differentiating neurites	30
2.4.3	Differentiating dendrites	33
2.5	Electron microscopy	36
2.6	Confocal microscopy	37
2.6.1	Pinhole size	37
2.6.2	Recording time series and sampling rate	38
2.6.3	Bleach parameters	39
2.6.4	Fluorescence recovery after photobleaching	41
2.6.5	Data loss during bleach recovery	44
2.7	Imaging active transport	45
2.7.1	Colchicine treatment	47
2.8	Image and data analysis	47
2.8.1	Import and kymogram generation	47
2.8.2	Manual versus automated puncta tracing	49
2.8.3	Contrast enhancement and thresholding	50
2.8.4	Puncta trajectory selection	50
2.8.5	Trajectory trimming	52
2.8.6	Intra- and inter-experimenter variation	53
2.9	Deterministic modeling: steady state analysis	54
2.10	Discussion regarding transport behavior	55
3	Microtubule transport and localization of puncta containing Kv4.2	57
3.1	Chapter summary and key findings	57
3.2	Introduction	58

3.3	Kv4.2 microtubule-based trafficking is observed more frequently in axons	59
3.3.1	Extended FRAP recordings	63
3.3.2	Axons and dendrites from the same neuron	63
3.4	Kinetic differences in axons versus dendrites	64
3.4.1	Calculating kinetic measures	64
3.5	Kv4.2 preferentially localizes to dendrites	69
3.6	Perturbing neural excitability does not immediately affect dendritic transport	73
3.6.1	KCl depolarization	73
3.6.2	AMPA stimulation	74
3.7	Discussion	76
4	Reconciling the distributions of microtubule-bound and delivered cargo	79
4.1	Chapter summary and key findings	79
4.2	Introduction	80
4.3	Coarse-grained modeling captures cargo transport and delivery	82
4.4	Mass action explains disparity between static localization and mobile frequency	85
4.5	Kinetic differences are attributable to cargo offloading and unidirectional runs	89
4.5.1	Modeling transport using a modified random walk	90
4.5.2	Drift-diffusion equation	93
4.5.3	Analysis of stochastic model	95
4.5.4	Inference of qualitative differences via stochastic modeling	96
4.6	Mass-action kinetics reconcile opposing gradients along somatodendritic axis	98
4.7	A summary of the relationships between <i>mt</i> and <i>del</i>	102
4.8	Discussion	105
5	Characterization of Kv4.2 longitudinal diffusion in dendrites	107
5.1	Chapter summary and key findings	107
5.2	Introduction	108
5.3	Diffusion and drift rates during single bleach recovery	109
5.3.1	A and τ are correlated but not attributable to experimental parameters	110
5.3.2	Spatial analysis of recovery reveals minimal distal drift	113
5.4	Inference of im/mobilization rates	115
5.4.1	Schematic of photobleaching and im/mobilization rates	116
5.4.2	Data analysis	117
5.4.3	Inference from reduced model of photobleach recovery	122
5.5	Trends with subsequent bleaches and recoveries	124
5.5.1	Simulations and interpretation	125

5.5.2	An analytical perspective	128
5.6	Impact on intracellular distribution	130
5.6.1	Discussion	133
6	Synaptic scaling: a tradeoff between stability, accuracy, and efficiency	135
6.1	Chapter summary and key findings	135
6.2	Introduction	136
6.3	A unified model of synaptic potentiation, scaling, and regulation	138
6.4	Navigating the tradeoffs	141
6.4.1	Global gain mediates tradeoff between stability and efficiency	143
6.4.2	Local gain mediates tradeoff between stability and accuracy	143
6.4.3	Internal pool size mediates tradeoff between accuracy and efficiency	144
6.5	Quantifying stability using classic control theory	144
6.6	Quantifying accuracy of synaptic potentiation and scaling	147
6.7	Defining efficiency	151
6.8	Summary of tradeoffs	153
6.9	Reduced-order neuron models capture scaling performance	156
6.10	Neuron size and symmetry significantly impact scaling performance	157
6.11	Discussion	162
7	Summary and implications	163
7.1	Summary of contributions	163
7.1.1	Active transit versus passive diffusion	165
7.1.2	Timescale of global versus local regulation	165
7.1.3	Implications for other cargoes and neuron types	166
7.2	Closing remarks	167
	References	169
	Appendix A Derivations	187
A.1	Derivation of advection-diffusion equation	187
A.1.1	Random walk master equation	187
A.1.2	Finite difference approximation	189
A.1.3	Discrete to continuous space and time	189
A.2	Estimation of diffusion coefficient from FRAP	190

Appendix B Stochastic model: analysis and inference	193
B.1 Distributions of kinetic measures in stochastic model	193
B.1.1 Total distance traveled	193
B.1.2 Average speed	195
B.2 Statistical inference using stochastic model	197
B.2.1 Maximum likelihood estimation	198
B.2.2 Least squares method of optimization	201
Appendix C Synaptic scaling: full model description	205
C.1 Unified model of synaptic potentiation, scaling, transport, and regulation . .	205
C.1.1 Model formulation and methods	205
C.1.2 Cargo insertion (activation and inactivation)	205
C.1.3 Cargo trafficking via active transport	206
C.1.4 Homeostasis and feedback regulation	207
C.1.5 Model interpretation	209
C.1.6 Local cargo regulation	210
C.2 Transfer functions and Nyquist plots	211

List of figures

2.1	Cell culture containing pyramidal neuron	28
2.2	Cell culture containing another cell, likely an interneuron	29
2.3	Pyramidal neuron with distinct axon and dendrites exhibiting clear morphological differences	31
2.4	Differentiating neurites by diameter	32
2.5	Ankyrin-G staining in axons for definitive neurite differentiation	33
2.6	Comparison between definitive and probable axons	34
2.7	Variable dendritic appearance, such as in fluorescence pattern, can be attributed to neuron type, age, health, and other factors	35
2.8	Sampling rate imposes a trade off between imaging data and unintentional photobleaching	39
2.9	Increasing photobleach iterations imposes a tradeoff between total bleach time and degree of bleaching	40
2.10	Typical frame from a FRAP time series with bleach region indicated	42
2.11	Prebleach fluorescence intensity is stable	43
2.12	Typical FRAP recovery curve and exponential fit	44
2.13	Comparison between fast and slow sampling rates during bleach recovery	45
2.14	Time series and kymogram generation	46
2.15	Kymograms of neurites during colchicine administration	48
2.16	Puncta mobility with colchicine administration	48
2.17	Kymogram post-processing: contrast enhancement, thresholding, and puncta selection	51
2.18	The standardized protocol for image and data analysis has minimal intra- and inter-experimenter variation	53
3.1	Kv4.2 microtubule-based trafficking is observed more frequently in axons than in dendrites	60

3.2	Puncta frequency in neurites is independent of neuron development over DIV 8 to 14	61
3.3	Weak correlation between transit frequency and degree of branching	62
3.4	No correlation between puncta frequency and standardized neurite intensity	62
3.5	Low correlation between puncta frequency and neurite diameter	63
3.6	Extended recordings that substantiate the discrepancy in puncta frequency between axons and dendrites	64
3.7	Puncta frequency is higher in axons for neurites from the same soma	65
3.8	Kv4.2 trafficking is qualitatively different in axons and dendrites (kymograms)	66
3.9	Kv4.2 trafficking is qualitatively different in axons and dendrites (histograms)	67
3.10	Trajectory kinetics correlate weakly with neurite diameter, suggesting that mobile puncta are not constrained by neurite size	68
3.11	Endogenously expressed Kv4.2 visualized with EM localizes to dendrites	70
3.12	Endogenously expressed Kv4.2 visualized with immunolabeling localizes to dendrites	72
3.13	Transfected Kv4.2 visualized with fluorescence microscopy localizes to dendrites	72
3.14	Increased KCl does not immediately affect microtubule transport	74
3.15	AMPA stimulation does not immediately affect microtubule transport	75
4.1	Microtubule-bound (<i>mt</i>) and delivered (<i>del</i>) subunit densities	83
4.2	Compartmental models of transport in axons and dendrites	86
4.3	Result of lumped model simulation with experimentally-constrained rates corroborates <i>mt</i> and <i>del</i> densities	88
4.4	Analytical result demonstrating negative correlation between a_{del} and a_{mt} or d_{del} and d_{mt}	89
4.5	Model of modified random walk	91
4.6	Demonstration of stochastic model that compares visually to experimentally-obtained kymograms	92
4.7	Normalized puncta frequency decreases with distance from soma in dendrites	93
4.8	Histograms for various kinetic transport parameters with model fits	97
4.9	Fitting for mean squared displacement reveals higher degree of superdiffusivity in axons	98
4.10	Box diagram of a mass action model of dendritic transport and delivery with feedback	99
4.11	Mean instantaneous velocities for dendritic puncta plotted along the length of the dendrite	100

4.12	Simulation of mass action model of dendritic transport and delivery with feedback	101
4.13	Mass action transport causes discordance of delivered and transported cargo densities between axons and dendrites	103
4.14	Mass action transport causes discordance of delivered and transported cargo densities along the length of a neurite	104
4.15	The kinetic properties of individual puncta trajectories in <i>mt</i> reflect cargo demand in <i>del</i>	104
5.1	Single exponential recovery parameters for over 250 dendrites	110
5.2	Raw kymograms reveal variability in cargo recovery	111
5.3	Raw kymograms reveal a directional bias during bleach recovery, corresponding to drift	111
5.4	Experimental variability is not strongly correlated with bleach recovery parameters	112
5.5	Bleach recovery rate and mobile fraction are reciprocally related	113
5.6	Drift is computed by spatially binning kymograms	114
5.7	Distribution of drift depicted as a histogram	115
5.8	Schematic of recurrent photobleaching reveals increasing mobile fraction with low immobilization rates	118
5.9	Example of recurrent photobleaching with increasing mobile fractions	119
5.10	Example of recurrent photobleaching with no trend in mobile fraction	119
5.11	Trends in A and τ with successive photobleaching	121
5.12	Im/mobilization rates are inferred from mass-action model of photobleach and recovery	123
5.13	Sorted mobile fractions from recurrent bleaches	125
5.14	Simulation of recurrent photobleaching and immobilization with varying im/mobilization rates	126
5.15	Steady state mobile fraction as function of bleach rate and im/mobilization rate	129
5.16	Inferred parameters markedly affect cargo distribution in real neuron morphologies	131
6.1	Constructing a unified model of synaptic potentiation, scaling, and regulation to realize phase lag time delay	139
6.2	Defining stability, efficiency, and accuracy of synaptic scaling	141
6.3	Navigating the tradeoffs	142
6.4	System stability is quantified using principles of classic control theory	146

6.5	Accuracy of synaptic potentiation is quantified as a percentage of full potentiation	148
6.6	AMPA inactivation s_{-i} modulates internal pool size m at steady state . . .	149
6.7	Sample computation of scaling error q	150
6.8	Asymmetric morphologies scale less accurately than symmetric morphologies, mitigated by large receptor pools	152
6.9	The tradeoffs are summarized in a toy model by rigorously quantifying each attribute.	154
6.10	The same tradeoffs result if Arc communicates the global activity signal . .	155
6.11	Transfer functions and reduced-order models of neuron morphologies predict scaling performance	158
6.12	Ball-stick parameters for Martinotti cell converge with increasing n	159
6.13	Neuron size and symmetry significantly impact scaling performance.	160
6.14	Variance in neuron length strongly correlates with scaling performance . . .	161
A.1	Fluorescence recovery in a neurite for estimation of diffusion coefficient . .	191
C.1	A generic labeled Nyquist plot	213

List of tables

2.1	List of antibodies	27
3.1	Density of immunogold particles identified by electron microscopy in synapses of axons and dendrites	71
6.1	Ball-stick model parameters fitted to various neuron morphologies	157
6.2	Size and symmetry metrics of neuron morphologies	159

Chapter 1

Introduction

1.1 Background

Neurons are excitable cells that process and transmit information in the form of electrical and chemical signals. A typical neuron consists of a soma, axons, and dendrites. The soma, or cell body, is the bulbous center of the cell that contains the nucleus housing genetic material as well as organelles for energy production, protein translation, processing, and storage. The dendrites are long, thin projections of plasma membrane that branch and extend hundreds of microns in a tree-like arborization, allowing the cell to receive signals from numerous inputs and electrically and chemically propagate and integrate them into the soma. Axons are a specialized projections extending and branching for thousands of microns through which the cell relays output information. Neurons connect to each other and to end organs, forming neural circuits. Though not the only cells found in neural tissue, neurons are regarded as the basic functional unit of the nervous system. Neurons are the foundation of signal and information transfer in the brain. Neurons therefore have centralized control over an organism's functions and are integral to learning, memory retention, and all other major cognitive functions.

The complex functions of a neuron (and all other cells) requires continual cargo trafficking and distribution. The most primitive and simplest of cells, including prokaryotes, are small (~1 μm in diameter) and therefore rely on simple diffusion as a means of transport. As life and cells became more complex, eukaryotic cells evolved to larger sizes [249] and developed active mechanisms of long-range transport. Typical eukaryotic cells are fairly symmetric and ~10 μm in diameter, and cargo can be transported on a timescale of minutes.

The intracellular environment of a neuron, like all cells, is compact and incredibly complex with many moving parts. Individual cells contain tens of millions of protein molecules [96] with specialized functions that are often site-specific. Transporting all

proteins to their proper location is a challenging endeavor. To complicate matters, proteins and other cargo do not last forever, and cells must continuously recycle and replace them. To further complicate matters, neurons are among the longest, most asymmetric cells. This poses a problem: transport takes longer (on the order of hours to days) and thus is harder to regulate.

How can cells that are so integral to the workings of our minds and bodies overcome a challenge exacerbated by their unique morphologies? Long-range longitudinal transport is necessary for localization of proteins throughout a large cell. Continual active delivery of cargo is therefore crucial to the functioning of neurons. This thesis concerns the dynamics of such transport as well as the challenges associated with regulating cargo activity over long distances.

1.1.1 Perspective

This project is unique in that it combines the expertise in experimental neuroscience, molecular/cellular biology, and imaging of one research group with the knowledge of computational neuroscience, bioengineering, control theory, and mathematics of another group. This integration of distinct disciplines encourages new perspectives and approaches to open questions relevant to both fields.

The experimentalists working alone might have an excellent working knowledge of the structure and mechanisms of an ion channel and the manifestation of phenotypes, but they might overlook the global function in the context of a full neuron or circuit, or how that function might be regulated. Theorists might have a comprehensive understanding of cell conductance and transport, but without an experimental basis, their results lack grounding in reality. This project ideally combines the skills and eliminates the drawbacks of both disciplines, which creates an advantage in these fields of study.

1.1.2 Organization of the thesis

This chapter introduces the high-level concepts that unify the entire thesis. This chapter also establishes the premises of the major results. Relevant background information from the conventional pillars of neuroscience is introduced, covering cell and molecular biology from the experimentalist's perspective as well as modeling and feedback regulation from the theorist's view. The overarching questions of the dissertation are also outlined and addressed. More specialized introductions and thorough reviews of concepts and literature are reserved for the following chapters.

Chapter 2 covers the experimental and computational methods, materials, and procedures for obtaining the results. This includes experimental protocols from the wet lab; equipment and settings for microscopy; techniques for image/data analysis; strategies for modeling; and methods of statistical inference. This chapter also includes the preliminary results for dissection and culturing of hippocampal cells as well as techniques for imaging and microscopy. This includes pilot trials and optimization experiments that established competency required for efficient collection of consistent, meaningful data.

Chapter 3 contains experimental results on active microtubule-based transit of Kv4.2. This includes comparisons of puncta frequencies between axons and dendrites with experimental controls and attempts to perturb Kv4.2 active transit. We also compare transit frequency with static localization data collected with collaborators, revealing a paradoxical relationship.

Chapter 4 reconciles the aforementioned discordant relationship between static and transported cargo introduced in the previous chapter. This includes deterministic, compartmental models that illustrate the discordance both across neurite types and along the somatodendritic axis. This chapter also includes inference of mechanistic differences in puncta transit between axons and dendrites using a stochastic model.

Chapter 5 broadly covers measurement and modeling of Kv4.2 longitudinal diffusion in dendritic shafts. This analysis reveals that measurements of fluorescence recovery after photobleaching can approximate rates of cargo transfer between mobile and immobile fractions, which shapes intracellular distribution of Kv4.2.

Chapter 6 examines a logistical problem regarding intraneuronal distribution of ion channels. Transport, activation, and regulation of AMPA receptors are modeled in real neuron morphologies, revealing the limitations of synaptic scaling. The tradeoffs imposed by neuron morphology are quantified based on experimental data.

Chapter 7 is a brief summary that condenses our key findings, ties together the results chapters, and includes closing remarks.

1.2 Historical introduction

The study of neuroscience has matured substantially throughout history. To introduce each topic of this thesis, the relevant historical foundations are discussed. A condensed overview of each topic follows. This introduction is by no means an exhaustive account of the vast history of neuroscience. Rather, this historical introduction covers events and discoveries that are most significant for neuroscience and/or most relevant to this dissertation.

1.2.1 Early history

Greek philosopher Alcmaeon of Croton was among the first people in recorded history to consider the brain rather than the heart as the seat of intelligence, cognition, and consciousness. From the pre-Socratic era, this is the earliest description of the fundamental functions of the central nervous system [83]. The study of the brain largely progressed through early civilizations with crude methods and macroscopic observations. Human neuroscience in ancient Greece was limited since the human body was considered sacred. In contrast, ancient Egyptians introduced nervous system anatomy through their embalming practices. Roman anatomists further dissected the nervous system, linking the brain to bodily movements [83, 12]. The Islamic Golden Age introduced early treatments of the nervous system, as Avicenna and Al-Zahrawi became known as the fathers of modern neurology and neurosurgery [2, 158].

In more recent history, the field of neuroscience has broadened to overlap with many other disciplines. Many modern day neuroscientists, projects, and institutions cover multiple subfields and adapt data and methods from one domain to another. This dissertation is most closely associated with neurobiophysics and computational neuroscience and uses techniques from fluorescence microscopy and control theory. The foundational breakthroughs that established these specialized disciplines are outlined next.

1.2.2 Microscopy

A major advancement for neuroscience and experimental biology in general was the development of optical microscopy. The earliest compound microscopes, or upright microscope with two lenses, date back to around 1590, with claims of invention by Dutch spectacle-maker Zacharias Janssen and/or his father [240]. Microscope usage soon spread among biologists and was improved and popularized by Antonie van Leeuwenhoek. Three quarters of a century later, Robert Hooke observes and is credited for the discovery of cells using optical microscopy [79, 44]. Other major advancements in optical microscopy include mass production by Carl Zeiss [67] and combinations of lenses to resolve aberrations by Joseph Jackson Lister [56].

For the past century and a half, optical microscopes have become essential instruments for experimental biologists and neuroscientists. Advanced microscopy techniques have been and are continually adapted to experimental neuroscience. Fluorescence microscopy is a method that relies on emission rather than scattering or reflection of light. This brought about several advantages, including improved resolution, labels for multiple structures, and filters for emitted wavelengths [218].

Confocal microscopy further reduces the scattering of light for improved image resolution and feature distinction. A sample is illuminated with a small beam of light focused by a pinhole at a narrow plane depth. By restricting the region of sample excited by light, signal that is out-of-focus or scattered is minimized. However, the pinhole that produces focused light also reduces excitation intensity. The light detector must therefore be sensitive and the signal is often amplified. [181]

One of the main advantages of fluorescence and confocal microscopy is the ability to distinguish multiple structures and features of cells and molecules. Identifying, measuring, or tracking molecules and structures using advanced microscopy techniques is often limited by the sample fluorescence. Cells can be visualized with their own intrinsic fluorescence—called autofluorescence. More frequently, structures and molecules are labeled with fluorescent stains and/or expressed with fluorescent tags [159]. One such fluorescent tag that is very prevalent in cellular and molecular biology is green fluorescent protein (GFP). Originally purified from jellyfish *Aequorea victoria* by Osamu Shimomura in the 1960s [211], GFP has become a widely used reporter gene and fluorescent tag (2008 Nobel Prize). Several improved derivatives of GFP are continually developed for broad applications of fluorescence microscopy in the life sciences. [206]

A number of methods beyond single frame captures have been developed using fluorescence microscopy. Confocal microscopy at several depths can produce three-dimensional spatial reconstructions of a sample. A time series of micrographs can be captured to study the dynamics of a system, such as in particle tracking. [223] Another set of methods involves photobleaching, or the exposure of fluorophores to high intensity light to induce chemical alternations such that they no longer fluoresce. For instance, fluorescence recovery after photobleaching (FRAP) was first analyzed for quantification of diffusion in the 1970s [9]. These methods, among others in fluorescence microscopy, are especially useful in the study of molecular biophysics. Biological events, such as protein dynamics and transport kinetics, can be observed and manipulated. Confocal microscopy with fluorescence labeling can elucidate the physical mechanisms that drive biological phenomena.

Experimental neuroscience broadly involves empirical approaches and the scientific method to investigate the nervous system. This includes biophysics, physiology, and cellular/molecular biology applied to neurons. By contributing substantially to each of these fields, the optical microscope and its subsequent iterative improvements have ushered in the modern era of experimental neuroscience.

1.2.3 The neuron doctrine

Modern neuroscience at the level of single cells and their interconnections in neural circuits is largely made possible by improving microscope technology. Microscopy first enabled early observations of unbranched tubular processes that were termed axons. This led to the development of reticular theory, which contends that all nervous tissue is joined in a single network called reticulum. A proponent of this theory, Italian biologist Camillo Golgi developed a silver stain that contrasts neurons against a yellow background. Thanks to microscopy and Golgi's stain, a neuron's morphology was wholly visible for the first time in the 1870s. [50, 140]

Over the next few decades, Spanish neuroscientist and artist Santiago Ramón y Cajal used Golgi's staining method to produce hundreds of neuron illustrations. Among these anatomical images were dendritic arbors, neural networks, and forests of cells. Ramón y Cajal's work facilitated the decline of reticular theory and rise of the neuron doctrine, which states that a neural system made of individual cells with distinct terminals. [48] Despite their opposing theories, Golgi and Ramón y Cajal were jointly awarded the 1906 Nobel Prize in Physiology or Medicine "in recognition of their work on the structure of the nervous system" [18]. It wasn't until the 1950s that the neuron doctrine was reinforced following the development of electron microscopy. [140]

A neuron comprises a central cell body called the soma with long projections—or neurites—for input and output of signal. Biophysicists Kenneth Cole and Howard Curtis were among the first to establish the function of each neurite with early intracellular recordings in the 1930s. [70] However, the identification and coinage of axons and dendrites dates farther back. German neuroanatomist Otto Deiters was among the first to describe the axon, calling it an "axis cylinder" around 1860 [59]. Swiss anatomist Wilhelm His was among the first to describe the "protoplasmic processes" that he observed as dendrites, which he differentiated from axons in 1889 [70]. By then, the functional unit of the nervous system and its major structures had been identified.

1.2.4 Intracellular organization and transport

The past century saw the maturation of biochemistry, biophysics, and molecular/cell biology. What follows is a brief survey of the most relevant advancements from these fields. The biologic flow of information from nucleic acid to protein was considered central dogma by Francis Crick in 1957 [51]. Over the next few decades, biologists Claude, de Duve, and Palade gradually uncovered the structural organization of the cell, elucidating the specialized functions of organelles and establishing cellular biology (1974 Nobel Prize) [189]. The

novel view of a compartmentalized cell raised new questions. How does the cell maintain its organization? How do molecules and organelles arrive at their functional sites? In the following decades, Günter Blobel discovered signal peptides, which direct proteins through post-translational processing in the endoplasmic reticulum, Golgi apparatus, and targeting to terminal sites (1999 Nobel Prize) [17]. But open questions still remained. How is cargo transported for secretion or membrane integration? Rothman, Schekman, and Südhof elucidate the packaging, trafficking, and secretion of membrane vesicles—small cargo-containing structures surrounded by a phospholipid bilayer (2013 Nobel Prize). In neurons, vesicular trafficking is prominent as a means of cargo distribution and neurotransmitter release, among other functions [152].

The inner workings of the eukaryotic cell were revealed to be exceedingly complex—with compartmentalization, organelles, specialized functions, and self-regulation. Between all cellular components are networks of interlinking protein filaments collectively called the cytoskeleton. Connecting the variety of cell compartments are numerous transactions of molecular cargo and signals. The cytoskeleton—consisting of microfilaments, intermediate filaments and microtubules—serves as tracks for molecular motors that carry out all direct transport in the cell. This movement is termed intracellular transport. [55]

The earliest record of intracellular transport was cytoplasmic streaming in algae genus *Chara* observed by Italian botanist Bonaventura Corti in 1774 [229]. Over the next century, the movement of chromosomes during cell division was observed in detail [151]. The first reported observation of transport unique to neurons was fast axonal trafficking in the 1980s [237, 6]. In recent years, with advanced microscopy and fluorescent tagging with GFP, intracellular trafficking of more and more cargos are visualized and studied. [238]

1.2.5 Neuron excitability and ion channels

Neurons are among a select group of cells that exhibit electrochemical excitability. This was first recorded in the late 1700s, when Italian biologist Luigi Galvani dissected frog legs, applied electrical current, and observed muscle contraction he described as "animal electricity" [184]. The underlying mechanism of neuron excitability, however, would not be elucidated for another hundred years. Galvani's work inspired Alessandro Volta to develop an early electric battery, the Voltaic pile, to study animal electricity [185]. In 1843, the action potential was discovered by Emil du Bois-Reymond, student of Johannes Peter Müller [72]. In 1850, the conduction velocity of action potentials was measured by du Bois-Reymond's friend and fellow student Hermann von Helmholtz [175]. This team of three are regarded as pioneers in experimental electrophysiology.

Several decades later, a student of du Bois-Reymond and assistant to Helmholtz, Julius Bernstein established the concept of resting potential. In 1902 and 1912 publications, Bernstein proposed that action potentials result from changes in potassium ion permeability of a membrane [204]. The threshold potential was first proposed by Louis Lapicque in 1907 [129]. The membrane hypothesis and threshold potential were supported by the early intracellular recordings of Cole and Curtis, who in 1939 demonstrated increased membrane conductance during an action potential [54].

These early membrane recordings and related theory enabled a series of breakthroughs by Bernard Katz, Alan Hodgkin, and Andrew Huxley. They first amended the membrane hypothesis with a second ion, sodium [103]. In their next five papers, all in 1952, they apply voltage clamping to the giant squid axon and record changes in membrane permeability to sodium and potassium. From these measurements, they reconstruct the measured axon potential (1963 Nobel Prize). [102, 99, 98, 100, 101].

In the last of their 1952 papers, Hodgkin and Huxley propose that dynamic membrane permeability is a result of discrete ion channels existing in distinct states. Their original model used open and closed states with potassium channel activation, sodium channel activation, and sodium channel inactivation. [101] This expanded upon membrane pores proposed by Cole and Curtis in 1941 [53], the first models of ion channels passing current. The hypothesis of ion channels was confirmed in the mid-1970s by Erwin Neher and Bert Sakmann, who developed patch clamping and made the first conductance recordings of individual channels (1991 Nobel Prize) [163]. Patch clamping soon became a widespread technique and ion channels were extensively characterized in the following decades. For instance, neuroscientist Roderick MacKinnon made significant strides in elucidating the function of potassium channels, including determining their structure using X-ray crystallography (2003 Nobel Prize) [141]. As the fundamental carrier of current in excitable cells, research on ion channels continues to expand into relevant areas including channelomics, pharmacology, and intracellular trafficking.

All of these discoveries were made possible by the aforementioned advancements in optical microscopy and other modern methods. Altogether, experimental neuroscience has produced a wealth of information. This data—along with theory, models, and abstractions of neural function—have been consolidated and analyzed in computational neuroscience, which developed concomitantly with experimental neuroscience.

1.2.6 Computational neuroscience and control theory

Computational neuroscience is defined as an interdisciplinary field that links neuroscience, physics, and mathematics. In practice, computational neuroscience is the application of

theory, modeling, and other mathematical methods to the study of the brain. [58] The pioneers of computational neuroscience vary by subfield or subject. What follows is a short history of the major breakthroughs in the subjects most applicable to this thesis. Among these are advancements in single-neuron modeling, transport, and classical control theory.

One of the earliest and simplest models of the biological neuron is the integrate-and-fire model introduced by Louis Lapicque in 1907 [129]. Integrate-and-fire models track input current that modulates the membrane potential of a single neuron until action potential firing upon reaching a threshold potential [1]. A more complex single neuron model is the aforementioned Hodgkin-Huxley model in the 1950s with nonlinear differential equations describing dynamic membrane permeabilities. In the ensuing decades, both the integrate-and-fire and Hodgkin-Huxley models yielded numerous variants for a broad range of applications [58]. In the next decade, Wilfred Rall made significant advancements to biological representations of neurons in compartmental models [190–192]. Rall’s cable theory became fundamental for the study of currents transfer in neurites [120]. Since then, detailed multi-compartment neuron models have become widely used and adapted to various software tools, such as GENESIS and NEURON [20, 35].

Among the physics concepts most relevant to cargo distribution in neurons are transport and diffusion. Macroscopic observations of pollen grain diffusion in water were observed by botanist Robert Brown in 1827; the jittery movement was thus called Brownian motion [239]. Adolf Fick first reported on diffusion in 1855, introducing diffusive flux, the diffusion coefficient, and the partial differential equation that became the common diffusion equation [69]. Fifty years after Fick’s macroscopic findings, Albert Einstein reported his microscopic observations of Brownian motion, in which he presented a solution in statistical mechanics [66]. In 1906, Marian Smoluchowski independently solved Brownian motion [216], and the resultant Einstein-Smoluchowski equation has become a major foundation in stochastic processes. [183] Fick’s diffusion equations can be derived from an unbiased random walk, linking the stochastic motion of individual particles to the diffusive behavior of the population. A similar derivation with a biased random walk produces the drift-diffusion equation [39]. Much like cable theory for the study of neuronal currents, these transport equations became essential first principles for the study of intracellular trafficking.

Classical control theory is also relevant to regulation of cargo in neurons. A control system is a set of devices that cohesively performs a regulatory task. For instance, a thermostat contains an input, a sensor, and a controller to regulate temperature. Control systems were first formally analyzed following the industrial revolution and turn of the twentieth century. Two major contributions were Maxwell’s analysis of the centrifugal governor [150] and the Wright brothers’ control of sustained manned flight [108]. A number

of mathematical operations were integral to the development of control theory and regulation in computational neuroscience today. In the early 1820s, Pierre-Simon Laplace formulated the Laplace transform and the generalized Z-transform, [130, 149, 187] which change a system from time domain to frequency domain. In the 1930s, Harry Nyquist published a seminal paper on the stability of now-obsolete vacuum tube oscillators, which was the origin of Nyquist stability criterion for feedback control theory [170]. Laplace and Nyquist's contributions form the basis of classical control theory. Control theory was later modernized for analysis of state-space systems using linear algebra with controllability and observability among other principles [7, 68].

Control theory and feedback regulation most plainly relate to biology through the concept of homeostasis. Homeostasis is the condition in which an organism, cell, organelle, or other biological entity tends to maintain its current state for optimal functioning. This resistance to changing a number of intrinsic properties is implemented through autoregulation. This concept was first described by physiologist Claude Bernard in 1849 in the context of organisms self-regulating their milieu intérieur, French for "internal environment," referring to interstitial fluid between cells. The term *homeostasis* was coined by Walter Bradford Cannon, who popularized the idea in a 1932 book [32, 33]. Joseph Barcroft was the first to discuss homeostasis in the context of the nervous system. In a 1934 book [10], Barcroft suggested not only that the brain mediated efferent mechanisms for homeostasis, but also that the brain required strict fixity of internal environment [11, 215]. The study of biology through the lens of control theory coincides well with the concept of homeostasis. Nervous system homeostasis and control theory thus form an emerging subfield within computational neuroscience.

Computational neuroscience covers a broad scope of theoretical principles and methods applied to the study of the nervous system. This limited outline highlights the historical origins of multi-compartment neuron models, transport, classic control theory, and homeostasis which are most relevant and applicable for this work. Next is a more detailed introduction to topics with open questions in computational neuroscience that unify this thesis.

1.3 Overview of ion channels

The excitability of neurons is based on the maintenance of electrochemical potentials across the plasma membrane. These electrochemical potentials, or voltage gradients, are caused by an imbalance in the number of positive-charged ions on either side of the plasma membrane. Voltage gradients are created through the functioning of ion pumps, and ions are transmitted between intra- and extracellular compartments through ion channels embedded

in the membrane. Some of these ion channels are ligand-gated; that is, they are opened by binding of a ligand, such as AMPA and NMDA receptors which are opened by glutamate binding. Many of these ion channels are voltage-gated: they are activated by voltage potentials across the plasma membrane, which can be induced by ion currents passing through the channels themselves. This positive feedback results in an electrochemical pulse that can travel down neurites (dendrites or axons). The primary function of ion channels is to initiate and propagate these signals.

The propagating electrochemical pulse consists of a region of membrane whose electrochemical potential rises and falls. This activates a cascade of voltage-gated ion channels that depolarize and repolarize, which causes adjacent regions of membrane to repeat the cycle. In axons, this propagation begins near the soma at a site called the axonal initial segment. An electrochemical propagation in axons is called an action potential. Action potentials are rapid with no attenuation in an all-or-none response, depending on whether the initial depolarization exceeds the threshold potential. Action potentials excite the entire cell and backpropagate into dendrites. In dendrites, there are weaker electrochemical pulses called dendritic potentials or dendritic spikes, which have variable shape, propagation, and attenuation. Dendritic potentials do not behave as a fixed, stereotyped, all-or-none response like an action potential. Nonetheless, dendritic potentials are still regenerative events that require active, nonlinear dynamics, allowing signals to propagate long distances unlike in passive cables.

The properties of dendritic potentials are largely determined by the ion channels available for activation in the neurite. Distinct dendritic potentials are aptly named for the type of channel providing current for the regenerating electrochemical pulse: sodium and calcium spikes are propagated by voltage-gated sodium and calcium ion channels, respectively, and NMDA spikes are sustained by ligand-gated NMDA channels. Therefore, the degree of propagation and attenuation of dendritic potentials is largely dependent on the distribution of ion channels throughout the dendrites. Moreover, the distribution of ion channels through the vast, branching structure that is the dendritic arbor is quite complex.

1.3.1 Ion channel transport

Molecular trafficking refers to how macromolecules are distributed throughout a cell. This field encompasses the activity of molecules between organelles (endoplasmic reticulum to Golgi apparatus) during protein production; microtubule transport along cell protrusions; and movement to/from/within the plasma membranes. Protein transport can occur over short distances between the soma, organelles, and around the plasma membrane. In neurons, local trafficking of ion channels occurs during synthesis in the soma or spines, interactions with

scaffold/cytoskeleton, membrane insertion, endocytosis, and membrane clustering/dispersion. Local transport over short distances of ion channels has been reviewed elsewhere [205, 207, 127, 63] and will not be covered here. This overview primarily focuses on transport of ion channels over longer distances between production site in the soma and functional site on the plasma membrane.

The transport of ion channels to a complex arborization of dendrites is by no means a simple feat. Given that the bulk of channel protein subunits are produced and processed in a central location and exported from the cell soma, the neuron requires an established, purposeful mechanism for allocation of ion channels into the dendritic arbor that expands up to one millimeter away from this production site. The active mechanisms of microtubule-based transport are sufficient for this purpose and are strongly implicated in the delivery of cargo throughout a neuron.

Microtubules are tubulin-based structures that with actin make up the structural network, or cytoskeleton, that spans the neuron's dendrites and axons. Microtubules thus provide both structural integrity in and transport throughout a neuron. Microtubules exhibit polarity according to whether the alpha- or beta-subunit of the tubulin protein dimer is exposed. The alpha- and beta-subunits of the dimer correspond to (-) and (+) ends of the filament, respectively. This asymmetry is relevant when observing the direction of microtubule transport. Cargo is transported on tubulin via motor proteins that utilize energy from ATP hydrolysis for mechanical movement. Two such motor proteins are dynein and kinesin, which attach to microtubules and move toward the (-) and (+) ends, called retrograde and anterograde transport, respectively. Kinesin has also been observed in retrograde transport toward the (-) direction with the ability to switch direction. [203, 138]

Microtubules in neuronal projections also exhibit polarity that is relevant to transport of subunits in or out of axons and dendrites. Axons are oriented such that the (+) end of microtubules aligns with the axon terminal. Microtubules in most dendrites have mixed polarity, with fibers oriented in both directions. In distal dendrites, like axons, the (+) directions point toward the distal tips. Trafficking in neurons is generally mediated by kinesin motor proteins from the KIF gene family. Ion channels can either be (1) transcribed in the soma and transported as mRNA for translation in dendritic shafts/spines or (2) translated in the soma and transported in pre-protein or final protein form. Ion channels can attach directly to the microtubule structure but often attach within membrane vesicles exported from the Golgi apparatus after post-translational processing. [63, 203]

Ion channels in dendrites and axons are crucial to the normal functioning of a neuron. Voltage-gated ion channels are essential for signal initiation and propagation within a neurite, which ultimately contributes to neuronal intrinsic excitability within a network. Nucleic

acids and their protein products are relatively transient molecules in human cells, with average half-lives for human mRNA and protein at ~50 minutes and ~6.9 hours, respectively [201, 65]. A cell with numerous subtypes of voltage-gated channels must therefore have a precise, accurate, and robust mechanism of producing ion channels and segregating and distributing them throughout the cell. In multipolar neurons spanning over one millimeter in length, microtubule-based transport is hypothesized to be the primary means of transferring proteins to their site of function. This is especially true for ion channels with peak density in the distal dendrites and ion channels that are modulated for homeostatic or neuroplastic regulation of excitability.

1.3.2 Candidate cargo Kv4.2

To study transport and delivery in neurons, we select a candidate cargo from many prospective options. Of the dozens or hundreds of ion channel variants, the ideal cargo would be thoroughly studied and established as well as have an interesting distribution profile. For these reasons, we choose voltage-gated potassium channel Kv4.2 for experimental studies in this thesis.

In hippocampal CA1 neurons, Kv4.2 produces A-type current present in the membranes of soma, dendrites, and dendritic spines. Kv4.2 has an unusual expression profile—increasing density with distance from the soma [105]. Although other cargoes also exhibit this distribution (such as HCN channels), they are of particular interest because they contrast significantly with profiles arising from passive diffusion (decreasing density with distance from the source, the soma). Kv4.2 distribution is also polarized across neurite types; it is largely localized in dendrites with little or no static density in axons [208, 117, 3].

Further, there was also evidence of Kv4.2 regulation in response to excitation of the neuron. The ion channel redistributes to distal dendrites when the neuron is excited with AMPA stimulation, which is a chemical surrogate for electrical stimulation of the cell [118]. A trafficking study (discussed further in Sec. 1.3.4), also found increased local cycling rates—observed via fluorescence recovery—with AMPA stimulation [164]. These studies demonstrated that, at some level, Kv4.2 is regulated by neural excitability. Kv4.2 is therefore a good prospect for studies on global regulation of ion channel transport.

1.3.3 Kv4.2 function

Although not the primary subject of study, the function and computational roles of Kv4.2 are of tangential interest in the context of the channel's distribution and transport. A localization profile with increasing density from the source requires more energy than a profile resulting

from passive diffusion. Why would a neuron contribute resources to this distinct distribution if not for a critical function?

In hippocampal CA1 neurons, Kv4.2 produces A-type current present in the membranes of soma, dendrites, and dendritic spines. A-type currents are transient currents, which undergo rapid activation and inactivation. In contrast, delayed rectifier channels (such as Kv2.x, Kv3.x, and others) pass sustained potassium currents, which are slowly inactivating or non-inactivating. [219]

There are a few proposed functions of Kv4.2 in the published literature, largely related to dendritic excitability and signal integration. Kv4.2 is hypothesized to attenuate back-propagating action potentials, prevent action potential initiation in dendrites, prevent excessive postsynaptic depolarization, and temper long-term potentiation. [106, 105, 155, 114, 30, 119, 43, 118] Kv4.2 has also been implicated in the pathogenesis of several neurological disorders, including fragile X syndrome, autism, epilepsy, and Alzheimer's disease. [16, 213, 82, 84, 87, 153]

1.3.4 Kv4.2 trafficking

Limited studies have focused specifically on long-distance subcellular trafficking of Kv4.2. For instance, Kv channel-interacting proteins (KChIPs) have been established as auxiliary subunits that promote Kv4.2 exit from the endoplasmic reticulum for surface expression, partially mediated by CaMKII [209, 243, 196]. Another subunit, dipeptidyl aminopeptidase-like protein 6 (DPP6), is attached to Kv4.2 by a transmembrane domain and extends into the extracellular space [143], and, like KChIPs, assists in trafficking Kv4.2 out of the endoplasmic reticulum to the plasma membrane and during inactivation recovery [134]. Kv4.2 was found to interact with kinesin Kif17, lending support to transport on microtubules. In the absence of Kif17, Kv4.2 fails to localize in dendrites [49]. Deletion of 16 aa at the C-terminus or fusion with myosin Va restricts expression of Kv4.2 in the somatodendritic region [112, 133, 194]. Duménieu et al summarize these results with a hypothesis that Kv4.2 is trafficked short distances on actin filaments with myosin Va, such as to proximal dendrites or within spines, whereas Kv4.2 is trafficked longer distances on microtubules with KChIPS and Kif17 [63].

Kv4.2 density on the plasma membrane decreases in response to cell stimulation, and internalization is mediated by protein kinase A [118, 88]. Membrane-bound Kv4.2 subunits appear to have different sites of phosphorylation based on location along the dendrites of various cell types. This suggests that phosphate groups might contribute to targeting of subunits to specific regions of dendrite [242]. In addition, dephosphorylated Kv4.2 has been phosphorylated at different sites by CaMKII (at Ser438 or Ser459) and PKA (Ser552) to increase and decrease surface expression of the channel, respectively [243, 88].

Even fewer studies have explored the distribution and motion of Kv4.2 on the plasma membrane, the protein's final destination and site of its primary function. Nestor and Hoffman performed one of the few published accounts of microscopic visualization of Kv4.2 membrane trafficking [164]. They used fluorescence recovery after photobleaching (FRAP) microscopy to observe cycling rates of GFP-tagged Kv4.2. The authors found that basal cycling rates increased tenfold as distance from soma increased. AMPA-stimulation increased diffusion rates in distal dendrites, but a Kv4.2 mutant lacking a phosphorylation site for PKA abolished this distance-dependent change in cycling. They lastly conclude that their FRAP recovery curve fits a two-phase function of exponential decay, indicating "that Kv4.2g channels transiently interact with immobile cellular structures." Filamins and large adaptor proteins are suggested as immobile structures that might be anchoring and constraining the diffusion of Kv4.2. [164]

All in all, the details of Kv4.2 trafficking are largely unknown with many open questions. There is great potential for study of both the molecular mechanisms of Kv4.2 transport as well as the general logistics of ion channels with this unique somatodendritic profile.

1.3.5 Relation to drift-diffusion

The transport of ion channels and other cargo through neurites can altogether be described with the one-dimensional drift-diffusion equation. The evolution of cargo concentration over time is related to a diffusion term with coefficient D and an drift term with coefficient v . D and v describe the bulk flow of a population of particles. In the context of ion channel trafficking, D corresponds to a combination of diffusive processes, including diffusion in the cytosol, diffusion in the plasma membrane, and movement on microtubules. v corresponds to the bias of the random walk on the microtubule, which manifests as a velocity.

Because drift-diffusion in observed transport of cargo is the superposition of at least three types of linear transport, the magnitude of each can be analyzed independently. For instance, one might isolate the active (energy-dependent) process of microtubule diffusion from other passive diffusion processes by disrupting microtubules, depriving of the cell of energy carriers, or otherwise disrupting microtubule function.

1.4 Overview of neuroplasticity and regulation

The biological neuron is the elementary unit of signal transmission in the brain. In the context of a network, a neuron can be represented as an input-output model. A typical neuron receives one or more inputs in the form of excitatory postsynaptic potentials (EPSPs)

or inhibitory postsynaptic potentials (IPSPs) to the neural dendrites. These signals are propagated throughout the complex, branching dendritic arbor and integrate in the cell soma. The singular output is the action potential transmitted along the neural axon. Action potentials are often initiated in the axon initial segment and are direct functions of the membrane potential in the soma. The description of a neuron as an input-output system facilitates the study of its homeostatic tendencies, such as when exposed to perturbations or changing environments.

Like many biological organisms and cells, neurons exhibit a tendency to maintain stability and auto-regulate a number of their features and properties. This collective proclivity to maintaining a stable internal state is termed homeostasis. For instance, a neuron whose neurites are severed or otherwise damaged can regrow axons and dendrites to reestablish synaptic connections and maintain connectivity in a circuit. Another example can be found in intracellular calcium: a stable calcium concentration is maintained with buffers and internal stores, since calcium is an important biochemical regulator of enzyme cascades and neurotransmitter release. A typical method of homeostatic maintenance is through feedback regulation, in which a neuron detects a change in some feature or property and makes appropriate internal adjustments to accommodate or control that change.

Another accommodation that a neuron can make in response to perturbations is regulation of transport. To this end, the cell can modify cargo trafficked long or short distances. For instance, a membrane-bound protein might be externalized/internalized to/from a nearby surface in response to an electrochemical stimulus. Further, new subunits of this protein can be transcribed in the soma and distributed over long distances to functional sites. This problem of cell regulation is particularly unique for some neurons given their size. For instance, pyramidal neurons have cell projections that span hundreds or thousands of microns from the cell body. This necessitates an interplay between global and local regulation mechanisms to maintain homeostasis. Global and local regulation both have distinct advantages and disadvantages, so this interplay creates a number of trade-offs that warrant discussion. Closed-loop models of cargo trafficking allow for the study of these trade-offs in the context of neuron adaptation.

What follows are experimental examples of cargo transit that modifies cell properties in response to perturbation. The models and simulations of cargo transport in this thesis are agnostic to cargo type and can be applied to these examples or others.

1.4.1 Intrinsic excitability

Homeostasis has been observed for the maintenance of intrinsic excitability. The property of intrinsic excitability is complex, but it can be broadly described as the degree to which

a neuron responds with output when exposed to a given input. A discussion of neuron excitability can comprise all elements of the neural response, such as response time, degree of depolarization, firing rate, and number of spikes. Moreover, neuron excitability incorporates all cell processes involved in this response, ranging from transmission of input into dendrites, propagation through branches, integration of signals into the primary trunk, spread of signal to the soma, finally resulting in action potential initiation. Experimentalists have found evidence for feedback regulation in several of these mechanisms. A few studies have directly attributed a mechanism of homeostatic maintenance to regulation of ion channels [60, 24, 241]. No studies thus far have examined how longitudinal trafficking of ion channels in dendrites might play a role in homeostasis.

Dendrites have adapted to boost signals in a unique way. Signal propagation in dendrites operates in a finely-tuned middle ground between that of passive cables and fully-excitabile axons. Because dendritic potentials are far from the unyielding, all-or-nothing response found in axons, they are more amendable to regulation by membrane conductances. The active tuning of dendritic potentials is therefore likely to be strongly related to ion channel density and distribution. In turn, the trafficking of ion channels is thereby implicated in regulation of dendritic potentials. The role that ion channel trafficking plays in modulating dendritic signal propagation and thus in homeostasis and feedback regulation of neuron excitability has yet to be explored.

Indeed, global regulation of ion channels has been implicated in regulation of intrinsic excitability [178, 179, 78]. However, no study thus far has evaluated Kv4.2 in this regard. We observe longitudinal transport of Kv4.2 while perturbing neurons in Chapter 3. We also theoretically analyze the global regulation of AMPA receptors in the well-established phenomena of synaptic scaling in Chapter 6.

1.4.2 Spike-timing-dependent plasticity

Perhaps the most prominent example of regulation in neurons is synaptic plasticity. Synaptic plasticity refers to modulation of neuronal excitability at the level of the synapses, the junctions through which signals pass from one cell to another. Synapses can strengthen or weaken over time. Synaptic plasticity can be broadly categorized according to whether changes in synaptic strength are based on the relative timing of activity in the pre- and postsynaptic neurons. Synaptic plasticity that is induced by high temporal correlation of activity between cells of a synapse is called spike-timing-dependent plasticity (STDP). The major, relevant forms of STDP are discussed here.

STDP can be further categorized according to whether changes in synaptic strength are positively or negatively related to synaptic activity. Hebbian plasticity is a change in

synaptic strength that is consistent with (positively correlated with) synaptic activity. Hebbian theory is typically summarized with Hebb's rule: "neurons that fire together wire together" [93]. If a synapse experiences increased activity, the strength of that synapse increases. Similarly, decreased activity results in decreased synaptic strength. With regard to neuron excitability, Hebbian plasticity is not homeostatic. The neuron does not maintain an internal excitability; rather, excited synapses are made more excitable and inactive synapses are depressed further. Hebbian plasticity in its simplest form is positive feedback and unstable; many implementations modify the theory with thresholds, limits, or other modifications to account for this. The principles of Hebbian plasticity are thought to underlie learning and memory in the brain. [26] Hebbian is hypothesized to be mediated by homeostatic plasticity, which is non-STDP (discussed in Sec. 1.4.3). STDP that follows a *reversal* of Hebb's rule is termed anti-Hebbian. Here, synaptic strength decreases with increased association in action potential firing between pre- and postsynaptic neurons. [121]

We can also categorize synaptic plasticity at the level of individual synapses. An activity-dependent increase or decrease in a synapse's strength is called long-term potentiation (LTP) or long-term depression (LTD), respectively. LTP and LTD can occur at varying levels of granularity—from individual synapses to dendritic branches. LTP and LTD can be either Hebbian or anti-Hebbian, and they can happen at excitatory and inhibitory synapses alike. The mechanisms underlying LTP and LTD are complex and vary between brain regions and organisms [13, 145, 76]. In this study, we model LTP and LTD with changes in AMPA receptor density in the context of synaptic scaling (see Secs. 6.3 and C.1.6). Activity-dependent changes in synapses are not necessarily permanent. Brief, transient changes in synaptic strength are called short-term potentiation (STP) or depression (STD) and last over timescales of minutes [200, 171]. These processes specifically—LTP, LTD, STP, and STD—are widely believed the basis of learning and memory.

1.4.3 Other synaptic plasticity

Non-STDP refers to mechanisms of synaptic plasticity that do not depend on coordination between pre- and postsynaptic neurons.

Homeostatic plasticity is a change in synaptic strength that is independent of synaptic activity, returning a neuron to an initial state. The neuron maintains an internal excitability: overactive synapses are scaled down and underactive synapses are scaled up to minimize distortions to net neuron excitability. This is by definition homeostatic, and such plasticity might limit the synaptic changes induced through Hebbian theory. A proposed method of homeostatic plasticity is synaptic scaling. If synaptic scaling is implemented as a multiplicative (rather than additive) manner, a neuron maintains the relative strengths of the synapses,

thus preserving any information encoded in them. [233–235]. Homeostatic synaptic scaling is further discussed in Sec. 6.2.

The physiologic mechanisms of Hebbian and homeostatic plasticity revolve around the glutamate receptors. This includes receptor trafficking as well as modulation with calcium and second messenger systems. The models described in Chapter 6 concern both mechanisms. Short-distance trafficking includes recruitment and withdrawal of glutamate receptors to/from the plasma membrane. Long-distance trafficking supplies local regions of the neurite with a pool of receptors for shuttling to and from distant compartments.

Lastly, any change in the structure of the nervous system is broadly termed structural plasticity. Structural plasticity can range from the molecules present in the synapses to interconnections that form new neural circuits, changing anatomical organization. Structural changes can be induced by STDP and non-STDP means, alike. [128, 27, 36]

1.5 Research questions

The overarching research goals are stated in the following questions. These aims are organized under **key questions**, each with several sub-questions that state specific, testable objectives.

1.5.1 Empirical investigation

How are ion channels, such as Kv4.2, distributed throughout a pyramidal neuron? The first set of research questions are testable by means of laboratory experiments. The answers to these questions can be directly observed using neuron cultures and microscopy. Collecting a large and organized data set is crucial to this empirical investigation. Does transport occur via passive diffusion, active microtubule-based mechanisms, or some combination of both?

To study passive transport, we can perform a series of photobleaches and measure the diffusive recovery of ion channels. Can a directional bias in bleach recovery measured during FRAP microscopy be used to compute drift within neurites? Does bleach recovery rate or mobile fraction change with recurrent photobleaching?

To study active transport, we observe the stochastic bidirectional movement of membrane vesicles containing Kv4.2. How does transport behavior quantitatively and qualitatively differ throughout the neuron—by neurite type, with neurite distance? How do puncta kinetics differ between these categories? Does the neuron modulate Kv4.2 transport as a means of regulating its intrinsic excitability in response to perturbation?

1.5.2 Analytical inquiries

What additional physiologic conclusions can be deduced from our empirical data on Kv4.2 transport? The second set of research questions depends on the data set gathered during experiments. These involve mathematical methods including modeling, statistics, and inference.

Regarding passive transport: Does bleach recovery after photobleaching reflect rates of cargo transfer between mobile and immobile fractions, and what are these estimated rates for Kv4.2? How does this impact the distribution and settling time of cargo in real neuron morphologies?

Regarding active transport: Can discordance between static localization and mobile frequency of Kv4.2 be reconciled with discretized mass action models of lumped or discretized neurites? To what degree do underlying mechanisms (propensities for microtubule offloading, directional memory) result in kinetic differences in axons versus dendrites?

1.5.3 Theoretical study

What are the limitations of cargo distribution in large morphologies, and how does the interplay between global and local regulation affect this? The last set of inquiries apply concepts, data, and trends from the previous types of inquiries to reach broader conclusions on neuron logistics.

How long does it take for a cargo like ion channels to fully distributed and settle in a realistic neuron morphology? Does this settling time impose any limitations for highly regulated ion channels?

Synaptic scaling is a neuronal mechanism of homeostatic plasticity that requires global regulation of AMPA receptors. How do the dynamics of ion channel distribution, as explored in previous inquiries and other experimental studies, impose limitations on synaptic scaling? How does a neuron balance the stability, efficiency, and accuracy of synaptic scaling? How can these attributes be quantified in a rigorous manner, and what are the resultant tradeoffs between them? Do these limitations drastically depend on neuron morphology—size, symmetry, and/or bottlenecks? How and to what degree do these metrics affect scaling performance?

1.6 Recapitulation

Neurons are distinct among cells in their morphology, with projections that spread hundreds to thousands of microns. The size and asymmetry of neurons pose a challenge for autoregulation

of properties that require cargo transport across the cell. Ion channels are one such cargo with strong implications for neural excitability. This dissertation concerns the intracellular distribution of ion channels in the context of global neuron regulation. To this end, passive and active mechanisms of Kv4.2 transport are studied with a focus on trafficking kinetics and channel distribution in axons and dendrites. Synaptic scaling is a quintessential mechanism of ion channel regulation, as it requires global modulation of AMPA receptors for homeostasis of neural excitability. This thesis also explores the limitations imposed by neuron morphology on synaptic scaling.

The study of ion channel distribution and regulation is complex with many unconfirmed hypotheses, unclear mechanisms, and open questions. This work describes a small advancement in this field. These contributions are in the form of experimental measurements, data analysis, and theoretical study.

Chapter 2

Methods and experimental validation

2.1 Chapter summary and key findings

Experimental validation establishes competency required for efficient collection of consistent, meaningful data. Routine protocols include dissection and culturing of hippocampal cells as well as techniques for imaging and microscopy. This chapter also includes pilot trials and optimization experiments.

1. Pyramidal cells are reliably identified in hippocampal cell cultures for terminal experiments. A number of features are observed during microscopy as indicators of neuron health and maturity. Microscopy also differentiates cell types and between axons and dendrites.
2. The sampling rate of a time series balances the number of data points obtained with the amount of unintentional photobleaching and damage to the sample. Low sampling rate can produce misleading estimates of transport dynamics. An ideal time series maximizes the number of frames captured while ensuring no or negligible damage to the sample.
3. The set number of bleach iterations during FRAP microscopy is a tradeoff between degree of bleaching and time required for bleaching. The ideal number of bleach iterations is the minimum required to bleach to 30 to 70% of original sample fluorescence.
4. FRAP microscopy curves can be normalized and fit to single or double exponential curves. This provides an estimate for recovery rate and mobile fraction.
5. Time series fluorescence microscopy can visualize mobile puncta containing Kv4.2. Photobleaching can clear static fluorescence for improved puncta tracking. Puncta mo-

bility decreases following colchicine administration, suggesting an active mechanism of transport that is microtubule-based.

6. Raw time series can produce kymograms of 1D transport to reliably visualize puncta trajectories. Kymogram post-processing, thresholding, and strict protocols for puncta appearance/disappearance, merging/splitting, and stalling ensure that puncta trajectories are tracked objectively and carefully.

2.2 Introduction

This chapter broadly covers the methods for all experiments, data analysis, modeling, and inference. I describe the materials, recipes, and methods for performing experiments, microscopic imaging, and obtaining data. The analysis of images and data is reported here. In some cases, detailed methods are more appropriately described in the context of their specific results. Therefore, some methods described here are general protocols that are broadly applicable to the subprojects of this thesis. An overview of the computational methods is covered, including modeling, statistical inference, and other heuristic methods. Analytical solutions and derivations that are supplemental to experimental or modeling results are included in the Appendices.

The remaining chapters of this thesis contain the main results of these graduate studies. The experimental validation in this chapter serve as an introductory results for the rest of this work. These preliminary experiments were performed both as exploratory research and in preparation for future experiments.

Experimental validation ensures experimental consistency not only among results in this thesis but also with the surrounding scientific community. For instance, what is deemed a cultured pyramidal cell in these results should be compatible with typical pyramidal cells in other studies. These established standards then translate to terminal experiments. For example, the morphological features, structures, and antibodies used to differentiate axons and dendrites should be well established before interpreting results based on neurite type.

Many of these results were obtained early in this course of study. Much of this chapter confirms methods and results from our groups or others before us. But these experiments were nonetheless necessary. Some of these protocols, such as hippocampal dissections, require hours of practice for even minimal proficiency. Many of the protocols are difficult and require mastery for consistent results.

The methods and experimental validation presented here is not necessarily novel or groundbreaking, but they are certainly beneficial for several reasons. Some results have

inspired new investigations, as in FRAP microscopy revealing underlying microtubule-based transport. Some of these results, such as differentiating axons and dendrites, directly precede more impactful terminal experiments. Experimental controls increase the reliability of our results. Some results impacted the course of the thesis and are promising leads for future projects. All preliminary results form the foundation for the remaining work in this thesis.

2.3 Animals and cell culture

All animal procedures are conducted with accordance of the National Institutes of Health Guide for the Care and Use of Laboratory Animals under a protocol approved by the National Institutes of Child Health and Human Development's Animal Care and Use Committee.

2.3.1 Hippocampal dissection and dispersed cultures

The neurons used here and throughout the remainder of this thesis are from primary hippocampal cultures. Hippocampal cultures are prepared from gestational day 18-19 wildtype Sprague-Dawley rats or wildtype mice as previously described [118]. Briefly, fetal pups are removed from the mother and hippocampus tissues are dissected and placed in dissection media (DM). For 500 ml of DM, we filter sterilized: 50 ml 10x HBSS (Gibco™, 14185-052), 5 ml pen/strep (Gibco™, 15140122), 5 ml pyruvate (Gibco™, 11360070), 5 ml HEPES (1M, Gibco™, 15630080), 15 ml of 1 M stock solution glucose (from powder, Sigma), 420 ml Ultra Pure Water (Kd Medical Inc).

Tissue was mixed with papain (Worthington Biochemical Corp., Lakewood, NJ) for 45 min at room temperature. Tissues were rinsed for removal of extracellular material with dissection media several times, and dissociated cells were plated in Neurobasal™ media (ThermoFisher, Waltham, MA) with 5% FBS (HyClone Characterized Fetal Bovine Serum, SH30071.03, GE Healthcare LifeSciences, Pittsburgh, PA), 2% GlutaMAX (ThermoFisher), and 2% Gibco™ B-27™ supplement (ThermoFisher) (subsequently called NB5 media). Cells were incubated in 5% CO₂ at 37 deg C. After 24 hrs, cells were transferred to Neurobasal™ containing 2% GlutaMAX, 2% Gibco™ B-27™ supplement (NB0 media). Half of the media is replaced with fresh NB0 media every three to four days, and cells are imaged after 9-13 days *in vitro*.

Despite strict protocols for rat hippocampal dissection and culturing, there is inevitable variability in the results. During dissection, pregnant rats were found to have a variable number of pups. Typical litter sizes for our supplier ranged from 10-12 pups. As many as 17 and as few as 2 pups per litter were observed. Oftentimes, the pups varied in size. A typical

litter also has at least one significantly smaller, runted pup that was omitted from neuron preparation.

Dissection of the hippocampus itself also varies with the size of the pups. Smaller pups require more manual dexterity and increased precision to obtain a clean cut of the hippocampus. However, smaller pups might be less developed such that their brains contained a greater fraction of stem cells. We therefore extracted hippocampi from pups of all sizes with the exception of visibly runted pups. The hippocampus was often unintentionally broken but still collected in fragments. We aimed to minimize the collection of extraneous, non-hippocampal tissue to amass a sample with a high fraction of hippocampal cells.

2.3.2 Construct

A Kv4.2 construct was conjugated at the N-terminus to strongly enhanced green fluorescent protein (SGFP2) [123], henceforth referred to as Kv4.2-SGFP2. pSGFP2-C1 was a gift from Dorus Gadella (Addgene plasmid # 22881 ; <http://n2t.net/addgene:22881> ; RRID:Addgene_22881). We sub-cloned mouse Kv4.2 into the SGFP2 plasmid using NheI and SalI restriction sites.

2.3.3 Transfection

Lipofectamine® 2000 transfection was performed following manufacturer protocol with some modifications. 2 µl of Lipofectamine® 2000 Transfection Reagent (ThermoFisher) and 2 µg of DNA plasmid were each diluted in 200 µl of Neurobasal™ media and incubated at room temperature for 5 min. The two solutions were then combined and incubated at room temperature for 15-20 min. 100 µl of total mixture was added to each well and incubated at 37 deg C for 4 hrs before changing media. The cells were then incubated for an additional minimum of 1 hour before imaging.

2.3.4 Immunostaining

Following hour-long time series, samples reserved for antibody staining were fixed/permeabilized and immunostained as previously described [119, 136] and briefly reiterated here. Upon completion of time series, the coverslips were removed from the imaging chamber and the location of the neuron of interest was labeled with a fine tip marker. Coverslips were fixed with 4% paraformaldehyde (Electron Microscopy Sciences, R 15710, Hatfield, PA) with 4% sucrose (Sigma, S9378) at room temperature for 15 min followed by three 1X PBS (Gibco™, 14190) washes before overnight storage in 1X PBS at 4 deg C. Coverslips were permeabilized

Table 2.1 This table compiles all antibodies used for fluorescence immunostaining and electron microscopy in this study.

<u>Name</u>	<u>Species</u>	<u>Manufacturer</u>	<u>Catalog #</u>	<u>Dilution/concentration</u>	<u>Clonality</u>
Primary antibodies					
Ankyrin G	Mouse	NeuroMab	75-146	1:100	mono
Tau-1	Mouse	Chemicon	MAB-3420	1:1000 to 1:3000	mono
MAP-2	Mouse	Millipore	MAB-3418	1:300	mono
Kv4.2 (for human & mouse)	Rabbit	Made in lab	-	1:200	poly
Secondary antibodies					
Alexa Fluor® 555 anti-mouse IgG	Goat	Invitrogen	A-21424	1:500	poly
Alexa Fluor® 488 conjugate anti-GFP	Rabbit	Invitrogen	A-21311	1:400	poly
Alexa Fluor® 488 anti-Rabbit IgG	Goat	Invitrogen	A-11034	2 mg/mL	poly
Anti-rabbit IgG 10 nm gold conjugate	Goat	Ted Pella, Redding, CA	17010-1	-	mono

in 0.2% Triton X-100 (Sigma, T8787) for five minutes at room temperature and washed once in 1X PBS for 5 min. Cells were incubated for one hour at room temperature in 0.04% Triton X-100 solution in 1X PBS containing primary antibody. Upon completion of primary incubation, coverslips are washed three times with 1X PBS for 5 min. Coverslips are then incubated with secondary antibodies for one hour at room temperature before another three washes with 1X PBS. Coverslips were then mounted onto glass slides using ProLong™ Diamond Antifade Mountant containing DAPI (Invitrogen, Carlsbad, CA). A full list of antibodies used in this study is provided in Table 2.1.

2.4 Cell and neurite morphology

Cultured neural hippocampal cells undergo extensive preparation—from plating tissue to feeding cells and terminal experiments. It is therefore important to understand cell and neurite morphology throughout this process and when identifying cells and neurites for data collection. Morphology as observed through a light or confocal microscopy can reveal telling signs regarding cell type, neurite type, as well as neuron development and health. A good understanding of morphology allows a scientist to identify not only proper cell/neurite subtypes for observations but also pathological signs or conditions that might disrupt experiments. Given the large degree of natural variation in biological experiments, these guidelines are crucial for collection of consistent data.

2.4.1 Differentiating cell types

It is firstly important to differentiate cells in the cell culture. Ideally, dispersed hippocampal cultures contain predominantly CA1 and CA3 hippocampal pyramidal neurons. However, this

is not always the case, since these are mixed cultures. Other cells might include interneurons, cortical neurons (which can be pyramidal or other morphologies), epithelial (blood vessel) cells, and glial (nonneuronal support) cells.

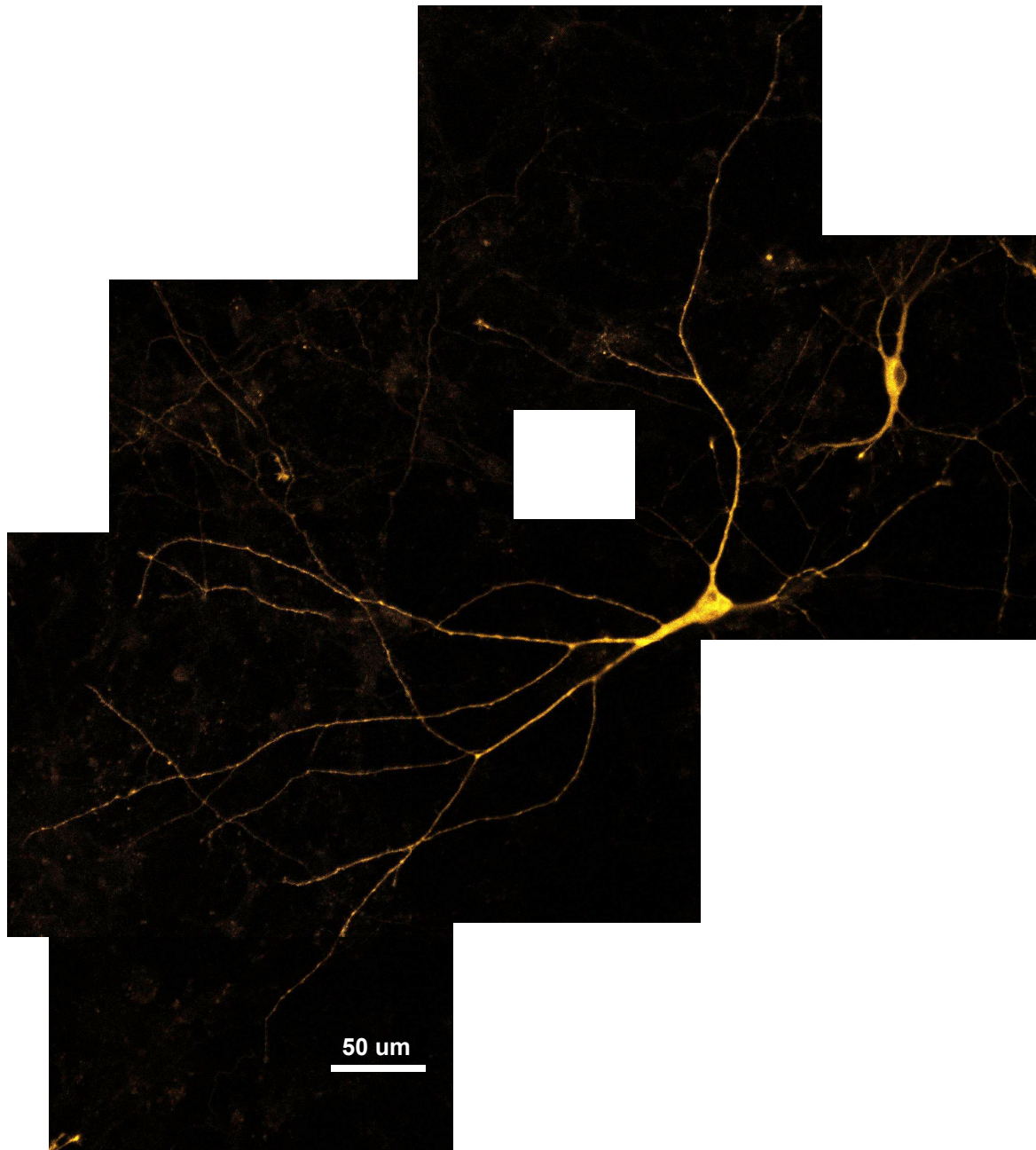


Fig. 2.1 This collage of micrographs from a hippocampal cell culture depicts a prominent pyramidal cell with the characteristic conical-shape soma in the center. A non-pyramidal cell with a rounded, spherical soma is visible to the right. Orange indicates transfected subunits of Kv4.2-SGFP2.

Terminal experiments in this study use exclusively pyramidal cells. Pyramidal cells are so called because of their triangular-appearing or conic-shaped soma. In this study, pyramidal cells are categorized according to the conic-shaped soma, and non-pyramidal cells are not categorized any further. A neuron that is clearly pyramidal is prominent in Fig. 2.1. Note the apical dendrite, the thickest dendrite extending out the apex (in Fig. 2.1 pointing southwest). The other neurites emerging from the base (northeast) of the soma are the basal dendrites. In this image, we can appreciate the full length of the neurites, bifurcating regularly and extending hundreds of microns from the soma. This micrograph also contains a smaller neuron (right) that is not pyramidal.

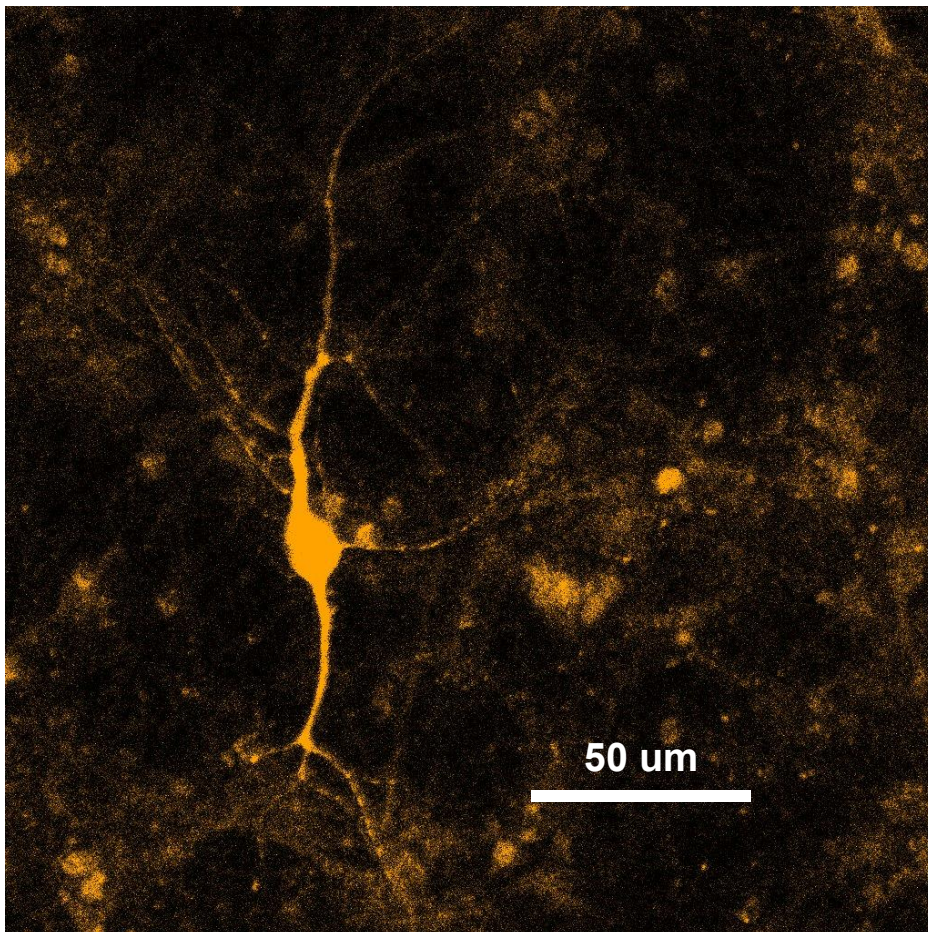


Fig. 2.2 This micrograph contains a cell with a soma that is distinctly non-pyramidal. This cell lacks the conical-shaped soma or the definitive apical dendrite of a pyramidal cell. Orange indicates transfected subunits of Kv4.2-SGFP2.

A prominent example of a non-pyramidal neuron is depicted in Fig. 2.2. Note the round, spherical soma that does not have a well-demarcated apical tip. This cell has two large, similar-sized dendrites—neither of which is differentiable as the apical dendrite. Such a cell

would not be used in terminal experiments of this study. This micrograph also highlights the degree of background noise surrounding neurons, especially in samples with low fluorescence. The patterned fluorescence behind the non-pyramidal cell is a combination of neurites from other neurons, glial cells, noise, and autofluorescence from transfected cells.

In an attempt to reduce variability in results, terminal experiments exclusively use pyramidal cells. To this end, differentiation between cell types on the basis of soma morphology is a useful skill.

2.4.2 Differentiating neurites

Pyramidal cells have significant morphological heterogeneity especially in dispersed cultures. The stereotypical assembly of a polarized neuron with distinct axon and dendrites does not necessarily hold for all observed pyramidal cells. For instance, neurons with multiple axons have been observed in dispersed cultures. Further, the axon frequently emerges from a dendritic trunk rather than the soma. [104, 227, 14]. This diversity in neuron structure motivates precise methods of differentiating neurites for terminal experiments, since both axons and dendrites are used in terminal experiments.

Axons and dendrites are primarily sorted based on their diameter and morphology. Axons are thinner ($\leq 1 \mu\text{m}$ in diameter), and dendrite thickness ranges (approximate range: 1 to 5 μm). Dendrites exhibit a steady decrease in diameter with distance from the soma and terminate well within 1000 μm . In comparison, axons extend for thousands of microns with diameters that taper less. The most significant differences in diameter are in the neurite trunks: the axon initial segment is thin like the rest of the axons, at a few microns, whereas dendritic trunks can be several microns thick and broadly blend into the plasma membrane of the soma. In addition, dendrites branch more frequently and at more acute angles, whereas axons can branch at perpendicular or even obtuse angles. Oftentimes, the morphological features differentiating axons and dendrites are not visible in the frame of the time series, and additional global images of the neuron must be referenced to distinguish neurites. An example of this is depicted in Fig. 2.3, where the frame of the time series is outlined in red, but the defining morphological features of the axon and dendrites are only visible in the larger, global image. In Fig. 2.3, an axon (red) and dendrite (blue) exhibiting the aforementioned characteristics are labeled.

During microscopy, neurites are differentiated according to the aforementioned morphological features. During image analysis, the diameters of the neurites are measured. We analyze our data to set a precise threshold in neurite diameter for categorizing axons and dendrites, depicted in Fig. 2.4. A histogram of undifferentiated neurite diameters produces a bimodal distribution with peaks at approximately 0.7 and 1.7 μm (Fig. 2.4 *top*). Categorizing

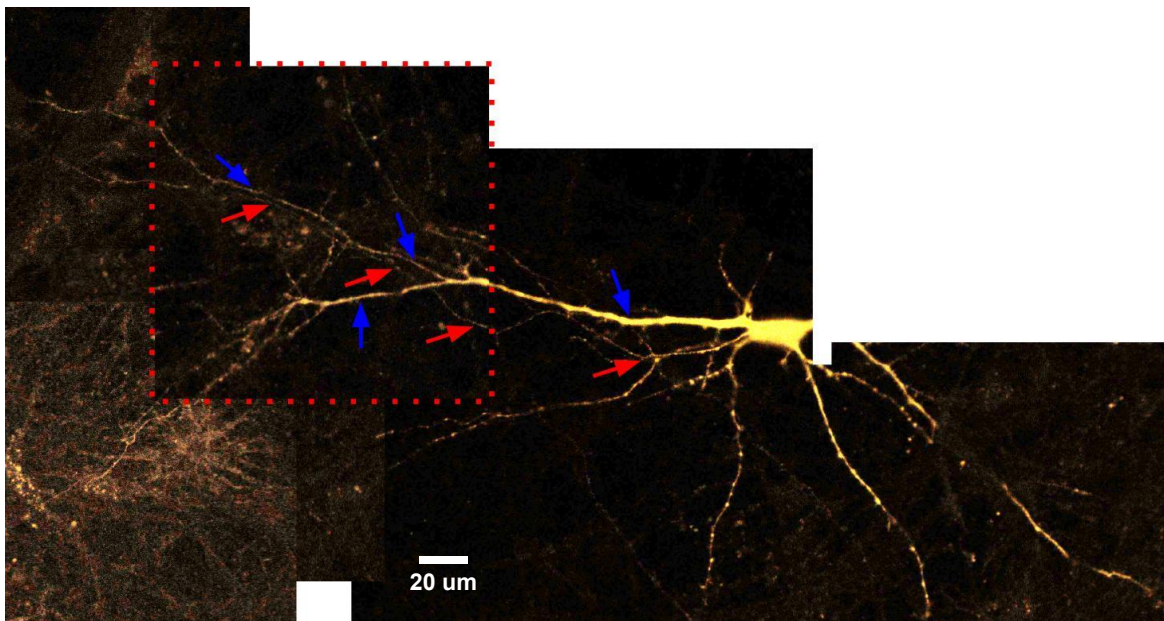


Fig. 2.3 A high magnification frame for time series (outlined in the red dotted line) can make differentiating axons (red) and dendrites (blue) difficult. Low-magnification global images tracing the neurites back to the soma can help with differentiation. In this neuron, the dendrite clearly has branching at acute angles and a thick trunk that blends into the soma. The axon branches at obtuse angles and has a thinner diameter that does not taper. Orange indicates transfected subunits of Kv4.2-SGFP2.

neurites according to the aforementioned morphological features during microscopy aligns well with the two observed peaks (Fig. 2.4 *bottom*). Based on this distribution, we set a precise diameter threshold at 1 μm . Neurites with axonal morphological features and diameters less than 1 μm are designated axons. Neurites with dendritic morphological features and diameters greater than 1 μm are designated dendrites. Only one neurite did not meet these criteria (axon #37) and was omitted from subsequent results. The mean diameter of populations of axons and dendrites are 0.698 and 1.91 μm , respectively. A two-sample t-test reveals that these populations have significantly different diameters ($P = 3.5 \times 10^{-35}$).

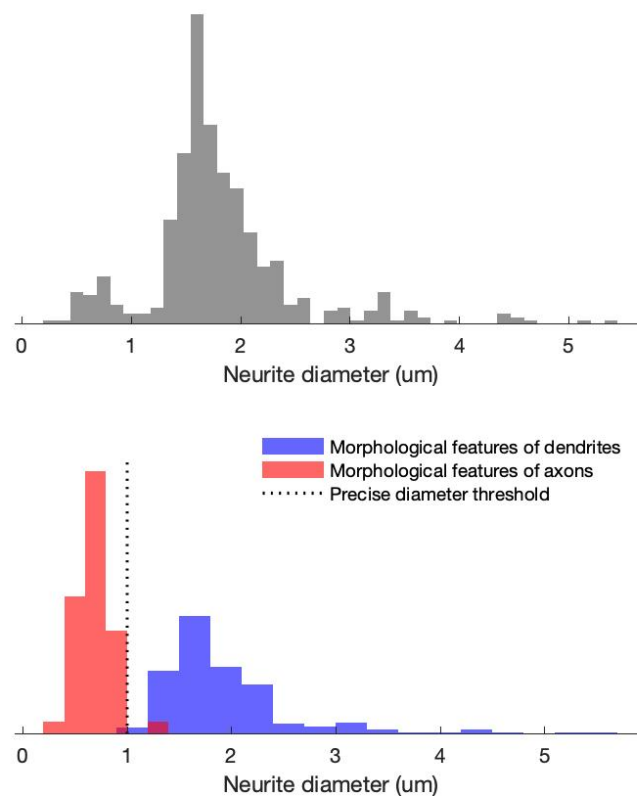


Fig. 2.4 A precise threshold for differentiating axons and dendrites is defined according to neurite diameter. *Top*: Undifferentiated neurite diameters show a bimodal distribution. *Bottom*: The observed morphological of axons and dendrites during microscopy separate well into the two modes in the distributions, motivating a precise diameter threshold at 1 μm . Differences between populations are statistically significant ($p = 3.5 \times 10^{-35}$). All histograms are normalized as probability density functions.

Aside from these morphological changes, a definitive way to differentiate neurites is with antibody staining for structural proteins exclusively found in one neurite type. Four coverslips were stained with ankyrin-G post live imaging to confirm identification of the axon initial segment. One such neuron is depicted in Fig. 2.5. We compare these definitive axons (stained

with ankyrin-G) to the dataset of probable axons (based on the aforementioned morphological features, including diameter $< 1 \mu\text{m}$ and obtuse-angled branching). We compare the number of mobile puncta per one-hour recording in Fig. 2.6 and demonstrate no significant difference between populations ($P = 0.37$). This comparison of neurites with live physiologic data validates our identification of dendrites by morphology with a precise diameter threshold.

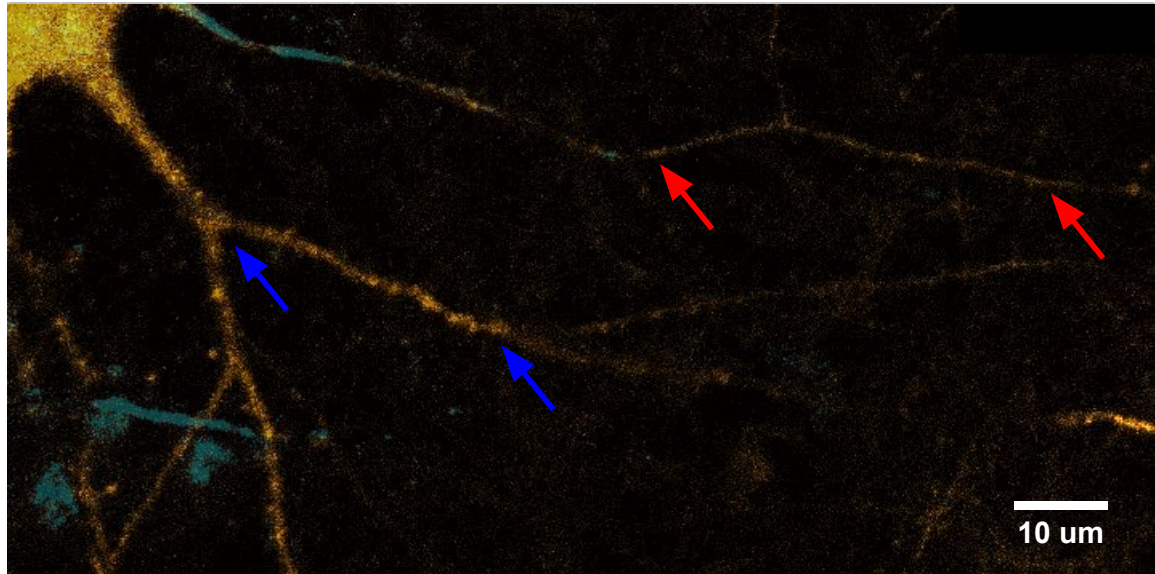


Fig. 2.5 Anti-GFP-488 (orange) indicates Kv4.2-SGFP2 expression and ankyrin-G (cyan) localized to axons are used for definitive neurite differentiation. This is a frame of a time series that depicts characteristic high frequency trafficking in axons (red arrow) compared to dendrites (blue arrow).

2.4.3 Differentiating dendrites

We have thus far discussed identifying pyramidal cells with the conical-shaped soma and apical dendrite. We have also differentiated axons and dendrites based on branch angle and diameter. However, micrographs of pyramidal dendrites still exhibit significant variability, which can be an indicator of cell age and health. Selecting healthy cells of consistent maturity is crucial for terminal experiments. To this end, the varying morphological features of pyramidal dendrites are discussed here.

Pyramidal dendrites firstly exhibit variability in their fluorescence heterogeneity. Fluorescence heterogeneity refers to the consistency of fluorescence patterns in the dendrites. For instance, the fluorescence might be evenly and uniformly distributed in a homogeneous pattern spread smoothly across the entire volume of the neurite. In contrast, the fluorescence

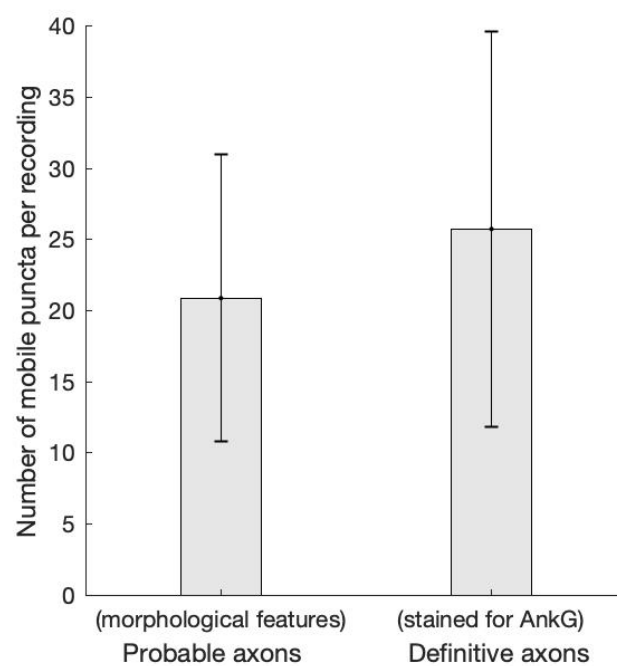


Fig. 2.6 Definitive axons (stained with ankyrin-G) and probable axons (identified by diameter and branch angle) are compared. The mean number of mobile puncta per recording for each population is plotted; error bars indicate standard deviation. Two-sample t-test indicates no significant difference between populations ($P = 0.37$), validating the use of morphological features as indicators for identifying axons.

can be clustered and aggregated into puncta or patterns with a patchy, uneven appearance, forming an irregular profile. These differences are visualized in Fig. 2.7.

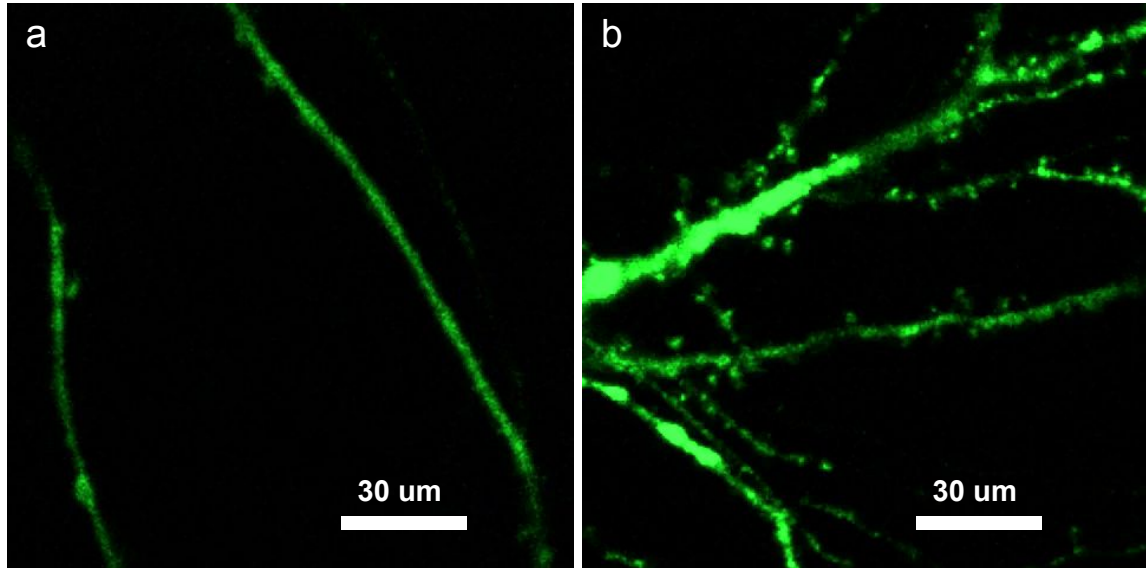


Fig. 2.7 These two dendrites demonstrate differences in morphology and fluorescence pattern. Dendrite (a) has a low degree of branching, a low spine count, and low fluorescence heterogeneity (with smooth, continuous intensity). Dendrite (b) has a higher number of branches and spines, a high fluorescence heterogeneity (with regions of patchy and variable intensity). These differences can be indicators of neuron age and health. Green indicates transfected subunits of Kv4.2-SGFP2.

Another observed difference is the presence of dendritic spines, also evident in Fig. 2.7. CA1 hippocampal pyramidal cells are known to be spiny, and spines might be used to indicate this cell type. However, spine development is not prominent until 12-14 DIV, so this differentiating factor is less useful for younger cultures. [169]

There are a number of potential reasons for these observed differences in Fig. 2.7. These cells might firstly be in varying stages of growth and development. For instance, Fig. 2.7a might resemble an underdeveloped neurite without spines that will eventually appear more like Fig. 2.7b. Neurons used in this study ranged in age from DIV 8-14, so cells with features as in Fig. 2.7a or b would both be used in terminal experiments.

Another possible difference is the health of the cells, especially considering the toxicity of reagents used for transfection. It is possible that the heterogeneous expression seen in Fig. 2.7b is indicative of an unhealthy, dying cell that previously looked like Fig. 2.7a but is now apoptotic. The patchy appearance might be caused by a membrane that has burst or fractured. It is therefore important to sample a number of cells per cover slip to get a general sense of cell health in that culture. It is good practice to do this repeatedly every few days during the

maturation of the neurons to ensure their health and normalcy. Typical signs of apoptosis or poor cell health include shrinkage, membrane blebbing, and fractured neurites. Cells with any of these features would not be used in terminal experiments in this study.

Familiarity with these differences can help with the selection of healthy cells for terminal experiments that produce consistent results. Next, we discuss the techniques and optimal methods for capturing micrographic images.

2.5 Electron microscopy

Electron micrographs used in this thesis were collected for a previous study [224]. Mouse hippocampi used for the postembedding immunogold localization were prepared as described previously [182, 224, 135, 89]. Mice were perfused with phosphate buffer, followed by perfusion with 4% paraformaldehyde + 0.5% glutaraldehyde in phosphate buffer. Fixed brains were vibratomed at 350 μm , then cryoprotected in glycerol overnight and frozen in a Leica EM CPC (Leica Microsystems, Wetzlar, Germany), and processed and embedded in Lowicryl HM-20 resin (Electron Microscopy Sciences) in a Leica AFS freeze-substitution instrument. Thin sections were incubated in 0.1% sodium borohydride + 50 mM glycine in Tris-buffered saline plus 0.1% Triton X-100 (TBST). Then they were immersed in 10% normal goat serum (NGS) in TBST, and primary Kv4.2 antibody in 1% NGS/TBST (overnight), Then incubated with 10 nm immunogold-conjugated secondary antibodies (Ted Pella, Redding, CA) in 1% NGS in TBST with 0.5% polyethylene glycol (20,000 MW), and stained with uranyl acetate and lead citrate.

Electron microscopy was used as a comparative measure of endogenous Kv4.2 subunit density in axons and dendrites, presented in detail in Chapter 3 and used as a modeling constraint in Chapter 4. Electron micrographs were captured from the hippocampus CA1-stratum radiatum wildtype mice for a total of 646 spine profiles. The *presynaptic* (axonal) compartment was identified by its synaptic contact and the presence of presynaptic vesicles associated with the synapse structure, called the active zone (AZ). The *presynaptic-extrasynaptic* region includes gold close to the membrane within approximately 100 nm along the entire visible profile of the axon terminal or spine excluding the AZ. The *postsynaptic* (dendritic) compartment was identified by postsynaptic densities (PSDs). The *postsynaptic-extrasynaptic* region includes gold within approximately 100 nm of but excluding the PSDs.

2.6 Confocal microscopy

Since the bulk of experimental results in this thesis are images or time series captured using confocal microscopy, it is crucial to understand the various settings and parameters of this instrument. As with many instruments and techniques, microscopy present a number of trade offs that are worth evaluating and understanding for optimal data collection. Basic settings for single frame capture are discussed first.

Single frame imaging parameters include image resolution, digital zoom, image exposure, laser intensity, color depth, gain amplification, digital gain, digital offset, and airy size. Color depth is set to the highest value—16-bit—to have a higher quality image with 65,536 intensity values in monochrome; this comes at the cost of disc write speed and storage space, which are nonissues. Gain amplification, digital gain, and digital offset are all adjusted such that the image is background corrected and adjusted to use the full range of 65,536 intensities. Digital gain and offset are also capped to prevent amplification of noise and to ensure sufficient signal is obtained from the sample. Proper imaging parameters, as described here, facilitate transfection confirmation and fluorophore expression.

Image resolution and digital zoom are set to 1024x1024 pixels and 2.5X with lens offering 40X and 63X optical zoom. Image exposure and laser intensity are adjusted such that they are high enough to produce a strong signal but not too high to photobleach the sample while imaging. Image exposure time is typically around 3-4 μ seconds per pixel, and laser intensity is set to 2-4 percent.

18-mm coverslips were removed from wells and placed in a Quick Release Chamber (Warner Instruments, QR-41LP, 64-1944, Hamden, CT). Cells were immersed in 800 μ l imaging buffer consisting of 1x Tyrode's solution: 135 mM NaCl, 5 mM KCl, 2 mM CaCl₂, 1 mM MgCl₂, 25 mM HEPES, 10 mM glucose (all Sigma-Aldrich) at pH 7.4. All confocal imaging was carried out at the NICHD Microscopy and Imaging Core using a Zeiss LSM 710 laser scanning confocal microscope (Carl Zeiss Microscopy LLC, White Plains, NY).

An example of micrographs imaged with these parameters is depicted in Fig. 2.1. In order to appreciate neurites in the context of the larger cells, the whole neuron can be captured in a series of snapshots that are stitched together. Global still images were captured using a 40X oil-immersion objective and stitched together in ImageJ.

2.6.1 Pinhole size

A microscope parameter that warrants discussion is the size of the pinhole, or aperture, through which light travels before capture. Changing the pinhole size changes the range of sample depth (in the z-dimension) from which light is captured.

Small pinholes (≤ 1 Airy units) only pass light from a narrow (focused) z-plane approximately $1 \mu\text{m}$ in depth. This minimizes light from extrafocal regions, which produces a sharper image with better lateral resolution.

A larger pinhole (>2 Airy units) passes light from a broader range of sample depth, including focused light from the z-plane and extrafocal light (and noise) from adjacent planes. Despite a blurrier image, a larger pinhole captured neurites of variable thickness in primary cultures which do not lie perfectly flat on the cover glass. Some thicker dendrites or winding neurites are not completely captured in the focal plane of a small pinhole image. For static images, a z-stack can be captured to produce a high resolution reconstruction of the 3D space. For time series, a larger pinhole was advantageous as it captured more signal from a broader sample depth with low sample exposure time. Pinhole size was set to 4 Airy units to produce a strong signal from a z-plane depth approximately equal to the diameter of large dendrites. Although this does capture noise as an artifact of a wide pinhole, the additional signal from static and mobile fluorescent subunits over the entire thickness of neurites makes for a reasonable comparative measure between axons and dendrites.

2.6.2 Recording time series and sampling rate

In order to study the motions of particles in a cell, series of frames in chronological order, known as a time series, must be captured. Similar to the frames of a video clip, this time series of images can be played back to observe motion, and the positions of particle(s) can be tracked over time to study their kinetics. Recording a time series involves a few additional microscope parameters that are worth considering in addition to those previously discussed for single image capture.

An important consideration, sampling rate, refers to how frequently images are taken. Fast sampling rates provide more information for curve-fitting and data analysis at the cost of unintentional photobleaching. Photobleaching is when repeated exposure to high intensity laser light, such as during imaging or intentionally (see Sec. 2.6.4), can render fluorophores dim and possibly damage the sample. Slow imaging rates reduce the risk of toxicity to the sample but might miss the bulk of cargo transport. Fig. 2.8 outlines this tradeoff between fast and slow sampling rates. In Fig. 2.8(a), the standardized intensities of an arbitrary region of interest (ROI) over a time series is compared across a range of sampling rates (16.67, 3.33, and 0.5 Hz). The fast sampling rate clearly captures the essential dynamics, whereas the slow sampling rates miss most of this information. After introducing fluorescence recovery after photobleaching, we later show how slow sampling rates fail to capture essential dynamics in the context of curve fitting in Sec. 2.6.5 and Fig. 2.13.

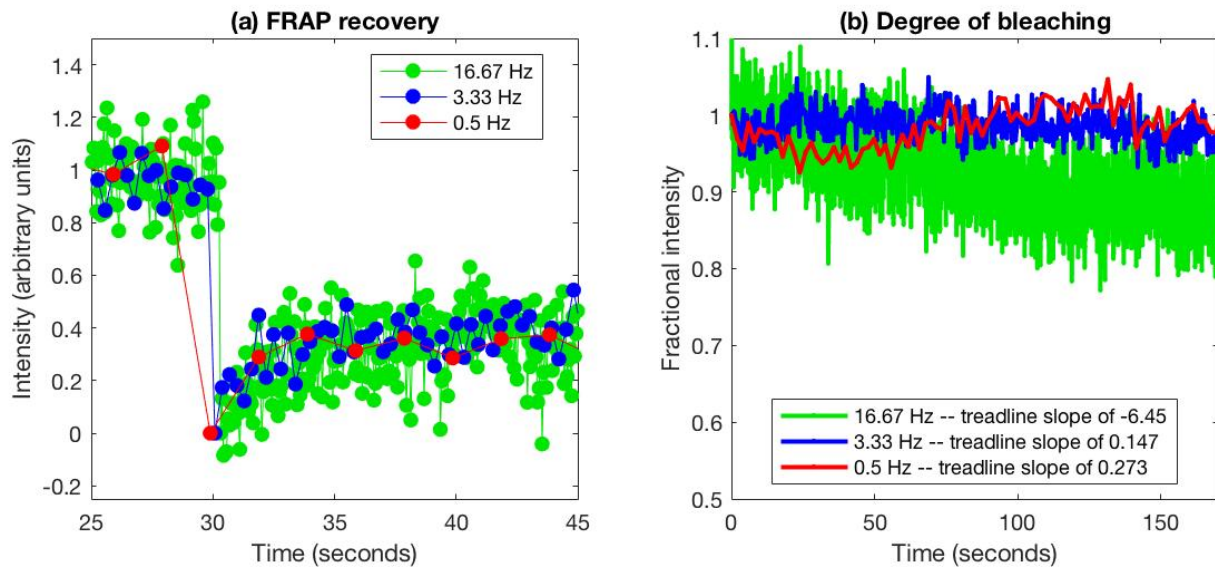


Fig. 2.8 Depiction of the trade off in using fast (16.67 Hz) or slow (0.5 Hz) sampling rates when measuring FRAP recovery (a, *left*) and with unintentional photobleaching of sample (b, *right*).

In Fig. 2.8(b), the intensity of an unbleached region is plotted over time, portraying the degree of unintentional photobleaching while imaging. The higher sampling rate (green) results in decreasing average intensity over time. This effect is minimized and becomes negligible at lower sampling rate. Although this photobleaching is correctable with post-capture processing, it decreases the sample fluorescence, reducing the signal-to-noise ratio. Over a long time series (> 1 hr), unintentional photobleaching can make a once bright sample dim or undetectable. An optimal sampling rate will therefore capture sufficient dynamics without significant unintentional photobleaching (blue).

2.6.3 Bleach parameters

Controlled and localized photobleaching can be used as a tool to study molecular dynamics in neurons. Confocal microscopes have a few modifiable settings for photobleaching. Among these are laser wavelength, laser intensity, number of bleach iterations, region of interest (ROI) size, and ROI shape. The ideal degree of bleaching results in a post-bleach fluorescence intensity between 30 to 70% of the pre-bleach intensity, consistent with other FRAP studies. The general aim of photobleaching is to achieve this degree of bleaching (1) in as little time as possible and (2) with as little damage to the sample as possible.

Photobleaching parameters are adjusted to achieve this goal. The same 495-nm laser line is used for photobleaching, since the laser that best fluoresces the sample also most

effectively photobleaches the sample. Laser intensity is set to 100 percent to minimize the number of iterations required to bleach. ROI size and shape are set such that a segment of neurite is bleached as fast as possible, covering only the neurite and not any adjacent blank space.

The number of bleach iterations refers to the number of times the microscope iterates over a ROI designated for bleaching. The total bleach time is the time required to bleach the sample for a set number of iterations. Total bleach time increases linearly with number of iterations, whereas the degree of bleaching is nonlinearly related to number of iterations, as shown in Fig. 2.9. These results vary with ROI size and shape; data in Fig. 2.9 was collected from a characteristic dendrite with the parameters outlined above. Least squares regression for a line in Fig. 2.9a and logarithmic curve in Fig. 2.9b are depicted, with equations and coefficients of determination (R^2) as insets. In order to achieve 30 to 70% of bleaching in as little time as possible, 5 to 20 bleach iterations are required with the aforementioned set of parameters.

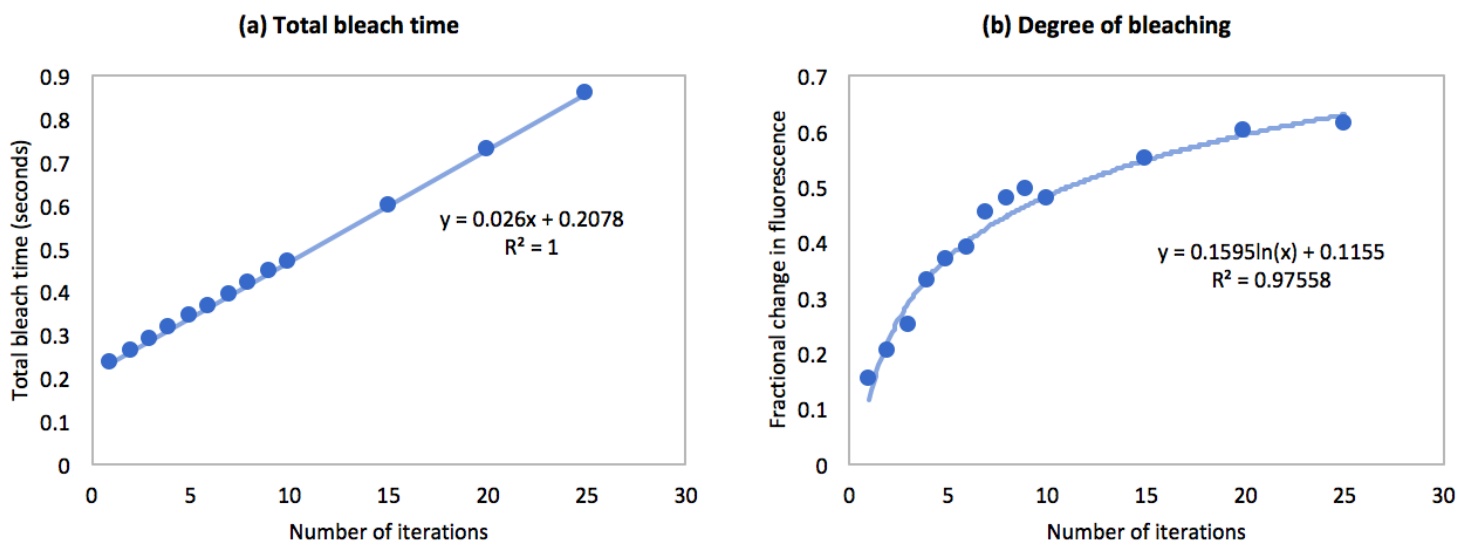


Fig. 2.9 Increasing the number of photobleach iterations imposes a tradeoff between (a) the total time required for bleaching and (b) the degree of bleaching achieved, related linearly and nonlinearly, respectively. The degree of bleaching saturates at approximately 70% at high iterations, so the optimal number of bleach iterations for this characteristic sample is 10 to 20.

2.6.4 Fluorescence recovery after photobleaching

Fluorescence recovery after photobleaching (FRAP) microscopy is a technique used to study the transport kinetics of a fluorescent molecule. In FRAP, a light source is focused on a small region in the viewable area of an image. This region of interest is then exposed to high intensity laser light to photobleach a fluorophore. The laser used for photobleaching is the same wavelength as that used for imaging at substantially lower intensities. Photobleaching itself is an irreversible quenching of a molecule's fluorescence, typically caused by covalent changes in the chemical structure. After photobleaching, a time series of images is taken as the bleached fluorophore diffuses out of the region of interest and as the unbleached fluorophores diffuse into the region. This technique allows scientists to measure a molecule's rate of diffusion into a region.

Time series for FRAP microscopy were captured using a 63X oil-immersion objective with the pinhole diameter set to 4 Airy units. The 495-nm laser line was used for both imaging and bleaching. During imaging, laser power was set to 4%, and during bleaching power was set to 100%. Images were acquired at 1024 x 1024 resolution at 1.0X optical zoom with 750x gain. Time-lapse images were captured at 0.2 Hz for 60 to 85 min using Zeiss LSM Image Browser software. Z-plane focus was maintained using Zeiss Definite Focus after each frame captured. The cells were temperature- and CO₂-controlled at 37 deg C and 5% during imaging using a stage top incubator (Tokai Hit, STXG-WSKMX-SET, Fujinomiya, Japan). Every 10-20 minutes, Kv4.2-SGFP2 was bleached to 30-70% of baseline intensity by the same 495-nm laser (100% power, 10 iterations) over the bleach region of interest (ROI).

A sample frame of a FRAP time series is depicted in Fig. 2.10. The ROI over which photobleaching occurred (bleach region) is enclosed in a red rectangle and is approximately 100 um from the cell soma (located northeast of image). This frame was captured following photobleaching. Note the reduced fluorescence in the bleach region. This neurite is suitable for FRAP given its initial strong fluorescence of Kv4.2-SGFP2 both in and out of the bleach region as well as regions without neurites. Strong fluorescence inside the bleach region is important for suitable recovery for curve fitting. Strong fluorescence outside the bleach region is helpful to monitor total cell fluorescence for (1) unintentional photobleaching while imaging and (2) unintentional depletion of total fluorescence in the cell, known as fluorescence loss in photobleaching (FLIP). Finally, imaging regions without neurites provides a background fluorescence that can be subtracted for a more accurate measure of fluorescence intensity.

We capture a brief series of frames before photobleaching in order to capture a baseline before recovery. Prebleach fluorescence intensity is stable over at least one hour, depicted in

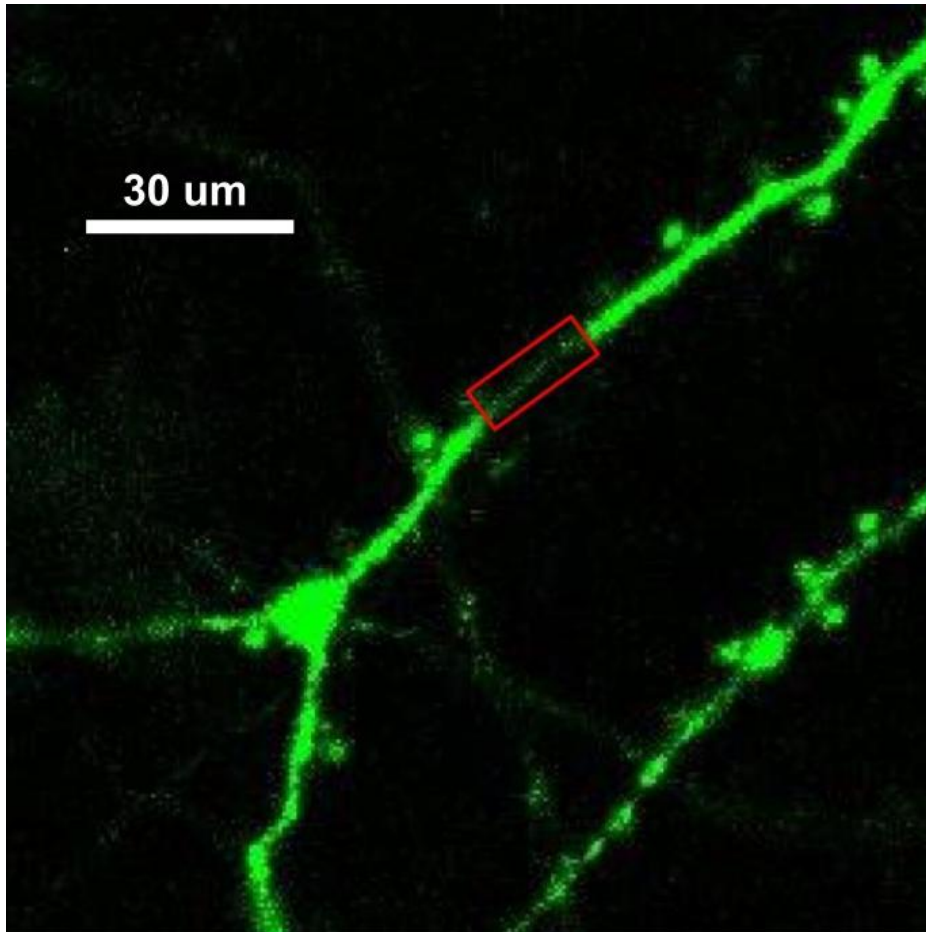


Fig. 2.10 A sample frame of an ideal neurite during FRAP microscopy is depicted. The bleach region is enclosed in a red rectangle. Also visible in this image are dendritic spines, a bifurcation point, and an adjacent neurite. Green indicates transfected subunits of Kv4.2-SGFP2.

Fig. 2.11, indicating minimal unintentional photobleaching as a result of sampling. Signal-to-noise ratio (SNR) of neurites without photobleaching is estimated using the mean (μ) and standard deviation (σ) of fluorescence intensity: $\text{SNR} = \frac{\mu}{\sigma} = \frac{10672}{174} = 61$. The coefficient of variation, or relative standard deviation, is the reciprocal of SNR: 0.0164.

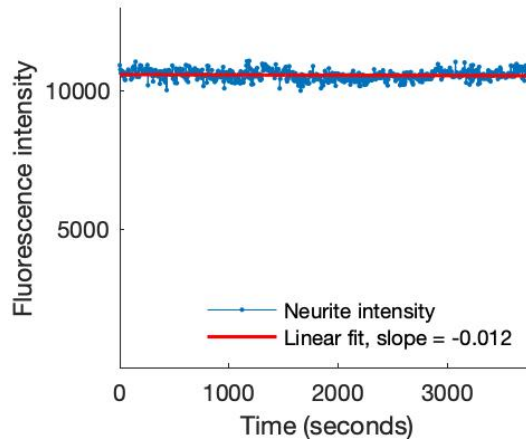


Fig. 2.11 Prebleach fluorescence intensity in a neurite is stable for at least one hour. A linear fit produces a low magnitude slope, indicating minimal unintentional photobleaching of the sample as a result of laser exposure while imaging. Estimated signal-to-noise ratio is 61 with a coefficient of variation of 0.0164.

A typical FRAP recovery curve is depicted in Fig. 2.12. The fluorescence intensity of the bleached region is averaged over the course of the time series. The data is normalized such that the average prebleach intensity is 1 and the minimum intensity is 0. In this case, the time scale has been adjusted such that recovery begins at time = 0 seconds. Several frames are captured before the start of photobleaching (in Fig. 2.12, 10 frames).

Bleaching is indicated by the precipitous decline in intensity occurring over one time frame. Intensity then increases immediately after bleaching, with the fastest recovery occurring immediately after photobleaching (0 to 50 seconds). This is characteristic of exponential recovery. The recovery curve then begins to settle and appears to reach a steady state towards the end of the time series (800 to 1000 seconds).

The recovery portion of the curve can be approximated as an exponential. After normalizing fluorescence intensities between 0 and 1, the curve is fit to a single (f^1) or double (f^2) exponential recovery curve:

$$f^1 = A(1 - e^{-\tau t}) \quad \text{or} \quad f^2 = A_1(1 - e^{-\tau_1 t}) + A_2(1 - e^{-\tau_2 t}) \quad (2.1)$$

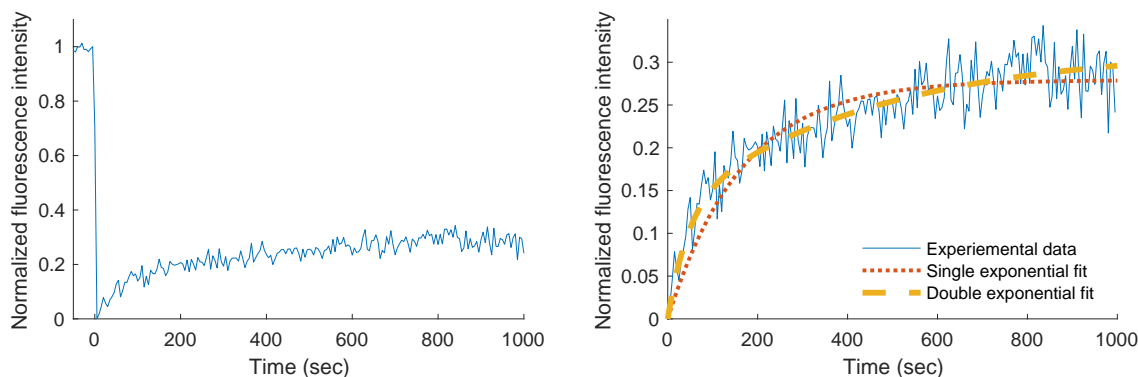


Fig. 2.12 *Left*: A typical FRAP recovery curve shows the prebleach intensity, the precipitous decline during of bleaching (at 0 seconds), the rapid recovery, and settling at a steady state. *Right*: The recovery portion of *left* can be fit to single or double exponential recovery curves.

where f is the fluorescence intensity, t is time, τ is the rate of recovery, and A is the mobile fraction. Superscripts indicate single or double exponential fits. Subscripts differentiate between terms in f^2 .

The curve fit is performed for A s and τ s using least squares. The mobile fraction estimated for the recovery shown in Fig. 2.12 was $A = 0.279$ for the single and $A_1 + A_2 = 0.316$ for the double exponential fit. This corresponds to the steady state intensity of the standardized curves. Recovery rate τ is the reciprocal of the time constant of recovery. Further, another parameter typically used to characterize recovery is the time to half recovery, $t_{1/2} = -\frac{\ln 0.5}{\tau}$. For the single exponential fit depicted in Fig. 2.12, $\tau = 0.0061$ and $t_{1/2} = 114.3$. The latter appropriately corresponds to the number of seconds required to reach half the mobile fraction, $\frac{1}{2}A = 0.1396$.

2.6.5 Data loss during bleach recovery

We explore the aforementioned tradeoff imposed by sampling rate in the context of bleach recovery. Sample data of bleach recovery is normalized and fitted to a single exponential recovery curve (as in Eq. 2.1), depicted in Fig. 2.13a. For a fair comparison between sampling rates, this same signal is down-sampled and re-fitted in Fig. 2.13b-c. A moderate decrease in sampling rate (20-fold decrease from 0.2 to 0.01 Hz) results in underestimating the bleach recovery rate τ (Fig. 2.13b). A significant decrease in sampling rate (100-fold decrease from 0.2 to 0.002 Hz) results in markedly overestimating τ (Fig. 2.13c). Re-fitting a down-sampled signal still produces a good exponential fit with $R > 0.9$. This analysis prompts caution in choosing low sampling rates, which can produce a misleading result with

a high-confidence fit. This further motivates our choice for a fast sampling rate (0.2 Hz) in our time series.

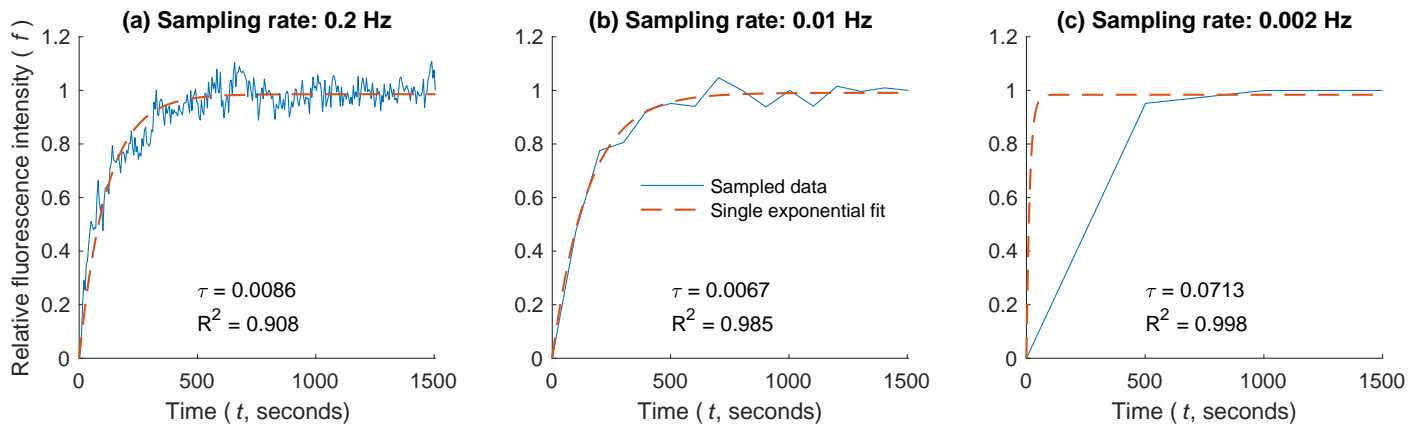


Fig. 2.13 We compare fast and slow sampling rates with sample normalized bleach recovery data. A signal (a) is down-sampled (b-c) and fitted to single exponential recovery curves. This produces a markedly different τ with high-confident fits, motivating the use of a high sampling rate (0.2 Hz) for minimal data loss and more accurate rate estimation.

2.7 Imaging active transport

Imaging active cargo transport requires a combination of previously discussed methods—mainly time series recording and photobleaching. A frame of a sample time series with active transport is depicted in Fig. 2.14A. While imaging active transport, the aforementioned considerations in Sec. 2.6.2 for the sampling rate and number of bleach iterations still apply. The purpose of photobleaching here is to clear static and diffuse fluorescence such that underlying active transit is easily visualized. Therefore it is often necessary to recurrently bleach the static or slow-moving fractions. We found that recurrent photobleaching every 15-20 min, as depicted in Fig. 2.14B, provides sufficient clearance of extraneous fluorescence without excess damage to the neuron. Fig. 2.14B was generated by selecting a neurite in Fig. 2.14A and generating a kymogram. The method of generating and analyzing kymograms is detailed in next section (Sec. 2.8).

Upon photobleaching, we observe diffuse fluorescence recovery. We also notice movement of dense, high fluorescence particles into the bleached region. We call these mobile puncta, and they appear distinct to the other fluorescence in the background and unbleached neurite. We next evaluate whether these mobile puncta are moving via an active, microtubule-based process.

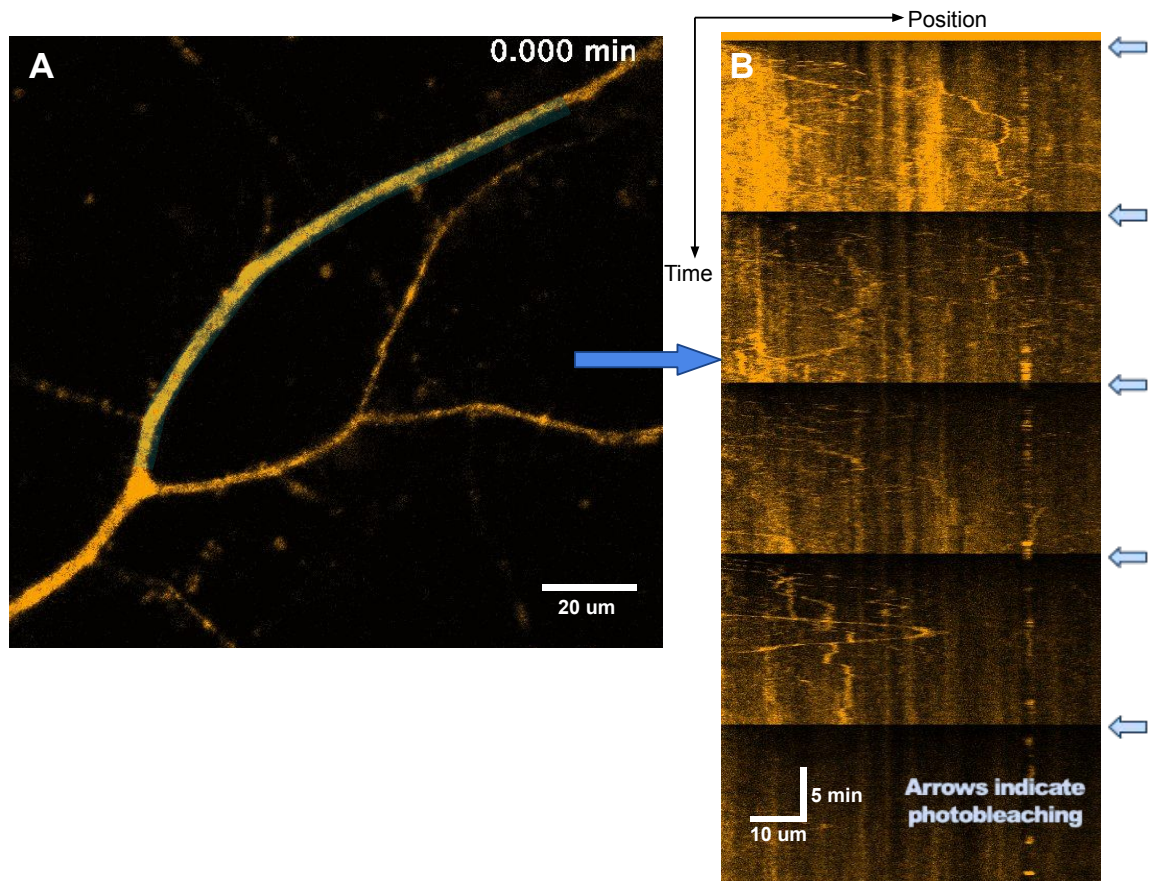


Fig. 2.14 (A): A sample time series of Kv4.2-SGFP2 trafficking (orange) depicts a dendrite branch exhibiting frequent transport. The segmented line selection (cyan) surrounding the neurite is used to generate a kymogram in (B). (B): Kymogram created from segmented line selection in (A). X-axis indicates neurite position and y-axis indicates time. Left-pointing arrows indicate time points for intermittent photobleaching.

2.7.1 Colchicine treatment

During several time series, we administer the microtubule-disrupting drug colchicine [124, 71, 8] to confirm that the observed movement of puncta occurs via motor proteins on microtubules. Six coverslips were treated with colchicine (Sigma, C9754) during hour-long recordings, and six are treated with solvent (DMSO) without colchicine as a control. Samples were prepared as previously described and time series were captured and analyzed (detailed in Sec. 2.8). At 30 minutes into the recording, 1 μ l DMSO (control) or 1 μ l DMSO containing 40 μ g colchicine was mixed into the imaging chamber, for a final colchicine concentration of 125 μ M. Number of mobile puncta per minute was then counted for the duration preceding administration and starting 10 min post administration.

Examples of representative kymograms for control and colchicine treatments are depicted in Fig. 2.15 *left* and *right*, respectively. These examples show the qualitative, visual differences from administration of colchicine or control (DMSO) (indicated by the green line). During control treatments, puncta trajectories appear mobile before and after DMSO administration, and two-sample t-test indicates no significant change ($P = 0.59$). During colchicine treatments, the drug reduces the number of mobile puncta. The motion of some puncta is ceased mid-trajectory by colchicine administration, and this change is statistically significant ($P = 5.7 \times 10^{-7}$).

We next average the number of mobile puncta per unit time before and after drug administration and average the results. Colchicine administration resulted in a substantial (> 60%) decrease in number of mobile puncta in axons when compared to control (Fig. 2.16). The Kv4.2-SGFP2 puncta transport that we observe here and elsewhere is thus likely to be an active, microtubule dependent process.

2.8 Image and data analysis

We next describe the the image processing that occurs after collection of the time series. The methodical steps of image and data analysis are described with examples.

2.8.1 Import and kymogram generation

In order to generate kymograms from a raw time series, raw microscope time series were imported into ImageJ with StackReg and Bio-Formats plug-ins. A segmented line selection is drawn through the neurite of interest with thickness adjusted to cover the diameter of the neurite, with a resultant region of interest (ROI) as shown in Fig. 2.14A. The width of the selection is minimized such that it just covers the neurite at its widest point. Using the plugin

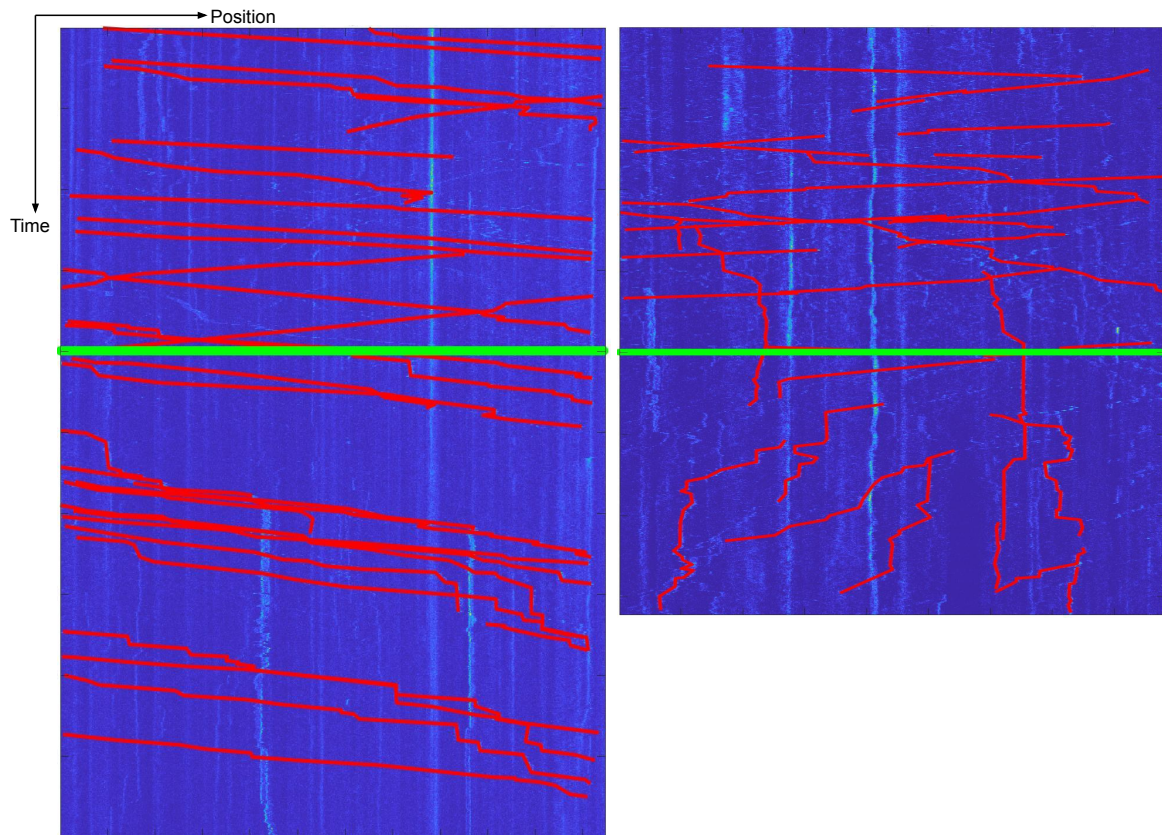


Fig. 2.15 Two representative kymograms of neurites undergoing administration of control (DMSO) (*left*) and colchicine (*right*) are depicted. The green horizontal line indicates DMSO or colchicine administration.

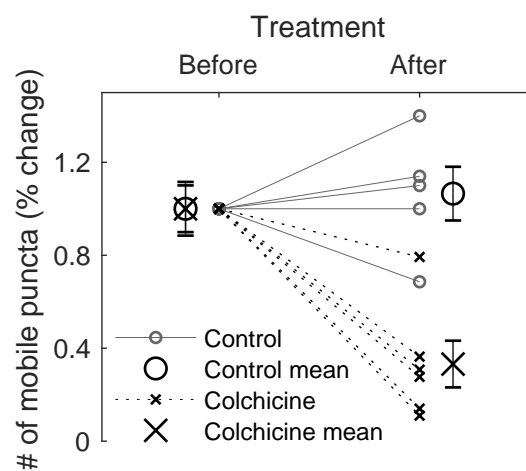


Fig. 2.16 Percent change in number of mobile puncta following administration of microtubule disrupter (colchicine) compared to control (DMSO) during live recording. Colchicine causes a significant change in mobile puncta ($P = 5.7 \times 10^{-7}$), whereas control does not ($P = 0.59$)

KymoResliceWide, a kymogram was generated from the time series where the horizontal dimension corresponds to the average pixel intensity along the diameter of the cell for each pixel distance from the soma and the vertical dimension was time. A sample segment of kymogram from a bleached neurite is shown in Fig. 2.14B. The intermittent photobleaching of the ROI is marked in Fig. 2.14B with blue leftward facing arrows. All kymograms were saved as TIF files.

2.8.2 Manual versus automated puncta tracing

A noteworthy point of discussion is the method of tracing puncta trajectories. The decision to trace puncta trajectories manually was a significant and difficult decision. Tracing trajectories would ideally be automated with an unbiased algorithm or script. Single particle tracking is a complex and unsolved problem, even in one dimension such as in the kymograms shown in Fig. 2.17. A number of existing tools and methods were attempted using sample data. Some of the packages explored with sample data are surveyed here, focusing on those adapted to kymograms.

Chaphalkar et al. wrote a summary of kymogram tracking tools described in the literature [40]. Their own tool, Automated Multi-Peak Tracking Kymography (AMTraK), cites Otsu's method [177] for row-wise segmentation for peak detection. Other peak detection methods were *findpeaks* [25], *watershed* [154], or *canny edge detection* [34]. Chaphalkar et al. also write an algorithm for branch-point detection. Another promising option was KymoButler, developed by Jakobs et al. [110], which, in short, is a trained neural network that traces puncta on kymograms.

From a high-level perspective, particle tracking algorithms process a time series with two sequential steps:

1. Peak intensities in individual frames are identified as puncta locations.
2. Paths are connected between puncta locations across consecutive frames.

These tools and others were tested on Kv4.2 sample data with minimal success. The limiting factors were low signal-to-noise ratio and the sampling rate in our time series. KymoButler predicted short trajectories but failed to connect the traces to create the total puncta path. One option to address this limitation would be to increase the sampling rate during time series capture. This, of course, is constrained by the limitations described in Sec. 2.6.2. The physical constraint is the fluorescence intensity of the puncta. The exposure time used in most time series (3.4 sec) already makes up the majority of the sampling period (5 sec). Increasing exposure time further can result in photobleaching or damage to the sample.

Increasing sampling rate therefore requires either decreased frame size or exposure time. Decreased frame size reduces the area of neurites captured. Decreased exposure reduces fluorescence intensity, exacerbating the low signal-to-noise ratio. Reproducing the data set with higher frame rate might improve the ability of an algorithm or neural network to connect short traces in our kymograms. However, it could also make the detection of puncta locations more difficult. In other words, increasing sampling rate with reduced exposure time might improve the aforementioned Step 2 but worsen Step 1. For these reasons, the use of automated trajectory tracing was discontinued.

In the end, particle tracing is still very much an unsolved problem outside the scope of this thesis. Given our experimental constraints, we found no suitable tool for automated trajectory tracing in our use case. We instead standardize the manual puncta tracing process as much as possible, as described in Sec. 2.8.4.

2.8.3 Contrast enhancement and thresholding

To improve the visibility of puncta trajectories, kymograms were enhanced using automated and manual methods in ImageJ. As an example, raw kymogram sections from a representative axon and dendrite are depicted in Fig. 2.17A-B(i). ImageJ's automatic optimization of brightness and contrast is first performed based on the image's histogram (Fig. 2.17A-B(ii)). Next, the brightness and contrast settings were manually adjusted by narrowing the visible display range (Fig. 2.17A-B(iii)). The brightness was manually increased until the upper visible range was approximately 95% of all total signal, based on the fluorescence intensity histogram of each kymogram. Lastly, a lower threshold was set at approximately 2% of the lowest intensity values. This sets pixel values below this threshold to zero, as shown in Fig. 2.17A-B(iv). The trajectories in (iv), although still imperfect, are much clearer for tracing than the raw images in (i).

2.8.4 Puncta trajectory selection

Puncta trajectories were traced using a segmented line selection in ImageJ. In lieu of automated tracing, we manually trace trajectories with a systematic protocol. The standardized methods are outlined here.

In some cases, puncta appear to merge into one trajectory or split into multiple trajectories. An example of this is depicted in Fig. 2.17C. In these cases, our standardized procedure was to trace each parent and child path as an individual trajectory, as in the three trajectories depicted in Fig. 2.17C(ii). The same protocol is followed for two puncta that seemingly merge into one trajectory.

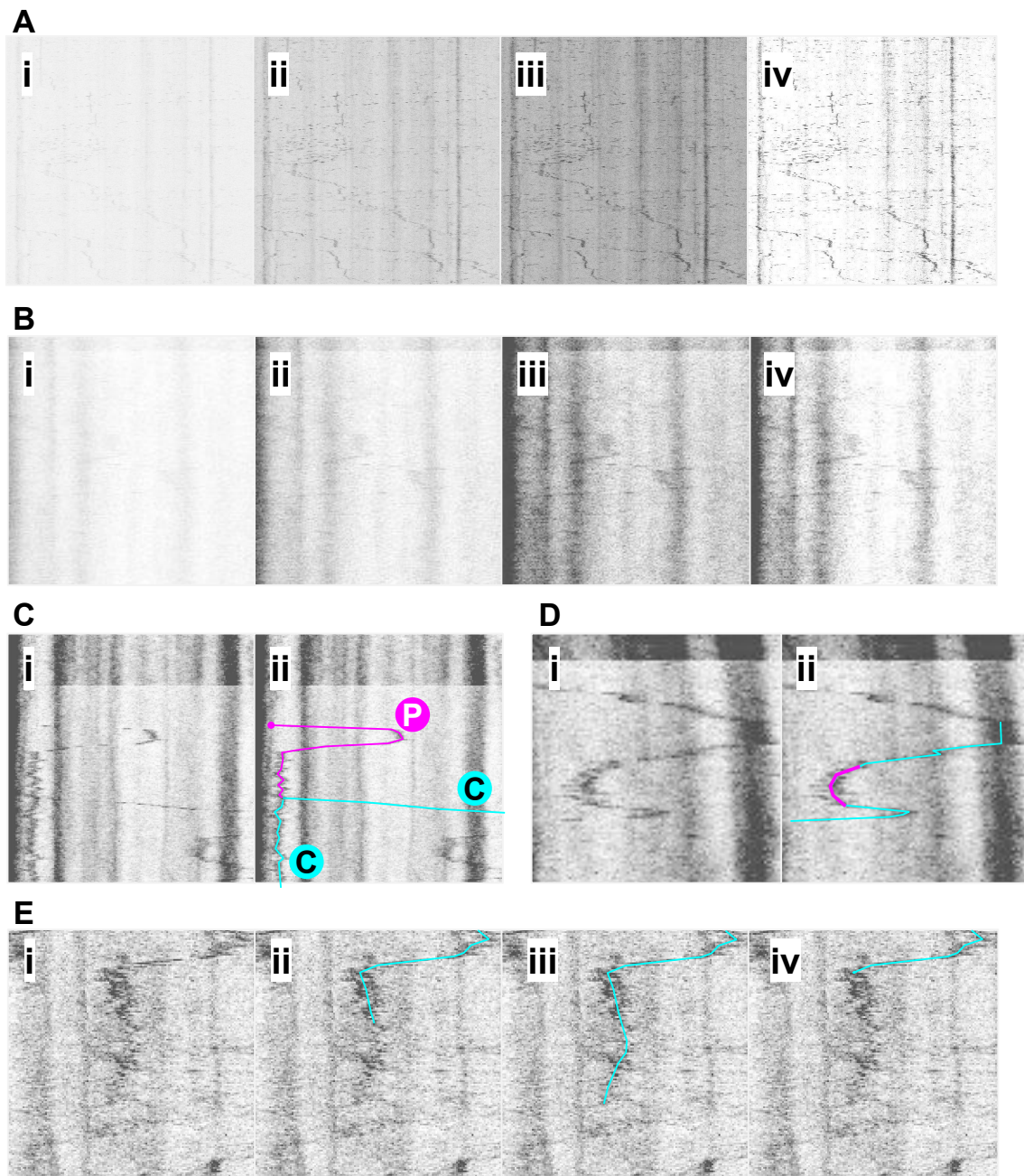


Fig. 2.17 (A): An example of axonal kymogram processing, where (i) is the raw image, (ii) is following automatic brightness/contrast adjustment, (iii) is following manual brightness/contrast adjustment, and (iv) is following thresholding. (B): A segment of dendritic kymogram is undergoing the same processing as (A). (C): Parent trajectories P that appear to merge or split into children C trajectories are recorded as distinct trajectories. In (ii), one P (magenta) splits into two Cs (cyan), for a total of three trajectories. (D): If puncta appear to oscillate and the specific path cannot be resolved (i), trajectories are traced through the center of the oscillations (magenta segment) (ii). (E): To eliminate subjectivity in puncta trajectories that appear or fade away, immobile segments of trajectories are trimmed before and after mobile segments. For the disappearing trajectory shown in (i), both (ii) and (iii) would yield the same trajectory (iv) post trajectory trimming.

Mobile puncta sometimes rapidly oscillate or vibrate in position. At the molecular level, this might be caused by stochastic movement of membrane vesicles either on or off the microtubule tracks. This visual artifact is also likely exacerbated by the limited frame rate in the time series. In these cases, if the specific path of the oscillations cannot be resolved, a trajectory was drawn through the mean position of the puncta. An example of this is depicted in Fig. 2.17D, with a trajectory drawn through the mean position of an oscillation marked in Fig. 2.17D(ii).

All trajectories were saved as TXT files of [time, space] coordinates were imported into MATLAB for further processing.

2.8.5 Trajectory trimming

In many cases, especially in dendrites, puncta seem to appear or disappear. Bleach regions were carefully selected around branch points, so these occurrences are unlikely related to entire puncta moving into or out of the neurite. At the molecular level, puncta disappearance might be membrane vesicle fusion with the plasma membrane, dispersing fluorescent subunits across the lipid bilayer. Puncta appearance might be aggregation of subunits into vesicles, for instance, to modulate dendrite excitability or transport channels for degradation. On kymograms, these occurrences look like gradual appearances or disappearances of fluorescence intensity with little spatial movement, as seen in Fig. 2.17Ei.

To further standardize our manual tracing, only mobile trajectories are considered. Puncta with an immobile segment of trajectory before and/or after a mobile segment were trimmed. This was achieved by iterating through each trajectory and summing the net distance traveled. Portions of the trajectories up to the mobility threshold were removed, eliminating stall time before and after mobile segments. The minimum distance threshold was 5 μm for both axon and dendrite trajectories. We process all trajectories to eliminate periods of stalling at their temporal beginnings and ends to account for puncta appearance and disappearance, respectively. This essentially normalizes the trajectories to minimize stalling before and after mobile segments, and the end result is trajectories with minimal regions of puncta appearance/disappearance.

As an example, both trajectories shown in Fig. 2.17E(ii) and 2.17E(iii) are interpreted as the same trajectory with objective shortest length (Fig. 2.17E(iv)) following trimming. This was useful in cases where puncta appear or disappear on a kymogram, as in Fig. 2.17E(i). This also relieves some degree of subjectivity surrounding puncta start/end points and in measurements of stall time (Sec. 3.4).

2.8.6 Intra- and inter-experimenter variation

To validate that this standardized method of manual puncta tracing is consistent, we test for intra-experimenter and inter-experimenter variation. I repeat my protocol for image and data analysis for 10 axons and 10 dendrites, and another scientist (experimenter #2) also repeats the protocol. The selected metric for comparison is the number of mobile puncta per recording. The results are depicted in Fig. 2.18, which compares axons and dendrites within and between each of the three replicates. Two-sampled t-tests firstly reveal significant differences between axons and dendrites for each replicate (a significant result further discussed in Sec. 3.3). Statistics also show minimal variation between my protocol replicates (low intra-experimenter variation) and between my replicates and that of the other scientist (low inter-experimenter variation). P-values are depicted in Fig. 2.18. This analysis demonstrates that, although repeated iterations of our protocol are not identical, the observed differences between axons and dendrites are consistent and the intra- and inter-experimenter variability is not significant.

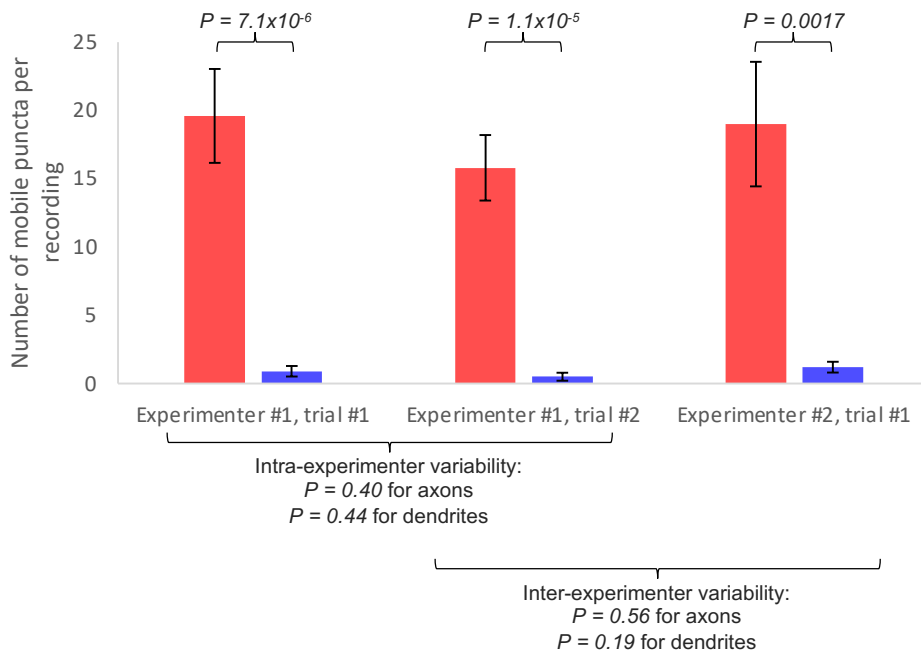


Fig. 2.18 The standardized protocol for image and data analysis has minimal intra- and inter-experimenter variation. The number of mobile puncta per recording is analyzed for same 10 axons and 10 dendrites over three replicates. Two trials are performed by me (experimenter #1) and one by another scientist (experimenter #2). All three replicates demonstrate a significant difference between axons and dendrites but no significant intra- or inter-experimenter variability (P-values displayed on figure).

By following a standardized protocol for tracing and passing trajectories through a normalizing script, we created a semi-automated method of collecting objective measurements of puncta movement. It is important to note that the trajectories captured here are not intended to be an absolute measure of subunits trafficked in a neurite. However, these methods provide a comparative measure for comparing different neurite types. In subsequent chapters, we compare axons and dendrites, and we analyze and draw conclusions from this data set.

2.9 Deterministic modeling: steady state analysis

This section provides a generalized overview to deterministic compartmental modeling. These techniques are used throughout the remaining chapters and are described in detail for each use case.

A compartmental model is a mathematical model that describes how populations of species in different groups (called compartments) interact. Compartmental models of transport capture the mass action kinetics of trafficked cargo across different spatial and structural compartments.

The cargo content of each compartment in a model is defined by a differential equation that sum the quantities of cargo entering and exiting that compartment. A generalized rate $v_{d,r}$ from a donor d to receiver r transfers an amount of mass $dv_{d,r}$. As an example, the system of differential equations describing transport for a simple model with two compartments a_{tot} and d_{tot} (depicted in Fig. 4.2C) is as follows:

$$\dot{a}_{\text{tot}} = s_{d,a}d_{\text{tot}} - s_{a,d}a_{\text{tot}}$$

$$\dot{d}_{\text{tot}} = s_{a,d}a_{\text{tot}} - s_{d,a}d_{\text{tot}}$$

This system of equations can be solved at steady state to estimate the ratio of these rates. The steady state assumption sets $\dot{a}_{\text{tot}} = \dot{d}_{\text{tot}} = 0$. Then, rearranging either equation yields

$$\frac{d_{\text{tot}}}{a_{\text{tot}}} = \frac{s_{a,d}}{s_{d,a}}$$

We can now use our experimental data to restrict rates between axon and dendrite. This same protocol is used for other compartmental models, including lumped models of spatially discretized neurites:

1. Write out system of equations describing quantities of cargo $dv_{d,r}$ entering and exiting each compartment.

2. Set derivatives equal to zero (steady state assumption).
3. Rearrange system of equations to implement model constraints, such as from experimental data.

The steady state analysis as described here is used frequently and is referenced in context of specific results throughout this thesis.

2.10 Discussion regarding transport behavior

A notable point of discussion concerns the behavior of intracellular transport in endogenous cells. Broadly speaking, the goal of basic science in biology is to study life as it exists in nature. Since *in vivo*, *in situ* studies are often difficult or impossible, scientists often work with models of the ideal system. For instance, rather than studying human neurons in a living, functioning human brain, neurons of a deceased mouse are cultured on a Petri dish. Experimentalists must accept a number of assumptions when working with such a model. Such assumptions regarding transport are of interest and discussed here.

The ideal measurements of data for this thesis capture the behavior of some protein subunit during baseline, endogenous transport. Any assumptions that deviate from this ideal measurement warrant discussion.

The first assumptions are related to imaging. Molecular-level live imaging in a *in vivo*, *in situ* mammal is currently unfeasible, so we accept cultured, dispersed cultures as a model. Further, visualizing endogenous subunits with no fluorescence at high frame rate is difficult. Fluorescence-tagged subunits expressed endogenously (via genetically modified mouse models) would have low fluorescence levels. One solution is transfection of vectors with strong promoters. However, this brings into question the impact of highly-expressed subunits on the limited transport machinery. Does high expression saturate and change the dynamics of transport? Is transport behavior for high quantities of exogenous channel similar to baseline, endogenous levels? To address this question, we report quantitative results from both transfected and endogenous expression systems in Chapter 3.

Some experimental methods specifically modify mechanisms of subunit packaging, secretion, or transport. Intracellular mechanisms can be modified pharmacologically or by an exogenous vector. For instance, the RUSH system [19] interrupts puncta secretion from the ER and Golgi by design. The RUSH system aims to achieve better visualization using triggered release. How does this sequestration impact the release and transport mechanisms themselves? It is possible that arresting such a mechanism can impose changes on the dynamics of those mechanisms or surrounding mechanisms? The interpretation of data collected

using these method should consider these assumption and perhaps be cross-referenced with control experiments. Our methods take a different approach: we image non-sequestered trafficking, albeit at increased transport rates since we use a transfected expression system.

Chapter 3

Microtubule transport and localization of puncta containing Kv4.2

The results described in this chapter have been submitted to Biophysical Journal. Some sections were written in direct connection to that manuscript.

3.1 Chapter summary and key findings

This chapter contains experimental observations of localization and microtubule-based transit of Kv4.2.

1. Kv4.2 microtubule-based trafficking is observed more frequently in axons than dendrites. This result holds when standardizing for recording length and duration, for extended 10 hour recordings, and for neurites from the same soma.
2. Frequency of Kv4.2 active transport opposes its delivered localization profile, with increased puncta frequency^{4w} in axons compared to dendrites. Kv4.2 primarily localizes in dendrites in both endogenous and transfected expression systems, but axonal expression is not negligible.
3. Perturbing neural excitability does not immediately affect microtubule transport in dendrites. Incubation with neither KCl (chronic depolarization) nor AMPA receptors (stimulation) produces an observable effect during active transport.

3.2 Introduction

Kv4.2 is a voltage-gated ion channel prevalently expressed in dendrites of pyramidal cells in the CA1 hippocampus. Kv4.2 conducts A-type, transient outward potassium current, which is abundant in dendrites but scarce in axons [208]. Dendritic expression of Kv4.2 is consistent with its hypothesized role in dendritic integration and control of neural excitability [208, 106, 220]. Moreover, A-type current exhibits a five- to sixfold increase in current density over the length of the apical dendrite [106]. Localization studies of Kv4.2 corroborate this finding, showing a 70% increase in channel density along the apical dendrite [117].

Kv4.2-mediated A-currents have not been reported in axons, but other channels that pass A-current have been found in axons [208, 52, 232]. Effective surface expression and function of Kv4.2 in axons therefore seems unlikely. However, the reported amount of Kv4.2 subunits localized in axons of CA1 hippocampal neurons varies substantially among quantitative localization studies. Alfaro-Ruíz et al report only 1.2% of total CA1 immunogold-labeled Kv4.2 subunits are found in axons [3]. Kerti et al contrastingly report nearly 20%, and the authors remark that "[this result] is surprising, because the Kv4.2 subunit is conceived as a somato-dendritic ion channel" [117]. We found predominant endogenous expression of Kv4.2 in dendrites with a non-negligible presence in axons. Due to the imaging modality, these studies cannot establish whether subunits present in axons are in transit or whether they are membrane-bound, functional channels.

Other studies have characterized Kv4.2 transport and expression mechanisms. Kv4.2 interacts with kinesin Kif17, which suggests transport on microtubules. In the absence of Kif17, Kv4.2 fails to localize in dendrites of pyramidal cells [49]. Deletion of a portion of the C-terminus or fusion with myosin Va restricts expression of Kv4.2 to the somatodendritic region [194, 133, 112]. Further, KChIPs have been established as auxiliary subunits that promote Kv4.2 exit from the endoplasmic reticulum for surface expression [209, 244, 196]. An auxiliary subunit, DPP6, attached to Kv4.2 by a transmembrane domain [143], assists in trafficking Kv4.2 out of the endoplasmic reticulum to the plasma membrane [134]. Duménieu et al [63] summarize these results with the following working hypothesis for Kv4.2 transport in pyramidal cells: Kv4.2 is trafficked short distances, such as to proximal dendrites or within spines, on actin filaments via myosin Va, while long range transport is mediated along microtubules via KChIPs and Kif17. Although there is evidence for other mRNA presence in dendrites with local translation [31, 107, 80, 236], there is, as of yet, no evidence for dendritic synthesis of Kv4.2 specifically.

In CA1 hippocampal pyramidal cells, Kv4.2 passes an outward current, such that it primarily has an inhibitory effect on initiation and propagation of dendritic potentials. Kv4.2 production, localization, and function thus play significant roles in excitability or sensitivity

of a dendrite. Ion channels have indeed been implicated in homeostatic maintenance of intrinsic excitability [24, 60, 241], though no such evidence has been found for Kv4.2. The transport of subunits that shape dendritic excitability is of interest, since failure to deliver subunits can disrupt cellular homeostasis. Hence is the motivation for studying transport of Kv4.2 in this chapter. The data presented in this chapter are then unified into a working theory of Kv4.2 active transport and intracellular distribution in Chapter 4.

3.3 Kv4.2 microtubule-based trafficking is observed more frequently in axons than in dendrites

To establish reliable estimates of the frequency, density, and kinetic properties of actively transported Kv4.2 subunits, we performed 129 hour-long recordings of neurites in cultured rat hippocampal cells. In total, 507 mobile Kv4.2-SGFP2 puncta were identified among 478 recorded dendrites, and 961 mobile puncta were identified in 46 axons (see Methods). We define puncta as the smallest fluorescent particles resolved using our methods—the membrane vesicles containing Kv4.2-SGFP2. Puncta trajectories are visualized as in Fig. 2.14, and we later depict a schematic of puncta in the context of our modeling in Fig. 4.1Aii,Bi-ii.

Kv4.2 microtubule-based trafficking is observed more frequently in axons than in dendrites. The durations over which puncta are mobile are depicted in Fig. 3.1A for axons and Fig. 3.1B for dendrites. Of the 478 dendrites in hour-long recordings, only 213 dendrites (45%) exhibited at least one mobile punctum. Only data from this subset of dendrites is presented in Fig. 3.1B. Mobile puncta appeared consistently in axons, whereas in dendrites mobile puncta appear intermittently or not at all. The average length of a sampled region was 85.4 μm in axons compared to 52.3 μm in dendrites. We found no trend in transit frequency with degree of branching, from primary (apical) dendrites to quaternary branches (Fig. 3.3). To ensure that puncta visibility was not an artifact of fluorescence intensity, we plot puncta frequency versus standardized neurite intensity and find no strong correlation ($R^2 = 0.0065$ and 0.0274 in axons and dendrites, respectively), depicted in Fig. 3.4.

We also plot puncta frequency by neurite diameter to assess whether neurite diameter might limit or influence puncta trajectories (Fig. 3.5). We find low correlation in axons and dendrites ($R^2 = 0.048$ and $R^2 = 0.001$, respectively), so neurite diameter is unlikely to saturate transit of membrane vesicles in our system.

We assess puncta frequency over the course of neuron growth and development. We plot puncta frequency by recording versus age of the neurons in Fig. 3.2. With the power of our data set, puncta trafficking is not significantly different across DIV 8 to 14. Two-sampled

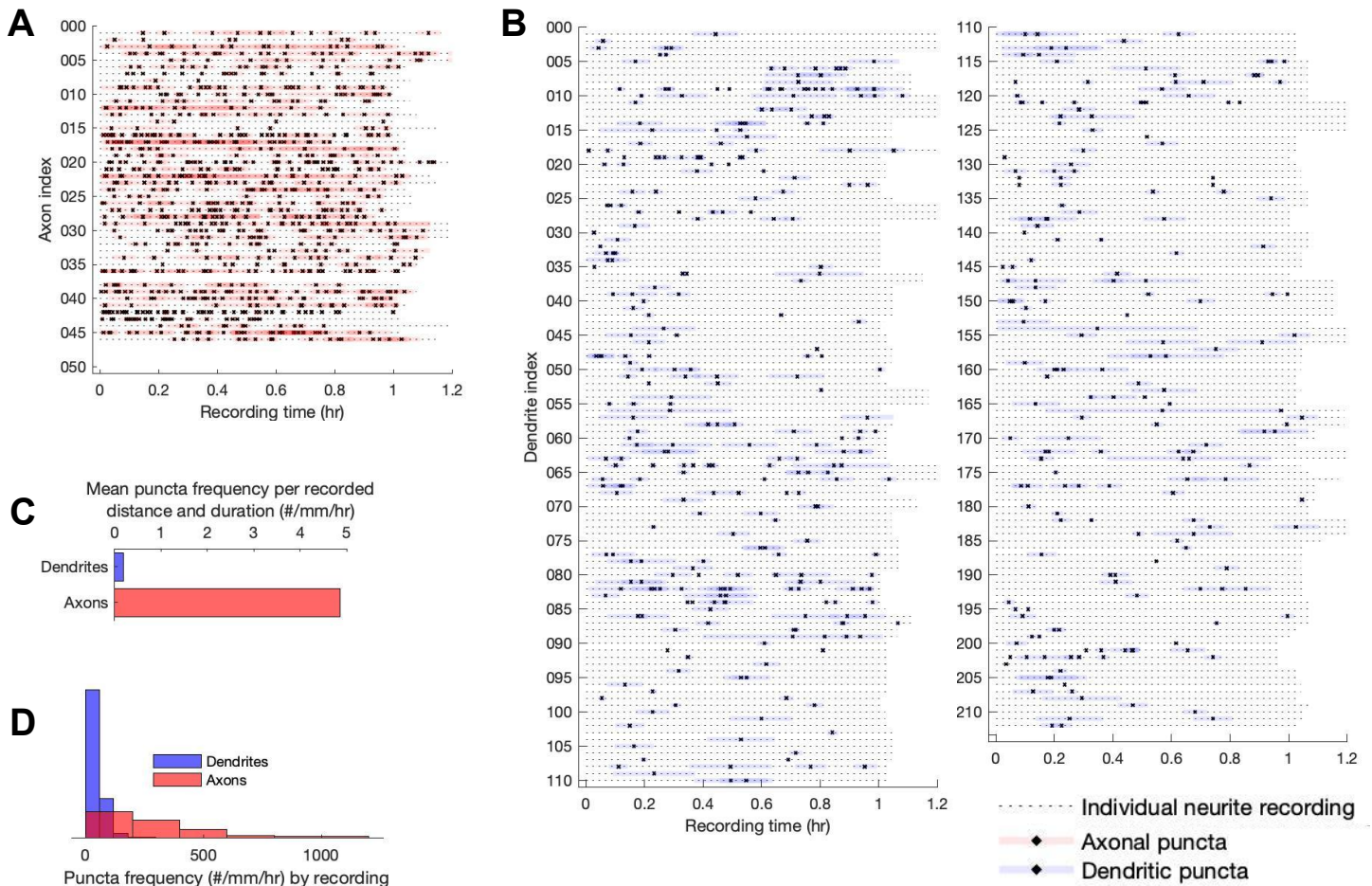


Fig. 3.1 There are more mobile Kv4.2 puncta in axons compared to dendrites. (A): Hour-long recordings of 46 axons are depicted, with highlighted sections indicating periods of puncta mobility. Note: Axon with index #37 did not meet criteria for axon diameter (as established in Fig. 2.4) and was omitted from analysis. (B): Hour-long recordings of 213 dendrites are depicted, with highlighted sections indicating periods of puncta mobility. This subset of 478 dendrites has ≥ 1 mobile puncta. (C): Puncta frequency in axons and dendrites is standardized by total neurite length visualized and time recorded (units: number of puncta/mm/hr). These quantities are used as a model constraint in a lumped model of Kv4.2 transport and delivery (Sec. 4.4). (D): Histogram depicting puncta frequency by neurite recording. Puncta frequencies in axons and dendrites were significantly different with $P = 4.6 \times 10^{-23}$.

t-tests between all combinations of DIV show no significant difference, with minimum $P = 0.185$ between DIV 11 and 14 in axons.

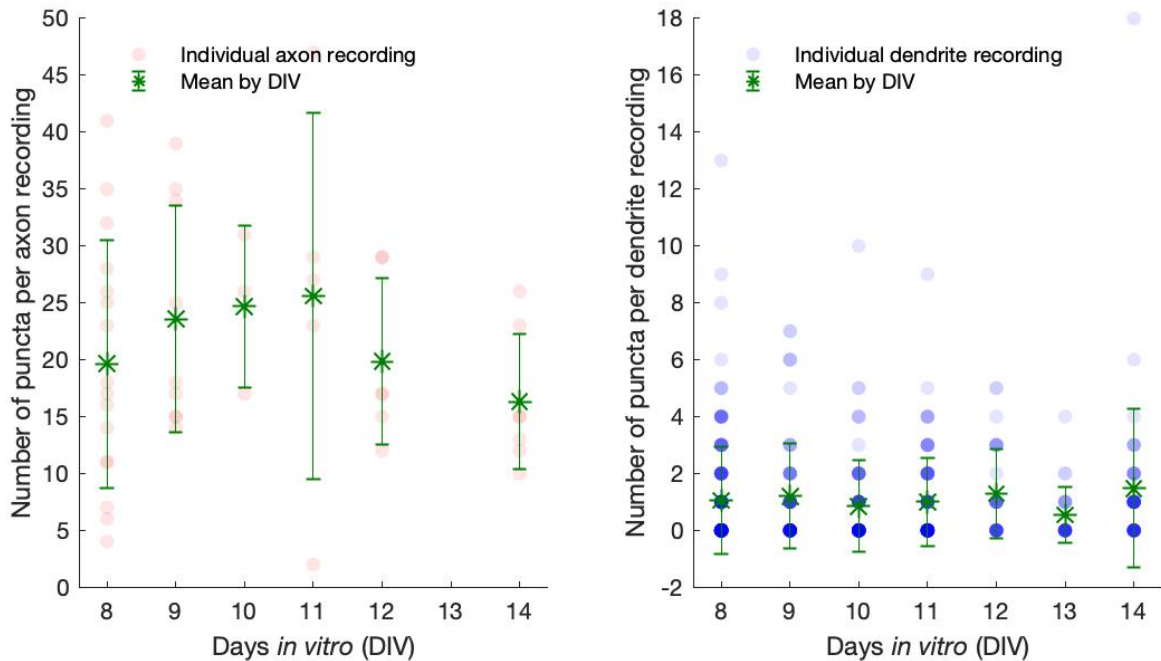


Fig. 3.2 Puncta frequency in both axons (*left*) and dendrites (*right*) does not significantly change with neuron development over DIV 8 to 14.

We do find a correlation between puncta frequency and distance from soma in dendrites, which is used for a sub-neurite analysis and constraining a discretized model of transport in Chapter 4.

When standardizing these measurements for recording duration and neurite length, the discrepancy in mobile puncta frequency is 4.9 puncta/mm/hr in axons versus 0.18 puncta/mm/hr in dendrites, depicted in Fig. 3.1C. Puncta frequency in dendrites drops to 0.039 puncta/mm/hr when considering dendritic recordings with zero mobile puncta (not depicted). A histogram showing puncta frequency by neurite recording is depicted in Fig. 3.1D, and a Mann-Whitney test demonstrates a significant difference between these populations with $P = 4.6 \times 10^{-23}$. In subsequent Sec. 4.4, this standardized data is used as an experimental constraint for the steady state densities of microtubule-bound puncta. We also later bin microtubule-bound puncta by distance from the soma to constrain distance-dependent data in Sec. 4.6.

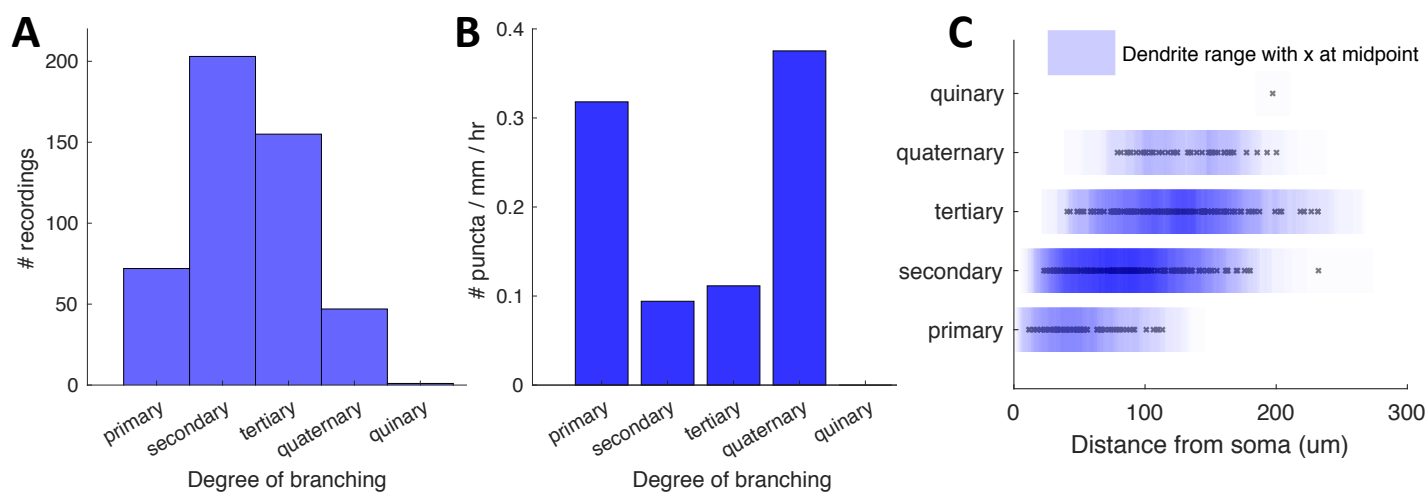


Fig. 3.3 A: Histogram depicting spread of dendritic recordings by degree of branching. Primary indicates the apical dendrite. B: Puncta frequency demonstrates no trend with degree of branching. C: The dendritic ranges along the somatodendritic axis are plotted by branch order.

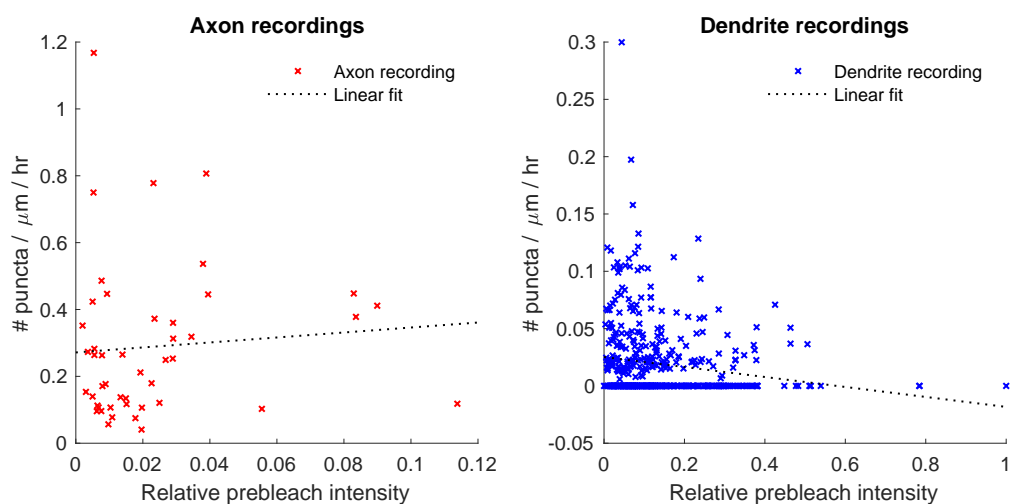


Fig. 3.4 To ensure that puncta appearance or visibility is not an artifact of fluorescence intensity, we plot standardized puncta frequency and recording duration versus average prebleach fluorescence intensity for recordings of axons (*left*) and dendrites (*right*). Neither neurite population shows a strong correlation: for linear fits, $R^2 = 0.0065$ and 0.0274 for axonal and dendritic population, respectively.

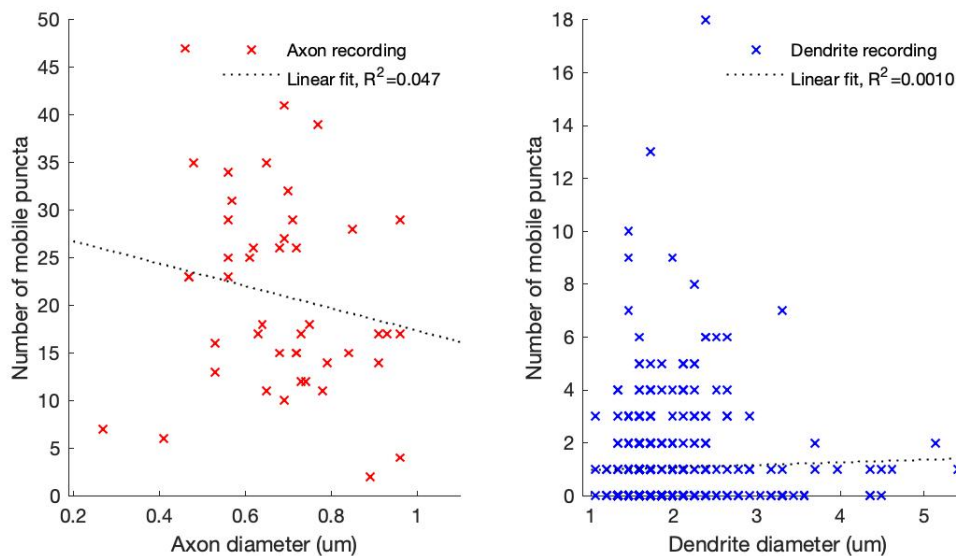


Fig. 3.5 To ensure that neurite diameter does not influence or limit the number of puncta trafficked, we plot number of mobile puncta as a function of diameter. The low correlations here suggest that saturation of transport in neurites with small diameters is unlikely.

3.3.1 Extended FRAP recordings

In order to control for the possibility of global trafficking failure in dendrites that did not show puncta during hour-long recordings, we performed extended recordings lasting up to 11 hours. A distilled water reservoir was placed adjacent to the imaging chamber, and the chamber was covered with a 35-mm Petri dish to maintain humidity. Time-lapse images were captured at a decreased sampling rate (0.1 Hz) with recurrent photobleaching every 15 min. All other procedures and conditions are as previously described (in Sec. 2.6.2).

The results are shown in Fig. 3.6. The trend in puncta frequency for extended recordings is consistent with that of hour-long recordings, suggesting that hour-long recordings with no puncta are simply a result of sampling.

3.3.2 Axons and dendrites from the same neuron

In some cases, it was possible to reliably identify and record from axons and dendrites originating from the same soma to control for intercellular variations in trafficking or metabolism. Axons and dendrites from these 28 recordings are depicted alongside each other in Fig. 3.7A. In all but one case, axons had the majority of mobile puncta, even though multiple dendrites were recorded for most neurons. Comparisons of raw puncta count (Fig. 3.7H) and standardized puncta count (units: number of puncta/ $\mu\text{m}/\text{hr}$, in Fig. 3.7I) are depicted. After

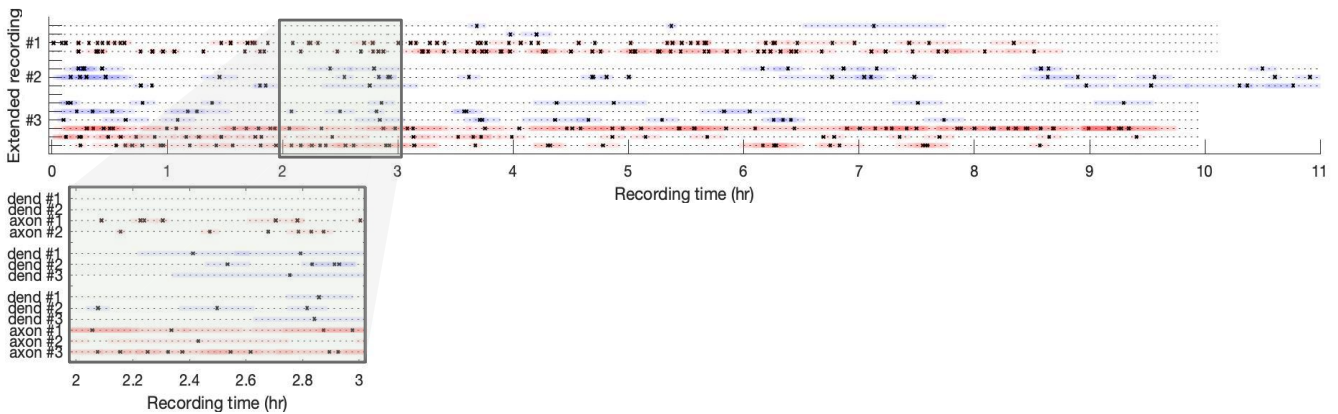


Fig. 3.6 Three extended recordings that substantiate the discrepancy in puncta frequency between axons and dendrites over extended periods of observation.

standardizing measurements to sampling distance and duration, the axons average a 36-fold increase over the simultaneously recorded dendrites from the same cell.

Thus far, we have imaged and analyzed mobile fractions of Kv4.2. Together, these data establish that actively transported Kv4.2 puncta are present in significantly higher densities in axons as compared to dendrites. We next observe qualitative differences in the behavior of individual puncta between neurite types.

3.4 Kinetic differences in axons versus dendrites

We next analyzed individual Kv4.2 puncta trajectories in axons and dendrites. Kymograms depicting representative puncta trajectories in axons and dendrites are shown in Fig. 3.8Ai and Fig. 3.8Bi, respectively. The same kymograms with puncta tracing overlaid follows in Fig. 3.8Aii and Fig. 3.8Bii. Upon initial observation, axonal puncta generally appear to undergo unidirectional runs at high speeds, whereas dendritic puncta seem to change direction more frequently and stall longer.

3.4.1 Calculating kinetic measures

Here, we briefly define the kinetic parameters used to compare puncta trajectories.

The total distance each Kv4.2-SGFP2 puncta travels was computed by summing the absolute value of the distance traveled between each frame in a time series. Moreover, the net displacement equals the puncta final position minus initial position.

To average speed, the instantaneous velocity was computed between each two frames of a time series. The mean of the absolute values of these instantaneous velocities equals the

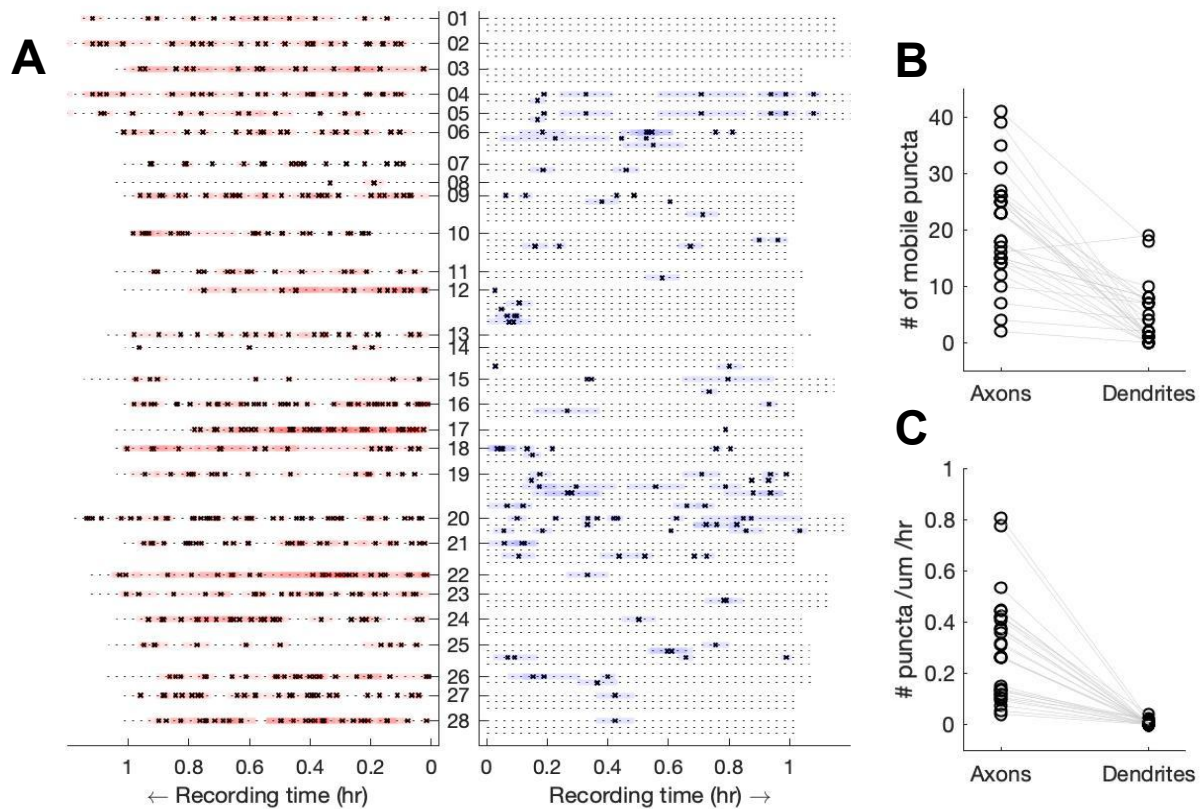


Fig. 3.7 (A): Axons and dendrites originating from the same soma (same neuron) are depicted, demonstrating similar trends as those observed in isolated recordings. The central column of numbers indicate an arbitrary recording index. (B): Number of mobile puncta per neurite for concurrent recordings from (A) shows a significant difference between axons and dendrites ($P = 2.4 \times 10^{-10}$). (C): Number of mobile puncta per neurite standardized by length and time for concurrent recordings from (A) is also significantly different ($P = 1.2 \times 10^{-9}$).

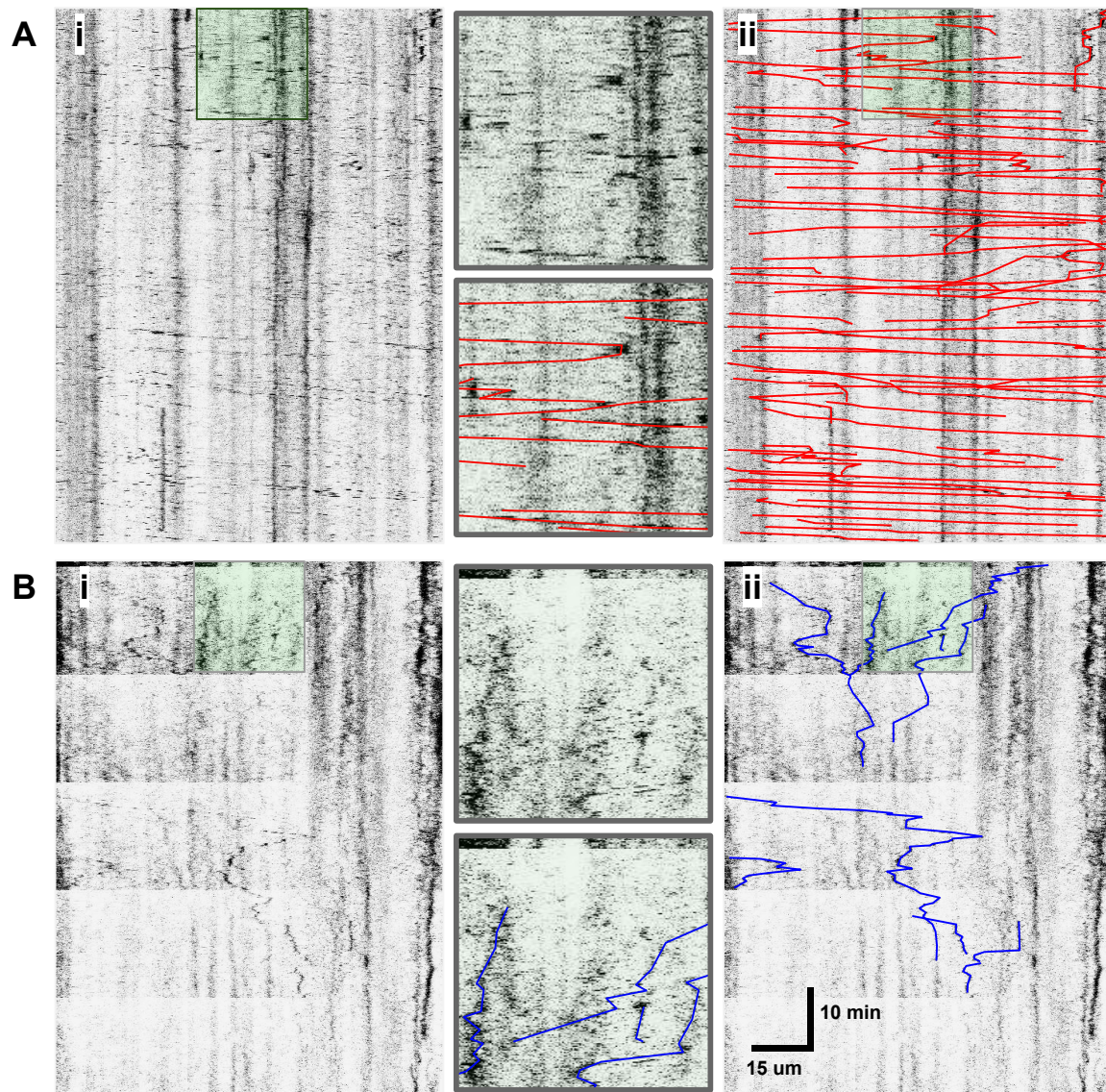


Fig. 3.8 Kv4.2 trafficking is qualitatively different in axons and dendrites (A): Kymograms depicting characteristic axon trajectories (i) with puncta tracing overlaid in (ii). Insets correspond to regions highlighted in green. (B): Same as (A) for characteristic dendrite trajectories.

average speed. Puncta stall time is defined as the fraction of total time during which puncta are traveling with a speed less than $0.1 \mu\text{m}/\text{sec}$.

Mean squared displacement (MSD) was computed by averaging the square of the difference between puncta coordinates some time τ apart. This was repeated for τ up to one fourth the length of the recording duration. MSD was then plotted against τ , and equation $\text{MSD}(\tau) = D\tau^\alpha$ was fit for each set of coordinates. D and α are then recorded as diffusion and superdiffusivity coefficients, respectively.

We then computed four key kinetic parameters, compiled as histograms in Fig. 3.9. Our initial observations are supported in these population measurements. On average, axonal puncta traverse a longer distance Fig. 3.9(A) with higher speeds (B) and longer unidirectional runs (D). Dendritic puncta exhibit longer stall times than axonal puncta (C), where stall fraction is defined as fraction of total time spent traveling slower than $0.1 \mu\text{m}/\text{sec}$. With the Mann-Whitney test, we show statistical significance between populations for all four kinetic measures (A-D) with P-values 3.7×10^{-89} , 8.7×10^{-98} , 4.1×10^{-29} and 1.6×10^{-35} , respectively. Since the same cargo is trafficked in both neurite types, we question the underlying mechanistic differences that might account for these kinetic differences. This is explored in Chapter 4.

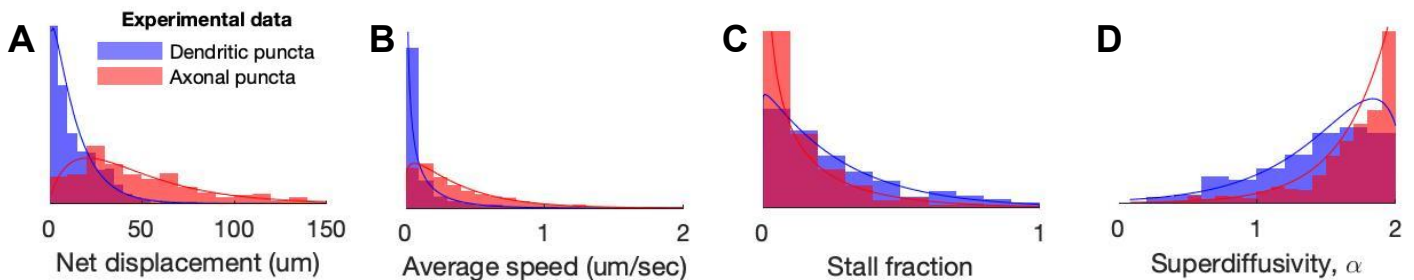


Fig. 3.9 Histograms for various kinetic transport parameters, normalized as probability density functions. On average, axonal puncta have greater net displacement (A), faster speed (B), decreased stall time (C), and increased unidirectional runs (D). Solid blue and red lines indicate kernel fits to experimental data (dendrites and axons, respectively). We use two-sample t-tests to reliably establish significant differences between populations in (A-D) with $P = 3.7 \times 10^{-89}$, 8.7×10^{-98} , 4.1×10^{-29} , 1.6×10^{-35} , respectively.

To assess whether these dynamics are partially explained by constraints of neurite size, we plot all four kinetic measures against neurite diameter in Fig. 3.10. None of these measures correlate with neurite diameter within each neurite type. Correlation for linear fits with net displacement, average speed, stall fraction, and superdiffusivity was low: $R^2 = 0.0012, 0.0234, 0.0004, 0.0016$ for axons and $R^2 = 0.0048, 0.0003, 0.0000, 0.0001$ for dendrites. None of the measures are significantly different in small-diameter dendrites com-

pared to large-diameter dendrites, suggesting that the difference in dynamics is not explained by the physical constraints of a thin neurite.

A physiologic feature that might influence the trajectories is microtubule orientation, which has been found to be different in axons vs dendrites. The presence/absence of molecular motors in each neurite type might also play a role, but these topics in molecular biology fall outside the scope of this work.

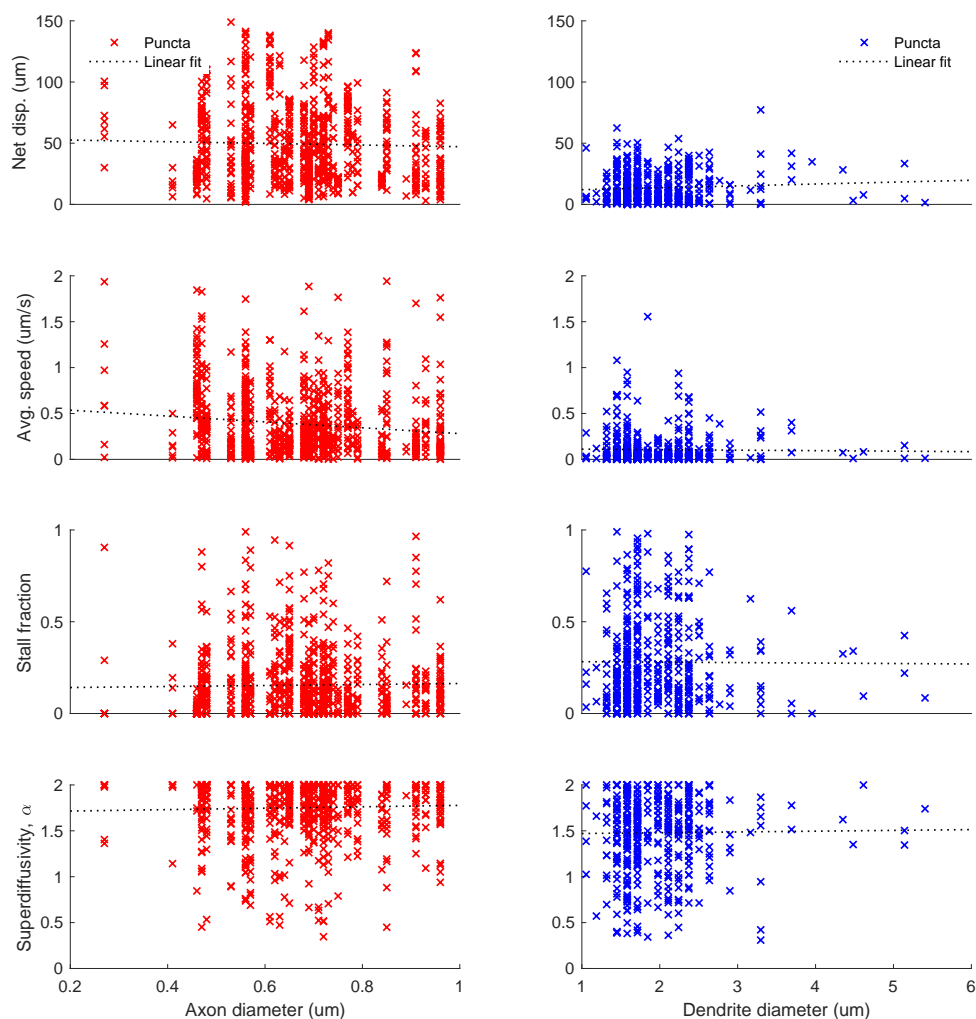


Fig. 3.10 Trajectory kinetics correlate weakly with neurite diameter, suggesting that mobile puncta are not constrained by neurite size. Correlations for linear fits were low (top to bottom): $R^2 = 0.0012, 0.0234, 0.0004, 0.0016$ for axons and $R^2 = 0.0048, 0.0003, 0.0000, 0.0001$ for dendrites.

By now, we have observed both quantitative and qualitative differences in active transport of Kv4.2-containing puncta between axons and dendrites. Axons have higher puncta frequency than dendrites, and axonal puncta travel farther distances at faster speeds with decreased stalling compared to dendrites.

3.5 Kv4.2 preferentially localizes to plasma membrane of dendrites compared to axons in both endogenous and transfected expression systems, but expression in axons is not negligible

This section was a collaboration with Ronald Petralia and Ya-Xian Wang from the National Institute on Deafness and Other Communication Disorders as well as Lin Lin from the National Institute of Child Health and Human Development.

To independently assess the static density of native Kv4.2 expression in axons and dendrites, we used electron microscopy (EM) following immunogold labeling of endogenous Kv4.2 subunits. Owing to the inherent constraints of EM imaging, we quantified axon/dendritic expression in identifiable pre- or postsynaptic compartments, respectively, and regions of neurite that were clearly contiguous with these compartments. We imaged 624 presynaptic and 646 postsynaptic regions. Example micrographs in Fig. 3.11A show an axon (ax) that can be traced to presynapses (pre), with gold particles present in both the axon shaft and terminals.

Sampled immunogold particles identified in the synapses and perisynapses are broadly divided into pre/postsynaptic regions. Presynaptic terminals (axons) contained 30.6% of all gold particles and 0.15 particles/synapse. Postsynaptic terminals (dendrites) contained 69.4% of particles and 0.33 particles/synapse. This is consistent with previous localization studies [117] in showing substantial, non-negligible subunit localization in axons. The pre/postsynaptic regions are subdivided into synaptic and extrasynaptic regions. In both axons and dendrites, under one third of particles (28.0 and 32.2%, respectively) of particles were found in synaptic spaces, with the remaining two thirds in extrasynaptic regions. These percentages and gold particle frequencies are summarized in Table 3.1 and depicted in Fig. 3.11B. In subsequent Sec. 4.4, this standardized data is used as an experimental constraint for the steady state densities of delivered Kv4.2 subunits (later defined as *del*).

We perform a few statistical tests on this electron microscopy data in order to reliably establish our claims. A two-way ANOVA with two categories: (1) gold particle location

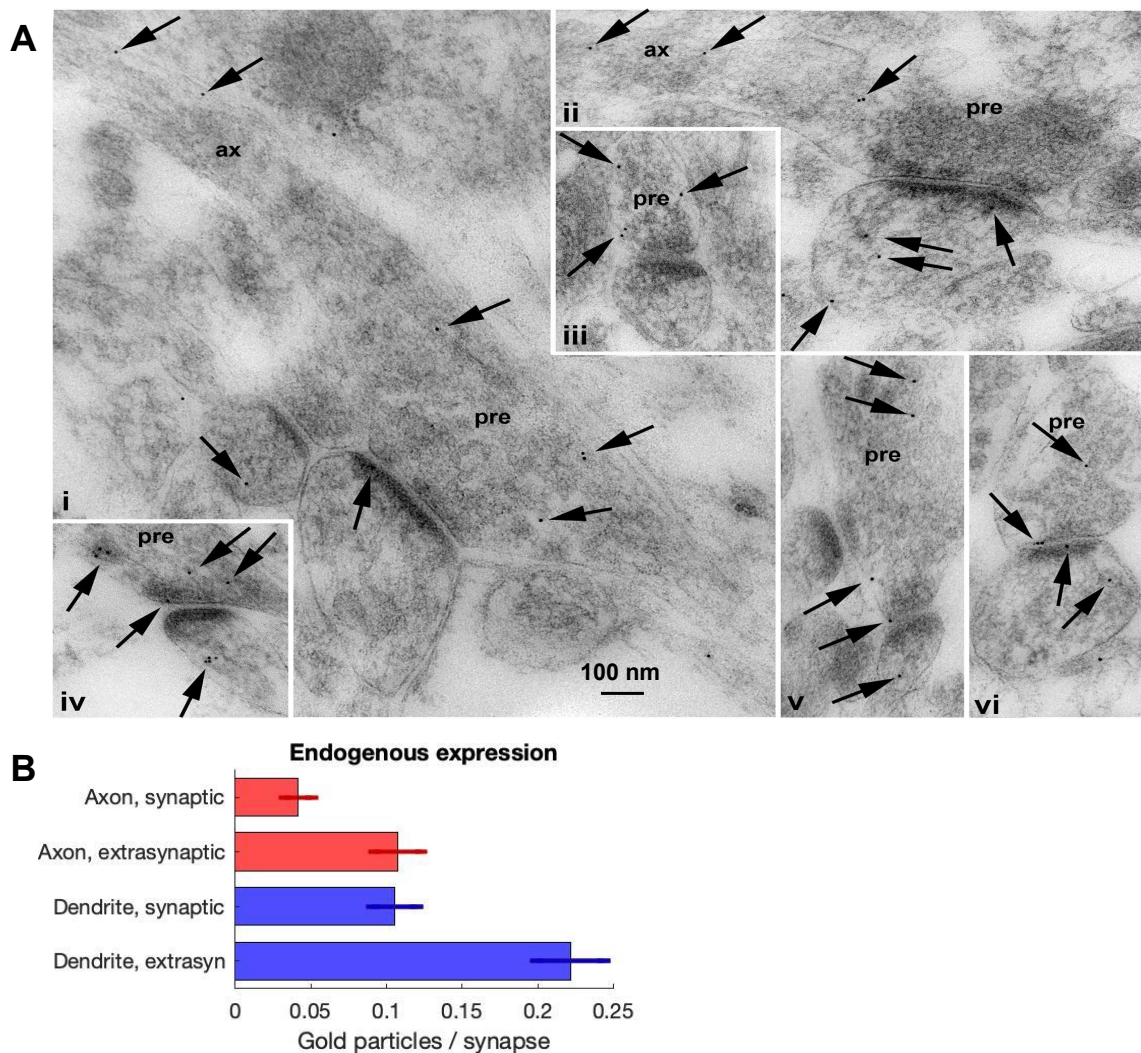


Fig. 3.11 Endogenously expressed Kv4.2 preferentially localizes to dendrites (A): Immuno-gold localization (arrows) of Kv4.2 in the CA1 stratum radiatum of the hippocampus of WT mice. Synapse profiles show the presynaptic terminal (pre) contacting one or two postsynaptic spines. In (i) and (ii), the axon (ax) can be traced from the presynaptic terminal. Gold labeling extends along the axon and into the presynaptic terminals. Examples of gold labeling associated with the plasma membrane of the synapse and counted in the accompanying graph include those at the axon synaptic membrane shown in (iv), (v), and (vi), the axon extrasynaptic membrane shown in (iii) and (v), the dendrite synaptic membrane shown in (i) and (vi), and the dendrite extrasynaptic membrane shown in (ii). (B): Quantification of (A). Concentrations in the four compartments are 0.0417, 0.1074, 0.1053, and 0.2214 gold particles per synapse. Error bars indicate standard error of the mean.

(axon synapses, axon extrasynaptic, dendrite synapses, extra-dendrite extrasynaptic) and (2) biological replicate (mouse #) is first performed. The results indicate that mean number of gold particles did not significantly differ between biological replicates ($P = 0.2018$) but did significantly differ by location ($P = 3.4 \times 10^{-7}$). Further, there is no significant interaction between particle location and biological replicates ($P = 0.1176$). Next, two-sample t-tests between each combination of particle locations (axon synapses, axon extrasynaptic, dendrite synapses, extra-dendrite extrasynaptic) are evaluated. Axonal and dendritic synapses have significantly different mean particle density ($P = 1.7 \times 10^{-4}$), and extrasynaptic regions in axons and dendrites are also significantly different ($P = 0.0011$). Each pair of puncta density locations are significantly difference with $P < 0.05$ except for [axon extrasynaptic, dendrite synapses], as is evident in Fig. 3.11B. Lastly, I combined all axonal particles (from axon synapses and axon extrasynaptic regions) and all dendritic particles, and again found a significant difference ($P = 1.4 \times 10^{-6}$).

Table 3.1 - Density of immunogold particles identified by electron microscopy in synapses of axons and dendrites.

Axons, N = 624		Dendrites, N = 646		<i>Neurite, number of synapses sampled</i>
	93		211	
	0.149		0.327	<i>Gold particles / synapse</i>
	30.6		69.4	<i>Percent of total</i>
<i>Synaptic</i>	<i>Extrasynaptic</i>	<i>Synaptic</i>	<i>Extrasynaptic</i>	<i>Subdivision</i>
26	67	68	143	<i>Number of gold particles</i>
0.042	0.107	0.105	0.221	<i>Gold particles / synapse</i>
28.0	72.0	32.2	67.8	<i>Percent of subdivision</i>
8.6	22.0	22.4	47.0	<i>Percent of total</i>

To further depict endogenous localization of Kv4.2 by neurite, we performed immunolabeling fluorescence. Immunolabeling confirmed low endogenous localization of Kv4.2 in axons. Fig. 3.12 depicts a neuron with multiple dendrites and one axon stained for somatodendritic marker MAP2 (Fig. 3.12(ii), red). Neurites lacking this marker are designated as axons. We found substantial Kv4.2 ((i), green) in both dendrites and the axon (marked with the arrow). Kv4.2 observed in the axon is well above levels of background staining, providing further evidence of non-negligible subunit density in axons. Our measurements of Kv4.2-sGFP2 transfected neurons also corroborates this trend.

To demonstrate and quantify Kv4.2 localization in an exogenous expression system, we use prebleach fluorescence intensity following transfection of Kv4.2-SGFP2. A histogram of the prebleach fluorescence intensity is depicted in Fig. 3.13. Dendrites contain significantly more Kv4.2 per unit area compared to axons. Mean relative prebleach intensities for axons

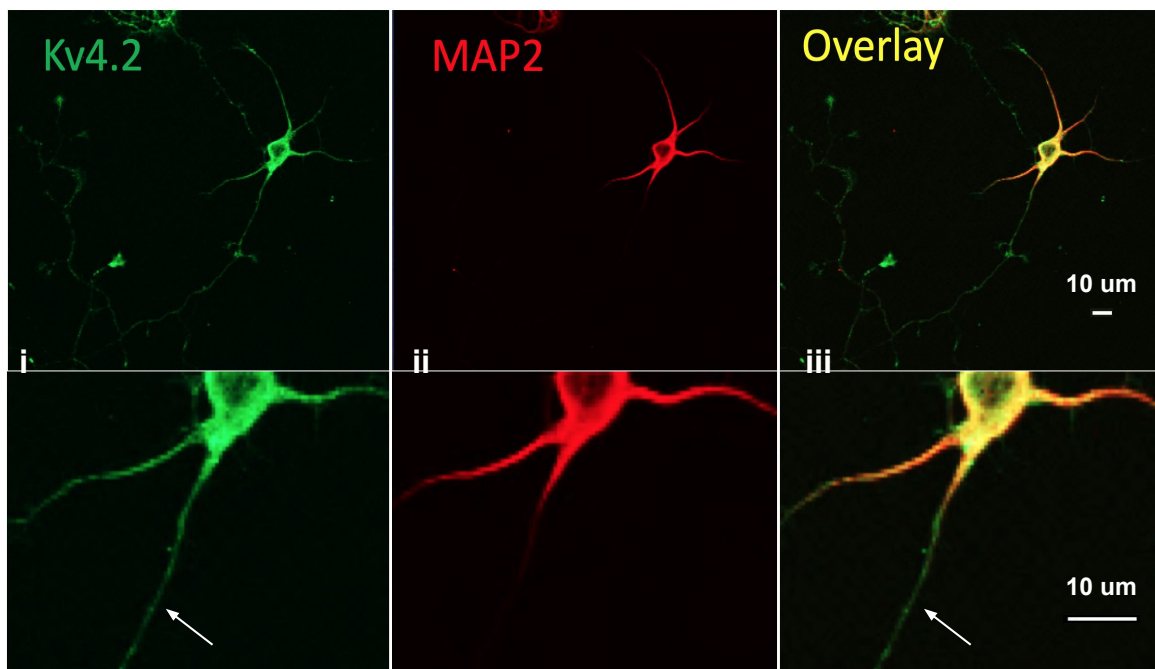


Fig. 3.12 Endogenously expressed Kv4.2 visualized with immunolabeling localizes to dendrites. E18 cultured rat hippocampal neurons at DIV5 were immunostained with Kv4.2 ((i), green) to visualize the endogenous Kv4.2 and MAP2 ((ii), red) to mark the dendritic arbor. The arrow indicates an example of an axon that still shows substantial endogenous Kv4.2.

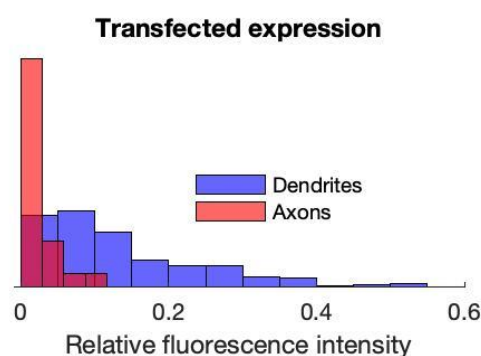


Fig. 3.13 Histogram of the relative prebleach fluorescence intensity for Kv4.2-sGFP2 transfected neurons. This data shows a higher density of total Kv4.2 in dendrites compared to axons ($P = 1.3 \times 10^{-19}$) and is used as a modeling constraint in Sec. 4.4.

and dendrites are 0.0788 and 0.1503, respectively—a significant difference ($P = 1.3 \times 10^{-19}$). Taken together, these results establish that Kv4.2 preferentially localizes in dendrites, but its expression in axons is non-negligible, consistent with other studies. The mean prebleach fluorescence intensity is used to constrain total Kv4.2 subunit density (later defined as *tot*) in subsequent Sec. 4.4.

3.6 Perturbing neural excitability does not have an immediate observable effect on dendritic transport

Thus far, we have collected data on Kv4.2 transport and localization. We now consider whether perturbations to neural excitability have any impact on our recent observations. Similar experiments have been performed for AMPA receptors and other ion channels [24, 60, 241]. Previous studies have also revealed that Kv4.2 surface expression is regulated as a function of neuron excitability [244, 118, 88]. Moreover, dendritic stimulation is reported to change local Kv4.2 trafficking rates as measured with FRAP microscopy [164]. We wonder whether Kv4.2 active transport too might be regulated in a similar way. To this end, we observe active Kv4.2 microtubule-based trafficking while perturbing the neurons. Neurons can be experimentally depolarized by incubation with AMPA, which activates synapses throughout the dendrites. Neurons can also be depolarized by incubation with extracellular KCl, which increases the resting membrane potential of the cell.

3.6.1 KCl depolarization

We began with elevated KCl. Membrane depolarization with excess KCl has been found to reduce transient outward current in ventricular rat cells [85]. We hypothesized that high KCl might reduce Kv4.2 trafficking to cause this decrease in transient outward current.

Samples treated with high KCl concentration were prepared and time series were captured as previously described (Sec. 2.6.2). A modified Tyrode's solution is prepared with 15 mM KCl. NaCl concentration is reduced to maintain isotonicity. Modified Tyrode's solution: 95 mM NaCl, 45 mM KCl, 2 mM CaCl_2 , 1 mM MgCl_2 , 25 mM HEPES, 10 mM glucose (all Sigma-Aldrich) at pH 7.4. Modified Tyrode's was added to standard 1x Tyrode's at 20 minute into live imaging. The final concentration of KCl is determined by the ratio of normal:modified Tyrode's. For instance, 3:1 normal:modified Tyrode's produces 15 mM KCl. 1:1 produces 25 mM KCl. All ratio combinations maintain the same osmolarity (isotonicity).

The immediate result of excess KCl incubation on active transport in 37 time series is depicted in Fig. 3.14. The red line indicates the time point at which high KCl solution was

added. Excess KCl has no significant effect on frequency of puncta transport in dendrites when comparing time periods 0-20 min (before administration) and 40-60 min (after administration). Some recordings (indices #7-13) have no or minimal puncta before and after KCl administration, whereas others (indices #35-36) have high transport frequency throughout the recording. To reliability establish this, we counted mobile puncta before and after KCl administration. An average of 0.7105 and 0.6316 mobile puncta per recording were present during the 20 min interval before KCl administration and 20 min from time 40 to 60 min, respectively. Two-sample t-test reveals no significant difference between these sample means ($P = 0.8193$). Excess KCl does not observably increase or decrease rates of puncta transport.

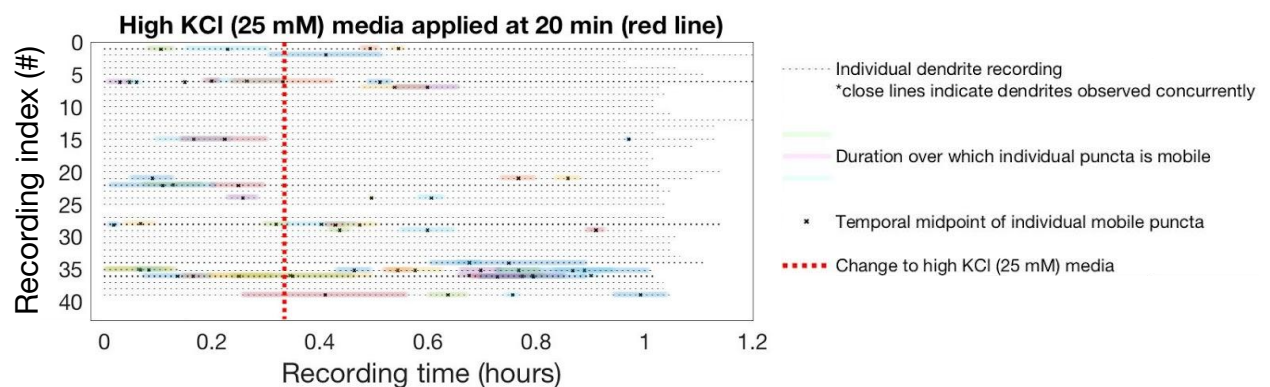


Fig. 3.14 Neuron depolarization by incubation with increased extracellular KCl concentration does not have an immediate observable effect on microtubule transport. We found no statistically significant difference in the number of mobile puncta observed from time 0 to 20 min to time 40 to 60 min ($P = 0.8193$).

3.6.2 AMPA stimulation

We next attempt similar trials with AMPA stimulation. AMPA is a compound that mimics the neurotransmitter glutamate and activates AMPA receptors, which are the most abundant excitatory neurotransmitters and receptors in the nervous system. Incubation with AMPA increases synaptic activity throughout the cell. We hypothesize that Kv4.2—an inhibitory channel that passes outward current—would be upregulated with such a perturbation, as indeed is observed with local Kv4.2 cycling rates [164].

Samples were stimulated with an AMPA agonist to study homeostasis as in previous studies [118, 164]. Time series were captured as previously described for hour-long recordings. (S)-AMPA (Tocris, 0254) was dissolved in nanopure water to concentration of 75 mM and frozen in aliquots. A range of AMPA concentrations were administered 10 to 50 μ M. AMPA

administration occurred 20 min into live imaging with an open chamber. AMPA solution was removed and replaced with fresh 1x Tyrode's 10 minutes later to prevent excitotoxicity.

The results of AMPA stimulation are mixed, as depicted in Fig. 3.15. In some dendrites, puncta transit stops with AMPA administration (Fig. 3.15A). In others, puncta transit begins 10 minutes after administration (Fig. 3.15B), seemingly triggered by AMPA. In most cases, there is no discernible trend with AMPA administration (Fig. 3.15C). Given the intermittent nature of trafficking in dendrites, a significant trend in puncta frequency does not emerge. Upon averaging number of mobile puncta during the first and last 20 min periods of each recording, we found no significant difference in puncta frequency with AMPA administration ($P = 0.301$).

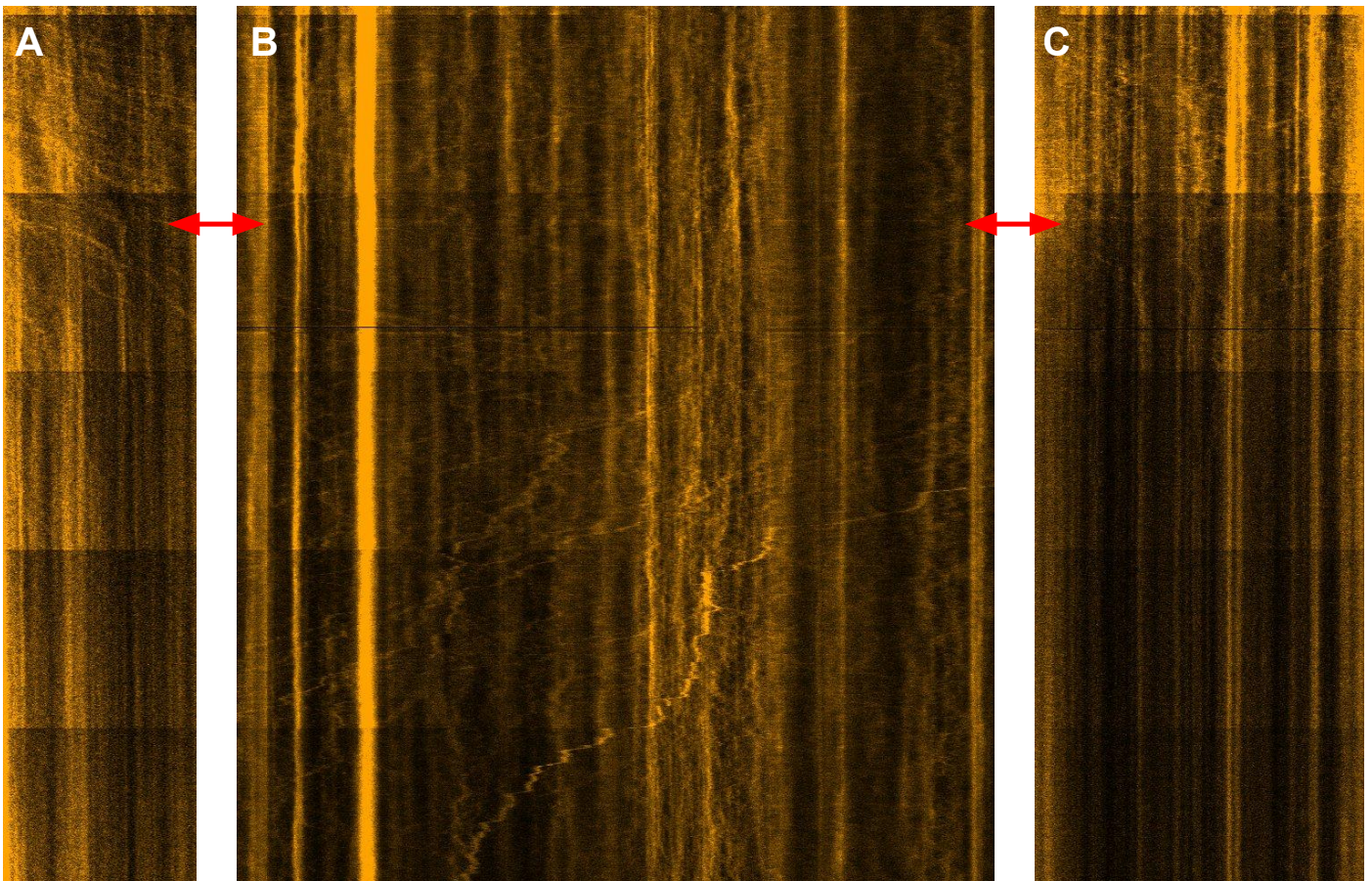


Fig. 3.15 Neuron stimulation by incubation with AMPA does not have a consistent effect on microtubule transport. Red arrows indicate the time point of AMPA administration. Depending on the recording, puncta frequency might decrease (A) or increase (B) with AMPA. In many cases, there is no discernible trend (C). We found no significant difference in puncta frequency with AMPA administration ($P = 0.301$).

3.7 Discussion

In this study, we measured mobile Kv4.2-SGFP2 in puncta using recurrent photobleaching while imaging live neurons. Rather than measuring fluorescence recovery as in standard FRAP experiments, we use photobleaching as a tool to remove static fluorescence. A benefit of this technique is that it allows for analysis of mobile puncta in bleached regions and basal trafficking of cargo in neurons. Other methods of visualizing cargo in transit require subunit sequestration, triggered release, and/or temperature blocks. Although we briefly explored triggered release with the RUSH system [19], our final methodology visualizes basal trafficking of cargo.

We found substantially higher Kv4.2 subunit trafficking in axons than in dendrites. This surprising result appears to contradict widely documented dendritic expression of this protein. However, just as a satellite photo of car traffic might reveal the highest density of cars on freeways as opposed to parked at a destination, our later analysis showed that our measurements are consistent with a mass action model of transport, as explored in Chapter 4. This implies that increased dendritic demand and local interactions with Kv4.2 depletes dendritic microtubule-bound subunit density, with axons obeying to opposite trend. Importantly, previous localization studies show a non-negligible density of axonal Kv4.2 [117, 3]. With no known presynaptic function, this axonal fraction might be subunits in transit, as our trafficking dataset suggests.

There are unavoidable methodological tradeoffs between attempting to quantify protein at physiologically low expression levels, and inducing high expression that enables live imaging. We assumed that the transport behavior of the transfected construct Kv4.2-sGFP2 is similar to that of endogenously-expressed subunits. Our results are therefore subject to this caveat. It is possible that transfection of a recombinant construct alters intracellular expression profiles. For this reason, we validated expression profiles by labeling and quantifying both endogenous and transfected Kv4.2 subunits, while using a construct that has been thoroughly compared to endogenous channel [119]. We anticipate that our approach can spur future work that will mitigate experimental challenges by designing enhanced fluorescent probes that might be suited to live superresolution imaging. Such methods will be crucial for peering deeper into the logic of intracellular protein regulation. Another potential method might involve CRISPR to study endogenously labeled channels. We discuss the methodological impacts on transport behavior in the context of other constructs in Sec. 2.10.

Another notable limitation is our expression system. We observed trafficking in cultured neurons rather than an *in vivo* system. It is possible that cargo trafficking and regulation for a neuron *in vivo* and in an active circuit differs from a neuron cultured on a dish. The cell's

orientation, adjacent neurons, surrounding glial cells, and tissue parenchyma vary between environments.

Lastly, we observed that perturbations to neural excitability with KCl and AMPA made no immediate impact to the rate of trafficking. Treatment with AMPA hours or days before imaging might have produced a more significant change in trafficking frequency. Similarly, longer incubation with KCl before imaging would be most consistent with so-called *chronic* depolarization. However, these perturbations would also have widespread effects throughout the cell, including on mechanisms involved in intraneural distribution. For instance, subunit biosynthesis, modifications, and expression might all be regulated by neural excitability. We intended to isolate the effect of the perturbations on active transport. Herein lies a major challenge of performing and interpreting experimental results. A simple perturbation undoubtedly has multiple effects, each with their own downstream effects. Over long time scales, chronic depolarization with KCl likely impacts Kv4.2 biosynthesis and trafficking. And of course, trafficking frequency depends on subunit biosynthesis. The challenge lies in determining whether chronic depolarization has a direct or indirect effect on subunit transit.

It would have been interesting if trafficking of Kv4.2 puncta was affected on a short time scale. From our experiments here, we cannot rule out such regulation occurs. However, we can conclude that it is unlikely to occur on a timescale as observed here (minutes to hours). We return to this question in Chapter 6, where we explore the sensitivity of feedback regulation at global and local scales. We later show that there are serious disadvantages to highly sensitive regulation, which might explain why perturbing neural excitability does not immediately affect microtubule transport as observed here.

Chapter 4

Reconciling the discordant distributions of microtubule-bound and delivered cargo densities

The results described in this chapter have been submitted to Biophysical Journal. Some sections were written in direct connection to that manuscript.

4.1 Chapter summary and key findings

Building on the experimental observations of the previous chapter, we next reconcile the static and transported cargo densities of Kv4.2. We establish our working framework of cargo distribution in neurites, where we differentiate mobile, microtubule-bound subunits (abbreviated *mt*) from delivered subunits (abbreviated *del*) which include cytosolic and membrane-bound ion channels.

1. The discrepancy between Kv4.2 localization (*del*) and subunits in transit (*mt*) is reconciled by simple mathematical models. Mass action kinetics reveal that the local density of actively transported intracellular cargo can show an inverse relationship with its static expression density. This is demonstrated first in lumped models.
2. A gradient static (*del*) and transported (*mt*) expression profiles of Kv4.2 along the somatodendritic axis is also sufficiently explained by simple mathematical models. Expression gradients in *del* at the sub-neurite level that oppose transport gradients *mt* can arise solely from a directional transport bias and mass action kinetics. This is illustrated for the previously unexplained, unique expression and functional profile of Kv4.2.

3. Kv4.2 puncta exhibit kinetic differences between axons a and dendrites d consistent with local interactions for cargo demand. These discrepancies are attributable to varying propensities for cargo offloading (p_{off}) and unidirectional runs (p_{mem}) in axons and dendrites. Using statistical inference with our experimental data, we make qualitative estimates: $p_{\text{off}}^a < p_{\text{off}}^d$ and $p_{\text{mem}}^a > p_{\text{mem}}^d$.

4.2 Introduction

Most cell types exhibit polarity, an intrinsic asymmetry that defines subcellular directionality and compartment identity. Neurons exhibit strong polarity, with most neuron types showing clear morphological and functional differences between axons and dendrites that shapes the flow of information. The functional differences between these compartments is underpinned by localization of proteins, organelles, and other material within these cell projections. Such global patterning of intracellular expression is thought to be largely mediated by intracellular transport [115, 142] which is increasingly well understood. However, we still lack an understanding of how intracellular transport gives rise to consistent expression profiles in complex neuronal morphologies [58, 220, 247]. To better understand this topic, we develop a framework of intracellular transport in which cargo is either actively transported on microtubules (termed *mt*) or delivered and localized in the cytosol or membrane (termed *del*).

How does cargo dynamically settle to a required distribution? Individual subunits of cargo are unlikely to have directions or otherwise be oriented to the cell morphology. Such a centralized addressing system is inconsistent with observations of stochastic and bidirectional cargo transport. Rather than directed navigation, leading conceptual models suggest that cargo is exported and sorted, while local interactions detect and sequester bypassing subunits as needed [165, 61, 28, 29]. This system is called the sushi-belt model, a hypothesized framework governing intraneuronal trafficking [61], which leaves a number of questions unanswered:

1. What is the expected relationship between mobile microtubule-bound cargo (*mt*) and delivered cargo (*del*)? For a specific ion channel, we find that mobile subunits are observed less frequently in regions of high localization, as a result of high cargo demand and sequestration.
2. Can this framework account for unique localization profiles at the sub-neurite level? The sushi-belt model constrained with our experimental observations reproduces a distinct delivered subunit distribution that increases with dendritic distance.

3. Do the kinetics of cargo motion reflect the regional demand and associated local interactions? For a specific ion channel, we report ballistic trajectories in regions of low demand and diffusive trajectories in regions of high demand, partially explained by region-specific interactions.

Is the sushi-belt model a plausible framework for intracellular trafficking in large neuron morphologies? We evaluate this for a candidate cargo by comparing densities of cargo in transit with distributions of delivered cargo.

We investigate Kv4.2 as a candidate cargo because of its polarized localization and unique distribution profile. As introduced in previous chapters, Kv4.2 is a voltage-gated ion channel prevalently expressed in excitatory neuron dendrites. Kv4.2 conducts A-type, transient outward potassium current, which is abundant in dendrites but scarce in axons [208]. Dendritic expression of Kv4.2 is consistent with its hypothesized role in dendritic integration and control of excitability [208, 106, 220]. Moreover, A-type current exhibits a five- to sixfold increase in current density over the length of the apical dendrite [106]. Localization studies of Kv4.2 corroborate this finding, showing a 70% increase in channel density along the apical dendrite [117]. Several studies have measured Kv4.2 trafficking and internalization in dendrites [242, 244, 118, 88], but none to date have enabled a quantitative, global model of transport and expression patterns.

We report observations that answer the aforementioned three questions for Kv4.2 subunits in hippocampal neurons. During live imaging of actively transported Kv4.2 subunits, we found a greater density of microtubule-based transport in axons than in dendrites (Chapter 3). The apparent discordance of high trafficking densities in regions of low cargo delivery turns out to be consistent with a simple mass action model of intracellular transport. Assuming higher propensity for cargo sequestration and delivery in dendrites, the model predicts a resultant lower density of microtubule-bound cargo. Conversely, a low probability of delivery in axons results in more cargo remaining on the microtubule.

A discretized variant of our model accounts for increasing Kv4.2 localization from proximal to distal compartments. This expression pattern has been extensively characterized and is important for dendritic function, but the question of how it emerges from a relatively simple trafficking mechanism has remained unanswered. We experimentally estimated model parameters including microtubule occupancy and transport rates as functions of distance from soma. Constrained with these data, we provide an analytical solution for the microtubule occupancy (mt) profile that can recapitulate the previously unexplained Kv4.2 localization (del) profile along dendrites.

Finally, a stochastic variant of our model accommodates and accounts for qualitative kinetic differences in individual cargo trajectories. We inferred that dendritic transport

with lower speed and displacement is consistent with increased local interactions on the microtubule. Consistent with lower subunit demand, axonal transport is faster and also mechanistically distinct with longer uninterrupted runs.

The global patterning of intracellular expression is largely mediated by intracellular transport which is increasingly well understood [115, 142]. However, we have yet to elucidate how intracellular transport gives rise to consistent expression profiles in complex neuronal morphologies [58, 220, 247]. Here, we reveal the transport dynamics of ion channel Kv4.2, a cargo with polarized localization (largely in dendrites) and unique density distribution (increasing profile). Our coarse grained models based on first principles accommodate a number of transport phenomena, fit various experimental observations, and are compatible with other mechanistic models of trafficking. This analysis generalizes to intracellular transport and delivery of other cargo and prompts caution in the interpretation of cargo distributions.

4.3 Coarse-grained modeling captures cargo transport and delivery with various levels of detail

In this chapter, we address the question of how cargo localization relates to the density of cargo transported on microtubules. We first discuss a conceptual model of cargo transport and delivery. A cartoon of a neurite segment in Fig. 4.1Ai depicts membrane vesicles (circles) containing cargo (green). An enlargement of the vesicle (Fig. 4.1Aii-iii) shows ion channel Kv4.2 with conjugated fluorescent probe sGFP2 embedded in the lipid bilayer. Each ion channel is a complex of four subunits containing four sGFP2 molecules (Fig. 4.1Aiii), and each membrane vesicles contains numerous ion channels (Fig. 4.1Aii)

In a neurite segment (Fig. 4.1Ai), vesicles containing Kv4.2-sGFP2 are either bound to the microtubule on motor proteins or delivered following local interactions for cargo demand. Delivered cargo includes both cytosolic vesicles as well as membrane-bound subunits. These microtubule-bound and delivered cargo fractions are henceforth referred to as *mt* and *del*. Both *mt* and *del* cargo degrade with rate w .

We use the described framework (Fig. 4.1A-B) to understand our results through a model built up from first principles. We begin with the smallest particles resolved using our methods—the membrane vesicles containing Kv4.2-sGFP2—termed puncta (Fig. 4.1Aii, Bi-ii). A single puncta of cargo is attached to opposing motor proteins (Fig. 4.1Bii) and is subject to numerous forces and interactions with motors, microtubules, and auxiliary proteins [73, 74, 122, 77, 165, 61, 28, 29]. We use coarse-grained modeling to represent the net

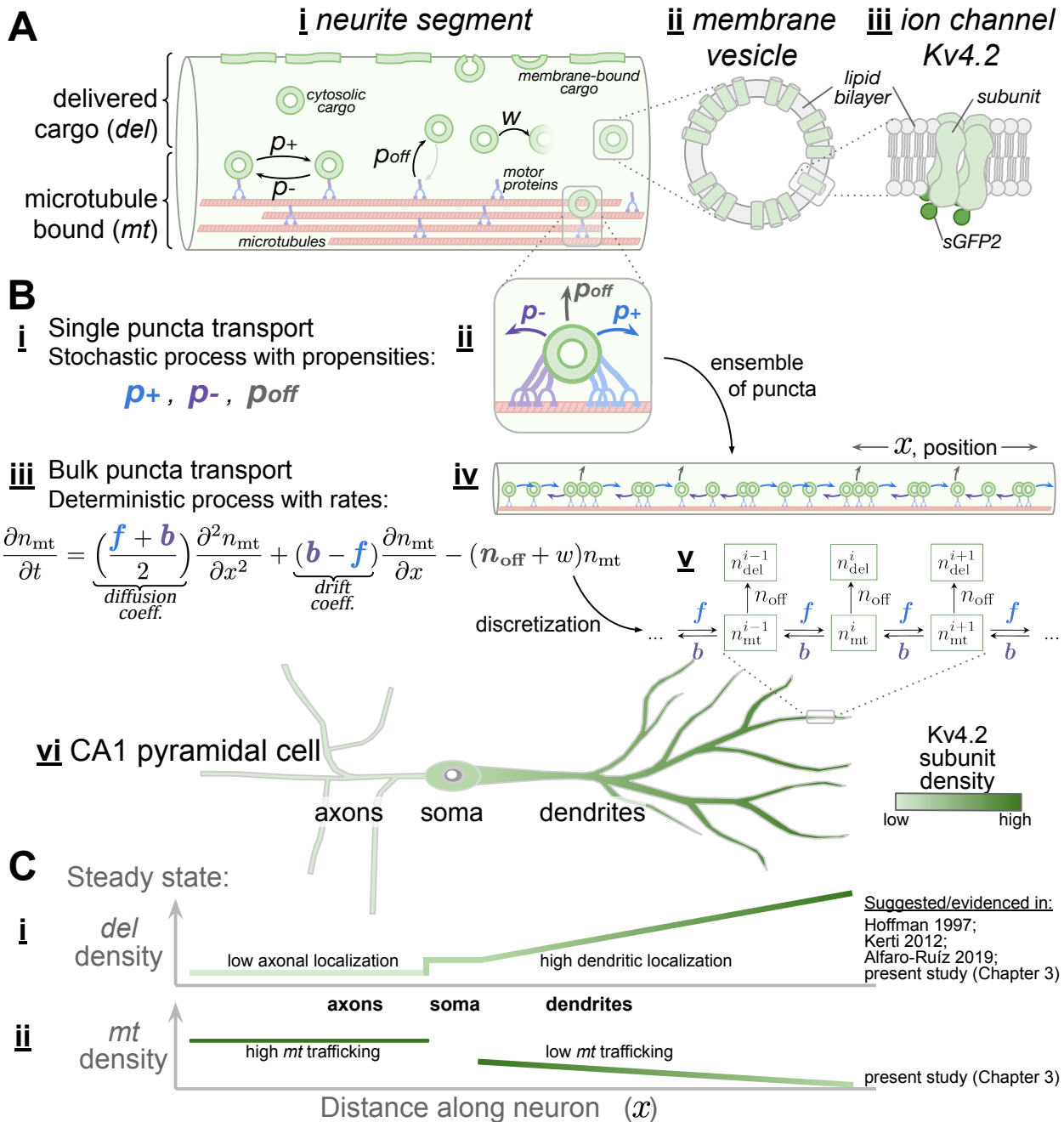


Fig. 4.1 Microtubule-bound (*mt*) and delivered (*del*) subunit densities. (A): Kv4.2 subunits, broadly categorized into microtubule-bound (*mt*) and delivered (*del*) compartments (i), are transported in membrane vesicles (ii), which contain Kv4.2-sGFP2 subunits embedded in a lipid bilayer (iii). (B): Our biophysical model captures various experimental observations. Beginning with first principles, individual vesicles containing cargo (termed puncta) behave stochastically as a random walk (i-ii). An ensemble of such punctas (iv) yields a deterministic process, described by the drift-diffusion equation with decay (iii), which can be discretized to mass action models of varying compartment size (v). Discretized compartments represent neurites of a full neuron morphology (vi). (C): Mass action models accommodate steady state cargo densities. Delivered (*del*) density is low in axons, high in dendrites, and increases with dendritic distance (i). Microtubule-bound (*mt*) trafficking densities are high in axons and low in dendrites (ii).

effects of collective forces on individual puncta. In the simplest variant of our model, puncta move right and left with propensities p_+ and p_- in a random walk. Puncta also detach and reattach with net propensity p_{off} . At this level, the stochastic model accommodates measurements of individual puncta with discrete trajectories (Fig. 3.8).

An ensemble of puncta undergoing stochastic motion behaves predictably according to the drift-diffusion equation with decay as shown in Fig. 4.1Biii-iv [214, 247]. This partial differential equation describes the position x and time t variation of microtubule-bound puncta density n_{mt} with rates for bulk flow directed to the right f , left b , and off the microtubule n_{off} . The drift-diffusion equation with decay can be discretized to represent neurites (Fig. 4.1Bv) of a larger neuron (Fig. 4.1Bvi). The resultant mass action models can be further discretized or lumped into smaller or larger compartments, respectively, for average or distance-dependent data [245, 247], depicted later in Fig. 4.2. These deterministic models accommodate measures of bulk puncta flow.

With steady state assumptions, mass action models can also accommodate bulk puncta densities or frequencies (Figs. 3.1, 3.11, and 3.13). The CA1 pyramidal cell in Fig. 4.1Bvi is shaded according to the steady state density of delivered (*del*) Kv4.2 subunits from studies of A-current density and electron microscopy [106, 117, 3]. Delivered cargo localization (*del*) is low in axons and high along the somatodendritic axis with increasing density with dendritic distance, also plotted in Fig. 4.1Ci. In this study, we corroborate this trend of high delivered (*del*) localization in dendrites in both endogenous and transfected expression systems using electron microscopy and immunostaining (Figs. 3.11 and 3.12). In Fig. 4.1Cii, we depicted *mt* density as observed in the previous chapter (Fig. 3.1), which is notable because it mirrors the delivered (*del*) density.

Delivered (*del*) localization and microtubule-bound (*mt*) density appear to be negatively correlated. Experimental measurements and mathematical models reconcile these distributions in both lumped neurites (Fig. 4.2B-D) and along an intraneurite gradient (Fig. 4.10). Local demand for circulating cargo results in the observed profiles by simple mass action. We also report transport kinetics, from which we infer local cargo interactions that are consistent with the observed profiles (Fig. 4.8). We adapt variants of our biophysical model to numerous experimental observations to reach unified conclusions on the relationships between *mt* and *del* densities.

4.4 Disparity between Kv4.2 static localization and mobile frequency is explained by a mass-action model

Our results in the previous chapter show that the static distribution (*del*) of Kv4.2 is concentrated in dendrites (see Sec. 3.5 and Fig. 3.11), in agreement with known physiological function of this channel. On the other hand, we found in Sec. 3.3 that the vast majority of puncta undergoing active transport (*mt*) appear in axons (Fig. 3.1). How can these apparently conflicting results be reconciled? We addressed this question by constructing biophysical models of transport and delivery constrained with our experimental data from Chapter 3. We constrain *del* with electron microscopy data (Fig. 3.11), which quantified subunits in synapses or extrasynaptic regions. We constrain *mt* with frequencies of actively transported subunits (Fig. 3.1). We constrain total *tot* subunit density with prebleach fluorescence intensity (Fig. 3.13).

A full neuron morphology can be discretized into spatial compartments, depicted in Fig. 4.2A, as previously described. In each compartment, we assumed that cargo is either undergoing transport on microtubules (subscript *mt*) or delivered (subscript *del*) in axonal (*a*) and dendritic (*d*) compartments. Compartments *del* account for all channel subunits that have detached from microtubules, including those in local pools and on the plasma membrane. Rates from *mt* to *del* represent cargo offloading from the microtubules (a_{off} , d_{off}). The reverse rates (a_{reload} , d_{reload}) represent cargo reloading from *del* to *mt*.

Our puncta measurements sampled segments of dendrites and axons, which did not provide data at all locations along each neurite. To incorporate these measurements into a model, we coarsened into a lumped compartmental model that considers only the average density of material in axons and dendrites, irrespective of location (Fig. 4.2B). In the lumped model, $s_{a,d}$ and $s_{d,a}$ represent cargo passing between axons and dendrites. All other rates and compartments are as previously described.

The system of differential equations for this lumped compartmental model is shown below:

$$\begin{aligned}
 \dot{a}_{\text{del}} &= a_{\text{off}}a_{\text{mt}} - a_{\text{reload}}a_{\text{del}} - w_{\text{del}}a_{\text{del}} \\
 \dot{a}_{\text{mt}} &= P + a_{\text{reload}}a_{\text{del}} - a_{\text{off}}a_{\text{mt}} + s_{d,a}d_{\text{mt}} - s_{a,d}a_{\text{mt}} - w_{\text{mt}}a_{\text{mt}} \\
 \dot{d}_{\text{mt}} &= P + d_{\text{reload}}d_{\text{del}} - d_{\text{off}}d_{\text{mt}} + s_{a,d}a_{\text{mt}} - s_{d,a}d_{\text{mt}} - w_{\text{mt}}d_{\text{mt}} \\
 \dot{d}_{\text{del}} &= d_{\text{off}}d_{\text{mt}} - d_{\text{reload}}d_{\text{del}} - w_{\text{del}}d_{\text{del}}
 \end{aligned} \tag{4.1}$$

where a lumped rate $v_{d,r}$ describes flow of mass $dv_{d,r}$ from donor *d* to receiver compartment *r*. The lumped model does not contain a soma compartment. To account for biosynthesis, we add a fixed production term *P* to both dendritic and axonal microtubule compartments.

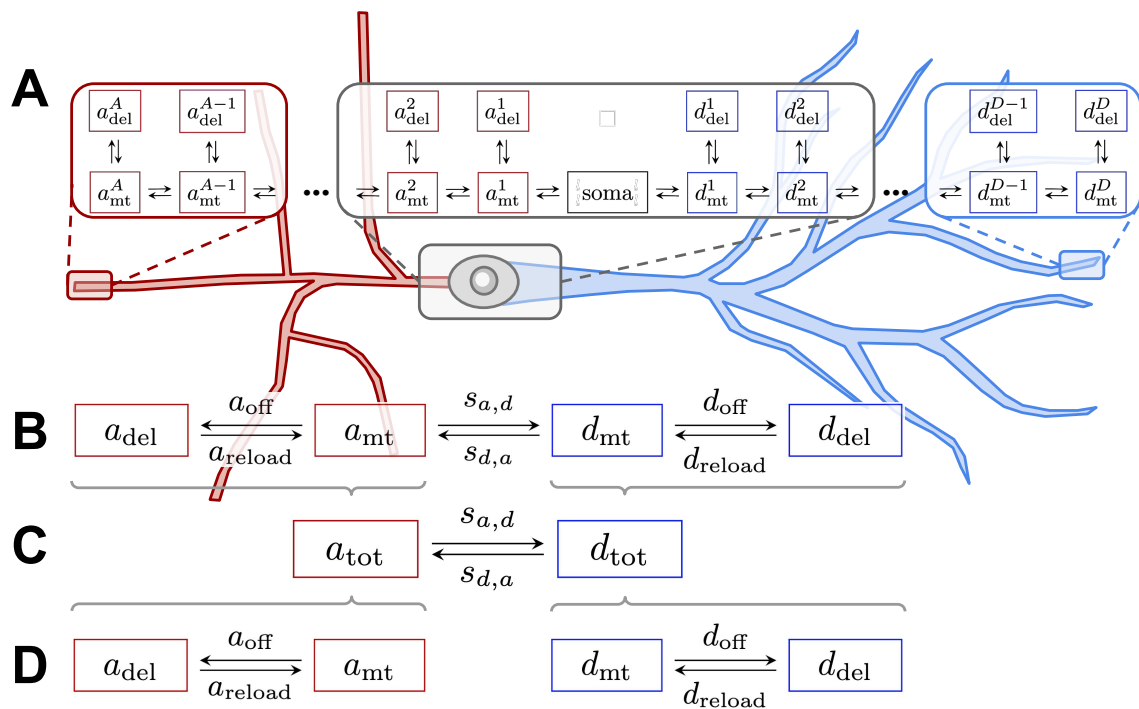


Fig. 4.2 Box diagrams of compartmental models of cargo transport in axons and dendrites. (A): In a full morphology, the central soma is surrounded by microtubule (*mt*) and delivered (*del*) cargo compartments for axons *a* and dendrites *d*. Arrows denote rates of cargo transfer between compartments. (B): A lumped variant can accommodate experimental constraints to simulate disparities in subunit density between axons and dendrites. (C): Simulation of (B) requires estimation of inter-neurite transit rates $s_{a,d}$ and $s_{d,a}$ using experimental constraints for total (*tot*) cargo. (D): Simulation of (B) requires estimation of cargo offloading (*off*) and reloading (*reload*) rates using experimental constraints for *mt* and *del*

Note that flux into both is not assumed to be equal, since flow between axons and dendrites is accounted for by parameters $s_{d,a}$ and $s_{a,d}$. w represents cargo degradation, which, consistent with endolysosomal and autophagic degradation pathways of membrane proteins [113], is faster in *del* than *mt*: $w_{\text{del}} > w_{\text{mt}}$. The remaining rates in Eqs. 4.1 are estimated from experimental results.

We assumed that $s_{a,d}$ and $s_{d,a}$ are slower than the other four rates for two reasons. First, the distances traveled on microtubules are substantially longer than from *mt* to *del*, as evident in the full morphology in Fig. 4.2A. The net flux due to active transport between dendritic and axonal compartments is lumped into the parameters $s_{a,d}$ and $s_{d,a}$. Allowing separate fluxes, $s_{a,d}$ and $s_{d,a}$, provides for asymmetric flow due to sorting mechanisms that are known to regulate cargo entry into both axons and dendrites [116, 161, 126], including for Kv4.2 [112]. To enable a (quasi) steady state estimate of cargo density we set rates $s_{a,d}$ and $s_{d,a}$ to a timescale ten-fold slower than the other rates, although more modest timescale separation produced the same qualitative result.

We next constrained the rates in this model with our experimental measurements. Rates $s_{a,d}$ and $s_{d,a}$ are estimated using the total cargo in axons a_{tot} and dendrites d_{tot} . We assumed that

$$a_{\text{tot}} = a_{\text{mt}} + a_{\text{del}} \quad \text{and} \quad d_{\text{tot}} = d_{\text{mt}} + d_{\text{del}} \quad (4.2)$$

We also assumed that fluorescence microscopy of Kv4.2 captures a_{tot} and d_{tot} , in which we found a $d_{\text{tot}} : a_{\text{tot}}$ ratio of 7.1 : 1 (see Fig. 3.13). Predominant dendritic segregation of the channel is corroborated by other localization studies [208, 117, 220, 3]. To estimate rates from *tot* densities, we grouped *mt* and *del* compartments (from Fig. 4.2B) to produce a model with only a_{tot} and d_{tot} , depicted in Fig. 4.2C. Steady state analysis of the differential equations (described more thoroughly in Sec. 2.9) for this model variant yields:

$$\frac{d_{\text{tot}}}{a_{\text{tot}}} = \frac{s_{a,d}}{s_{d,a}} \approx \frac{7.11}{1}. \quad (4.3)$$

Rates $s_{a,d}$ and $s_{d,a}$ are normalized to axonal measures.

Estimating offload (a_{off} , d_{off}) and reload (a_{reload} , d_{reload}) rates requires a measure of *mt* and *del* cargo in both axons and dendrites. We constrained the steady state densities of *mt* compartments (a_{mt} , d_{mt}) using experimental data (Sec. 3.3 and Fig. 3.1C). Normalizing to axonal puncta frequency, we estimated $d_{\text{mt}} = 0.04$ and $a_{\text{mt}} = 1$.

We estimate steady state *del* compartments (a_{del} , d_{del}) using our data from electron microscopy in synapses (see Sec. 3.5, Fig. 3.11, and Table 3.1). Normalizing to the axon, $d_{\text{del}} = 2.24$ and $a_{\text{del}} = 1$.

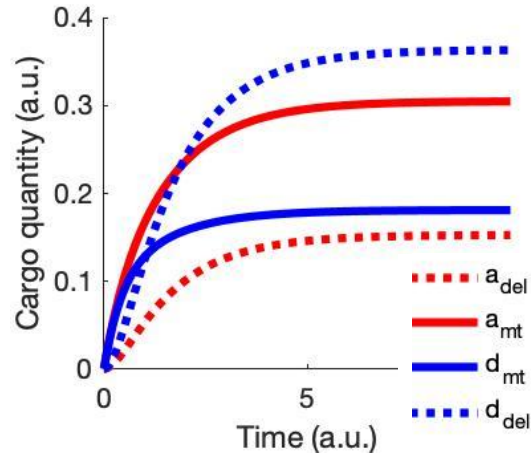


Fig. 4.3 Result of simulation with experimentally-constrained rates, corroborating observed *mt* and *del* densities.

To estimate offload and reload rates from *mt* and *del* densities, we modeled axons and dendrites individually as depicted in Fig. 4.2D. As twice before, we arrived at expressions that allowed us to solve for ratios of rates:

$$\frac{a_{mt}}{a_{del}} = \frac{a_{reload}}{a_{off}} \approx \frac{1}{1} \quad \text{and} \quad \frac{d_{mt}}{d_{del}} = \frac{d_{reload}}{d_{off}} \approx \frac{0.0374}{2.24} \quad (4.4)$$

Together these estimates (Eqs. 4.3-4.4) provide constraints for all rates in the lumped model variant (Fig. 4.2B).

The simulation of this model are depicted in Fig. 4.3. At steady state, the negative correlation between *mt* and *del* compartments in both neurites is clear: $a_{del} < a_{mt}$ and $d_{mt} < d_{del}$. In the context of mass action, the result is intuitive. Because cargo demand in axons is restricted ($a_{del} < d_{del}$), more cargo tends to accumulate in the microtubules of axons versus those of dendrites ($a_{mt} > d_{mt}$). The disparity between total Kv4.2 subunit density and puncta frequency is partially explained by the simple mass action model.

We analyzed negative correlation between *mt* and *del* compartments using Eq. 4.2 and the estimate in Eq. 4.3. We normalized the constraint in Eq. 4.3 to a total mass $a_{tot} + d_{tot} = 1$ ($a_{tot} = 0.12$, $d_{tot} = 0.88$) such that each density ($a_{mt}, a_{del}, d_{mt}, d_{del}$) is a fractional quantity. The resultant steady-state densities of *del* and *mt* cargo are plotted in Fig. 4.4. Shaded regions indicate the range of a_{tot} and d_{tot} from first to third quartiles on Fig. 3.13. Quantities of cargo *mt* have a clear negative correlation with *del*, and this result holds for any a_{tot} and d_{tot} . In other words, the negative correlation within a neurite exists regardless of cargo predilection for that neurite.

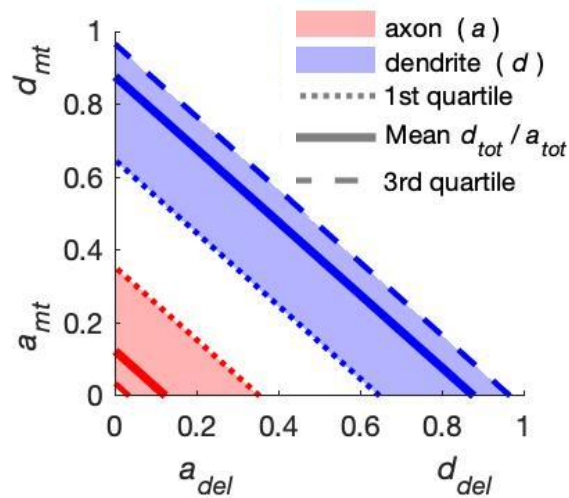


Fig. 4.4 Analytical result demonstrating negative correlation between a_{del} and a_{mt} or d_{del} and d_{mt} when restricted to a constant tot mass.

In summary, these results so far show that apparently contradictory densities of mobile (mt) and delivered (del) cargo are consistent with a simple transport model. This conclusion only required considering bulk flow between compartments that represented the entirety of the axonal and dendritic arbors. However, our experimental measurements also indicated strong differences in the detailed motion of axonal and dendritic puncta. We next analysed detailed transport kinetics in both axons and dendrites to infer whether differences could be accounted for by qualitatively different transport mechanisms.

4.5 Kinetic differences between axons and dendrites are attributable to varying propensities for cargo offloading and unidirectional runs

We analyzed Kv4.2 puncta trajectories in axons and dendrites. Kymograms depicting representative puncta trajectories in axons and dendrites are shown in Fig. 3.8Ai and Fig. 3.8Bi, respectively. Population measurements of puncta kinetics are shown in Fig. 3.9. We found that axonal puncta undergo unidirectional runs at high speeds, whereas dendritic puncta appear to change direction more frequently and stall longer. Since the same cargo is trafficked in both neurite types, we asked whether these differences in trafficking kinetics were better explained by an intrinsic difference in the microtubule transport mechanism, or whether they could simply be accounted for by a difference in dendritic and axonal propensities for

cargo offloading from microtubules. To infer which of these mechanisms best captured our observations we modeled out individual trajectories using a modified random walk.

Our previous models cannot represent individual puncta trajectories, since these kinetics were lumped into single compartments a_{mt} or d_{mt} . We require a model with fine spatial discretization of the microtubules. Two such models are the random walk and drift-diffusion, which respectively describe the motion of an individual particle and population of particles. These models are used in conjunction to draw conclusions from the experimental data.

4.5.1 Modeling transport using a modified random walk

We constructed a simplified compartmental model of active transport in the form of puncta undergoing modified random walks. This model is shown in Fig. 4.5A and contains three types of compartment: axon (A), soma (S), and dendrite (D). Each punctum begins in the S compartment and has some probability per unit time (propensity) of moving right p_+ and some propensity of moving left p_- . These transition propensities represent the stochastic movement of actively transported cargo along microtubules.

We incorporated local interactions by allowing neurite-specific cargo offloading. Puncta on axonal microtubules have a propensity of offloading, p_{off}^a , while puncta on dendritic microtubules have a distinct propensity p_{off}^d . Given our own observations (Fig. 3.11-3.13) and the extensive published evidence for Kv4.2 proclivity to dendrites versus axons [208, 106, 30, 118, 117, 220, 3], we explored ratios of p_{off}^a to p_{off}^d for which $p_{off}^a \ll p_{off}^d$.

In a variation of this model, we implemented our observation that axonal puncta travel unidirectionally with little stall time, which is characteristic of a superdiffusive process. Indeed, there is experimental evidence for microtubule-based transport undergoing superdiffusive unidirectional runs [37, 38, 193]. We therefore incorporated an additional probability parameter p_{mem} that acts as a memory term, depicted in Fig. 4.5B-C. p_{mem} is the probability that a punctum repeats its previous step, giving rise to extended runs if $p_{mem} > 0$. When $p_{mem} = 0$, the next step is independent of the previous step (Fig. 4.5B). When $p_{mem} = 1$, the next step is always the same as the previous step (Fig. 4.5C). A linear interpolation between these extremes, as described in [247], produces a range of memory propensities that scales the average length of the unidirectional run.

Fig. 4.6 depicts a simulation of 10 puncta over 500 time steps. The resultant simulated trajectories agree qualitatively with kymograms from experiments (Fig. 3.8). In this simulation, as in experiments, puncta in axons on average travel longer distances, at faster speeds, and with decreased stall times when compared to puncta in dendrites. We next rigorously examined the goodness of fit of our experimental data to this model to infer mechanistic differences between axons and dendrites. We start by estimating jump rates p_- and p_+ using

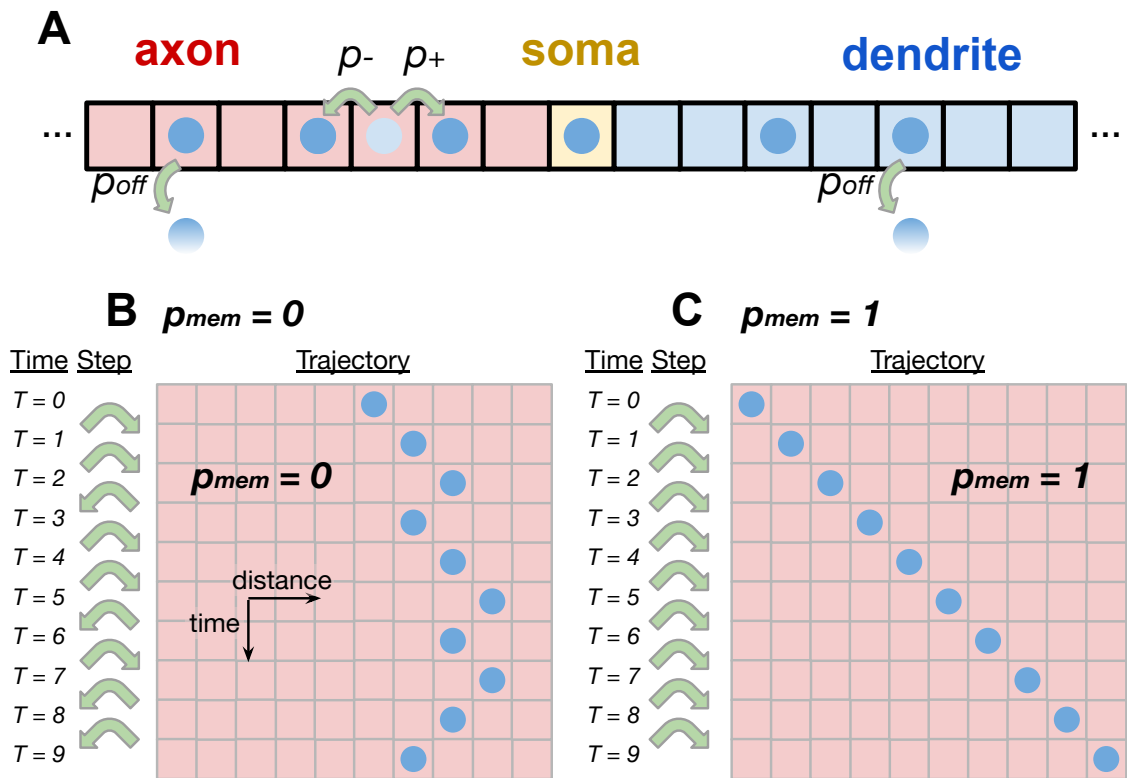


Fig. 4.5 Model of modified random walk. (A): Setup of stochastic simulations along linear multi-compartment model (axon-soma-dendrite), with left/right jump and offloading propensities depicted. (B) and (C) depict extreme cases for memory parameter p_{mem} .

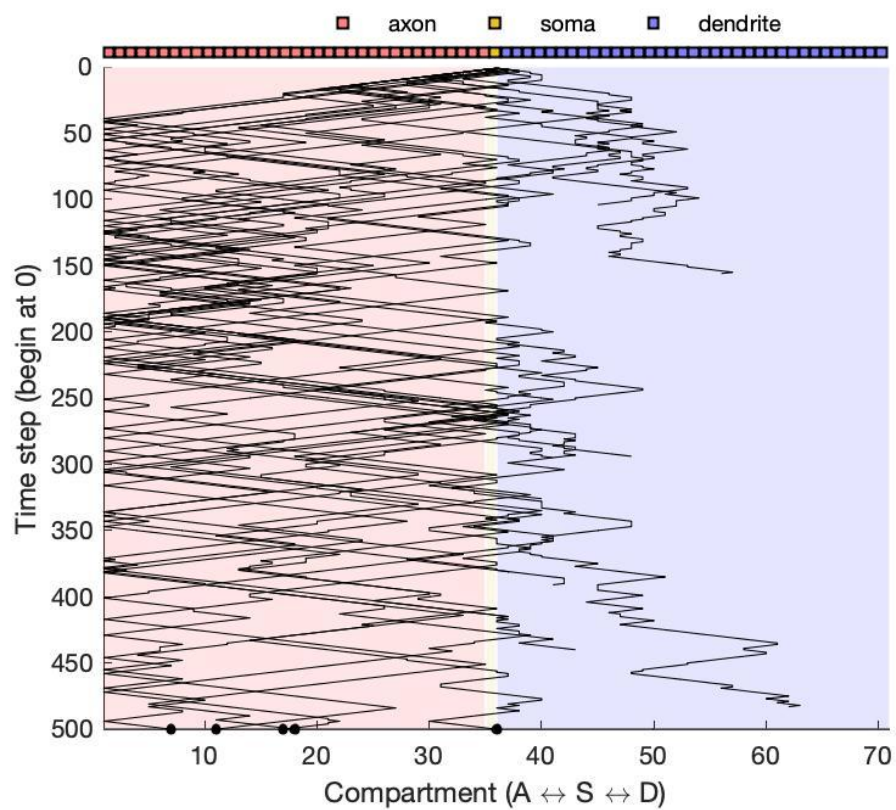


Fig. 4.6 For demonstration of the stochastic model, 10 puncta are simulated over 500 time steps with $p_{\text{off}}^a < p_{\text{off}}^d$ and $p_{\text{mem}}^a > p_{\text{mem}}^d$. The resulting simulated trajectories visually compare to the experimentally-obtained kymograms in Fig. 3.8.

bulk flow averages in the drift-diffusion model. We then infer parameters p_{off} and p_{mem} by simulating individual puncta trajectories with the modified random walk.

4.5.2 Drift-diffusion equation

We estimated left and right jump rates p_- and p_+ of individual puncta by analyzing the bulk flow of a population of particles. We used population dynamics for average puncta position as a function of distance along the dendrite. Fig. 4.7 depicts the observed puncta frequency of dendritic puncta versus their measured distance from the soma. Puncta trajectories are grouped in 1 μm bins along the dendrites, normalized by the number of dendritic recordings in each bin. To avoid numerical errors with low replicate count, we only considered bins with ≥ 30 dendrite recordings. The resulting distribution of puncta frequency is plotted (Fig. 4.7 *bottom*) and displays a trend of decreasing puncta frequency with distance from the soma.

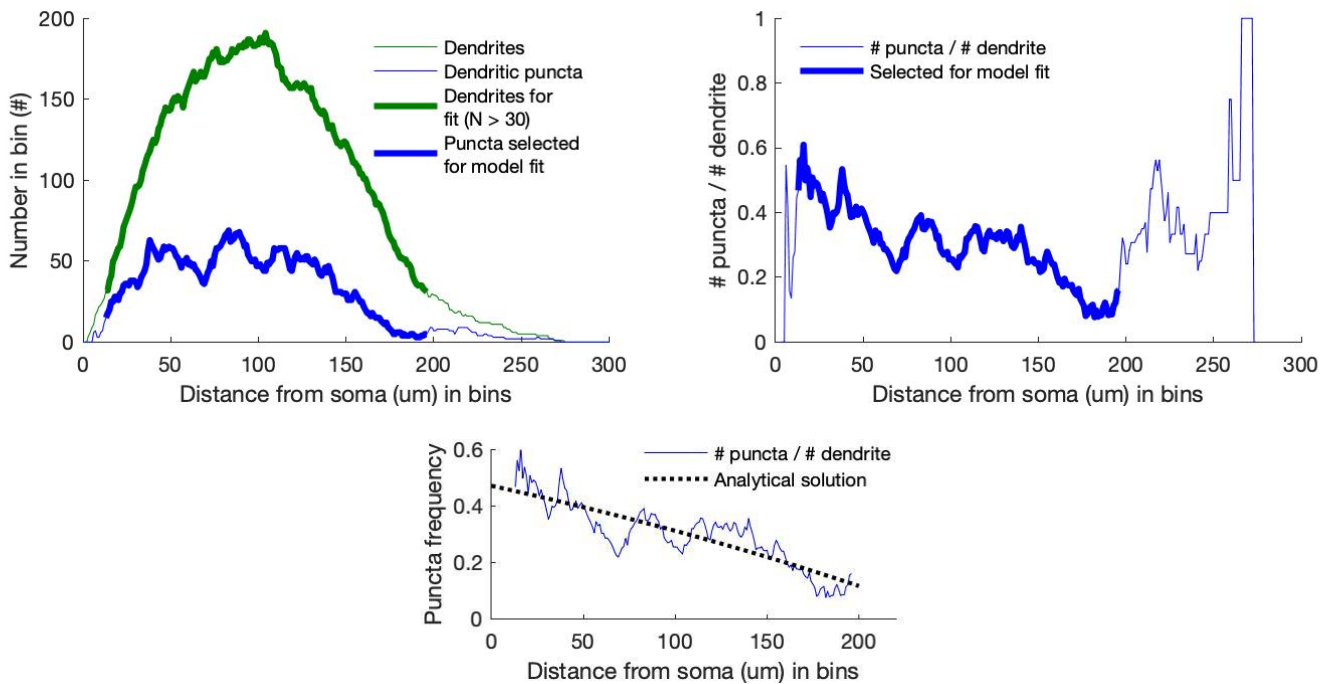


Fig. 4.7 Puncta frequency decreases with distance from soma in dendrites. *Top-left*: All dendrites and dendritic puncta are binned according to distance from the soma. Only distances with $N > 30$ dendrites (bolded) are selected for analysis to avoid numerical error with low replicates. *Top-right*: The number of dendritic puncta is standardized by number of dendrites for each recording, producing a normalized puncta frequency as a function of dendritic distance. *Bottom*: The puncta frequency is consistent with analytical solutions to the drift-diffusion equation ($R^2 = 0.74$). This result is used to constrain mt densities at steady state in the discretized model of Kv4.2 transport (Sec. 4.6).

This distribution of puncta frequency versus distance is expected for a collection of mobile particles obeying the drift-diffusion equation, which we can demonstrate analytically. The one-dimensional drift-diffusion equation (derived in Sec. A.1 of Appendix A) is as follows:

$$\frac{\partial m(x,t)}{\partial t} = D \frac{\partial^2 m(x,t)}{\partial x^2} + v \frac{\partial m(x,t)}{\partial x} \quad (4.5)$$

where $m(x,t)$ denotes the concentration of some substance (heat, particles—in this case, Kv4.2-containing puncta) as a function of position x and time t . D is the diffusion coefficient and v is the mean net velocity, or drift.

Since all of our measurements were in cells with strong fluorescence many hours after transfection, we may assume transport has reached a steady state in which an equal number of puncta enter and leave the recording region. Thus, $\frac{\partial m(x,t)}{\partial t} = 0$, reducing Eq. 4.5 to:

$$\frac{\partial^2 m(x)}{\partial x^2} + \frac{v}{D} \frac{\partial m(x)}{\partial x} = 0$$

This special case of the drift-diffusion equation is known as Poisson's equation, which we can solve as a boundary value problem using the boundary conditions observed experimentally. The endpoints of our data, $m(0 \mu\text{m}) = B_P$ and $m(200 \mu\text{m}) = B_D$, are set for fitting, where B_P and B_D are also the proximal and distal boundaries of the model. Our analytical solution is as follows:

$$m(x) = \frac{e^{-\frac{v}{D}x} (B_D e^{200\frac{v}{D}} (-1 + e^{\frac{v}{D}x}) + (e^{200\frac{v}{D}} - e^{\frac{v}{D}x}) B_P)}{-1 + e^{200\frac{v}{D}}} \quad (4.6)$$

We fitted this analytical solution to the experimental data using least squares to obtain B_P , B_D , and the drift/diffusion coefficient ratio $\frac{v}{D}$:

$$B_P = 0.47; \quad B_D = 0.12; \quad \frac{v}{D} = 0.002 \quad (4.7)$$

This analytical solution ($R^2 = 0.74$) and is overlaid on the experimental data in Fig. 4.7.

D and v describe the bulk flow of a population of particles. When Eq. 4.5 is discretized, D and v characterize the rates of cargo transfer between adjacent compartments:

$$D = \frac{\Delta x^2 (f + b)}{2\Delta n} \quad \text{and} \quad v = \frac{\Delta x (f - b)}{\Delta n} \quad (4.8)$$

where f and b are the forward and backward rates of the discretized compartmental model. Δx and Δn are discretizations in space and time, respectively, for a discrete-time random walk on a 1D lattice. The coefficients describing bulk cargo flow, D and v as defined in Eq.

4.8 are estimated from a population of particles undergoing the random walk, as derived in Appendix A.

In the limit of large numbers, the propensities of a particle undergoing a random walk p_+ and p_- are related to compartmental model rates f and b according to

$$f = \frac{2p_+ - (p_+ - p_-)^2}{2} \quad \text{and} \quad b = \frac{2p_- - (p_+ - p_-)^2}{2} \quad (4.9)$$

as derived in [247]. Using the result from the BVP (Eq. 4.7) along with Eqs. 4.8 and 4.9 and the constraint that $p_+ + p_- = 1$, we can estimate random walk jump rates: $p_+ = 0.5005$, $p_- = 0.4995$. Puncta thus have a modest directional bias and $p_+ \approx p_-$.

4.5.3 Analysis of stochastic model

Returning to the random walk model, we first produced analytical descriptions of the kinetic measures using model parameters. These analytical derivations are described in Sec. B.1 of Appendix B. The result of these derivations reveal that the distribution profiles of punctal distance traveled and mean speed are analytically complex. However, both are geometrically tractable and can be approximated as decreasing monotonic functions.

We next performed parameter inference of model parameters using experimental data and maximum likelihood. This heuristic method is fully described in Sec. B.2 of Appendix B and briefly summarized here. The fitting of this model to experimental data using a combination of maximum likelihood estimation (MLE) and least squares fitting is described here. A gamma distribution, given its continuity and coverage of a semi-infinite $[0, \infty)$ interval, accommodates the analytical solutions as well as experimental and model data. Experiment and model data are normalized and fit to a gamma distribution using MLE (MATLAB function `fitdist`). The shape and scale parameters of gamma fits are compared using nonlinear least squares data fitting (MATLAB function `lsqcurvefit`). Generating stochastic model estimates necessitates a large number of simulated puncta N_s to produce consistent distributions, which requires high computational cost. To resolve this, we employ a moderate $N_s = 10,000$ and increase the finite difference step size of `lsqcurvefit`. A script continuously iterates between (1) running N_s iterations of the stochastic model, (2) MLE of stochastic data, and (3) least squares fitting of distribution parameters to match those of experimental data.

4.5.4 Inference of qualitative differences in axonal and dendritic trafficking via stochastic modeling of experimental data

We compared models with ($0 < p_{\text{mem}} < 1$) and without ($p_{\text{mem}} = 0$) memory. Fig. 4.8 (second column) shows fits to a memoryless model ($p_{\text{mem}} = 0$). Optimal parameter estimates for surface delivery gave $p_{\text{off}}^a < p_{\text{off}}^d$ ($p_{\text{off}}^a = 0.01$ and $p_{\text{off}}^d = 0.04$) consistent with experiments and previous results in Figs. 4.3-4.4. A random walk with p_{off} alone is sufficient to explain the differences in net displacement and average speed (Fig. 4.8A and B). However, stall time and unidirectional runs are not captured (Fig. 4.8C and D). This result suggests that a memoryless random walk explains the speed and displacement of cargo. However, a memoryless model fails to capture unidirectional runs and stalling.

The result of fitting the model with a memory term ($0 < p_{\text{mem}} < 1$) is shown in the third column of Fig. 4.8. We again found $p_{\text{off}}^a < p_{\text{off}}^d$, producing the same trends in displacement and speed (Fig. 4.8A and B). Optimal estimates of the memory term were $p_{\text{mem}}^a = 0.60$ and $p_{\text{mem}}^d = 0.05$ which is consistent with superdiffusivity being more prominent in axons (Fig. 4.8C and D) and with longer unidirectional runs and with elevated stall times in dendrites, as observed in trajectories (Fig. 3.8A-B).

These observations are consistent with an analysis of mean squared displacement (MSD) for each trajectory (Fig. 4.9). We computed average MSD as a function of time interval, τ up to one quarter of the total recording duration. Resulting data were fitted to $\text{MSD}(\tau) = D\tau^\alpha$ for each trajectory to obtain parameters D and α . Puncta in both dendrites and axons appear to undergo motion with similar D (Fig. 4.9B). However, the MSD tends to increase more rapidly with τ for axonal puncta than for dendritic puncta (Fig. 4.9A). This corresponds to the axonal puncta taking more consecutive steps in the same direction, resulting in motion that is more directed than the memoryless walk of particles in typical diffusion. Axon puncta exhibited a higher degree of superdiffusivity than dendrite puncta (Fig. 4.8D). This discrepancy is consistent with simulated puncta behavior with inferred parameters $p_{\text{mem}}^a = 0.60$ and $p_{\text{mem}}^d = 0.05$.

Together, this analysis suggests mechanistic differences in the transport of Kv4.2 in axons and dendrites. Increased net displacement, average speed, and puncta frequency in axons are explained by a random walk with minimal delivery in axons, consistent with Kv4.2 predilection for dendrites. However, reduced surface delivery of cargo in axons only partially explains the longer observed runs. Other kinetic parameters—stall time and superdiffusivity—require an additional memory term in a modified random walk model, suggesting a distinct axonal transport mechanism.

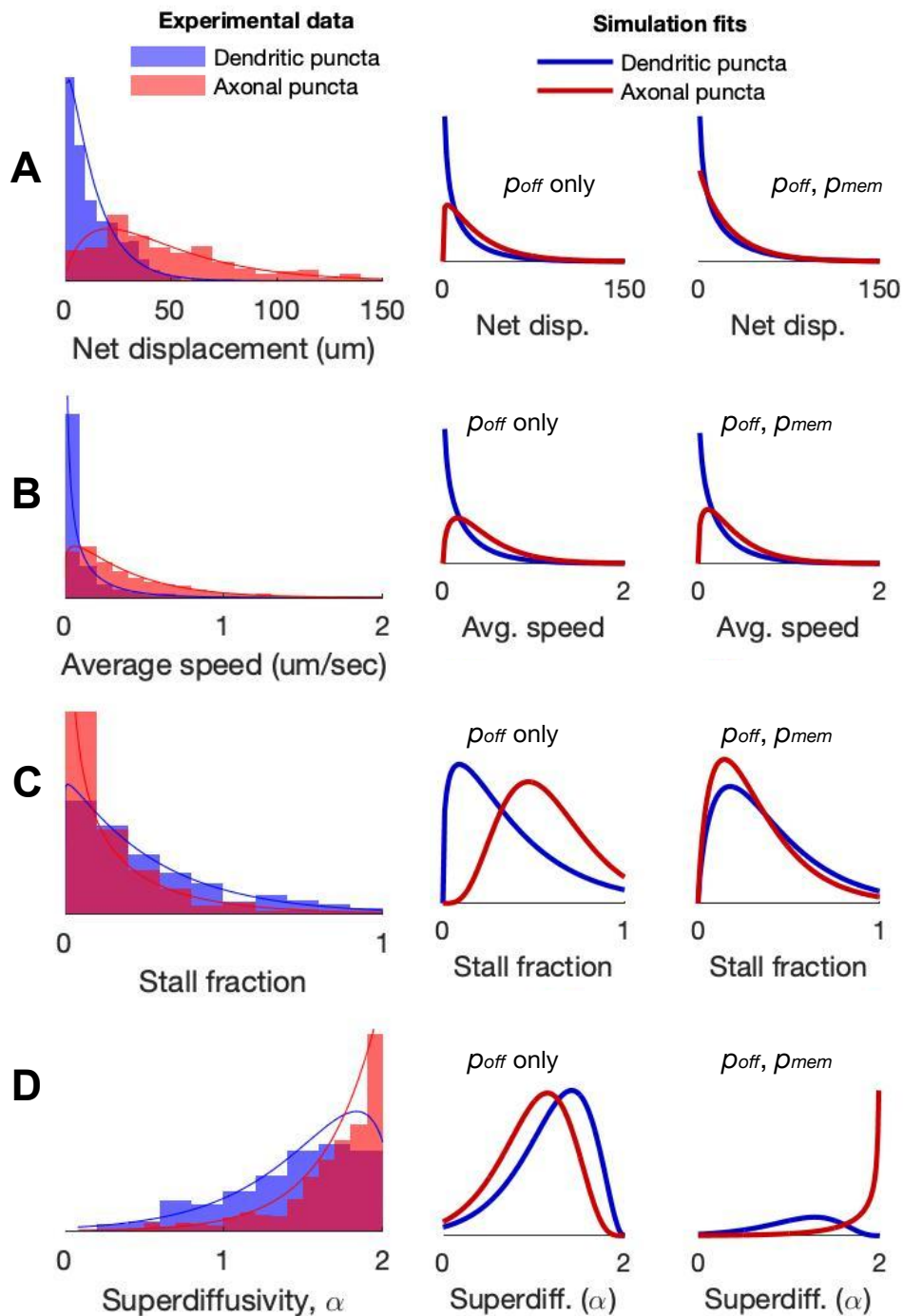


Fig. 4.8 Histograms for various kinetic transport parameters, normalized as probability density functions. On average, axonal puncta have greater net displacement (A), faster speed (B), decreased stall time (C), and increased unidirectional runs (D). Model fits to these results using p_{off} alone (second column) as well as using p_{off} and p_{mem} (third column) are depicted.

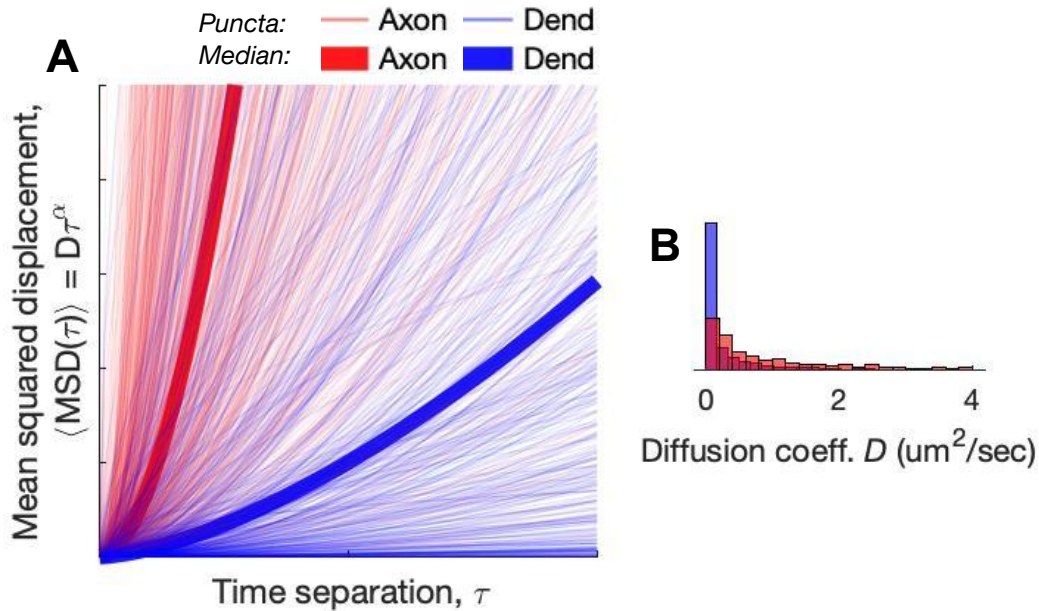


Fig. 4.9 Result of curve fitting for mean squared displacement (MSD) versus time separation (τ), revealing higher degree of superdiffusivity in axons compared to dendrites (A). Bold curves indicate the medians of the populations. Histograms show distribution for D (B), is significantly different (Mann-Whitney test) between axons and dendrites with $P = 3.9 \times 10^{-73}$. Histogram for α was depicted in Fig. 4.8D.

4.6 Mass-action kinetics reconcile *mt* and *del* gradients along the somatodendritic axis

We have established that lumped densities of delivered cargo (*del*) and cargo in transit (*mt*) are negatively correlated, consistent with models of mass action. In distance-dependent measurements, we observe a decreasing *mt* profile along dendrites with distance from the soma (Fig. 4.7). On the other hand, functional and localization studies show that surface density of Kv4.2 *increases* along this axis [106, 117]. Can our modeling and experimental results also account for this relationship? Does negative correlation between *mt* and *del* compartments hold along a sub-neurite gradient—in a spatially discretized dendrite? Are mass action kinetics sufficient to create a profile of increasing *del* with distance from the soma?

To address this, we constructed a model of distribution and delivery across a linear multi-compartment dendrite discretized in space. This model is depicted in Fig. 4.10, where d_{mt}^i and d_{del}^i represent *mt* and *del* compartments, respectively. d_{off}^i is the rate of microtubule offloading for each d_{mt}^i , and f_i and b_i denote the forward and backward transport rates along the length of the dendrite. Using our dendritic data (507 mobile puncta in 478 dendrites) to

estimate rates, we can infer compatible spatial profiles of cargo offloading d_{off}^i and delivery given our experimental data.

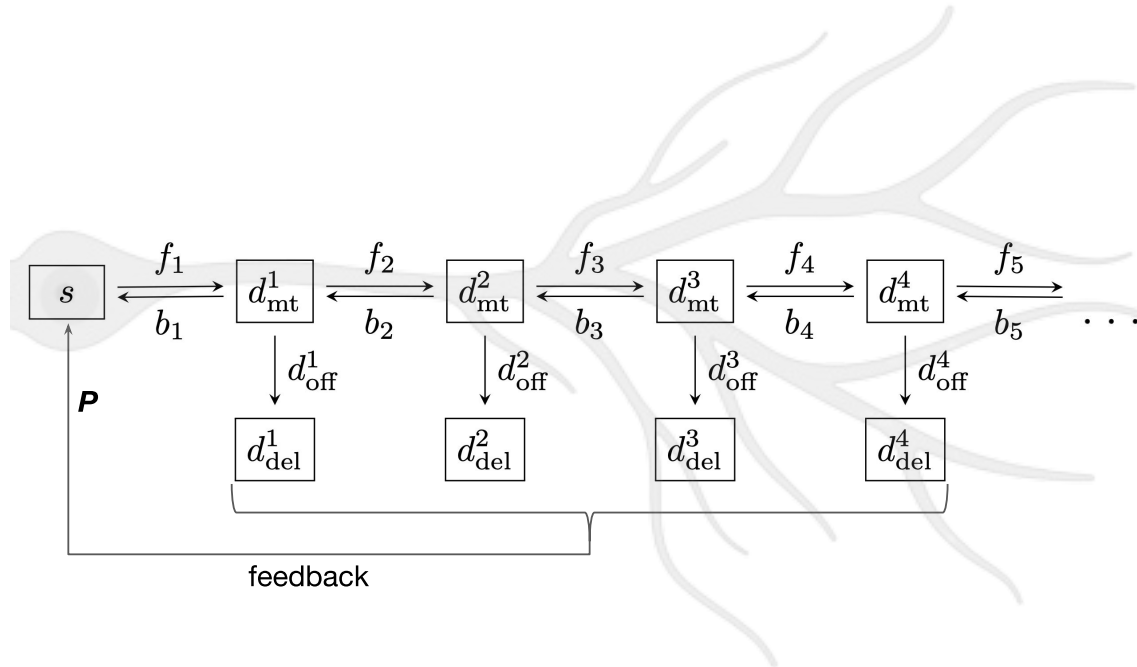


Fig. 4.10 Box diagram of a mass action model of dendritic transport and delivery with feedback. The dendrite is spatially discretized, with each discretization i comprising a microtubule d_{mt}^i and delivered d_{del}^i compartment. f_i s, b_i s, and d_{off}^i s denote rates between compartments. Degradation rates for all compartments are simulated but not depicted.

We considered a dendritic branch extending 250 μm from the soma, which captures typical distances over which trafficking and localization have been characterized. To constrain the steady state concentrations of mt compartments ($s, d_{\text{mt}}^1, d_{\text{mt}}^2, \dots, d_{\text{mt}}^{10}$), we used experimental values obtained in Fig. 4.7.

We next computed directional bias in punctal velocity as a function of distance to constrain rates f_i and b_i . We averaged the instantaneous velocities of each puncta trajectory in bins by distance from the soma. Mean puncta velocity was directed distally, away from the soma, and showed an increasing linear trend, as plotted in Fig. 4.11 ($R^2 = 0.0399$ with 90% confidence intervals). Despite low correlation for a linear trend, a two-sample t-test for bins between 0-50 μm and 150-200 μm indicates a significant increase ($P = 0.0136$) in mean velocity from 1.81 to 5.22 $\mu\text{m}/\text{s}$. With a positive y-intercept and slope, the mean punctal velocity is directed distally and increases with distance from the soma. That is, $f_i > b_i$ and $f_{i+1} \gg b_{i+1}$. The velocities in Fig. 4.11 range from 1.5 to 5.2 $\mu\text{m}/\text{s}$ and are scaled according to the spatial

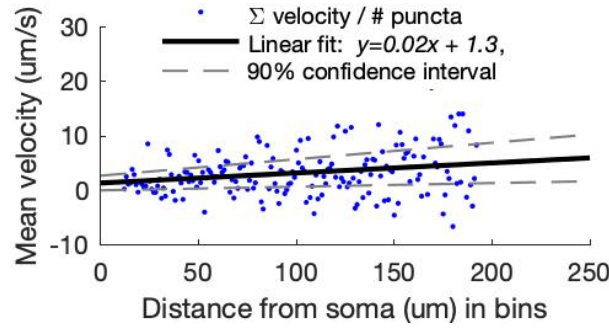


Fig. 4.11 The mean instantaneous velocities for all dendritic puncta are standardized by puncta frequency along the length of the dendrite. Mean velocity (y-axis) is directed distally, away from the soma. A linear trend line is plotted through the data with 90% confidence intervals, indicating a positive (distal) velocity bias that increases with distance from soma. This data is used to constrain rates between *mt* compartments.

discretization of the model to estimate f_i s and b_i s. The diffusion coefficient $D = \frac{f_i + b_i}{2}$ was estimated using Eq. 4.7, which we assume remained constant throughout the dendritic tree.

As in the previous mass action models, each d_{mt}^i has a corresponding differential equation describing cargo entering and exiting as depicted in Fig. 4.10. We use steady state analysis to solve for cargo offloading rates d_{off}^i in these equations. We find that a profile of increasing f_i s and decreasing b_i s with distance from the soma produces an increasing profile of d_{off}^i s. In other words, for cargo with an increasing directional bias such that $0 < f_i - b_i < f_{i+1} - b_{i+1}$ and decreasing *mt* profile, mass action dictates increasing offload rates $d_{off}^i < d_{off}^{i+1}$ with distance from the soma. This result is derived solely from equations describing mass action and conservation of mass.

Increasing d_{off}^i s can produce *del* profiles that have the opposite spatial trend to *mt* densities. To demonstrate this, we simulate regulated Kv4.2 production, distribution, and delivery in our model. In the soma, Kv4.2 biosynthesis P is regulated by active subunits in *del* compartments, as depicted in Fig. 4.10. The equation for negative feedback is

$$P = K_P \left(d_{avg,del}^{target} - \frac{\sum_{i=1}^{10} d_{del}^i}{10} \right)$$

where $d_{avg,del}^{target}$ is the target *del* concentration (setpoint), $\frac{\sum_{i=1}^{10} d_{del}^i}{10}$ is mean delivered cargo (process variable), and K_P is the sensitivity of the proportional controller. This control loop feedback mechanism is consistent with experimental observations that Kv4.2 expression is regulated as a function of neuron excitability [244, 118, 88, 164]. Averaging d_{del}^i s provides a realistic process variable for a global controller in a neuron.

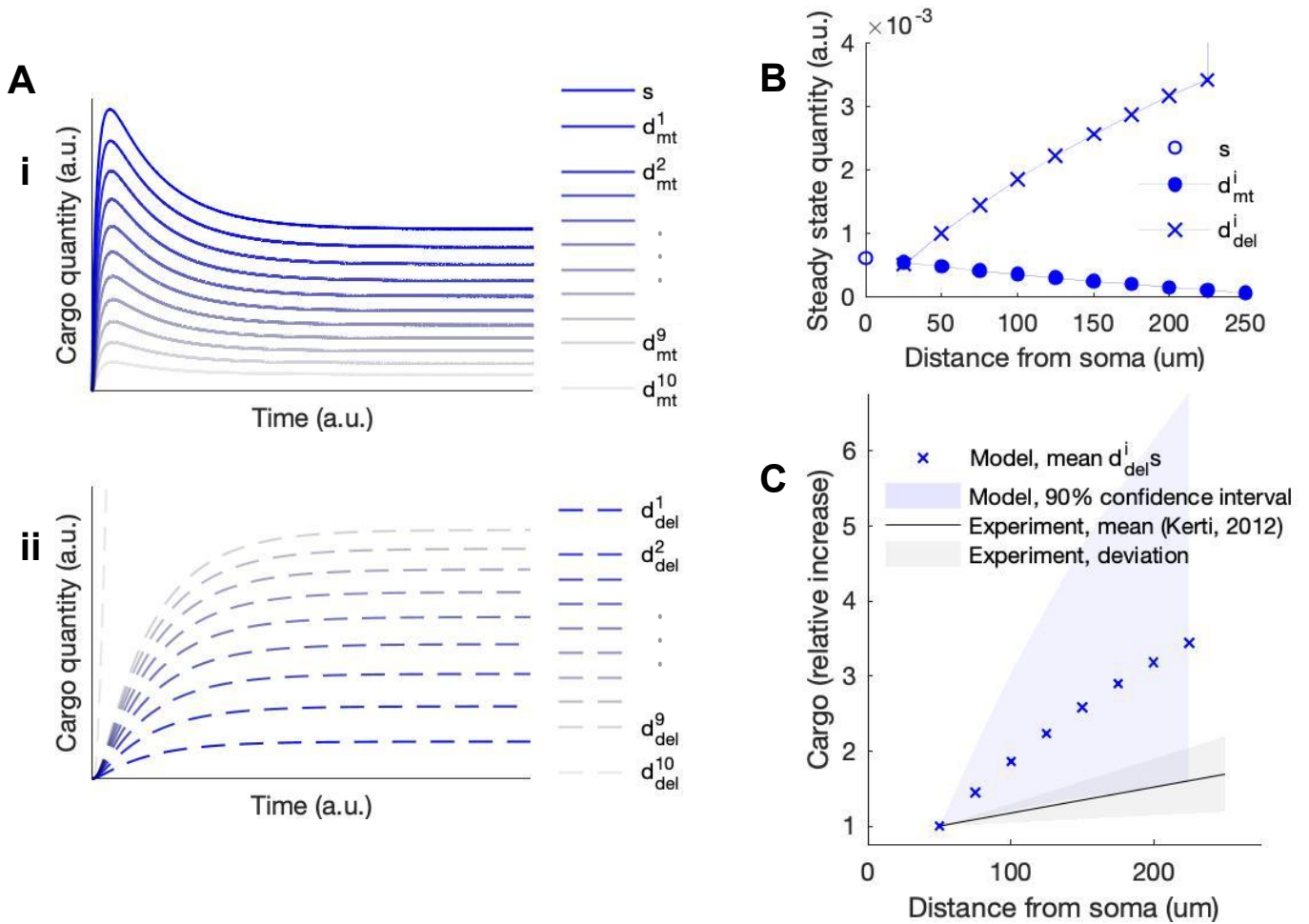


Fig. 4.12 Simulation of mass action model of dendritic transport and delivery with feedback. (A): Plot depicting cargo quantities on microtubules, d_{mt}^i (i), and delivered cargo quantities, d_{del}^i (ii). (B): Steady state concentrations of all compartments. (C): Steady state concentrations of d_{del}^i s standardized by d_{del}^2 at $50 \mu\text{m}$ overlaid on equivalently-standardized experimental data of Kv4.2 localization [117].

With all rates defined, the result of simulation is depicted in Fig. 4.12A. d_{mt}^i s assume a profile similar to that observed experimentally (Fig. 4.7), with decreasing density with distance from the soma (Fig. 4.12Ai). d_{del}^i s express the opposite profile—increasing density with distance from the soma (Fig. 4.12Aii). Steady state density versus position along the dendrite is plotted in Fig. 4.12B. The increasing d_{del}^i density is notable because localization experiments [117] and, to a larger degree, recordings of A-type current [106] both demonstrate increasing profiles with distance from the soma.

In this analysis, the increasing gradient of d_{del}^i s (Fig. 4.12B) largely depends on the gradient of the mean velocities (Fig. 4.11) used to constrain the directional bias $f_i > b_i$. In Fig. 4.12C, we plot d_{del}^i s for the linear fit and 90% confidence intervals from our measured directional bias. On the same plot, we shade the reported localization profile of Kv4.2 immunogold-tagged particles from Kerti et al's 2012 study [117]. Our model constrained by our measured Kv4.2 transport bias predicts an asymmetric profile of delivered Kv4.2 that falls within a standard deviation of localization data. Together these results provide an account of how a previously unexplained and highly organized protein expression pattern can emerge from relatively simple active transport mechanisms.

4.7 A summary of the relationships between microtubule-bound (*mt*) and delivered (*del*) cargo densities

The questions we address in this study concern how densities of actively transported cargo relate to their delivered localization. We discuss a conceptual model of how cargo densities on microtubules give rise to delivered densities. A cartoon of the potential relationships is shown in Fig. 4.13. Cargo on microtubules and cargo localized to the plasma membrane is depicted by the shading of the interior and outline of the cell, respectively (Fig. 4.13A). Intuitively, one might expect to measure higher densities of transported cargo in the compartments where the cargo eventually becomes localized (Fig. 4.13B). Indeed, this is the implicit assumption made in static imaging studies that attempt to quantify intracellular protein and mRNA distributions by labeling and counting puncta or integrating signal density [168].

However, under mass-action, the rate of transport between cellular compartments is proportional to density. In a well mixed system with homogeneous cargo affinity, cargo with strong offload proclivity can fill both *mt* and *del* compartments simultaneously, as in Fig. 4.13B. With heterogeneous, compartmentalized neurites, the *mt* in branches with lower offload proclivity act as a cargo sink. This can result in a negative correlation between *mt* and *del* within each section of neurite, as depicted in Fig. 4.13C.

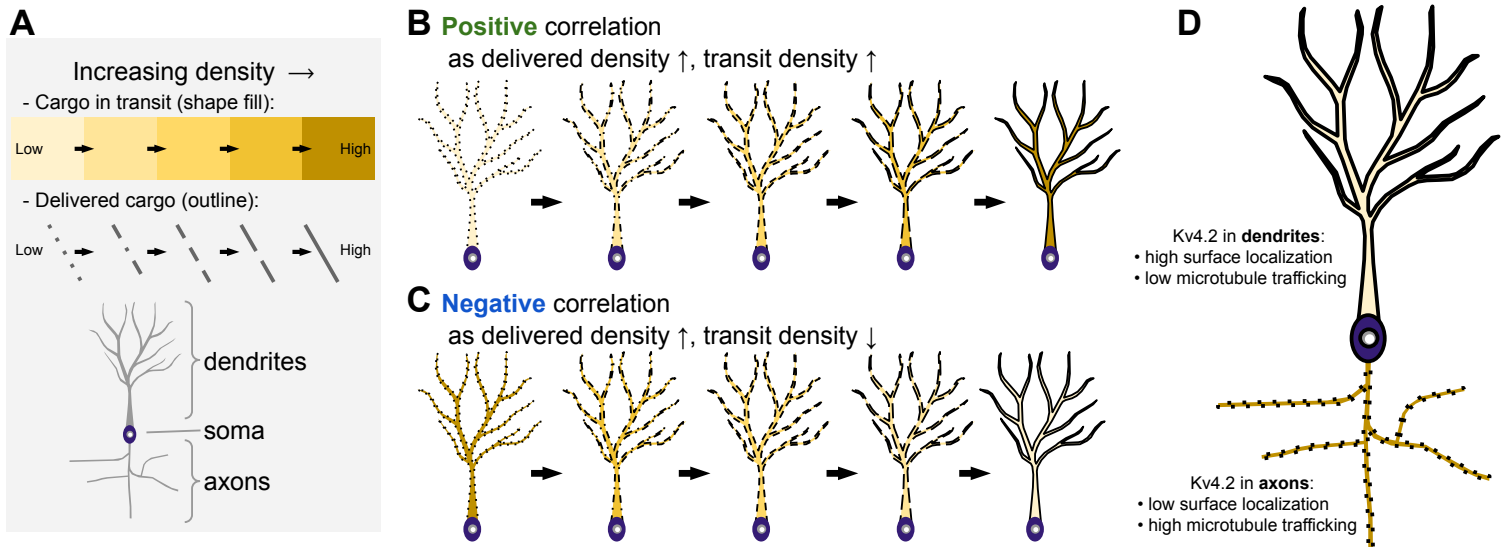


Fig. 4.13 Mass action transport causes discordance of delivered and transported cargo densities between axons and dendrites. (A): Schematic legend. (B): If membrane and microtubule densities are positively correlated, both quantities increase or decrease together. (C): In a negative correlation, an increase or decrease in *del* density results in the opposite deflection in *mt*. (D): Measured densities for Kv4.2 are negatively correlated, consistent with mass action models for a system with multiple neurites.

We experimentally measured and quantified the *mt* trafficking of a specific cargo, Kv4.2 subunits, whose distribution is especially relevant to these considerations. Kv4.2 has a highly regulated dendritic *del* expression whose density increases along dendrites with distance from the soma. We measured *del* and *mt* densities of Kv4.2 in neurites of varying surface expression. A summary of these results is depicted in Fig. 4.13D. Kv4.2 has high *del* density and surprisingly low *mt* density in dendrites.

We next summarize our results in a gradient at the sub-neurite level. We show that a gradient *del* density can have a positive, negative, or no correlation with the *mt* gradient in that neurite (Fig. 4.14A). We find that the density of Kv4.2 subunits in transit *mt* decreases in dendrites with distance from the soma. Taken with localization data (*del*) and the well-established functional profile of the channel, this is consistent with a continuous expression gradient with negative correlation, depicted in Fig. 4.14B.

Lastly, the kinetic properties of trafficked cargo in *mt* reflect the cargo demand in *del* (Fig. 4.15). Transport in axons is mechanistically distinct in that cargo is trafficked efficiently through regions of low, sparse demand with direct, unidirectional trajectories. Increased cargo demand in dendrites results in diffusive, winding, and meandering trajectories.

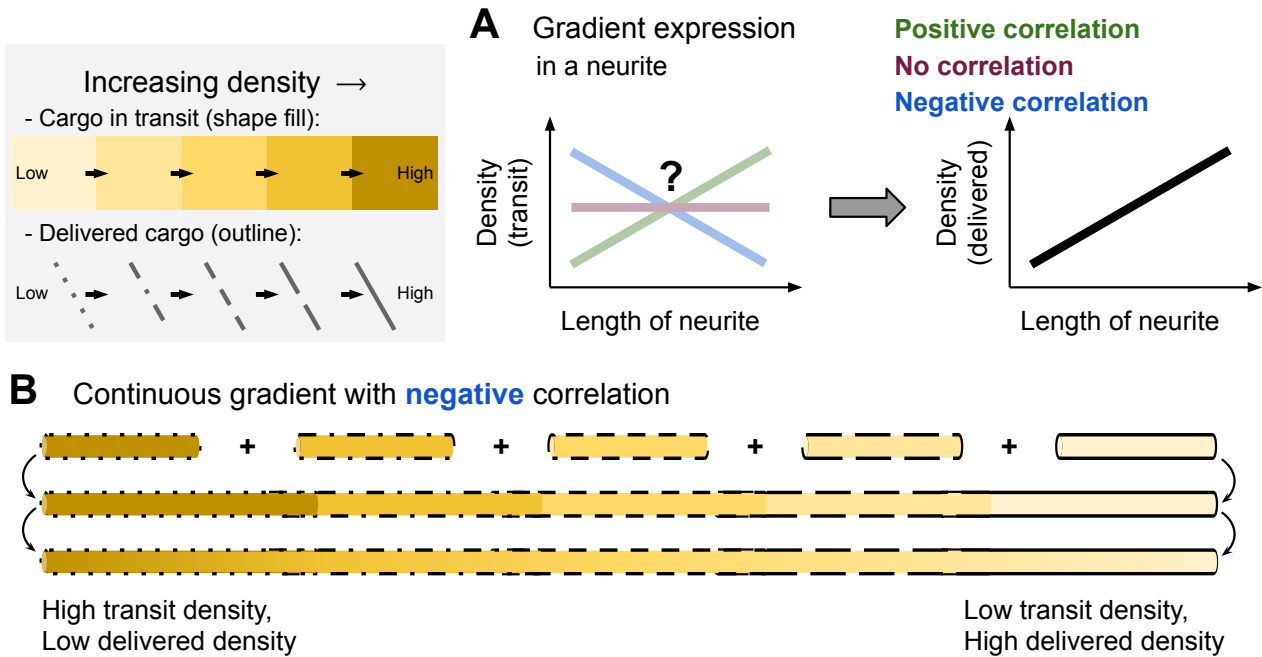


Fig. 4.14 Mass action transport causes discordance of delivered and transported cargo densities along the length of a neurite. (A): The question of positive, negative, or no correlation holds for gradient expression along a single neurite. (B): Kv4.2 exhibits continuous gradients of cargo delivered and in transit that are consistent with negative correlation.

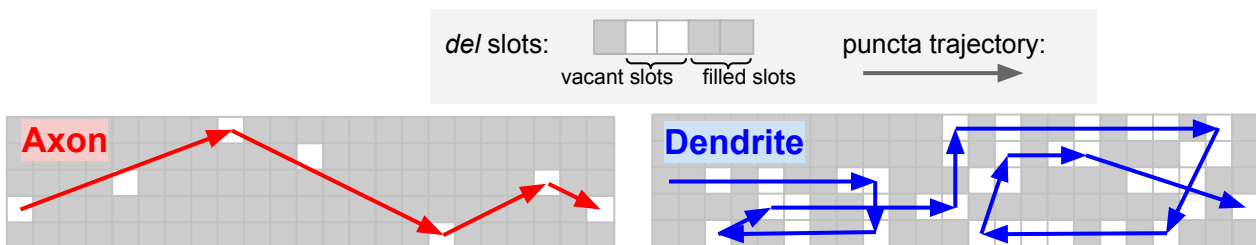


Fig. 4.15 The kinetic properties of individual puncta trajectories in *mt* also reflect cargo demand in *del*.

4.8 Discussion

Transport kinetics of Kv4.2 puncta in axons qualitatively differ from those in dendrites. Puncta in axons showed increased superdiffusivity, with increased net displacement, increased velocity, and decreased stall time. The opposite is observed in dendrites. This relationship makes sense physiologically, since we assumed that dendrites have a preponderance of sequestration mechanisms that need opportunity to bind cargo and offload it from the microtubules. However, increased microtubule offloading is not sufficient to explain the observed differences in kinetics. A random walk with memory better characterizes the experimental distributions for stall fraction and diffusivity. We therefore infer that transport in axons is mechanistically different, with an effective internal state increasing the probability of unidirectional runs.

A number of implicit assumptions are made in our modeling. For instance, microtubule orientation is not considered in mass action or stochastic simulations. Axons have a uniform arrangement of "plus-end-out" microtubules, whereas dendritic orientation is mixed. However, the microtubule motors are also mixed, with both kinesins and dyneins present in all neurites. Our understanding of Kv4.2 interaction with microtubule motors is incomplete. We have previously introduced the known transport mechanisms for Kv4.2 (Sec. 3.2), and the only microtubule motor identified to have a role in subunit trafficking is Kif17 [49]. Without a comprehensive understanding of all motors and localization mechanisms, we assume the molecular "tug of war" between motors is equivalent in dendrites and axons, and we implement no additional bias for microtubule orientation. Further investigation can elucidate the observed kinetic differences in axons and dendrites. For instance, Kv4.2 might be predisposed to unidirectional runs in axons if Kif17 is the only axonal motor protein for transport.

An intuitive analogy to ground transportation can be made for the observed kinetics in axons and dendrites. Consider public transit in regions of high versus low passenger demand. A bus or train in a dense city requires many stops, resulting in low net displacements, low velocity, and increased stalling per unit time, similar to puncta transit in dendrites with high subunit demand. On the contrary, in regions of low demand, such as axons or rural highways, a train or bus makes fewer stops, behaves less stochastically, and can achieve higher velocities, larger net displacement, and shorter stall times.

We also observed proximal-to-distal trends in dendrites, particularly in puncta frequency and directional bias. When these parameters constrain the rates of a mass action model, they account for the well-established, characteristic localization and functional profiles of Kv4.2 [106, 117]. A similar increasing profile also exists for hyperpolarization activated cyclic nucleotide-gated (HCN) channels [144]. Moreover, a study of HCN channel trafficking

and surface expression reveals similar dendritic trafficking dynamics to those reported here [167] (but with no mention of kinetic trends with distance along the dendrite). We suspect that the distance-dependent trafficking parameters observed here are partial contributors to the functional expression profiles of Kv4.2 and HCN channels. Our results reveal that an increasing expression profile does not require an increasing microtubule profile. The increased Kv4.2 expression profile is achievable with a distal directional bias in microtubule transport. By result of mass action, a seemingly complex profile can arise from low magnitude but increasing directional bias.

We have previously discussed (Sec. 3.7) the unavoidable tradeoffs involved in quantifying protein at physiologically low expression levels and inducing high expression that facilitates live imaging. This limitation is persistent in our methodology here. The majority of our data set is collected from a transfected expression system (Fig. 3.1). Further, sorting mechanisms from the dendritic trunk or axonal initial segment are not modeled, despite the specific sorting mechanism for Kv4.2 puncta being partially elucidated [111]. These concepts are interrelated: we can assume that the increased expression of transfected vector saturates post-Golgi sorting mechanisms such that they play a minimal role in transport.

Previous investigations have studied Kv4.2 localization, function, regulation and particular molecular pathways underlying these processes. Few studies examine Kv4.2 trafficking from a broad, logistical perspective. Our work provides new insights into long distance transit in both axons and dendrites without sequestration or stimulation of mobile puncta. We provide evidence for trends in Kv4.2 transport and their relevance to our understanding of cargo production and distribution in the neuron. Our results are grounded in physical measurements, and the trends observed corroborate Kv4.2 distribution from previous studies. This approach and the methods discussed here can be widely applied to other cargo to further our understanding of intraneuronal organization.

Chapter 5

Characterization of Kv4.2 longitudinal diffusion in dendrites

5.1 Chapter summary and key findings

We now study longitudinal diffusion of Kv4.2 in dendritic shafts through experimental observations, modeling, and analysis.

1. Bleach recovery in a large dataset of hippocampal dendrites contains significant variability in mobile fraction and recovery rate. Mobile fraction and recovery rate are inversely related. Heterogeneous fluorescence and patchy appearance correspond with high immobile fraction during FRAP microscopy.
2. Directional bias in fluorescence recovery can be computed from a spatially discretized bleach region. Diffusion of Kv4.2 is largely symmetric with a slight directional bias (drift) directed away from the soma.
3. Mobile fraction typically increases with subsequent bleaching. Contrastingly, recovery rate decreases after the first bleach and then remains constant.
4. Recurrent photobleaching can be used to analyze the rate of cargo mobilization and immobilization—i.e., the rate of cargo transfer on and off immobile structures. Cargos with increasing successive mobile fractions have low im/mobilization rates, whereas those with constant successive mobile fractions have high im/mobilization rates.

5.2 Introduction

The longitudinal transport of cargo in neurites can be categorized into active and passive mechanisms. Active transport requires cellular energy and motor proteins, whereas passive transport involves movement of material down a concentration gradient with no energy required. Cargo can be collected in vesicles and actively shuttled on microtubules. [94] The microtubule-based active transit of membrane vesicles containing Kv4.2 is the subject of Chapters 3 and 4. [55]

Here, we consider the diffusive component of transport along the length of the neurites. This was first observed as a wave of fluorescence during photobleach recovery, visible in kymograms such as Fig. 2.14B. This diffusive filling of the bleach region is distinct from the microtubule-based transit of vesicles. It is assumed that fluorescent cargo is consistently moving in this manner throughout the neurites, and that photobleaching simply reveals the rate of diffusion. [55]

This wave-like movement during photobleach recovery can be attributed to a number of mechanisms in/on the (1) cytosol, (2) microtubules, and (3) plasma membrane. These are briefly outlined here.

The first and most obvious mechanism is free diffusion of ion channels in the cytosol. Ion channels in the cytosol are likely contained in vesicles enclosed in a phospholipid bilayer. Ion channels are integral membrane proteins, meaning they are attached to the plasma membrane with protein domains that are structurally designed for lipophilic interactions with the nonpolar interior of the lipid bilayer. Ion channels are unlikely to float freely in the cytosol with no membrane integration—this would require conformational changes in protein structure, which could render channels nonfunctional and result in aggregations called inclusion bodies. Ion channels are stable in cytosolic membrane vesicles, in which they can be maintained as reserve pools for local demand. [139, 55]

Secondly, the wave-like movement can consist of microtubule-based transport as discussed in previous chapters. The motor-bound vesicles might differ in size from the observed puncta of previous chapters. It is possible that an aggregation of smaller vesicles produces the diffusive wave that is observed during bleach recovery. A collection of small vesicles drifting and diffusing in the neurite can appear wave-like in motion. This is analogous to particulates of water droplets or gas spreading throughout a volume in a diffuse manner. Such microtubule-based transport might be a significant source of drift, or bias in diffusion. In unbiased diffusion, an equal number of particles are transported in both directions. If more particles are actively trafficked in one direction, this would appear as a drift on microscopy time lapse. [55]

Lastly, another potential mechanism underlying the wave-like movement is longitudinal diffusion on the plasma membrane. The fluid mosaic model describes the consistency of the plasma membrane. The lipids and proteins in the bilayer flow freely like a two-dimensional liquid. [212, 109] In the context of neurites, this liquid is wrapped into a tube. Small-diameter neurites can be approximated as one-dimensional structures with free-flowing motion in the plasma membrane in one dimension along the longitudinal axis.

In this chapter, we study this longitudinal diffusion in dendritic shafts using FRAP microscopy and Kv4.2-SGFP2 as candidate cargo. The kinetics observed during bleach recovery are likely a combination of the aforementioned mechanisms. The contributions of these mechanisms to the net movement of cargo is unclear. Further, the variability in diffusion rate of cargo in the cytosol, microtubules, and plasma membrane is not known. Nonetheless, a general estimate of diffusion and drift can be measured.

The aforementioned mediums of transport—the cytosol, microtubules, plasma membranes—do not necessarily have uniform mobility. In this chapter, we perform a generalized analysis using photobleaching recovery that does not differentiate between those modes of transport. Cargo is not divided according to transport medium but rather into mobile and immobile fractions. We estimate the cargo's recovery rate, which is related to the cargo's diffusion coefficient. We introduce a method of spatial discretization, where cargo recovery is computed as a function of distance along the dendrite. From this analysis, we report a weak directional bias away from the soma.

We then explore the conventional division of cargo into mobile and immobile fractions in the context of recurrent photobleaching. We deduce a significant conclusion regarding immobile fraction on/off rates from subsequent measures of cargo mobility. From this analysis, we infer that Kv4.2 im/mobilization rates are slower than the experimental bleach rate and observed diffusion rate. We also explore the impact of Kv4.2 im/mobilization rates in the context of global intraneuronal distribution.

5.3 Diffusion and drift rates during single bleach recovery

These results begin with an estimation of drift and diffusion of Kv4.2 in dendrites. Recall the principles of FRAP recovery introduced in Sec. 2.6.4 and depicted in Fig. 2.12. The equations for fitting exponential recovery curves (Eq. 2.1) also apply here.

FRAP microscopy was performed on 484 dendrites. Bleach recovery was analyzed and fitted to single exponential recovery curves. Selecting for highest quality fits (based on sum of squares error (SSE) less than 0.5) yields a subset of 250 dendrites. Mobile fraction A

indicates the percentage of refilled cargo with recovery rate τ . The A and τ from these fits are plotted as histograms in Fig. 5.1, which depicts the variance of the data set.

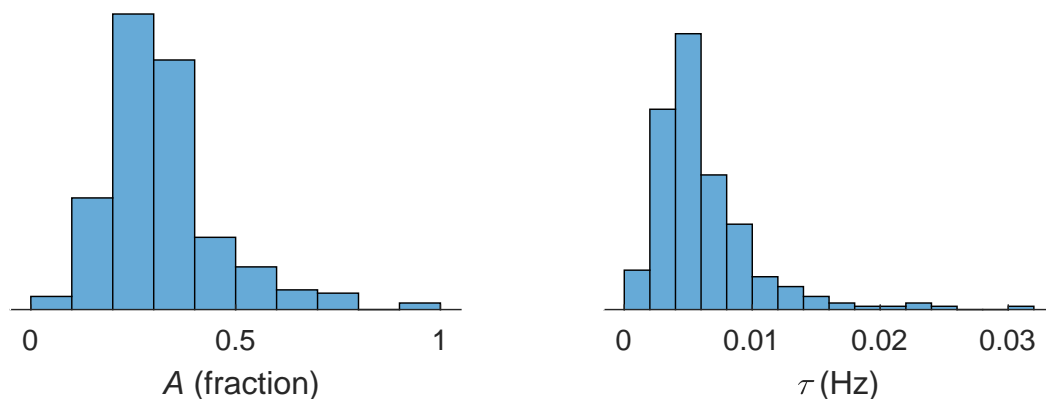


Fig. 5.1 A single exponential recovery curve is fitted to over 250 dendrites and yields these parameters. *Left*: The mobile fraction A has mean 0.322 with standard deviation 0.142. *Right*: Recovery rate τ has mean 0.0062 Hz with standard deviation 0.0041 Hz.

The variability in recovery was also evident in raw kymograms, depicted in Fig. 5.2. Some dendrites appear to have large immobile structures, resulting in an irregular, jagged recovery (Fig. 5.2 *left*). Other dendrites with higher mobile fraction appear to have smooth, fluid recovery (Fig. 5.2 *right*). These changes can likely be attributed to morphological differences between neurites as discussed in Sec. 2.4.3.

In addition, Fig. 5.3 shows examples of directional bias evident during bleach recovery. Notice that the left portion of the bleached region appears to recover more rapidly than the right side. This bias corresponds to the drift component of recovery. Kymograms are oriented such that increasing distances (x-axis) denote increasing distance from the soma. Therefore, in each of these examples, the directional bias of the drift appears to be directed away from the soma. Indeed, this was the result of mean drift, analyzed later in Sec. 5.3.2.

These parameters and observations give a broad overview of diffusion recovery in dendrites. Further analysis of this data can extract meaningful information, as explored in the following sections.

5.3.1 A and τ are correlated but not attributable to experimental parameters

Cultured neurons are highly variable in structure, size, and (in transfected expression systems) fluorescence. Measurements of pyramidal cells alone still reveal a wide range of distances

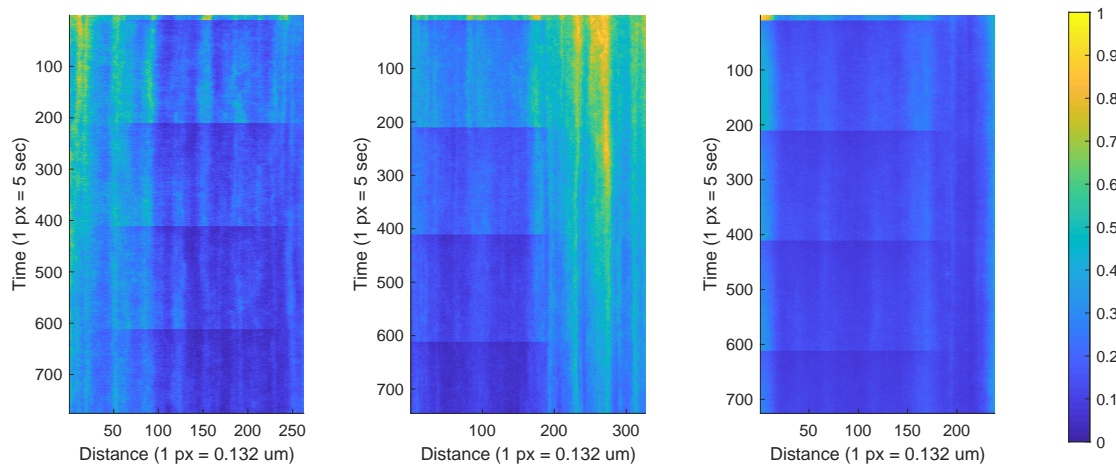


Fig. 5.2 These raw kymograms reveal variability in cargo recovery profiles. *Left* has the largest immobile fraction, indicated by the jagged, heterogeneous pattern during and after recovery. *Right* has a smaller immobile fraction and a smooth recovery. Note the decrease in dendrite fluorescence adjacent to the bleach region in the *middle* kymogram. The concept of subsequent bleaches are further analyzed in Sec. 5.5. A color bar indicates the color mapping of fluorescence intensity standardized between 0 and 1.

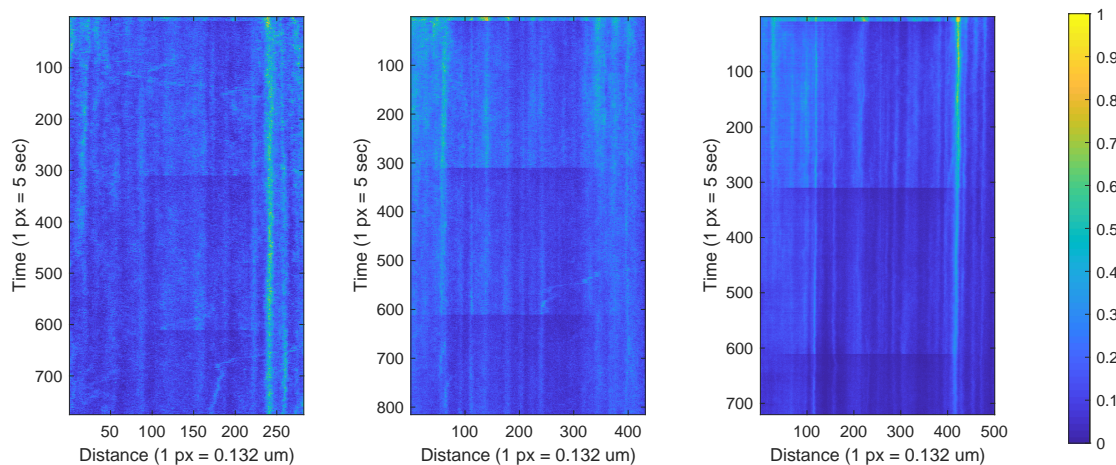


Fig. 5.3 These raw kymograms reveal a directional bias during bleach recovery, which corresponds to drift. The bias is directed away from the soma in each of these examples. A color bar indicates the mapping of fluorescence intensity standardized between 0 and 1.

from soma, branching degrees, fluorescence intensities, and bleach widths—in this discussion, these are all categorized as experimental parameters. It is reasonable to assume that the variability in our data set (Fig. 5.1) is partially attributable to experimental parameters. To address this, we plot recovery parameters (τ and A) against these experimental parameters (bleach width, fluorescence intensity, distance from soma, and branching degree) in Fig. 5.4.

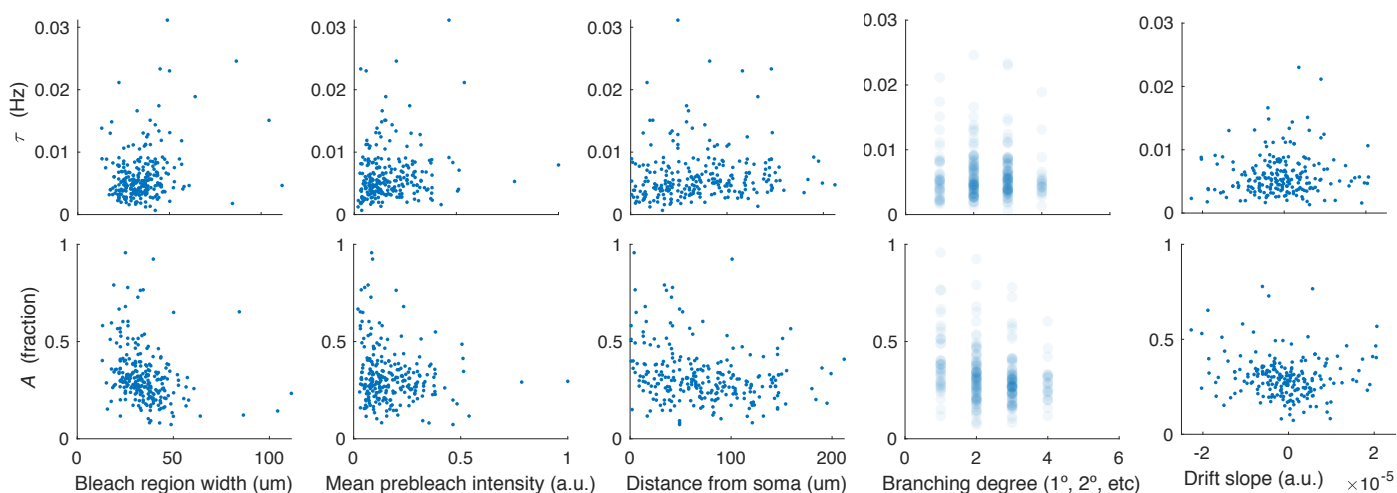


Fig. 5.4 Experimental variability is not strongly correlated with bleach recovery parameters. Variability in dendrites, bleach parameters, and imaging settings do not have a strong correlation with recovery rate or mobile fraction after photobleaching. Imaging and bleach parameters include the width of the bleach region (*first column*) and the mean prebleach intensity (*second column*). Biological parameters include distance from soma (*third column*) and degree of branching (*fourth column*). Drift as computed in Sec. 5.3.2 is in *last column*. None have a strong correlation with parameters τ or A .

Bleach region width refers to the width of the region bleached on the dendrite. Fluorescence intensity is measured using frames of the time series prior to bleaching. Distance from the soma is measured from the proximal end of the bleach region to base of the dendritic trunk using a collage of micrographs as shown in Fig. 2.1. Degree of branching refers to the number of branches from the soma, where primary is the apical dendrite, secondary is a branch of the primary, etc.

Each of these experimental parameters vary greatly in the data set. However, none seem to have a significant impact on fit parameters. The coefficients of determination R^2 for linear fits between these parameters (bleach width, prebleach intensity, distance from soma, branching degree, and drift slope) and τ are 0.0129, 0.0254, 0.0058, 0.0015, and 0.00706, respectively. R^2 for linear fits with A are 0.0656, 0.0366, 0.0231, 0.0225, and 0.0072, respectively. This indicates that bleach recovery parameters do not correlate strongly with experimental parameters.

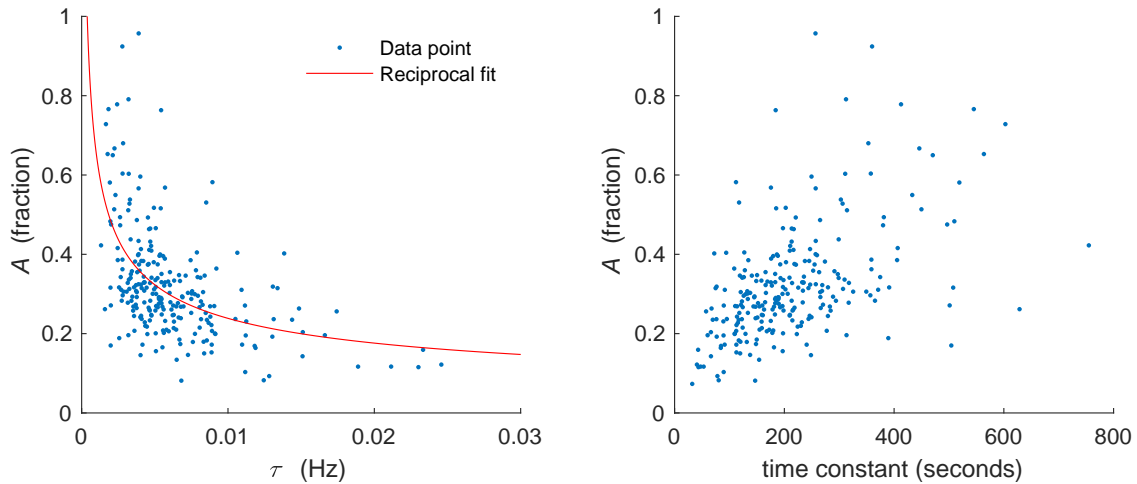


Fig. 5.5 *Left*: Bleach recovery parameters A and τ are reciprocally related. Dendrites with high A recover that mobile fraction at a slow rate τ . *Right*: Mobile fraction A and time constant ($1/\tau$) are directly related.

Interestingly, there is strong correlation between the recovery parameters τ and A themselves, depicted in Fig. 5.5. Here, R^2 for a linear fit is 0.2094, substantially higher than all previous scatter plots. Further, τ and A appear to have a multiplicative inverse or reciprocal relationship. The fit depicted is $A = 0.144/\tau^{0.433}$ with R^2 of 0.2837. This suggests that dendrites with high A have slower recovery (smaller τ).

One possible explanation is cargo mobility dependent on recovery source. Dendrites with large recovery fractions (high A) might recover from multiple sources of cargo transport (cytoplasmic, membrane, and microtubule transport), as discussed in Sec. 5.2. Some of these sources of cargo recovery might be slower than others (e.g., membrane transport), so the net τ would be slower. Dendrites with smaller A might recover fluorescence only from faster sources of cargo (e.g., microtubule transport) with larger τ .

5.3.2 Spatial analysis of recovery reveals minimal distal drift

We next analyze single bleach recovery profiles along the length of the bleach region to quantify directional bias. Each bleach region was binned by length and recovery profiles was fitted for each bin. Recovery rates were computed as a function of longitudinal distance down the bleach region. If one end of the bleach region has recovery that contrasts greatly from the other end, this suggests a drift in fluorescence recovery.

We expect material at both ends of bleach regions to recover more quickly given their proximity to stores of unbleached cargo. This was corrected in our analysis.

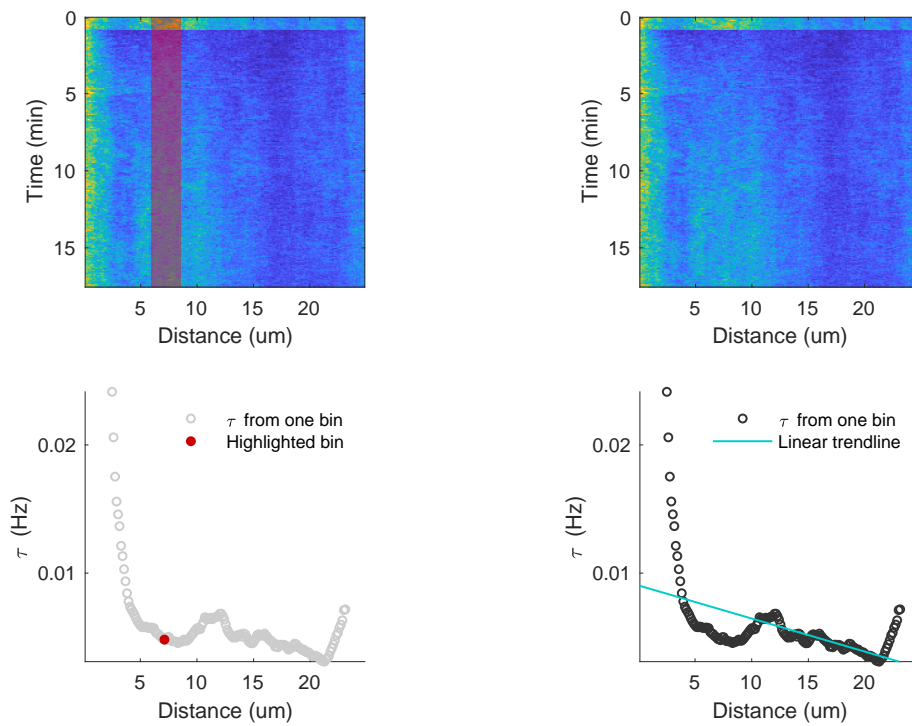


Fig. 5.6 Drift is computed by spatially binning kymograms. *Left*: A kymogram has one bin highlighted in red. The red τ corresponding to the strip highlighted in red. *Right*: A linear trend is traced through the τ s. The sign and steepness of the slope corresponds to the direction and magnitude of the drift.

An example of this spatial analysis is depicted in Fig. 5.6. A sample kymogram is referenced for demonstration purposes. Along the distance of the kymogram, bins with fixed width were fitted to exponential recovery curves with A fixed to 1. The resultant τ s are then plotted versus distance. A linear trendline is then fitted to the τ s. The slope of this line corresponds to the directional bias in bleach recovery. τ near the both borders of the bleach region is increased, as expected, and excluded from the linear fit. The slope of the line in Fig. 5.6 is negative (-3.41×10^{-5}), corresponding to a rightward directional bias, or a drift component directed away from the soma. This is consistent with the direction of drift depicted in the kymograms in Fig. 5.3.

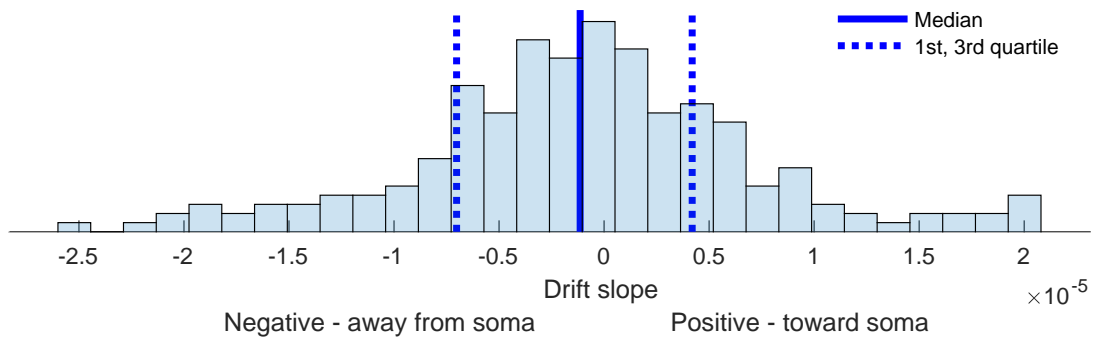


Fig. 5.7 The drift slopes as computed in Fig. 5.6 for 250 dendrites are depicted as a kymogram here. Negative slopes correspond to drift away from the soma; positive slopes indicate drift toward the soma. First, second (median), and third quartiles are labeled.

This method of calculating drift is repeated for 250 dendrites, and the resultant drifts are depicted as a histogram in Fig. 5.7. The median of the drift slopes is negative, corresponding to a slight directional bias away from the soma. Median drift slope is -1.14×10^{-6} with first and third quartiles at -7.02×10^{-6} and 4.19×10^{-6} , respectively. Variance in drift can largely be attributed to experimental variation; however, there is no strong correlation between drift and A or τ (Fig. 5.4, last column). Negative drifts are likely the result of cargo being produced in the soma and disseminating throughout the cell. The magnitude of drift is weak and is unlikely to be active transport on microtubules as studied in Chapters 3 and 4.

5.4 Inference of im/mobilization rates

FRAP microscopy is typically used to study the dynamics of freely diffusive particles in a one, two, or three dimensional space. FRAP is more extensively introduced and discussed in Sec. 2.6.4, and a typical FRAP recovery curve is shown in Fig. 2.12. In brief, the fluorescence

recovery data is normalized and plotted against fluorescence intensity normalized from 0 to 1. After photobleaching, some fraction of mobile particles recover within the bleached area. The percentage of fluorescent particles that recover is known as the mobile fraction A , which is graphically represented by the steady state of the exponential fit in Fig. 2.12. The remaining fraction of particles that does not recover from photobleaching is the immobile fraction $1 - A$. FRAP data is typically fitted to a single or double exponential recovery curve to solve for A and the recovery rate τ .

This well-established model for FRAP microscopy makes a few key assumptions. First, the recovering particles are assumed to exist in one of only two degrees of mobility. Particles are either (1) mobile with some diffusion coefficient $D > 0$ or (2) immobile with $D = 0$. Second, the mobility state of particles (mobile or immobile) is assumed persistent and unvarying over the course of fluorescent recovery: immobile fluorescent particles cannot mobilize and mobile particles cannot immobilize. These assumptions are largely invalid for some fluorescent particles. For instance, neurotransmitter receptors and ion channels are constantly trafficked within and between regions of varying mobility. An AMPA receptor might be shuttled into or out of a postsynaptic density to potentiate or depress a synapse [176, 75]. A diffusing ion channel might enter or exit regions of decreased mobility in the plasma membrane, such as lipid rafts, neurite branch points, and postsynaptic densities [230].

To address the assumption of unvarying mobility, the standard model of diffusion is revised with dynamic mobility states. Cargo transfer between mobile and immobile states is considered. Transport from an immobile to a mobile state is called mobilization, and the reverse is called immobilization. A series of photobleaches are performed in succession to study the fraction of molecules in the immobile fraction. This framework assumes that the total population of fluorescent particles (in the entire neuron) is not being depleted during the experiment. Since a small region of individual branches are being bleached, the impact of bleaching on total fluorescent particles is likely negligible.

In this section, we address how fluorescence recovery reveals the rate of cargo mobilization and immobilization. We begin by discussing a conceptual model of our experimental setup to define terms and to illustrate our analysis.

5.4.1 Schematic of photobleaching and im/mobilization rates

A compartment containing cargo (yellow particles) and immobile substrate (blue ribbons) is depicted in Fig. 5.8Ai. x_{mob} denotes mobile particles that are allowed to diffuse freely with rate v_d . x_{imm} denotes immobile particles that are bound to a static structure with restricted diffusion. Mobilization rate $v_{i,m}$ describes detachment from the immobile structures; i.e., particle transfer from x_{imm} to x_{mob} . For an ion channel, this biologically corresponds to

exiting a lipid raft or postsynaptic density that was previously restricting motility. The reverse process is immobilization: $v_{m,i}$, which describes particle transfer from x_{mob} to x_{imm} , such as an ion channel entering a restrictive region. The depicted compartment is part of a larger neurite (Fig. 5.8Aii) in a larger arborization like a dendritic tree (Fig. 5.8Aiii). A localized region (Fig. 5.8Ai) is bleached by a high intensity laser (yellow trapezoid). During photobleaching, cargo is bleached with rate v_b and fades in color (to dark particles, Fig. 5.8Aiv). This approximates discrete periods of photobleaching performed experimentally, as described in Sec. 2.6.

Two examples with differing im/mobilization rates $v_{m,i} \gg v_{i,m}$ and $v_{m,i} \ll v_{i,m}$ producing contrasting effects are depicted in Fig. 5.8B. Both examples undergo bleaching of all fluorescent cargo in the region of interest. Then, bleached cargo that is mobile (x_{mob}) recovers through diffusion.

In the case of high immobilization ($v_{m,i} \gg v_{i,m}$, Fig. 5.8Bi), most cargo is bound to the immobile substrate (static) and does not freely diffuse in/out of the bleach region. The majority of cargo after recovery is bleached and immobilized, resulting in a observed low mobile fraction A during FRAP. Now consider the example with low immobilization ($v_{m,i} \ll v_{i,m}$, Fig. 5.8Bii). During recovery, most cargo is mobile and can freely diffuse on/off the immobile substrates and in/out of the bleach region. The observed mobile fraction A during FRAP is higher.

Rates of im/mobilization and diffusion determine the speed τ and degree A of fluorescence recovery. Pursuing this principle, we design a model to infer $v_{m,i}$ and $v_{i,m}$ from FRAP recording.

5.4.2 Data analysis

To establish reliable estimates of bleach recovery, mobile fraction, and im/mobilization rates, we performed hour-long recordings with recurrent photobleaching in over 450 dendrites of rat hippocampal cells. Each dendrite was bleached 2-9 times, and each bleach diminished fluorescence intensity by 30-70%, with bleach intervals ranging from 5-20 minutes.

An example of recurrent photobleaching is depicted in Fig. 5.9, where a region of dendrite was recurrently bleached every 1000 seconds. Each recurrent recovery appears similar to the prototypical FRAP curve; however, individual recoveries are not identical. One of the most obvious changes between successive bleaches is the degree of recovery A_i . The standardized A_i s appear to increase with successive bleaches:

$$A_1 < A_2 < A_3 < A_4$$

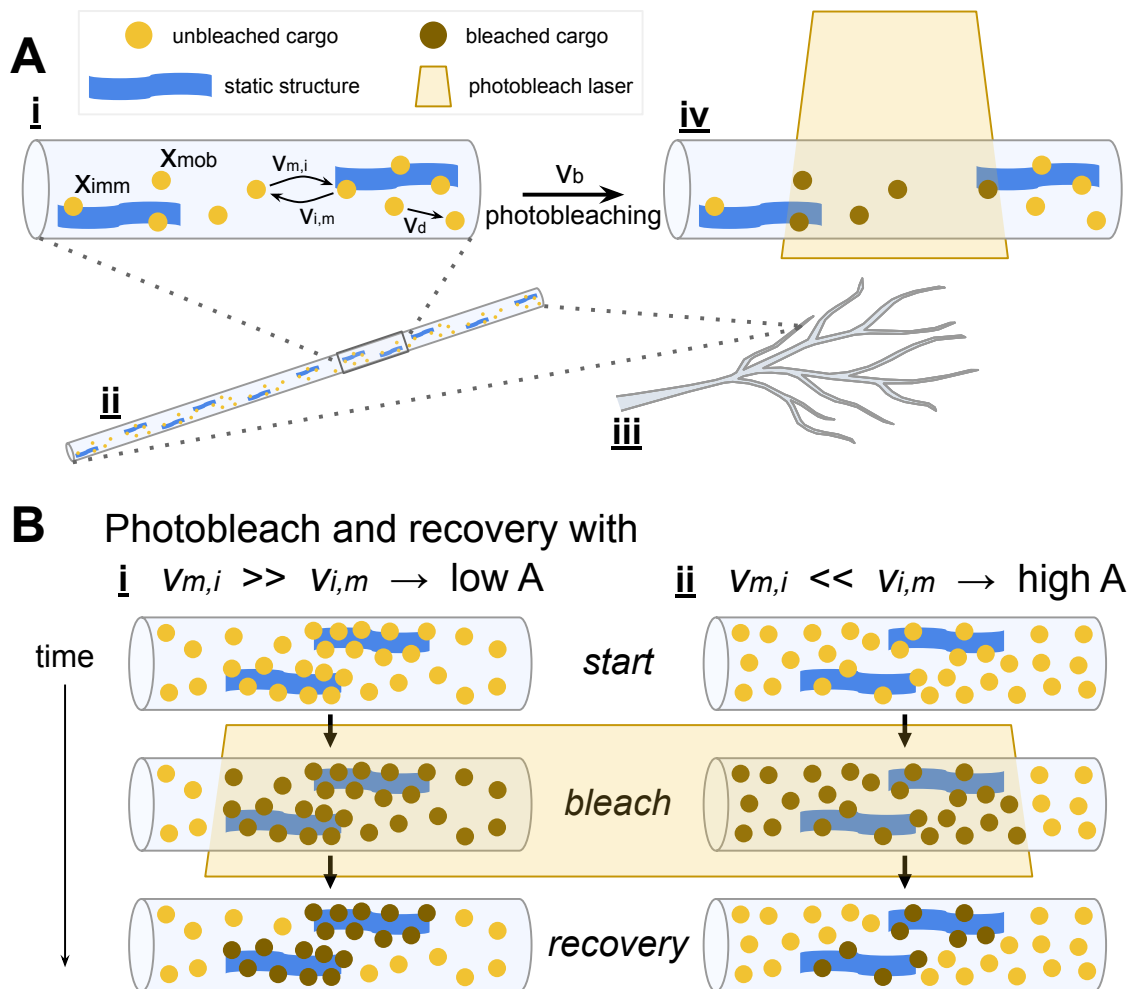


Fig. 5.8 Schematic of recurrent photobleaching reveals increasing mobile fraction with low immobilization rates. (A): Our experimental setup with defined rates and states is depicted (i). The region of interest is part of a dendrite (ii) from a larger dendritic arbor (iii). This region is photobleached, which fades the fluorescence intensity of cargo (iv). (B): Examples of photobleaching with (i) $v_{m,i} \gg v_{i,m}$ and (ii) $v_{m,i} \ll v_{i,m}$ are depicted. Bleached particles accumulate on static structures in (i), resulting in low mobile fraction at steady state compared to (ii).

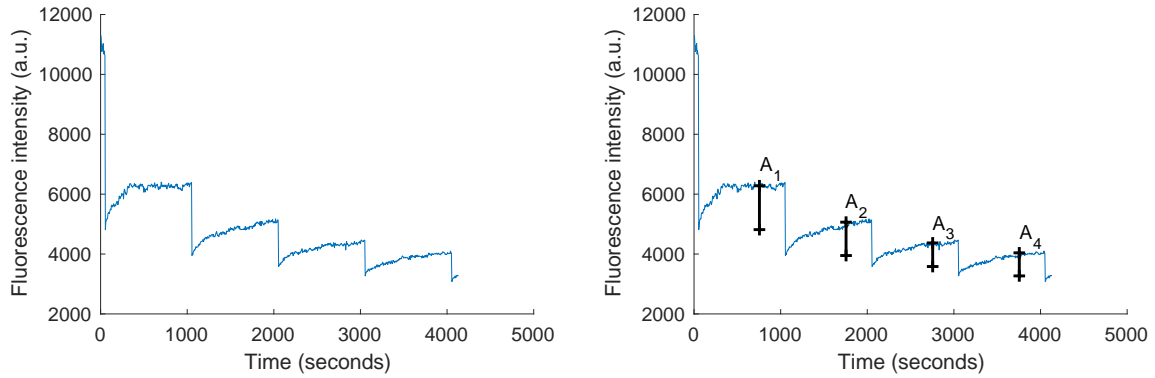


Fig. 5.9 *Left*: Typical example of recurrent photobleaching in a dendrite containing transfected Kv4.2-SGFP2. Mobile fraction increases with subsequent bleaching, indicating minimal mass transfer between im/mobile fractions. The first occurrence of bleaching occurs at 50 seconds and subsequent bleaches occur every 1000 seconds thereafter. *Right* is a replication of *left* with labeled mobile fraction A_i for each successive bleach i . A_i here is computed using a single exponential fit

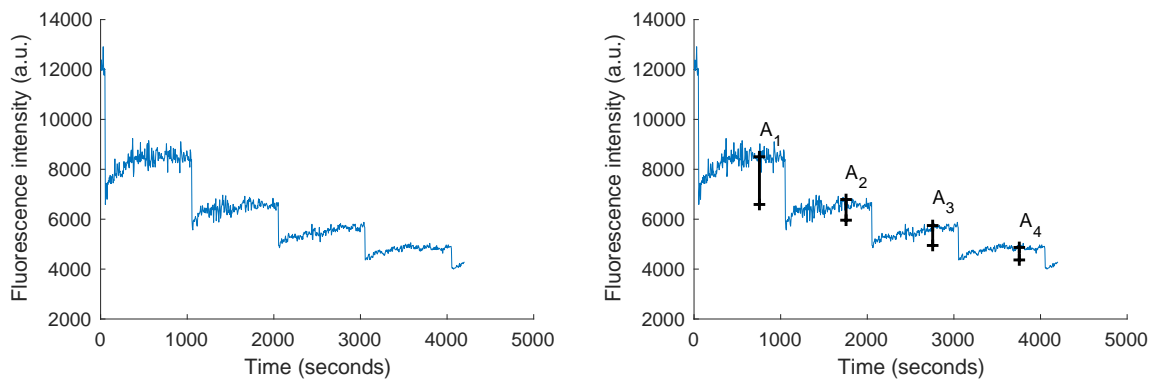


Fig. 5.10 *Left*: An example of recurrent photobleaching in a dendrite in which there appears to be no clear trend in successive mobile fractions, indicating a higher degree of mass transfer between im/mobile fractions than in Fig. 5.9. *Right* is a replication of *left* with labeled mobile fraction A_i for each successive bleach i . A_i is computed using a single exponential fit

$$0.2522 < 0.4571 < 0.5146 < 0.6439$$

If the mobile and immobile populations were static, as is assumed in typical FRAP microscopy, the mobile fraction would increase after each successive bleach, as shown here. The first bleach removes some percentage of the immobile population, leaving mobile fraction A_1 . The second bleach removes more of that immobile population, so the mobile population is a larger fraction A_2 of the total fluorescent intensity. If there is no cargo transfer between mobile and immobile fractions, this continues until all immobile subunits are bleached and $A_{i \rightarrow \infty} = 1$.

However, this is not always the case. Some neurites show no definitive increase in mobile fraction with successive bleaches. An example of a dendrite with no definitive trend in A_i s is depicted in Fig. 5.10. Here, successive mobile fractions are approximately equal:

$$A_1 \approx A_2 \approx A_3 \approx A_4$$

$$0.3594 \approx 0.3402 \approx 0.4655 \approx 0.3860$$

Dynamic mobile and immobile populations would explain this. That is, immobile cargo can be mobilized and mobile cargo can be immobilized.

Fig. 5.9 and Fig. 5.10 depict bleach recovery with a fundamental difference in cargo kinetics. The specific differences are not yet well elucidated and have not been studied. This section serves as a continuation of the discussion of the data set in Sec. 5.3. As before, parameters are obtained by fitting a single exponential recovery curve, as described in Sec. 2.6.4.

Histograms comparing parameters for first through fourth bleach recoveries are shown in Fig. 5.11. The top row shows the trend in A with successive bleaches. The A from the first bleach appears to be smallest, and each subsequent bleach produces a larger A . This trend appears for at least three or four bleaches. The bottom row shows the trend in τ . The first bleach clearly has a larger τ , and all subsequent bleaches appear to have a smaller but consistent τ .

The legends indicate the number of samples N that reached each bleach iteration. N varies with bleach iteration because of experimental variation—some samples were bleached five or more times whereas others were bleached just twice. N varies between parameters because outliers were removed from each distribution.

The median \pm standard deviations for A of the first through fourth iterations are 0.30 ± 0.12 , 0.49 ± 0.17 , 0.58 ± 0.20 , 0.69 ± 0.16 , respectively. Successive A seem to increase, and there is no obvious trend in variance for A .

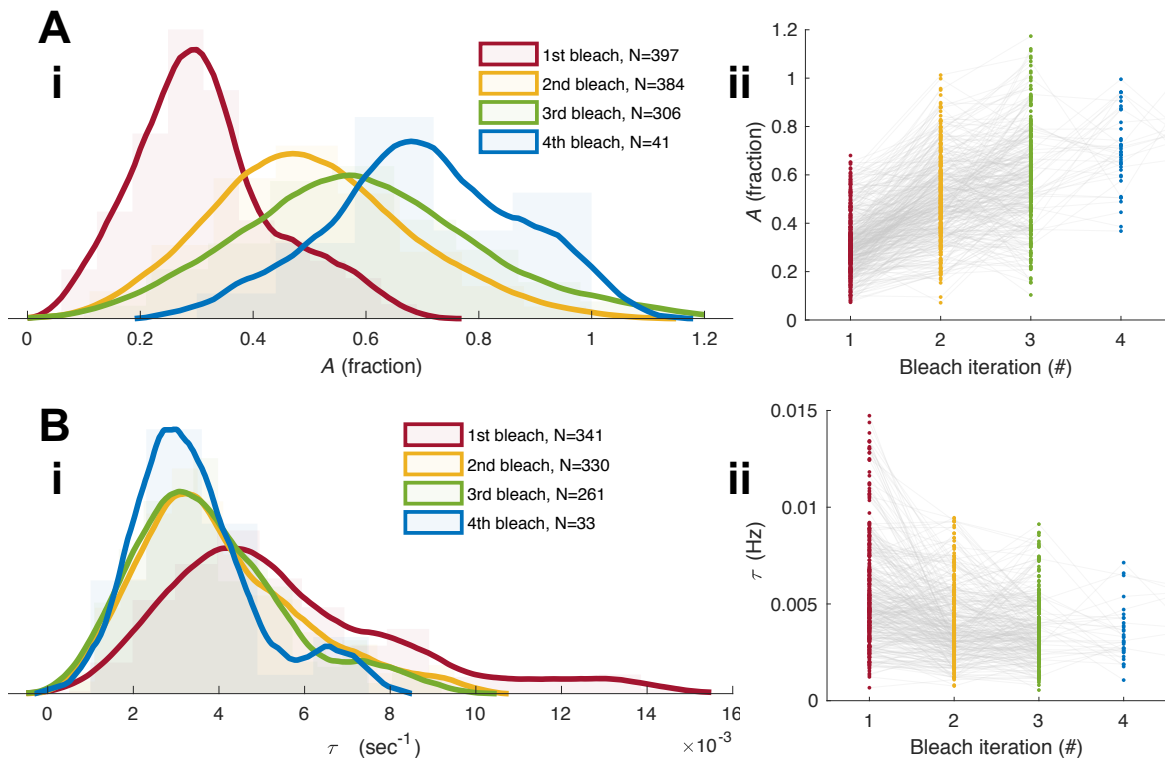


Fig. 5.11 Trends in A and τ following successive photobleaching. (A): Mobile fraction A increases with subsequent bleaches. Statistical analysis demonstrates significant change in A between all combinations of the four bleach iterations (with maximum $P = 5.4 \times 10^{-4}$). (B): Recovery rate τ decreases after the first bleach and then remains constant. Statistical analysis only demonstrates significant difference between the first and second bleaches ($P = 8.1 \times 10^{-16}$). All other subsequent pairs of τ are not significantly different (minimum $P = 0.0835$).

The median \pm standard deviations for τ are 0.0049 ± 0.0028 , 0.0035 ± 0.0019 , 0.0035 ± 0.0017 , 0.0031 ± 0.0014 for the first through fourth bleach iterations, respectively. The trend in mean τ might be a result of cargo saturation in the cell. The first bleach appears to recover quickly (large τ), perhaps because the borders of the bleach region are saturated with unbleached cargo that can immediately spill into the bleached region. Successive bleaches have a slower recovery (smaller τ) since unbleached cargo is no longer saturated at the bleach region borders. This is possibly explained by close proximity of replacement unbleached particles following the first bleach. During subsequent bleaches, unbleached particles diffuse from farther regions of the cell. Subsequent bleaches have similar τ_i with decreasing variance, which might indicate the cell achieving a steady state of particle flow into the bleach region.

We amassed a sizable dataset of fluorescence intensity during recurrent photobleaching using ion channel Kv4.2 as candidate particles. We also have a working theory on how this data might reflect im/mobilization rates that are otherwise difficult to measure. We next develop a mathematical model to make sense of this data and theory.

5.4.3 Inference from reduced model of photobleach recovery

We have thus far presented a conceptual model of cargo im/mobilization with photobleaching (Fig. 5.8) and experimental data of Kv4.2 subunits undergoing this scheme in hippocampal dendrites (Fig. 5.11). We now formalize these results in a mass-action model constrained to our empirical observations. We subsequently infer rates of Kv4.2 im/mobilization that are otherwise not directly measurable using our current methods.

In a region of interest, particles are categorized by fluorescence and mobility into four compartments: $x_{\text{mob}}^{\text{unbl}}$, $x_{\text{imm}}^{\text{unbl}}$, $x_{\text{mob}}^{\text{blea}}$, and $x_{\text{imm}}^{\text{blea}}$, depicted in Fig. 5.12Ai. Superscripts ^{unbl} and ^{blea} correspond to unbleached and bleached particles, respectively. Subscripts _{mob} and _{imm} indicate mobile and immobile particles, respectively. As in the conceptual model, particles are mobilized ($x_{\text{imm}} \rightarrow x_{\text{mob}}$) and immobilized ($x_{\text{mob}} \rightarrow x_{\text{imm}}$) with rates $v_{i,m}$ and $v_{m,i}$, respectively. Mobile particles diffuse freely with rate v_d and can disperse out of the region of interest into the external region—i.e., the rest of the neuron. $x_{\text{mob}}^{\text{unbl}}$ enters the region of interest with rate u .

Photobleaching ($x^{\text{unbl}} \rightarrow x^{\text{blea}}$) occurs in discrete events with high intensity laser power. We consider photobleaching v_b to be a series of impulses (δ function), between which fluorescence recovery f is modeled as an impulse response. We therefore use a variant of the model without photobleaching (Fig. 5.12Aii) for fitting to individual bleach recoveries.

The results of these fits are depicted as distributions in Fig. 5.12Bi-ii. Mean rates were $u = 0.0021$, $v_d = 0.0063$, $v_{i,m} = 0.00066$, and $v_{m,i} = 0.0016$. We established statistical

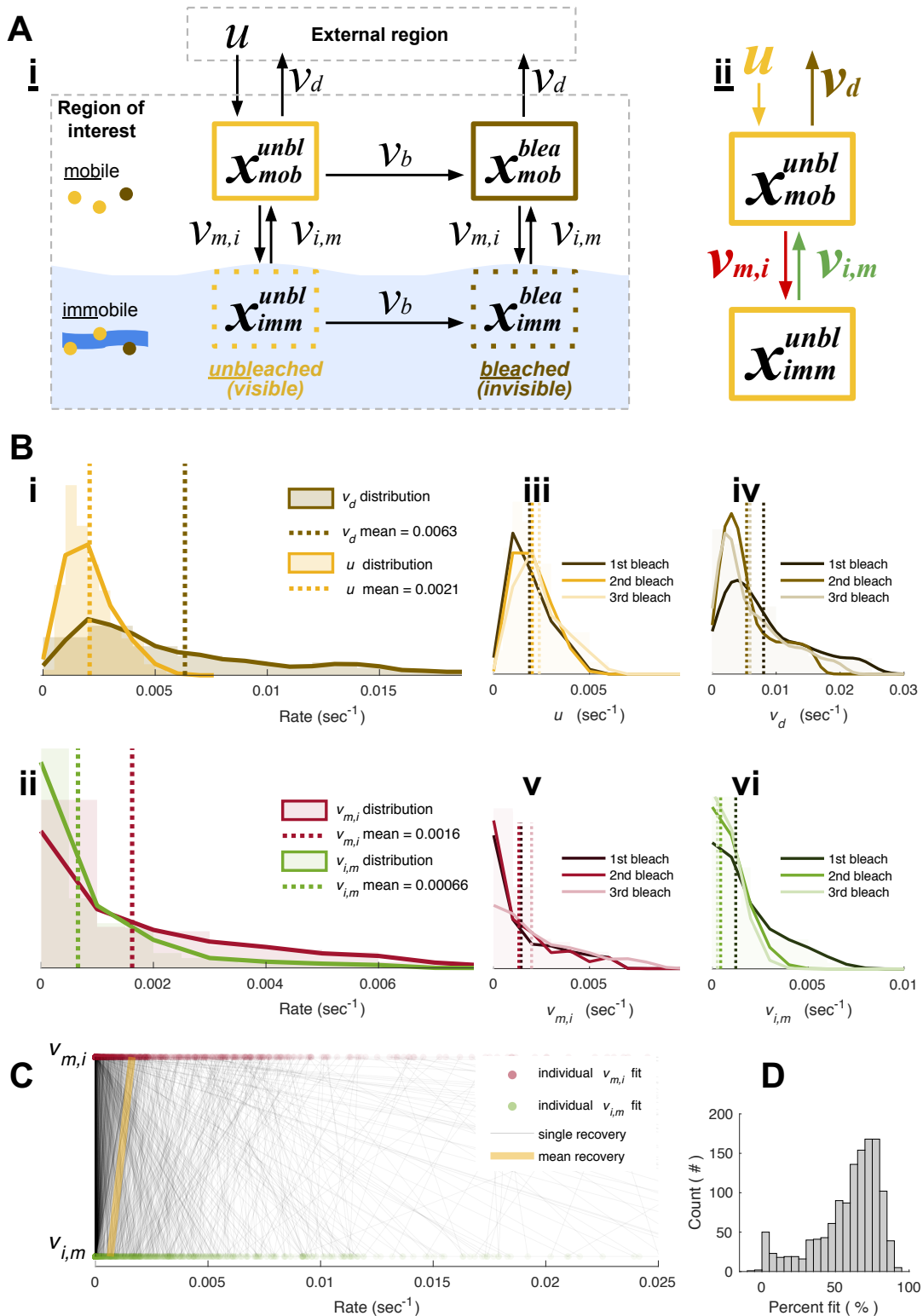


Fig. 5.12 Im/mobilization rates are inferred from a mass-action model of photobleaching and recovery. (A): A mass-action model of photobleaching categorizes cargo according to mobility and fluorescence (i). A variant of the model (ii) is fitted to experimentally observed fluorescence f for constraining rates. (B): The results of model fitting to > 1000 bleaches are depicted as distributions: u and v_d in (i) and $v_{i,m}$ and $v_{m,i}$ in (ii). A comparison of rate fits for first to third bleaches are depicted in (iii)-(vi). (C): $v_{i,m}$ and $v_{m,i}$ fits from individual recoveries are paired, showing $v_{m,i} > v_{i,m}$ with statistical significance ($P = 1.2 \times 10^{-10}$). (D): Model fits with at least 70% accuracy are used as rate constraints.

significance between $v_{i,m}$ and $v_{m,i}$ with the Mann-Whitney with $P = 1.2 \times 10^{-10}$. We also compare rate estimates from first, second, and third bleaches (Fig. 5.12iii-vi). This supports our modeling as a linear, time-invariant system. We depict $v_{i,m}$ and $v_{m,i}$ from individual recoveries to illustrate the variability in model fits. Our model fit the data with reasonable accuracy (Fig. 5.12D), and we used fits with $>70\%$ accuracy as rate constraints in a full neuron morphology in Sec. 5.6.

5.5 Trends with subsequent bleaches and recoveries

In our analysis thus far, we have fit each individual bleach recovery to a linear, time-invariant model (Fig. 5.12). We have made no observations during bleaching and could not estimate bleach rate. We therefore fitted a reduced variant of our model (Fig. 5.12Aii) to individual bleach recoveries. In this analysis, we observe minimal deviation in parameter estimates for u , v_d , $v_{m,i}$, and $v_{i,m}$ between the first, second, and third bleaches.

However, we previously alluded to changes in fluorescence recovery with recurrent photobleaching. In Fig. 5.9, we depicted a neurite whose mobile fraction increased with subsequent bleaches. In this section, we re-examine the data set for trends with subsequent photobleaching.

We begin by plotting whether subsequent A s increase or decrease with recurrent photobleaching in Fig. 5.13. Samples that experience monotonic increases in A with successive bleaching are plotted in green. 193 of the 308 samples with at least three bleaches (62%) experienced this trend—nearly two thirds of the samples. 113 samples (37%) that have no definitive increase or decrease in A are plotted in blue. The raw kymogram in Fig. 5.10 exhibits this trend. Two samples (less than one percent) of samples exhibited a monotonic decrease in A .

What do these trends reveal about our system? Less than two thirds of samples exhibit a monotonic trend, and there is certainly variability in the data set. It is likely that different dendrites have different $v_{i,m}$ rates. v_b might also vary between trials, since the same microscope parameters can have varying effects on different neurons. Further, dendrite diameter and bleach regions also varied slightly, so model parameters v_d and u might be expected to vary as well. These potentially confounding parameters were plotted in Fig. 5.4, although no significant correlation was found.

In an attempt to understand this, we perform simulations of all four compartments of the system (Fig. 5.12) with theoretical bleach rate v_b . We then analytically solve this system to understand how im/mobilization rates might impact subsequent A s.

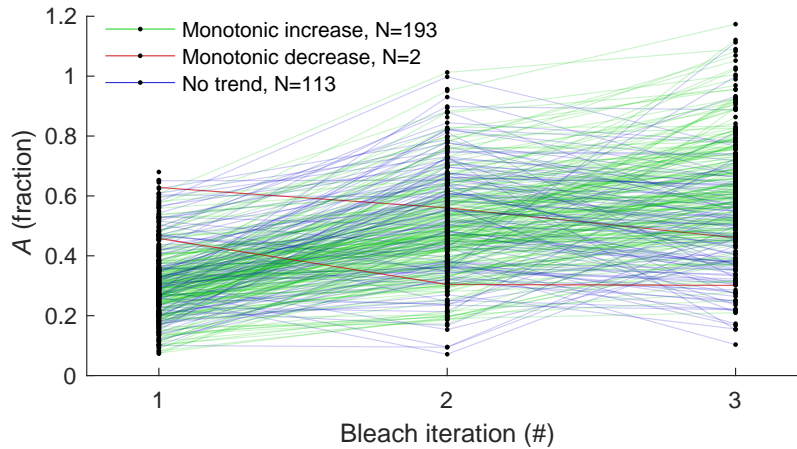


Fig. 5.13 According to the proposed model, the trend in mobile fractions from experiments with recurrent bleaching can reveal information about transport rates. This plot replicates Fig. 5.11 for samples with three bleaches organized by trend in A . Nearly two thirds of samples exhibit a monotonic increase in A (green). Approximately one third of samples have no obvious trend in A (blue). Statistical analysis demonstrates significant increase in A between first and second ($P = 5.6 \times 10^{-58}$) as well as second and third ($P = 3.6 \times 10^{-9}$) bleach iterations when averaged between all samples.

5.5.1 Simulations and interpretation

Preliminary simulations with all four compartments $x_{\text{mob}}^{\text{unbl}}$, $x_{\text{imm}}^{\text{unbl}}$, $x_{\text{mob}}^{\text{blea}}$, and $x_{\text{imm}}^{\text{blea}}$ of the model (Fig. 5.12Ai) are shown in Fig. 5.14. States were initialized such that all cargo was unbleached, half was mobile, and half was immobile. The states are then simulated with particle input, diffusion, and continuous bleaching: $u = 0.01$, $v_d = 0.1$, $v_b = 0.1$. We simulated varying degrees of im/mobilization, with $v_{m,i} = v_{i,m} = 0, 0.1, \text{ and } 0.5$ depicted in Fig. 5.14(a)-(c). Simulated rates $v_{m,i} = v_{i,m}$ range from below and above the other rates in the model. In simulations, bleaching is now a continuous event with a constant rate v_b , compared to discrete periods of photobleaching from the experiments.

In the top row of simulations, all four state variables are plotted versus time. In the middle row, bleached and unbleached compartments are combined. This makes for a suitable comparison between the yellow line indicating total unbleached cargo and the raw fluorescent recovery from an experiment with multiple bleaches (Figs. 5.9 and 5.10). Both appear to be decreasing, likely with some rate of exponential decay, and settle at a nonzero steady state.

The bottom row of Fig. 5.14 plots mobile A and immobile $1 - A$ fractions. In typical FRAP analysis, im/mobile fractions are percentages of the fluorescent population—rather

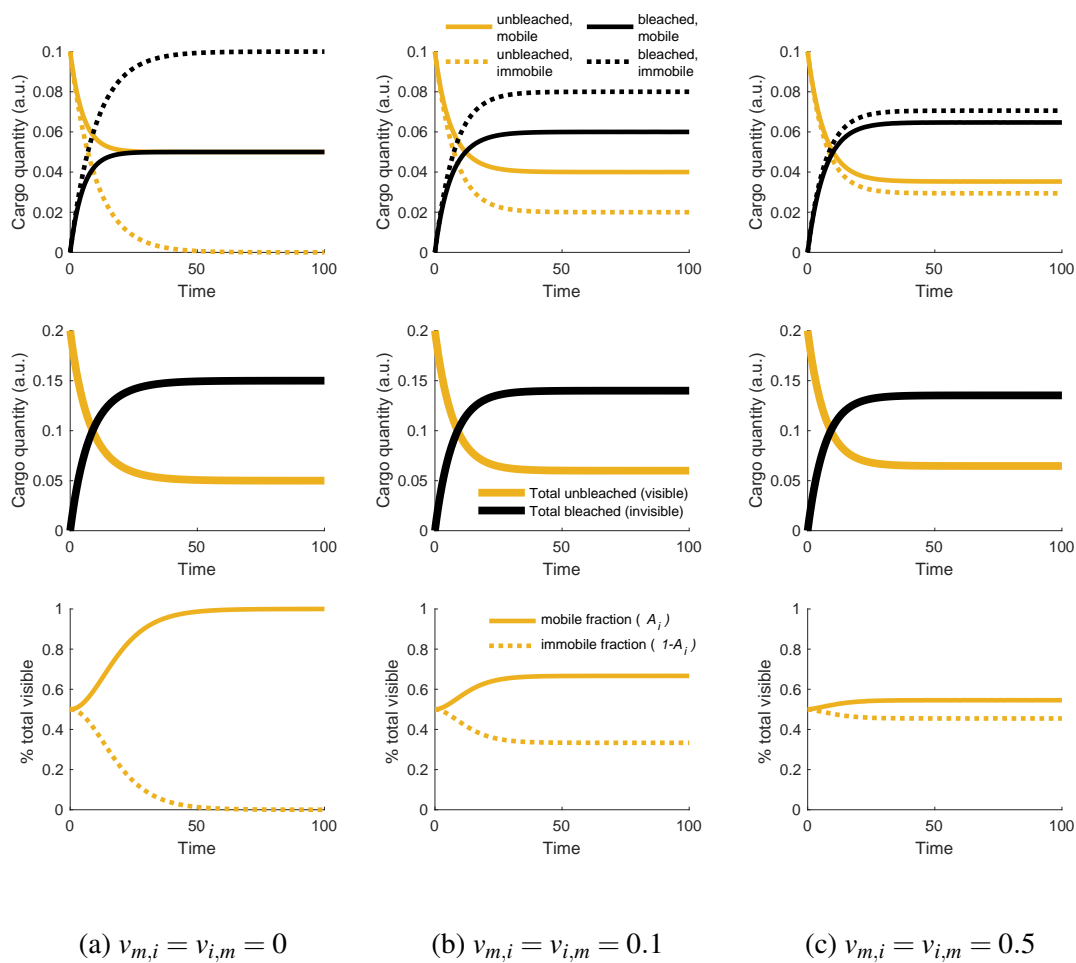


Fig. 5.14 Simulation of recurrent photobleaching and immobilization with varying im/mobilization rates. *Left, middle, and right* columns correspond to increasing cargo attachment and detachment from immobile structures ((a), (b), and (c), respectively). The top row shows all state values during simulation. The middle row combines bleached and unbleached compartments. The bottom row plots mobile A and immobile $1 - A$ fractions.

than the total (fluorescent+bleached) population. These are therefore computed as follows:

$$A = \frac{x_m}{x_m + x_i} \quad \text{and} \quad 1 - A = \frac{x_i}{x_m + x_i} \quad (5.1)$$

These values (Fig. 5.14, bottom row) show the greatest discrepancy between the three simulations. When cargo im/mobilization is lower than cargo diffusion and bleaching rate ($v_{m,i} = v_{i,m} = 0$, Fig. 5.14(a)), mobile fraction increases and immobile fraction decreases. When cargo im/mobilization is higher than cargo diffusion and bleaching rate ($v_{m,i} = v_{i,m} = 0.5$, Fig. 5.14(c)), the mobile and immobile fractions are largely unchanged. This model predicts that a static mobile fraction during recurrent photobleaching corresponds to high $v_{m,i} = v_{i,m}$ relative to other rates in the system.

We again consider the subsequent mobile fractions A_i from our data (Fig. 5.13), now in the context of the hypothetical simulations (Fig. 5.14). 62% of our samples exhibit monotonically increasing A_i s. This might correspond to Fig. 5.14(a) or (b), which have a low transport rate between im/mobile fractions relative to the other rates in the system. Fig. 5.9 is an example neurite that exhibits this trend of increasing A_i s. 37% have no monotonic increase or decrease in A_i s with subsequent bleaches. This corresponds to Fig. 5.14(c) or simulations with even greater $v_{i,m}$ (not shown) that have fast transport rates between im/mobile fractions relative to the other rates in the system. Fig. 5.10 depicts one such neurite. Less than one percent of samples showed a monotonic decrease in subsequent A_i s, which is theoretically impossible in the framework of the simulated model, and these can likely be attributed to experimental error and/or drastic variations due to noise.

A discrepancy between the model and experiments that warrants discussion is the (dis)continuity of photobleaching. In experiments, the neuron segment experiences recurrent, periodic photobleaching in short, discrete boluses. In simulation, bleaching occurs continuously at a constant rate. There are a few reasons as to why this discrepancy is necessary and useful. The first regards the practicality of photobleaching during experiments: a confocal microscope switching between imaging and bleaching modes is time consuming and taxing on the microscope. A better time series (with higher imaging frequency and decreased sample drift) is obtained when bleaching is performed in distinct boluses with high intensity laser power. Secondly, as evidenced in simulation (Fig. 5.14), the most substantial indicators of im/mobilization rates $v_{m,i} = v_{i,m}$ in simulation are the im/mobile fractions. In order to compute im/mobile fractions, some degree of recovery is required to fit an exponential recovery curve. A longer bleach recovery results in a better curve fit and a better estimation of im/mobile fractions. Lastly, from an analytical standpoint, it is easier to mathematically estimate the impact of parameter variations in a continuous rather than discrete system. In

fact, an analysis of discrete bleaching would first begin with approximating infinite bleaching events with infinitesimal partitions between events, such that bleaching becomes continuous anyway.

5.5.2 An analytical perspective

In addition to model simulation and inference with experimental constraints, this framework can be approached from an analytical perspective.

The analysis of the model of recurrent photobleaching and immobilization (Fig. 5.12Ai) begins with stating the ODE for each compartment:

$$\begin{aligned} \dot{x}_{\text{mob}}^{\text{unbl}} &= u + x_{\text{imm}}^{\text{unbl}} v_{i,m} - x_{\text{mob}}^{\text{unbl}} (v_{m,i} + v_b + v_d) \\ \dot{x}_{\text{imm}}^{\text{unbl}} &= x_{\text{mob}}^{\text{unbl}} v_{m,i} - x_{\text{imm}}^{\text{unbl}} (v_{i,m} + v_b) \\ \dot{x}_{\text{mob}}^{\text{blea}} &= x_{\text{mob}}^{\text{unbl}} v_b + x_{\text{imm}}^{\text{blea}} v_{i,m} - x_{\text{mob}}^{\text{blea}} (v_{m,i} + v_d) \\ \dot{x}_{\text{imm}}^{\text{blea}} &= x_{\text{imm}}^{\text{unbl}} v_b + x_{\text{mob}}^{\text{blea}} v_{m,i} - x_{\text{imm}}^{\text{blea}} v_{i,m} \end{aligned}$$

The steady states of this system are solved by setting each time derivative to zero and solving for the four state variables. The steady state solution is as follows:

$$\begin{aligned} x_{\text{mob}}^{\text{unbl}} &= u \frac{v_b + v_{i,m}}{v_b^2 + v_b v_d + v_b v_{i,m} + v_b v_{m,i} + v_d v_{i,m}} \\ x_{\text{imm}}^{\text{unbl}} &= u \frac{v_{m,i}}{v_b^2 + v_b v_d + v_b v_{i,m} + v_b v_{m,i} + v_d v_{i,m}} \\ x_{\text{mob}}^{\text{blea}} &= u \frac{v_b (v_b + v_{i,m} + v_{m,i})}{v_d (v_b^2 + v_b v_d + v_b v_{i,m} + v_b v_{m,i} + v_d v_{i,m})} \\ x_{\text{imm}}^{\text{blea}} &= u \frac{v_b (v_b v_{m,i} + v_d v_{m,i} v_{i,m} v_{m,i} + v_{m,i}^2)}{v_d v_{i,m} (v_b^2 + v_b v_d + v_b v_{i,m} + v_b v_{m,i} + v_d v_{i,m})} \end{aligned}$$

We use the aforementioned Eq. 5.1 for mobile fraction, now applied to the steady state solutions. This will produce a mobile fraction at a steady state after infinite bleaching and

recovery time. This is termed A^{ss} , defined using steady state values:

$$\begin{aligned}
 A^{ss} &= \frac{x_{\text{mob}}^{\text{unbl}}}{x_{\text{mob}}^{\text{unbl}} + x_{\text{imm}}^{\text{unbl}}} \\
 &= \frac{\frac{u(v_b + v_{i,m})}{v_b^2 + v_b v_d + v_b v_{i,m} + v_b v_{m,i} + v_d v_{i,m}}}{\frac{u(v_b + v_{i,m})}{v_b^2 + v_b v_d + v_b v_{i,m} + v_b v_{m,i} + v_d v_{i,m}} + \frac{u v_{m,i}}{v_b^2 + v_b v_d + v_b v_{i,m} + v_b v_{m,i} + v_d v_{i,m}}} \\
 A^{ss} &= \frac{v_b + v_{i,m}}{v_b + v_{i,m} + v_{m,i}}
 \end{aligned}$$

If we next assume that $v_{i,m} \approx v_{m,i}$,

$$A^{ss} = \frac{v_b + v_{i,m}}{v_b + 2v_{i,m}} \quad (5.2)$$

This can be plotted as a surface to visualize the effects of increased bleaching v_b and im/mobilization rate $v_{i,m}$ on steady state mobile fraction A^{ss} , as depicted in Fig. 5.15.

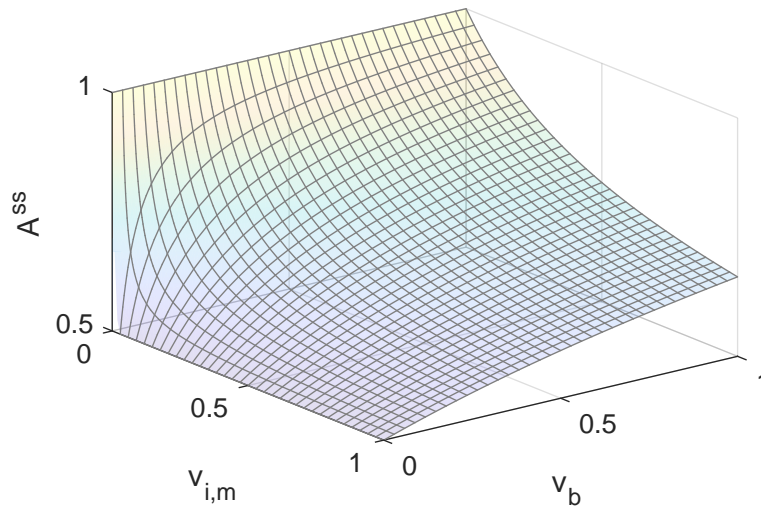


Fig. 5.15 A system containing mobile and immobile compartments with symmetric exchange rate $v_{i,m}$ and recurrent photobleaching with rate v_b has a steady state mobile fraction A^{ss} . A^{ss} can be solved analytically, and the result (Eq. 5.2) is depicted as a surface.

Eq. 5.2 and the associated surface can be evaluated at several edge cases to draw conclusions about the system. In the case with no mass transfer between im/mobile fractions ($v_{i,m} = 0$), fluorescent cargo always recovers completely, and $A^{ss} = 1$. Increasing v_b has a greater impact on systems with no or low $v_{i,m}$.

In the case with no photobleaching ($v_b = 0$), fluorescent cargo equalizes between compartments, and $A^{ss} = 0.5$. This is also the lower limit of the surface A^{ss} . In a system with capacity limits c in im/mobile compartments, A^{ss} would be equal to the size of mobile compartment over the total system capacity: $A^{ss} = \frac{c_m}{c_m + c_i}$. In this case with no capacity limits ($c_m \rightarrow \infty$ and $c_i \rightarrow \infty$) and $A^{ss} = 0.5$. Capacity was omitted from this analysis to preserve linearity.

The usefulness of this theory is largely dependent on how readily v_b can be controlled during the time series and estimated afterwards. An interesting experiment that might serve as a proof of concept for this theory would be a comparison between a protein known to be cytosolic and one known to be membrane-bound, with the expectation that the membrane-bound protein has a larger $v_{i,m}$. This theory might also be useful for a comparison within the same measurement. For instance, one might compare two isoforms of a fluorescent proteins to compare $v_{i,m}$. One might argue that comparisons made between two cells with similar morphology and imaging/bleach parameters would also be valid.

5.6 Impact on intracellular distribution

We next assess how im/mobilization rates and mobile fractions—estimated using model inference (Fig. 5.12)—impacts intracellular distribution of ion channels. We begin by adapting the measured kinetics of Kv4.2 (Fig. 5.11) to a full neuron morphology.

Our experiments revealed a distribution of recovery rates τ (Fig. 5.11B), from which we derive the diffusion coefficient D of Kv4.2 subunits. Dendrites in our FRAP experiment were modeled as small-diameter cylinders, which reduces complexity to diffusion only along the longitudinal axis. The one-dimensional diffusion equation was solved for D , as described in Scott et al, 2006 [202]:

$$D \approx 0.231 \frac{w^2}{t_{1/2}} \quad (5.3)$$

where w is the width of the bleached region and $t_{1/2}$ is the time to half recovery: $t_{1/2} = \ln(2)/\tau$. See Sec. A.2 for the full derivation of Eq. 5.3 based on the Supporting Text of Scott et al, 2006 [202].

Using fitted τ (Fig. 5.11B), measured w (Fig. 5.4, first column), and Eq. 5.3, we obtain a distribution of D , depicted in Fig. 5.16A. Estimated median D was $1.2 \mu\text{m}^2/\text{sec}$ with first and third quartiles at 0.69 and $2.0 \mu\text{m}^2/\text{sec}$. These estimates are reasonable for GFP-tagged Kv4.2 subunits—approximately 100 kDa in size. In comparison, GFP alone (26.9 kDa) diffuses with $D \approx 25 \mu\text{m}^2/\text{sec}$ [226, 186]. Further, our estimated D is approximately 30-fold smaller than a similarly-sized protein in water [162], which is the expected decrease in diffusivity between cytosol and dilute solution [156].

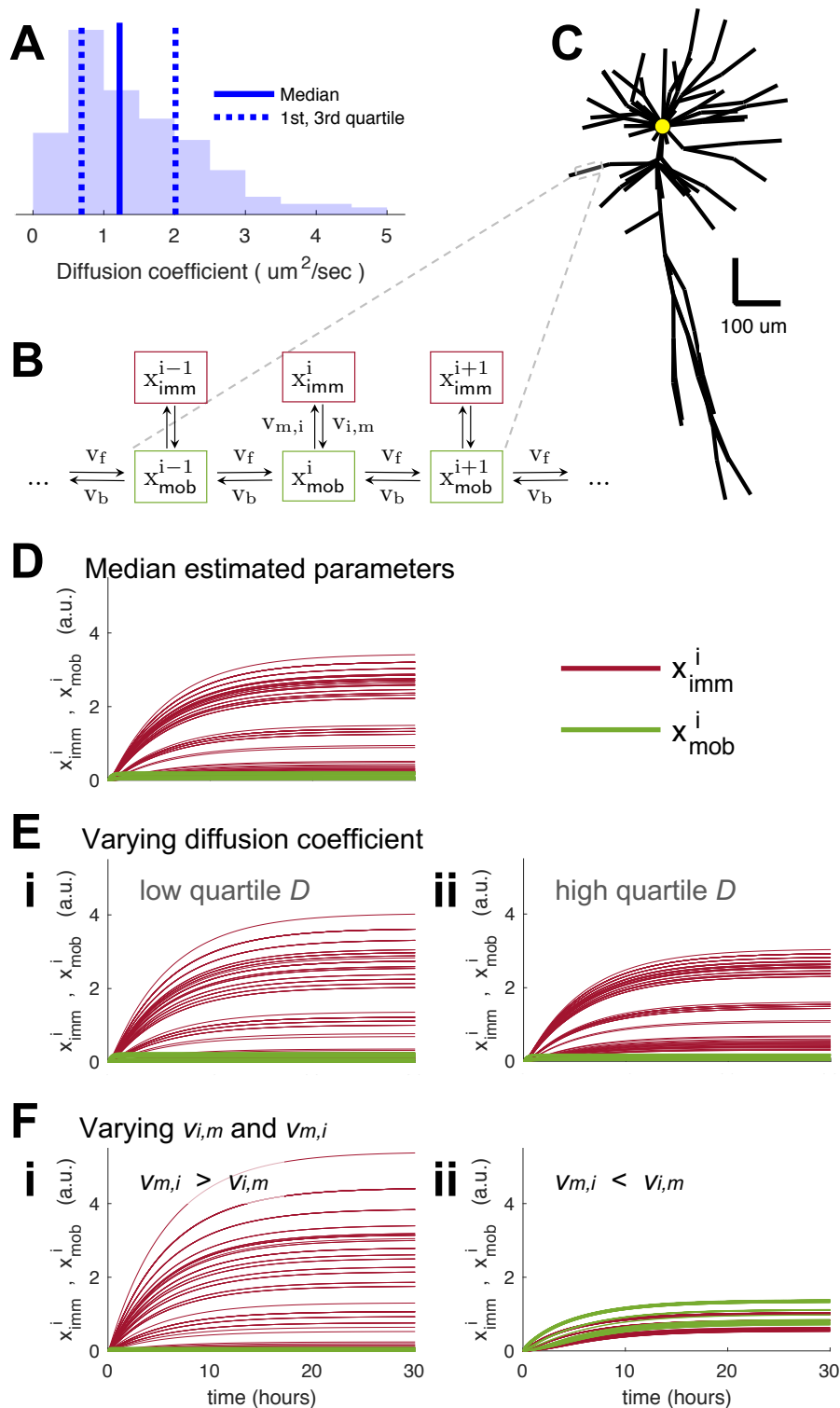


Fig. 5.16 Inferred parameters markedly affect cargo distribution in real neuron morphologies. (A): Histogram of diffusion coefficient D estimated from bleach recovery. (B): A multi-compartment, mass-action model of mobile x_{mob}^i and immobile x_{imm}^i particles is used to simulate intracellular distribution of cargo throughout (C): a full morphology of a pyramidal cell. (D): Simulation with median estimated parameters is depicted, showing a settling time within 20 hours and a majority of cargo immobilized. (E): Low D produces a decreasing localization profile (i), whereas high D normalizes the distribution (ii). (F): With $v_{m,i} > v_{i,m}$, the immobile fraction increases and x_{imm}^i has higher densities throughout the neuron (i). With $v_{m,i} < v_{i,m}$ the mobile fraction exceeds the immobile fraction (ii).

With realistic estimates of D , we built a compartmental model of a full neuron to quantify intracellular distribution of Kv4.2 subunits. The drift-diffusion equation describes transport rates, where diffusion D and drift v coefficients describe the bulk flow of a population of particles. When discretized (Fig. 5.16B), D and v relate to the forward v_f and backward v_b rates between compartments as follows:

$$D = \frac{\Delta x^2}{\Delta t} \frac{v_f + v_b}{2} \quad \text{and} \quad v = \frac{\Delta x}{\Delta t} v_f - v_b \quad (5.4)$$

as derived in Williams et al, 2016 [247]. In the continuous case, inter-site distance and time step, Δx and Δt , approach 0, and we estimate $D \approx \frac{v_f + v_b}{2}$ and $v \approx v_f - v_b$, as in Appendix A.1.

Since $D \gg v$ (Fig. 5.7), we assume $v = 0$ and use the distribution of D (Fig. 5.16A) to solve for $v_f = v_b$, which are then scaled to a compartment size of 100- μm . We simulate in a full size pyramidal cell from the human L3 neocortex (NeuroMorpho.Org ID: NMO_86957), as depicted in Fig. 5.16C. All cargo is produced in the soma (yellow circle) and degrades with rate $w = 0.000048 \text{ sec}^{-1}$, consistent with the observed half-life of Kv4.2 [210]. In simulation, a generalized rate v from a donor d to receiver r compartment transfers an amount of mass vd . As an example, consider the differential equation for the central compartment x_{mob}^i in Fig. 5.16B:

$$\begin{aligned} \dot{x}_{\text{mob}}^i = & + v_f x_{\text{mob}}^{i-1} (A^{ss} - x_{\text{mob}}^i) + v_b x_{\text{mob}}^{i+1} (A^{ss} - x_{\text{mob}}^i) + v_{i,m} x_{\text{imm}}^i (A^{ss} - x_{\text{mob}}^i) \\ & - v_b x_{\text{mob}}^i (A^{ss} - x_{\text{mob}}^{i-1}) - v_f x_{\text{mob}}^i (A^{ss} - x_{\text{mob}}^{i+1}) - v_{m,i} x_{\text{mob}}^i (1 - A^{ss} - x_{\text{imm}}^i) - w x_{\text{mob}}^i \end{aligned} \quad (5.5)$$

where each term corresponds to mass entering or exiting x_{mob}^i . Branch points have additional terms and terminal compartments have fewer terms. Such a system of ODEs—one for each compartment—describes the distribution of cargo.

With all parameters defined, we now simulate intracellular distribution of Kv4.2 with D ranging across the first to third quartiles (Fig. 5.16A) and $v_{i,m}$ and $v_{m,i}$ ranging from second (median) to third quartiles (Fig. 5.12Bii). We begin with median D , $v_{i,m}$, and $v_{m,i}$ plotted in Fig. 5.16D, where each line corresponds to an individual compartment. Mean x_{imm}^i is approximately 15-fold larger than mean x_{mob}^i , consistent with experimental fits. x_{mob}^i reach 95% of their steady states with a settling time of 1-2 hours, whereas x_{imm}^i require 17-19 hours.

Varying D primarily changes the cargo distribution profile (Fig. 5.16E). With high D (Fig. 5.16Eii), cargo has a flatter profile, with little deviation between proximal and distal

compartments. Low D results in a larger spread of cargo densities (Fig. 5.16Ei). Average x_{mob}^i and x_{imm}^i density across the entire neuron remains approximately the same.

Varying $v_{i,m}$ and $v_{m,i}$ changes the steady states of mean x_{mob}^i and x_{imm}^i (Fig. 5.16F). Simulation with median $v_{i,m}$ and upper quartile $v_{m,i}$ results in significantly increased x_{imm}^i , averaging 50-fold larger than mean x_{mob}^i but with similar settling times (Fig. 5.16Fi). Upper quartile $v_{i,m}$ and median $v_{m,i}$ drastically changes the distribution profile, with mean x_{imm}^i now 25% less than mean x_{mob}^i at steady state. Both x_{mob}^i and x_{imm}^i now have settling times between 16-20 hours, varying with distance from the soma.

5.6.1 Discussion

In the context of intracellular cargo distribution, these results can be interpreted in a few ways. The mobile fraction x_{mob}^i is a finite-capacity transport channel. Cargo diffuses in this channel with rate D . The immobile fraction x_{imm}^i behaves like a sink in which cargo becomes confined during dissemination. Inferred parameters $v_{i,m}$ and $v_{m,i}$ approximate which fraction of the dendrite behaves as a transport channel or a sink, which in turn shapes the speed and profile of cargo localization. Larger x_{mob}^i are achieved more rapidly with high $v_{i,m}$ and low $v_{m,i}$. Further, D is the speed at which cargo disseminates. High D allows more cargo into distal compartments, whereas low D produces a decreasing profile with distance from the soma.

The presence of two distinct mobile and immobile cargo states has potential benefits to cell function. Some proteins, like ion channels in postsynaptic densities, are fixed in position when functionally active. For such cargo, distinct mobile and immobile species are required for transport. An inactive, mobile state can also provide a local pool from which to replenish active cargo. We explore this interplay between mobile and immobile, inactive and active states in Chapter 6.

It is worth considering how diffusion might contribute to intracellular distribution in comparison to other modes of transport. Even with variation in diffusion coefficient and im/mobilization rates, the settling times (to 95% steady state) estimated here all fall within 24 hours. As discussed in detail in Chapter 6, this is within the range of observable global changes in complex neurons, such as in synaptic scaling or regulation of intrinsic excitability [235, 173, 178]. This brings to light the relative roles of active versus passive transport mechanisms, which raises a number of questions about models of intracellular distribution. A model with diffusion alone, such as in these simulations, is sufficient to capture the regulatory behavior of synaptic receptors or ion channels on the timescales observed *in vivo*. The specific contribution of microtubule-based transit, an energy-intensive process, versus passive diffusion is not fully understood.

Chapter 6

Neuronal morphology imposes a tradeoff between stability, accuracy, and efficiency of synaptic scaling

The results described in this chapter are being submitted to eLife. Some sections were written in direct connection to that manuscript.

6.1 Chapter summary and key findings

We again explore the global distribution of ion channels, now with feedback regulation in the context of synaptic scaling, which poses logistical problems for large, complex neuron morphologies.

1. Synaptic scaling in realistic morphologies is reproduced with a unified compartmental model of synaptic potentiation, AMPA receptor transport, and global/local regulation.
2. A system's scaling performance is measured using three attributes—efficiency, accuracy, and stability. Scaling efficiency is the speed with which a system reaches a steady state. Accuracy is the percent deviation from perfect scaling or potentiation. Scaling stability is quantified using Nyquist criterion for phase and gain margins from classic control theory.
3. Synaptic scaling requires a balance between stability, efficiency, and accuracy in realistic neuron morphologies. Sensitivity to global regulation mediates between scaling efficiency and stability. Sensitivity to local regulation mediates between

stability and accuracy. Internal AMPA receptor pool size mediates between efficiency and accuracy.

4. Neuron morphology, specifically size and symmetry, significantly impact scaling performance. Smaller and more symmetric morphologies, such as granule or Purkinje cells, exhibit better scaling performance than larger, more asymmetric cells, like pyramidal cells or interneurons.
5. Reduced-order neuron models, including linear representations with varying degrees of complexity, can predict scaling performance.

6.2 Introduction

Neuron physiology encompasses several neuroplastic mechanisms that regulate the electrical excitability of the cells in networks. Many of these mechanisms involve modulation of synapses, the electrochemical connections between neurons, and are thus aptly called synaptic plasticity. Synaptic plasticity comes in various forms, including synaptic scaling, Hebbian plasticity, and spike-timing dependent plasticity (covered in Sec. 1.4). Others, broadly categorized as nonsynaptic plasticity, involve regulatory changes throughout the rest of the neurons. This includes modification of intrinsic excitability by regulating ion channels, structural plasticity, and axonal modulation of spike frequency and propagation.

This chapter concerns the distribution and regulation of ion channels—specifically AMPA receptors—in the context of synaptic scaling. The motivations for specifically studying AMPAR regulation in synaptic scaling are multifold. AMPA receptors are densely localized in synapses and prevalently found across many neuron types. Further, AMPA receptors are highly relevant to synaptic plasticity, with many well-established mechanisms for local and global regulation. Although a similar theoretical analysis of other ion channels, such as in the context of intrinsic plasticity or dendritic excitability, could have been studied, AMPA receptors and synaptic scaling have an extensive literature of experimental characterization and validation. [217, 228, 235, 131, 233, 41]

Synaptic scaling is a homeostatic normalization mechanism that preserves relative synaptic strengths by adjusting them with a common factor [235]. This multiplicative change is believed to be critical, since synaptic strengths are involved in learning and memory retention [235]. Further, this homeostatic process is thought to be crucial for neuronal stability, playing a stabilizing role in otherwise runaway Hebbian plasticity [195, 42, 45]. Synaptic scaling requires a mechanism to sense total neuron activity and globally adjust synapses to achieve some activity set-point [235]. This process is relatively slow, which limits its ability to

stabilize network activity [248]. Here, we show that a slow global response is inevitable in realistic neuronal morphologies. Furthermore, we reveal that global scaling can in fact be a source of instability unless scaling efficiency or accuracy are sacrificed. Neuronal morphology therefore imposes a tradeoff between stability, accuracy, and efficiency of synaptic scaling.

A neuron with tens of thousands of synapses must regulate its own excitability to compensate for changes in input. The time requirement for homeostatic global feedback can introduce critical phase lags in a neuron's response to perturbation. The severity of phase lag increases with neuron size and expansive morphologies. Increasing sensitivity of global feedback improves response time (efficiency) at the cost of system stability. Homeostatic *local* feedback mitigates instability, but this comes at the cost of scaling accuracy. Local internal pools from which synapses can withdraw receptors improve accuracy of synaptic potentiation and scaling. However, production and transport of receptors is time- and energy-intensive and reduces scaling efficiency. These attributes—stability, efficiency, and accuracy—are balanced such that improving one always worsens one or both of the others. In this regard, a neuron has optimized its scaling performance.

Realization of this tradeoff requires a unified model of synaptic potentiation, scaling, regulation, and transport. A number of studies separately analyze these phenomena in detail, which we briefly survey here. Turrigiano et al [235] review global and local mechanisms of synaptic regulation but with no simulations or rigorous analyses. Triesch et al [231] model synaptic potentiation and scaling, and the authors report that larger internal pools improve scaling accuracy. However, this analysis considers only a single, central pool for all synapses and leaves open the question of morphology, effectively avoiding the phase lag. Our group has described the phase lag instability in toy neurons without realistic morphologies or synaptic scaling [5]. Williams et al [247] explore trafficking in realistic morphologies and attributes transport delays to bottleneck effects. Earnshaw et al [64] model AMPA receptor transport with detailed synapse dynamics in open loop with no feedback. No model to date has combined these mechanisms to study phase lag instability and the ensuing balance of stability, efficiency, and accuracy of synaptic scaling.

We present a complete biophysical model of AMPA receptor transport, activation, and regulation with synaptic potentiation and scaling in realistic neuron morphologies (Fig. 6.1). This framework makes a number of predictions that lead to new conclusions. First, we demonstrate the tradeoffs imposed by neuron morphology in a pyramidal cell (Fig. 6.3). We discuss mechanisms by which a neuron navigates each tradeoff between stability, accuracy, and efficiency of synaptic scaling. We devise methods of quantifying each attribute, including the application of Nyquist criterion for stability (Fig. 6.4). We observe location- and

morphology-dependent effects on scaling accuracy (Figs. 6.5 and 6.8). In turn, we establish the fundamental, underlying relationships between stability, accuracy, and efficiency (Fig. 6.9). We create a reduced-order representation of complex dendritic trees that captures their behavior and predicts their scaling performance (Fig. 6.11). Lastly, we explore scaling performance in other neuron morphologies (Fig. 6.13).

6.3 A unified model of synaptic potentiation, scaling, and regulation

We begin by setting out a schematic that outlines the components of our unified model of synaptic potentiation, scaling, and regulation. A full mathematical description of the model is presented in Appendix C. Here, we depict these mechanisms using cartoons of AMPA receptors (AMPARs) in a cell soma and dendritic arbor (Fig. 6.1A).

To prevent excitotoxicity and harm to the cell, a neuron maintains its level of excitability through global regulation, which occurs in the soma (Fig. 6.1B). The sum of all active AMPARs, $\sum g$, produces an average membrane potential V , representing a change in neural firing rate. This modulates the concentration of internal $[Ca^{2+}]$, which in turn regulates biosynthesis and release u of new receptors into circulation. The global gain K_G is the sensitivity of the global regulator to perturbations in $[Ca^{2+}]$ based on some set point $[Ca^{2+}]_{\text{target}}$. If neuron activity is too low, more AMPARs are produced; if activity is too high, AMPAR production is slowed. Global regulation as depicted is sufficient for normalization of synaptic strengths. [235, 231]

Significant assumptions are made in the modeling of V and internal $[Ca^{2+}]$ that warrant discussion. There are numerous synaptic inputs and ion channels in addition to AMPA receptors that contribute to V . Moreover, there are a number of cellular mechanisms that affect internal $[Ca^{2+}]$ along with total electrical activity in the neuron. Here, we opt for coarse-grained models with a simple representation of these complex biological properties. Rather than simulating all details of membrane potential and somatic $[Ca^{2+}]$, we capture the crucial dynamics for a comparison of global and local homeostasis.

Returning to the model schematic, AMPARs are freely transported on microtubules throughout the dendrites (Fig. 6.1C). Internal, inactive receptors m are transported with forward rate v_f and backward rate v_b . Active, external AMPARs on the surface are denoted g . Synaptic sites on the plasma membrane c are required for AMPAR activation ($m \rightarrow g$). c is the capacity of the synapse, i.e., the number of available slots for AMPARs. We impose an abrupt change in c to emulate long term potentiation or depression (LTP or LTD). This is

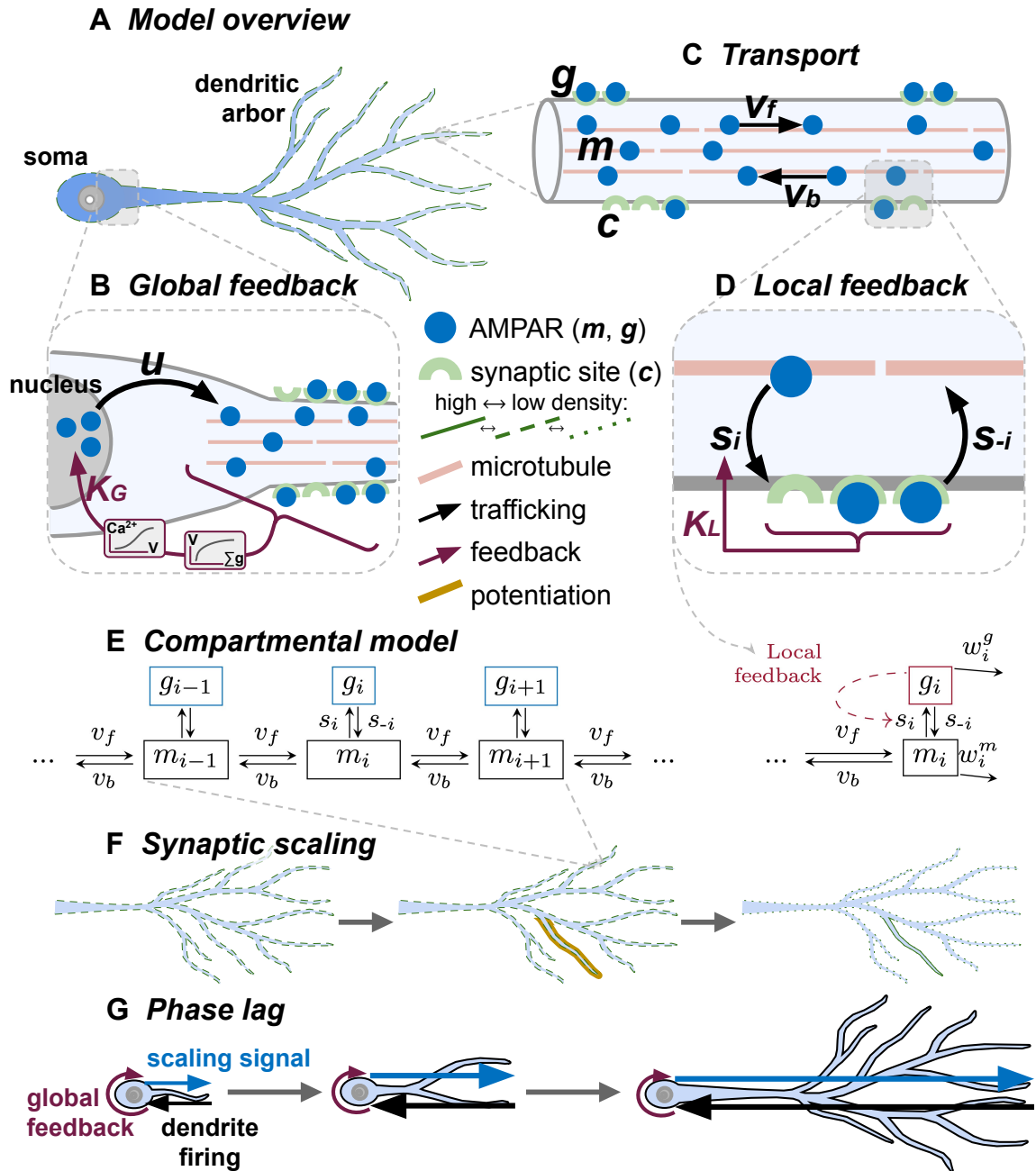


Fig. 6.1 Constructing a unified model of synaptic potentiation, scaling, and regulation to realize phase lag time delay. (A): Cell soma and dendritic arbor in which synaptic scaling occurs. (B): Global feedback in the soma averages active AMPARs ($\sum g$) to modulate biosynthesis and release u of new receptors into circulation. (C): Inactive AMPARs m are transported on microtubules with forward rate v_f and backward rate v_b . Active AMPARs g and synaptic sites c are depicted on the dendrite surface. (D): Cargo is activated ($m \rightarrow g$) with activation rate s_i , which is modulated via local feedback. (E): Components (B)-(D) are incorporated into a compartmental model of a discretized dendritic arbor. (F): A model with (B)-(D) alone replicates synaptic scaling following potentiation, as shown for a single branch. (G): AMPARs act as a global scaling signal, which creates a phase lag for global feedback, exacerbated in large and asymmetric morphologies.

consistent with the physiologic increase in structural proteins that support AMPARs on the plasma membrane during potentiation. [147, 166]

We next focus on the membrane itself—the site of cargo insertion (Fig. 6.1D). Cargo is activated ($m \rightarrow g$) with activation rate s_i and inactivated ($g \rightarrow m$) with rate s_{-i} . Homeostatic local feedback occurs in each synapse, where local g regulates s_i based on $[\text{Ca}^{2+}]_{\text{target}}$, similar to the global controller. Local gain K_L is the sensitivity of the local controllers to perturbations in local g . s_i increases or decreases when local excitability is too low or high, respectively.

By law of mass action, parameter s_{-i} modulates m at steady state. In other words, s_{-i} changes the size of an internal reserve pool of AMPARs, as depicted later in Fig. 6.6. Maintaining a large m requires considerable time and resources, which imposes a tradeoff for synaptic scaling.

AMPA transport with global and local feedback are incorporated into a compartmental model of a discretized dendritic arbor, as depicted Fig. 6.1E (detailed further in Appendix C). The aforementioned components are sufficient for localized potentiation with subsequent synaptic scaling (Fig. 6.1F). The unified model can also illustrate the phase lag that imposes limitations on synaptic scaling (Fig. 6.1G): a neuron globally regulates the strengths of its synapses to maintain intrinsic excitability through synaptic scaling. This requires a scaling signal propagated throughout the dendritic arbor to modify synaptic strengths. Scaled synapses continue to initiate dendritic firing, which is regulated globally. This cycle repeats and thus is the process of homeostatic synaptic scaling. Transport of a signal over large distances is the slowest of these processes, which increases phase lag. Further, given that the scaling signal must travel the full lengths of all dendrites, this time delay increases in larger neurons. Expansive morphologies are therefore more prone to instabilities induced by the phase lag of global regulation.

We have schematically introduced the components of our model to establish how morphology contributes to a phase lag. We aim to make this model data driven with conservative estimates for parameters that can be broadly quantified from experiments, including velocities, insertion speeds, and degradation rates. Other model mechanisms, including global and local feedback, encompass numerous physiologic processes and are set as free parameters. Varying these free parameters balances the limitations of synaptic scaling induced by neuron morphology. We next navigate the tradeoffs of synaptic scaling by sweeping through these free parameters.

6.4 Navigating the tradeoffs

Homeostatic synaptic scaling requires transport of a global scaling signal, which is slow in large neuron morphologies. This results in limitations in the stability, accuracy, or efficiency of synaptic scaling. These attributes are defined rigorously in later sections (Secs. 6.5, 6.6, and 6.7) and are qualitatively depicted in Fig. 6.2. Depicted is a trace of active AMPAR (g_i) density over time in a multi-compartment neuron model undergoing synaptic potentiation. g in each compartment is plotted; black and red lines denote non-potentiated and potentiated compartments, respectively. Stability is the degree of overshoots and oscillations as a system approaches steady state. Efficiency is the rate at which the system approaches a steady state. Accuracy is how well synapses potentiate and how well non-potentiated synapses maintain the ratios of their strengths following potentiation.

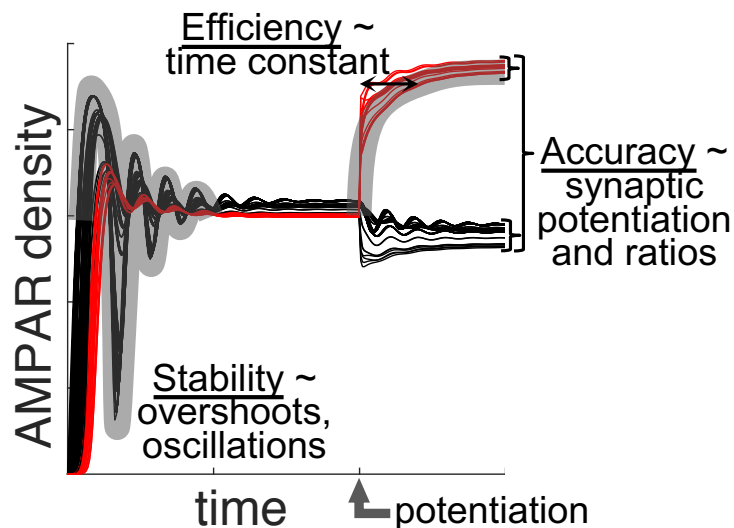


Fig. 6.2 The attributes in question—the stability, efficiency, and accuracy of synaptic scaling—are qualitatively defined here.

Tradeoffs between these attributes are mediated by three free parameters in our model: (1) global gain, (2) local gain, and (3) internal pool size. We demonstrate these tradeoffs in a full size pyramidal cell from the human L3 neocortex (NeuroMorpho.Org ID: NMO_86957) approximately 1000 μm in length, depicted in Fig. 6.3A.

The three tradeoffs are portrayed in a triangle schematic in Fig. 6.3B. The free parameters that mediate these tradeoffs are depicted in a simplified model schematic in Fig. 6.3C. All other parameters are held constant between simulations. We next demonstrate simulations that exemplify each tradeoff.

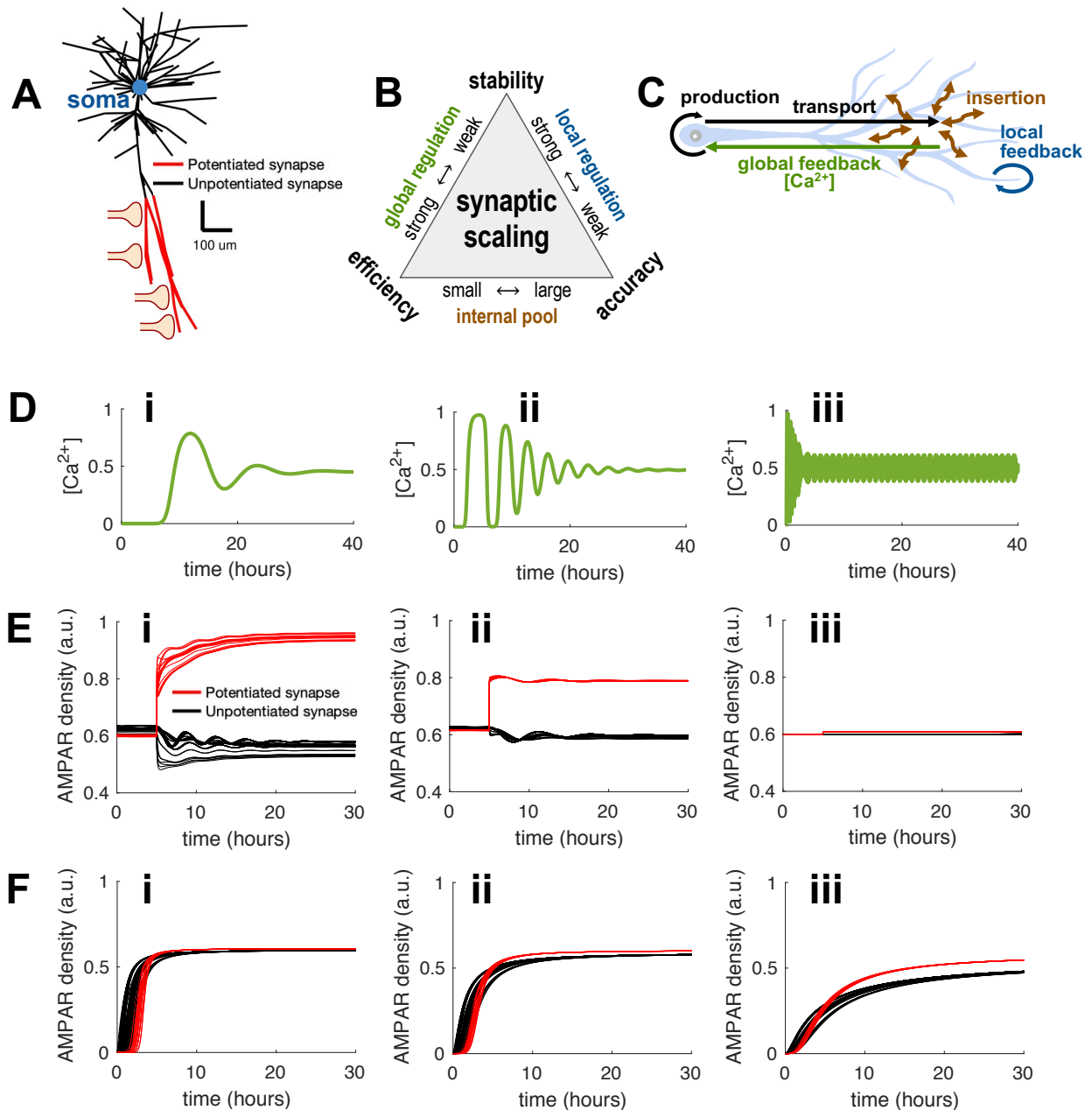


Fig. 6.3 Navigating the tradeoffs. (A): The balance between stability, accuracy, and efficiency of synaptic scaling is demonstrated in an neocortical L3 pyramidal cell with LTP in distal compartments (red). (B): Three tradeoffs are portrayed in a triangular schematic, where each attribute is a vertex and each free parameter that mediates a tradeoff is an edge. (C): The corresponding model mechanism that mediate tradeoffs are depicted. (D): Global gain (K_G , increasing from i to iii) mediates tradeoff between stability and efficiency. (E): Local gain (K_L , increasing from i to iii) mediates tradeoff between stability and accuracy. (F): Internal pool size (s_{-i} , increasing from i to iii) mediates tradeoff between stability and accuracy.

6.4.1 Global gain mediates tradeoff between stability and efficiency

The sensitivity of the global regulator to changes in total neural firing rate mediates the stability and efficiency of synaptic scaling, as depicted in Fig. 6.3D. We use $[Ca^{2+}]$ as an approximate measure of global neuron activity. Low global regulation results in a stable system that is slow to reach steady state (Fig. 6.3Di). Increasing global gain improves time to steady state but decreases stability, evident in $[Ca^{2+}]$ with overshoots and dampened oscillations (Fig. 6.3Dii). Increasing global gain further results in the neuron firing even faster but with full non-dampening oscillations (Fig. 6.3Diii). This tradeoff demonstrates that there's a hard limit to how quickly a neuron can respond before it becomes unstable.

Suppose a neuron requires a response time as in Fig. 6.3Dii with reduced oscillations. This can be achieved with increased regulation at the local level.

6.4.2 Local gain mediates tradeoff between stability and accuracy

The sensitivity of the local regulator to changes in local neural firing mediates between stability and accuracy of synaptic scaling, as depicted in Fig. 6.3E. To demonstrate this tradeoff, we simulate synaptic potentiation of the distal synapses, depicted as red compartments in Fig. 6.3A, with varying local gain and constant global gain. We plot the AMPAR density in each of these compartments as approximate measures of local firing rate.

The absence of local control results in synaptic scaling with moderate accuracy and oscillations (Fig. 6.3Ei). LTP occurs at 5 hours in the distal (red) synapses, which make up 14% of total compartments. The red synapses strengthen, as expected during LTP. The unpotentiated, black compartments are scaled down, which is notable because the synaptic capacity of these compartments was not changed. Fig. 6.3Ei validates that synaptic scaling works with global control alone. Note that the relative weights of the synapses are preserved with moderate accuracy. Further, the difference between potentiated (red) and unpotentiated (black) synapses is prominent.

If we introduce local regulation at low gain (Fig. 6.3Eii), the oscillations are improved at the cost of accuracy. The difference between potentiated and unpotentiated synapses begins to diminish. If we increase the local gain (Fig. 6.3Eiii), the oscillations are eliminated and the system is fully stable now. However, synaptic scaling is no longer accurate, and red synapses hardly increase compared to black. The degree to which local regulation can improve stability is limited by a reduction in the accuracy of synaptic scaling.

6.4.3 Internal pool size mediates tradeoff between accuracy and efficiency

We next consider a stable neuron with strong local control and sweep through internal pool sizes of inactive AMPARs (m). Internal pool size is mediated by changing AMPAR endocytosis rate ($g \rightarrow m$), as depicted in Fig. 6.6. The neuron with a small internal pool fills relatively quickly (Fig. 6.3Fi). If we increase internal pool size, cell fill time is slower, and synaptic scaling is less efficient (Fig. 6.3Fii). However, we can begin to differentiate between potentiated and unpotentiated synapses. Further increasing the internal pool size (Fig. 6.3Fiii) continues to improve the scaling accuracy; however, cell fill time becomes very slow.

Thus far, we have presented a number of simulations in a model pyramidal neuron. These simulations sweep through ranges of global gain, local gain, and internal pool size to demonstrate the limitations imposed on the stability, efficiency, and accuracy of synaptic scaling. How do we know that these examples in this neuron model generalize to other morphologies? If we reduce the complexity of this example, are we still left with the fundamental, underlying tradeoffs observed here?

We aim to rigorously quantify these tradeoffs to better understand the relevant dynamics that limit synaptic scaling. We begin with a didactic introduction to stability from classical control theory applied to regulation of neuron excitability. We then devise formal definitions of efficiency and accuracy for synaptic potentiation and scaling. We formalize the tradeoffs in a simplified model. We are then equipped to make realistic predictions about scaling performance in a variety of neuron morphologies.

6.5 Quantifying stability using classic control theory

This section was a collaboration with Saeed Aljaberi and Fulvio Forni in the Control Group, Department of Engineering, University of Cambridge.

The unified model of synaptic potentiation, scaling, and regulation is complex (Fig. 6.1). To quantify stability, we evaluate feedback regulation in a simplified model—a single compartment with two states m and g for inactive and active cargo, respectively. A third state u represents cargo production. Strength of global control is mediated by gain K_G . This

three-dimensional system is described by equations:

$$\begin{aligned}\dot{m} &= u - s_1 m(c - g) + s_{-1} g - \omega^m m \\ \dot{g} &= s_1 m(c - g) - s_{-1} g - \omega^g g. \\ \dot{u} &= k_G([\text{Ca}^{2+}]_{target} - [\text{Ca}^{2+}]) - \gamma_G u \\ [\text{Ca}^{2+}] &= \psi(g)\end{aligned}$$

$\psi(g)$ is a static map of g to $[\text{Ca}^{2+}]$ from Eqs. C.4-C.6. The connections between linearized subsystems are summarized in the block diagram in Fig. 6.4B and briefly described here. The model has a preset $[\text{Ca}^{2+}]_{target}$ that sums with $[\text{Ca}^{2+}]$ to produce error e_G . Function G_u outputs cargo production u . Function G_m transports cargo throughout the dendrites. Function G_g activates cargo by insertion into dendritic spines. Active cargo g then feeds back to modify $[\text{Ca}^{2+}]$.

We next simulate this system as described with increasingly aggressive global regulation (by increasing K_G), as depicted in Fig. 6.4C. For low K_G , cargo does not reach $[\text{Ca}^{2+}]_{target} = 0.5$ within the simulation time (Fig. 6.4Ci). Gradually increasing K_G decreases settling time (Fig. 6.4Cii-iv). However, dampened oscillations begin to appear, and excessive K_G results in overshooting $[\text{Ca}^{2+}]_{target}$ (Fig. 6.4Civ). Further increasing K_G results in the emergence of oscillations and ultimately instabilities in the form of limit cycles (Fig. 6.4Cv).

These degrees of increasing instability (Fig. 6.4Ci-v) can be quantified using the Nyquist stability criterion, described in Appendix C and summarized here. We conceptually define an instability as when the ratio of output to input, called the transfer function, tends toward infinity. Using the block diagram in Fig. 6.4B, we can define instability as

$$\frac{\text{output}}{\text{input}} = \frac{g}{[\text{Ca}^{2+}]_{target}} = \frac{G_g G_m G_u}{1 + K \partial \psi G_g G_m G_u} \rightarrow \infty$$

The transfer function approaches infinity when the denominator approaches 0:

$$\begin{aligned}1 + K \partial \psi G_g G_m G_u &\rightarrow 0 \\ K \partial \psi G_g G_m G_u &\rightarrow -1\end{aligned}$$

We can plot the proximity of $K \partial \psi G_g G_m G_u$ to -1 on a Nyquist plot, a graphical representation of the transfer function parameterized into real and imaginary parts on the x- and y-axis, respectively (Fig. 6.4D). A line on the Nyquist plot corresponds to a system, and its proximity to (-1, 0) quantifies system stability.

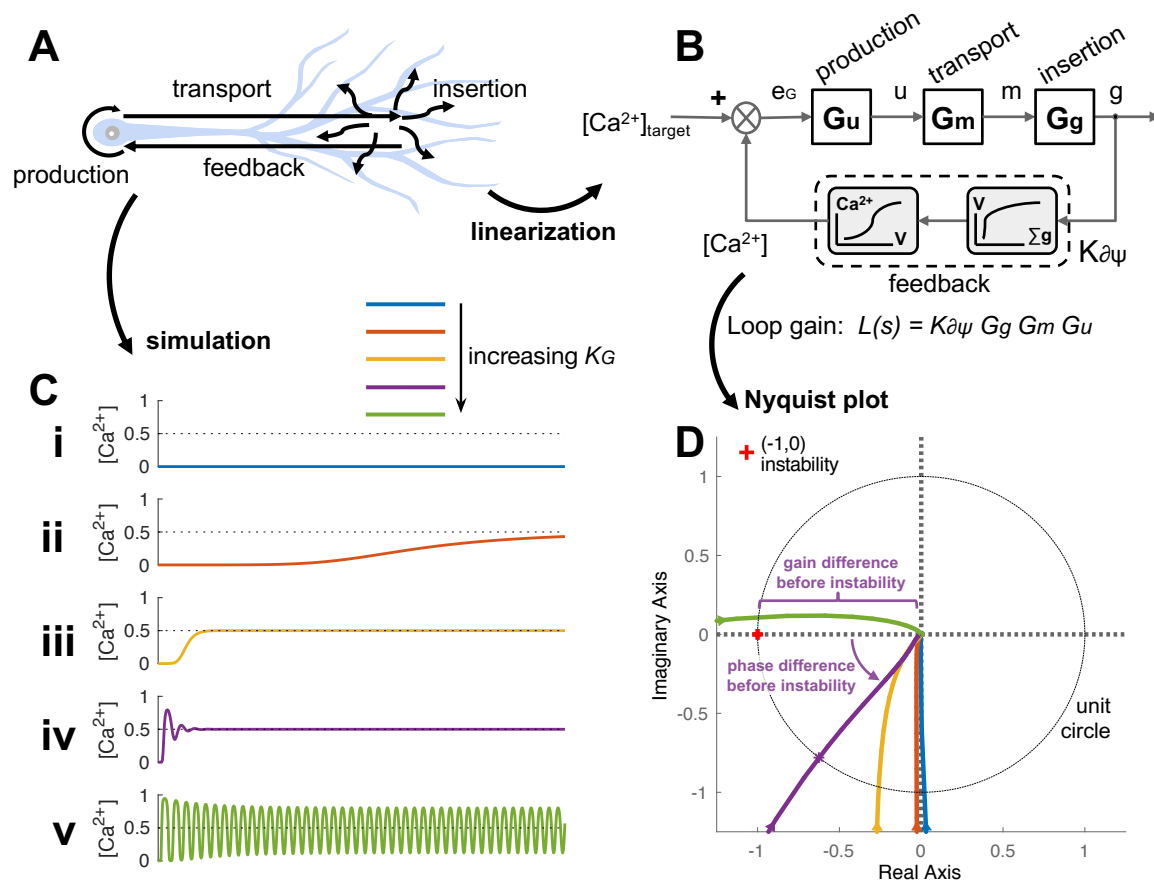


Fig. 6.4 System stability is quantified using principles of classic control theory. (A): Schematic showing all linear and nonlinear model dynamics. (B): A linear approximation of model dynamics as an input-output system is depicted as a box diagram. (C) Model dynamics are simulated, and resultant intracellular calcium signal is depicted for increasing K_G (i-v). (D) Model dynamics represented as a Nyquist plot for linear approximations with increasing K_G . Gain margin (GM) and phase margin (PM) are depicted.

Stability margins can be computed from the Nyquist plot. The gain margin (GM) is the horizontal distance to $(-1, 0)$. The phase margin (PM) is the angle of rotation to $(-1, 0)$. Both are marked for the purple system (Fig. 6.4Civ) on the Nyquist plot in Fig. 6.4D. Note that Nyquist plots with increasingly aggressive regulation (Fig. 6.4Ci-v) approach and eventually surpass (Fig. 6.4Cv) the $(-1, 0)$ point. Derivations and equations for the gain and phase margins are provided in Appendix C.

6.6 Quantifying accuracy of synaptic potentiation and scaling

We next derive a rigorous definition of accuracy. We discuss both accuracy of synaptic potentiation and accuracy of synaptic scaling. These concepts are related, and both improve with larger internal pool size.

During LTP, a synapse increases demand for synaptic proteins. The degree of synaptic potentiation depends on the availability of cargo near the synapse. Adjacent synapses have indeed been observed to compete for plasticity related proteins [197]. We simulate synaptic potentiation by increasing cargo demand in synapses, a method originally formulated in the sushi belt model [62] and its mathematical implementation [247]. An increased number of slots c_i in the synapse does not necessarily fill to capacity, such as in neurons with small internal pools or widespread potentiation. How capable are neurons at meeting this demand? We explore accuracy in the context of morphology and internal pool size.

We assess how well a neurite can potentiate its synapses at varying locations in the dendritic tree. To this end, we compare potentiated synapses to equivalent unpotentiated compartments on an identical branch (Fig. 6.5A). We potentiate single synaptic compartments with varying strength and at varying distances from the soma. For a small internal pool (Fig. 6.5B), a neuron only fulfills half the demand for increased AMPARs in distal synapses. Internal pool size dwindles with distance from the AMPAR source, and full synaptic potentiation is not achieved. Neurites with increasing internal pool size (Fig. 6.5C-D) more readily fulfill demand during LTP, thus improving accuracy of potentiation.

Synaptic potentiation allows a neuron to maintain the relative strengths of its synapses following potentiation. We thus explore how internal pool size impacts the accuracy of synaptic scaling. During scaling, neurons undergo multiplicative changes in synaptic strength such that the relative strengths of the synapses are preserved. Such modification of synapses forms the foundation of learning and memory. Stable, reliable changes at the molecular

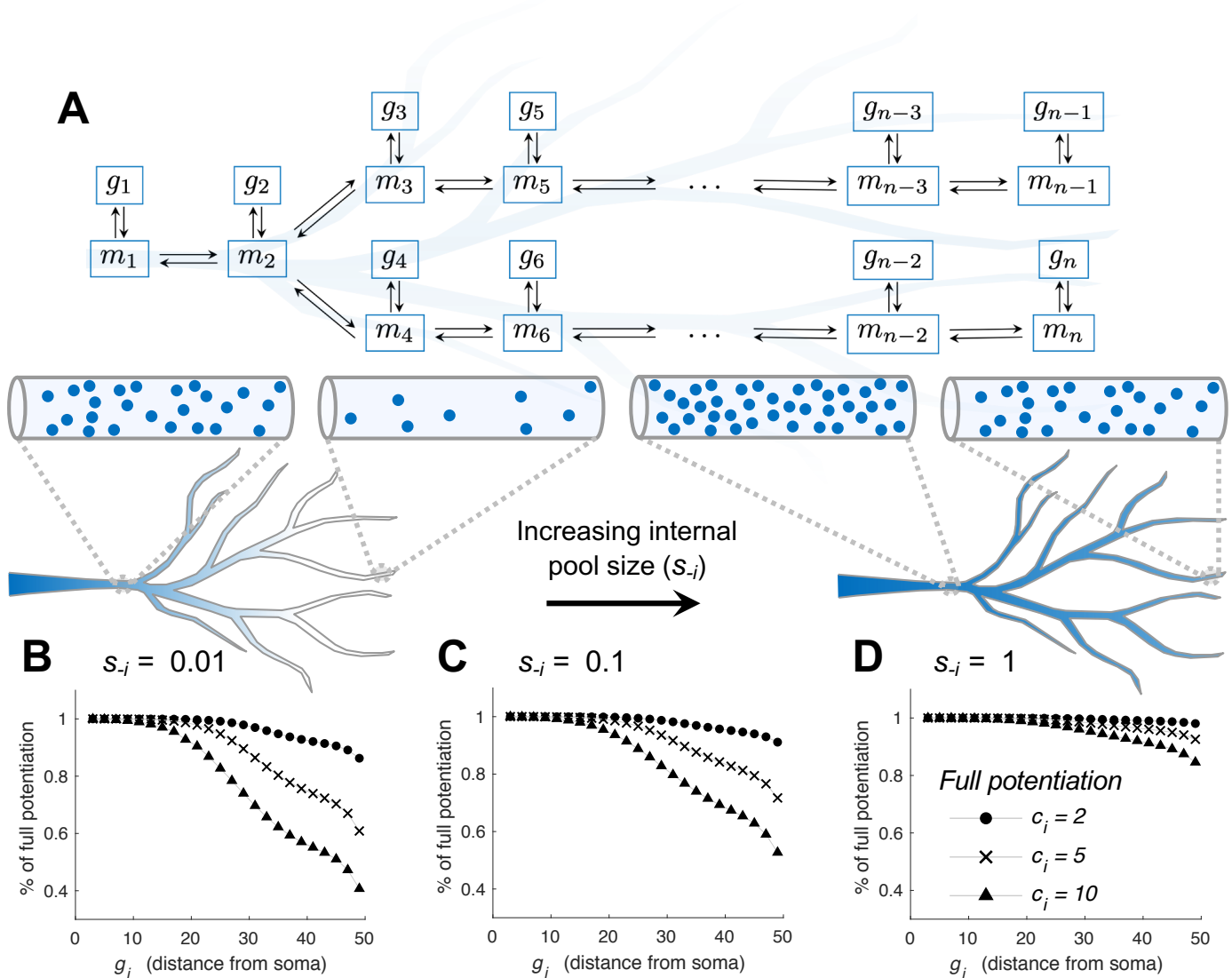


Fig. 6.5 Accuracy of synaptic potentiation is quantified as a percentage of full potentiation. (A): Toy model of multi-compartment model with two parallel, identical branches allows for comparison between potentiated synapse and equivalent unpotentiated synapse as control. Single g_i are potentiated individually with varying strength (marker shape) in systems with varying s_i (B-D). Distal synapses potentiate poorly compared to proximal synapses, mitigated by large receptor pool size.

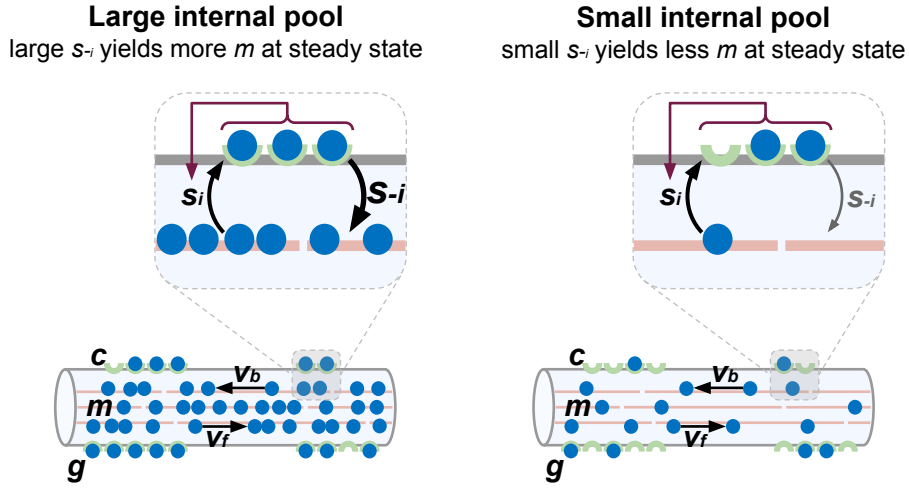


Fig. 6.6 By law of mass action, AMPAR inactivation s_{-i} modulates m at steady state, effectively changing the sizes of internal reserve pools of AMPARs.

and cellular level correspond with stable, reliable memories, which motivates quantifying accuracy of synaptic scaling.

We demonstrate our measure of scaling accuracy with examples in the ball-stick model with distributed LTP and LTD (Fig. 6.7). Prior to potentiation, all synaptic capacities c_i are close to 1 (Fig. 6.7A). During simulation, one compartment $i = 3$ undergoes LTP/LTD, depicted with dashed lines. The remaining compartments scale and maintain their synaptic ratios. We trace $[Ca^{2+}]$ and g_i for all compartments (Fig. 6.7B,Cii,iii). We next describe a metric for quantifying the accuracy of scaling in g_i .

Prior to LTP/LTD, the steady states of all non-potentiated synapses g_i^{ss} are recorded and averaged as follows:

$$\mu^{ss} = \text{mean}(g_{\text{unpot}}^{ss})$$

μ^{ss} is the mean active cargo content for all non-potentiated synapses. We standardize all g_i^{ss} by the mean μ^{ss} . We then compute the steady state mean following LTP/LTD: $\hat{\mu}^{ss}$, indicated by $\hat{\cdot}$. We compare the mean-standardized g_i^{ss}/μ^{ss} between the pre- and post-LTP states. A synapse that scales perfectly has:

$$\frac{g_i^{ss}}{\mu^{ss}} = \frac{\hat{g}_i^{ss}}{\hat{\mu}^{ss}} \quad \text{and} \quad q_i = \frac{\hat{g}_i^{ss}/\hat{\mu}^{ss}}{g_i^{ss}/\mu^{ss}} - 1 = 0 \quad (6.1)$$

where q_i measures scaling deviation for each individual synapse (Fig. 6.7B,Civ). $q_i < 0$ indicates excess scaling during LTP or incomplete scaling during LTD. $q_i > 0$ corresponds to incomplete scaling during LTP or excess scaling during LTD. We can use q_i s to compute

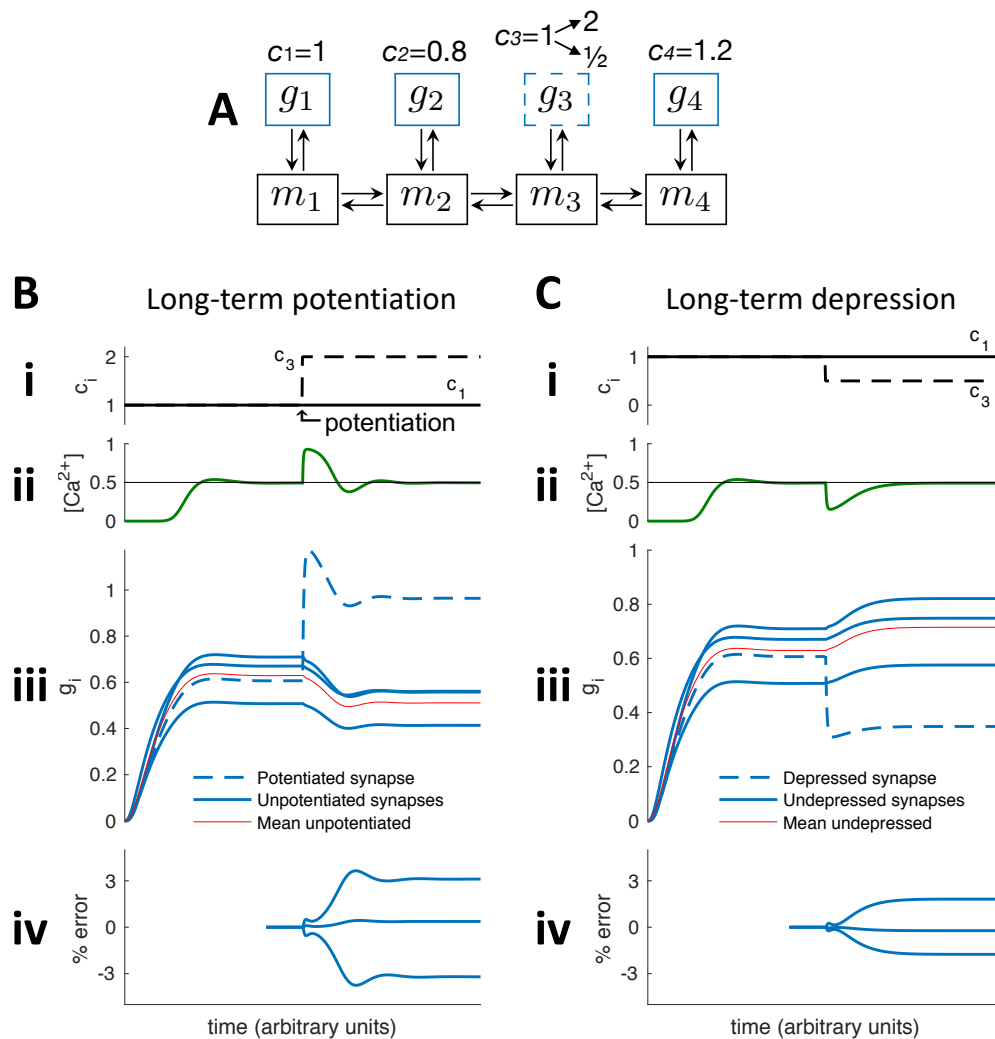


Fig. 6.7 Sample computation of scaling error q . (A) A toy model undergoes a synaptic change in compartment $i = 3$. (B-C): During long-term potentiation (B) and depression (C), c_3 increases or decreases (i) and the global controller maintains homeostasis (ii). Other compartments exhibit the opposite deflection in synaptic strength (iii)—called synaptic scaling. The average steady state values of unpotentiated/undepressed synapses are used to compute scaling error (iv).

mean absolute percent error Q from perfect scaling:

$$Q = \text{mean}(|q_i|) \times 100\% \quad (6.2)$$

Larger Q indicates a greater deviation from perfect scaling, i.e. more inaccurate synaptic scaling.

We next compute Q for varying internal pool sizes and potentiation ratios in distinct neuron morphologies. We examine linear and stellate architectures—the extreme cases of structural symmetry, depicted in Fig. 6.8A,Bi. In both, m_1 is the soma and site of AMPAR production and global regulation. Model parameters are scaled such that AMPARs are transported at 1 $\mu\text{m/s}$ and the linear and stellate models are 1000 μm in length and 250 μm in radius, respectively. In the symmetric, stellate model, each compartment has proximate access to the soma with minimal transport of scaling signal and AMPARs. In the asymmetric, linear model, the effect of transport and resultant phase lag increases, particularly for distal compartments. This results in significantly reduced scaling accuracy in asymmetric morphologies (Fig. 6.8A,Bii).

In both, scaling accuracy decreases with increasing potentiation ratios. Higher demand for AMPARs results in scaling error. Scaling accuracy also increases with larger internal pools. Larger reserves allow synapses to meet demand for AMPARs. The fundamental tradeoffs of synaptic scaling (Fig. 6.3B) still apply here. We observe that tradeoff constraints are largely shaped by network morphology.

6.7 Defining efficiency

We lastly define efficiency of synaptic scaling. We use active AMPAR density g_i to compute a meaningful measure of efficiency in the context of synaptic scaling. Efficiency is the average time for the states to reach within some percentage of steady state across all compartments in a neuron.

For instance, consider a neuron with $i = 1, 2, \dots, N$ compartments. In simulation, some fraction of these compartments are potentiated and approach a new steady state in synaptic strength following potentiation. Non-potentiated synapses are also perturbed by potentiation and exhibit a corresponding decrease in synaptic strength (as depicted in Fig. 6.7). Both potentiated and non-potentiated synapses are used to compute the average efficiency of the system.

For each compartment i , the steady state active AMPAR density before g_i^{pre} and after g_i^{post} potentiation is recorded. A threshold $X\%$ is set for proximity to post-perturbation steady

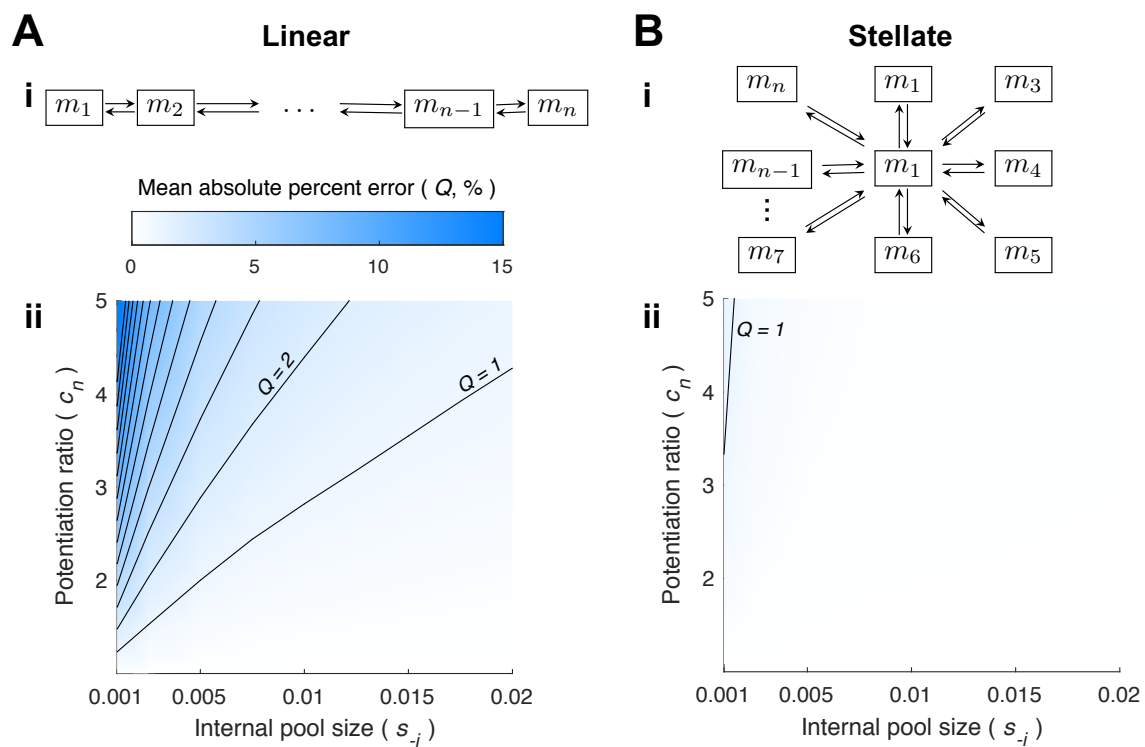


Fig. 6.8 Asymmetric morphologies scale less accurately than symmetric morphologies, mitigated by large receptor pools. (A): A linear morphology (i) is simulated for varying c_n and s_{-i} while quantifying mean absolute percent error Q (ii). (B): The same parameter sweep and quantification (ii) is performed for a stellate morphology (i), demonstrating more accurate synaptic scaling in symmetric morphologies.

state: $g_i^{\text{post}} \pm X|g_i^{\text{pre}} - g_i^{\text{post}}|$. The time between perturbation and each compartment i first entering this range is recorded as the time to steady state t_i^{ss} , which is estimated from the data vector output of simulations. The time to steady state of the system t^{ss} is then computed as the average of all t_i^{ss}

$$t^{ss} = \frac{\sum_{i=1}^N t_i^{ss}}{N} \quad \text{in sec}$$

Efficiency is then defined as the reciprocal of the average time to steady state for all compartments.

$$\text{efficiency} = \frac{1}{t^{ss}} \quad \text{in sec}^{-1}$$

In this definition, the efficiency of a system is analogous to a rate or time constant of a system returning to a steady state following a perturbation.

6.8 Summary of tradeoffs

By now, we have discussed the tradeoffs involved in balancing the stability, efficiency, and accuracy of synaptic scaling. We have also introduced a rigorous method of quantifying each attribute. Using these measures, we create a succinct summary of these tradeoffs, depicted in Fig. 6.9.

We simulate a toy model with $n = 4$ compartments. The gain margin (defined in Eq. C.11) approximates stability. The settling rate, or reciprocal of settling time, approximates efficiency. The reciprocal of mean absolute percent error (Q^{-1}) approximates accuracy. We sweep through parameter K_G to vary global regulation that modulates the stability-efficiency tradeoff (Fig. 6.9A). We then sweep through parameter K_L to vary local regulation that modulates the stability-accuracy tradeoff (Fig. 6.9B). Lastly, we sweep through parameter s_{-i} to vary internal pool size that modulates the efficiency-accuracy tradeoff. The axes for each tradeoff are adjusted to cover the stable regulation region, characterized by real eigenvalues of the first order linearization. Beyond the limits of these axes, the system is unstable and has oscillations, as in Fig. 6.4Cv.

Each tradeoff is hyperbolic in shape, suggesting a negative correlation. No attribute can be improved without worsening at least one of the other attributes. Further, no modification to the system can simultaneously improve all attributes. These tradeoffs imply that the balance of attributes is Pareto optimal.

Experimental studies have suggested that Arc protein is the global scaling signal dissipated throughout the dendrites in response to changes in neural firing rate [222, 47, 221, 235]. In our simulations and analysis thus far, we lump the transport of the scaling signal with AMPAR trafficking. Our modeling assumption is reasonable since AMPARs and Arc are

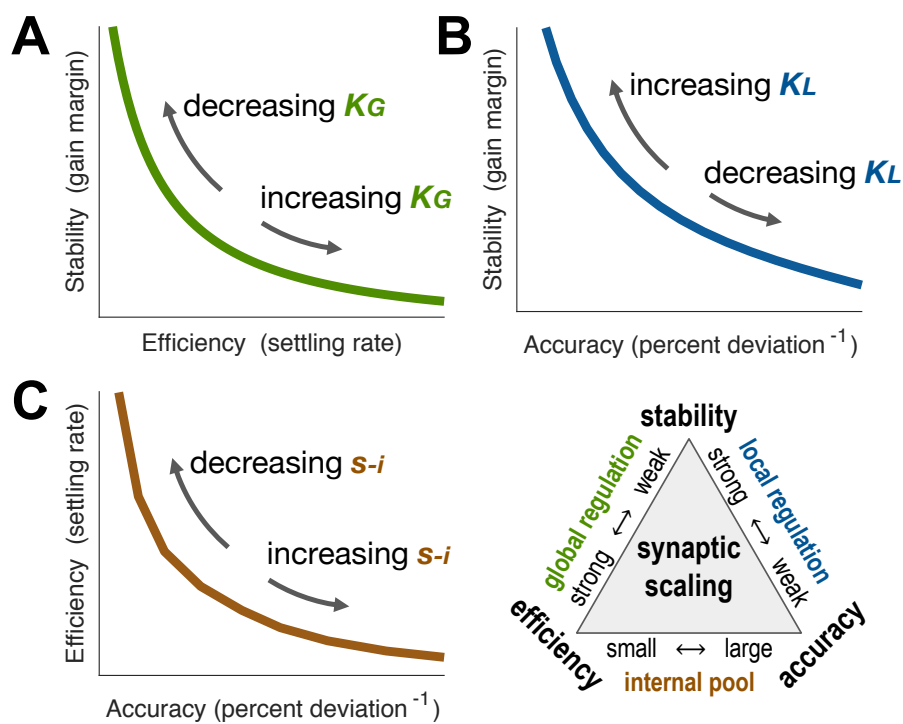


Fig. 6.9 The tradeoffs are summarized in a toy model by rigorously quantifying each attribute. (A): The stability-efficiency tradeoff is mediated by tweaking K_G . (B) The stability-accuracy tradeoff is mediated by tweaking K_L . (C): The efficiency-accuracy tradeoff is mediated by tweaking s_{-i} .

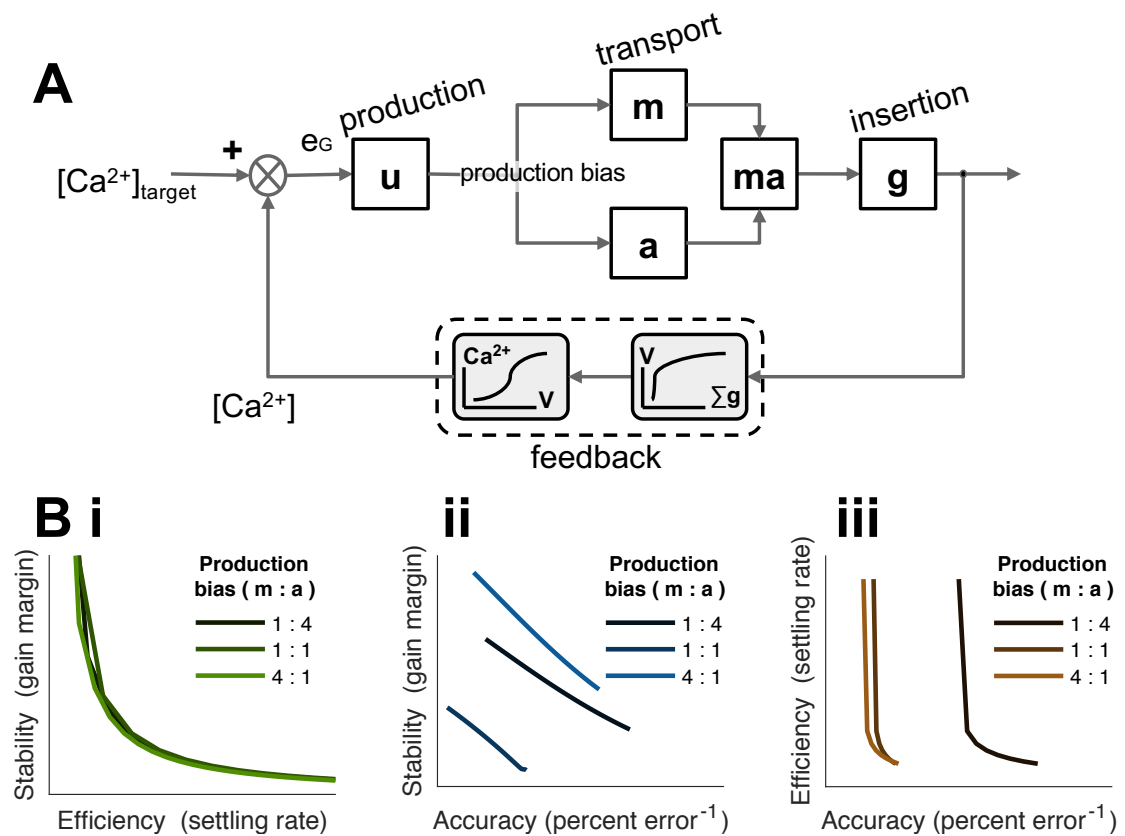


Fig. 6.10 In a second system, plasticity protein Arc communicates the global activity signal. (A): Block diagram of closed-loop model with additional species a for Arc. (B): All three tradeoffs are replicated in the Arc system. The global regulator produces both inactive AMPARs m and Arc a with some production bias $m : a$, indicated by different colored lines.

trafficked at similar rates (300 $\mu\text{m/hr}$, [246]). As a conservative estimate, we use fast rates for AMPAR transport. To further evaluate this assumption, we also perform simulations with Arc protein as a separate communication channel to validate that lumping the scaling signal with AMPAR trafficking produces similar results (Fig. 6.10A). In this system, the global controller regulates production of both m and a with some bias $m : a$. This system replicates the same tradeoffs of synaptic scaling for a wide range of $m : a$ (Fig. 6.10B).

6.9 Reduced-order neuron models capture scaling performance

This section was a collaboration with Saeed Aljaberi and Fulvio Forni in the Control Group, Department of Engineering, University of Cambridge.

To further simplify neuron morphology and predict scaling performance, each structure is approximated as a ball-stick model with distal LTP. Reduced-order models capture the qualitative behavior with significantly less states, allowing for intuitive predictions made with improved computational efficiency. In the ball-stick model, morphology is replaced by a line of compartments with a single synapse placed at the tip. The general ball-stick with distal LTP is replicated in Fig. 6.11B, with parameters for diffusion d , capacity c , number of compartments n , and degradation w . Real neuron morphologies vary in size and symmetry, which are expected to impact parameters in the optimal ball-stick representation. For example, a longer neuron like a pyramidal cell would best fit a longer ball-stick than that of a smaller granule cell.

Fitting to a ball-stick model begins with a raw neuron morphology (Fig. 6.11Ci). The morphology can be coarsened to some fixed distance (100 μm) between nodes using the TREES toolbox [57], shown in Fig. 6.11Bii. The layered depiction clarifies the logical progression of cargo through branches (Fig. 6.11Biii). The coarsened model is simulated, and input u and output $\sum g$ are recorded. Ball-stick parameters are estimated using Grey-Box Model Estimation from the MATLAB System Identification Toolbox. Grey-Box Model Estimation uses the structure of the nonlinear ball-stick model with fixed n for fitting to input and output vectors.

System identification is performed to demonstrate that a ball-stick model alone can capture the dynamics of a real neuron morphology (Fig. 6.12). The ball-stick fit improves with increasing n . Ball-stick models with fixed $n = 4$ were fitted to each of the real morphologies, and estimated parameters are tabulated in Table 6.1.

To assess whether the ball-stick estimates capture scaling performance, the fitted parameters are then plotted against the corresponding stability, scaling error, and settling time of the morphology. Estimated parameter w best approximates scaling performance, as depicted in Fig. 6.11D. A ball-stick model with increasing w has increasing gain margins (high stability), increasing scaling error (low accuracy), and increasing settling time (low efficiency).

Table 6.1 - Ball-stick model parameters fits for various neuron morphologies constrained to $n = 4$ are tabulated here. Estimated parameters predict scaling performance.

Cell type	Estimated parameters			Quality of fit
	diffusion d	capacity c	degradation w	% fit
CA1 interneuron	1.072	0.80	0.1062	93
granule cell	0.084	0.93	0.0002	82
L3 pyramidal, asymmetric	2.134	0.99	0.0781	78
L3 pyramidal, symmetric	0.100	1.11	0.0651	87
Martinotti cell	0.040	3.03	0.0593	96
Purkinje cell	0.029	14.52	0.0672	69

6.10 Neuron size and symmetry significantly impact scaling performance

We have demonstrated that neuron morphology directly impacts its transfer function, equivalent line, and stability during synaptic scaling. Other scaling attributes, efficiency and accuracy, are also affected by neuron morphology. We continue to examine how real morphology shapes scaling performance. We survey dendritic arbors of varying neurons listed in Table 6.2.

We first simulate synaptic potentiation and scaling in each full morphology. Axon compartments were manually removed from neuron reconstructions, and dendrites were discretized to 100 μm -segments while preserving neurite length (using the TREES toolbox, [57]). Active transport speed was set to 1 $\mu\text{m}/\text{sec}$ for a conservative estimate of transport kinetics. Initial simulations used moderate internal AMPAR pool size ($s_{-i} = 0.05$) and no local control ($K_L = 0$). Global regulation (K_G) was calibrated for stability in symmetric L3 pyramidal cells (with minimal overshoot and oscillations, as in Fig. 6.3Ci). K_G was then linearly scaled by number of compartments in the remaining morphologies, which yielded stable convergence in all simulations (Fig. 6.13B). Fifteen percent of synapses most distal to the soma, indicated in red, underwent LTP with doubling of synaptic strength at time 0 hours.

A Transfer functions and symmetry reduction

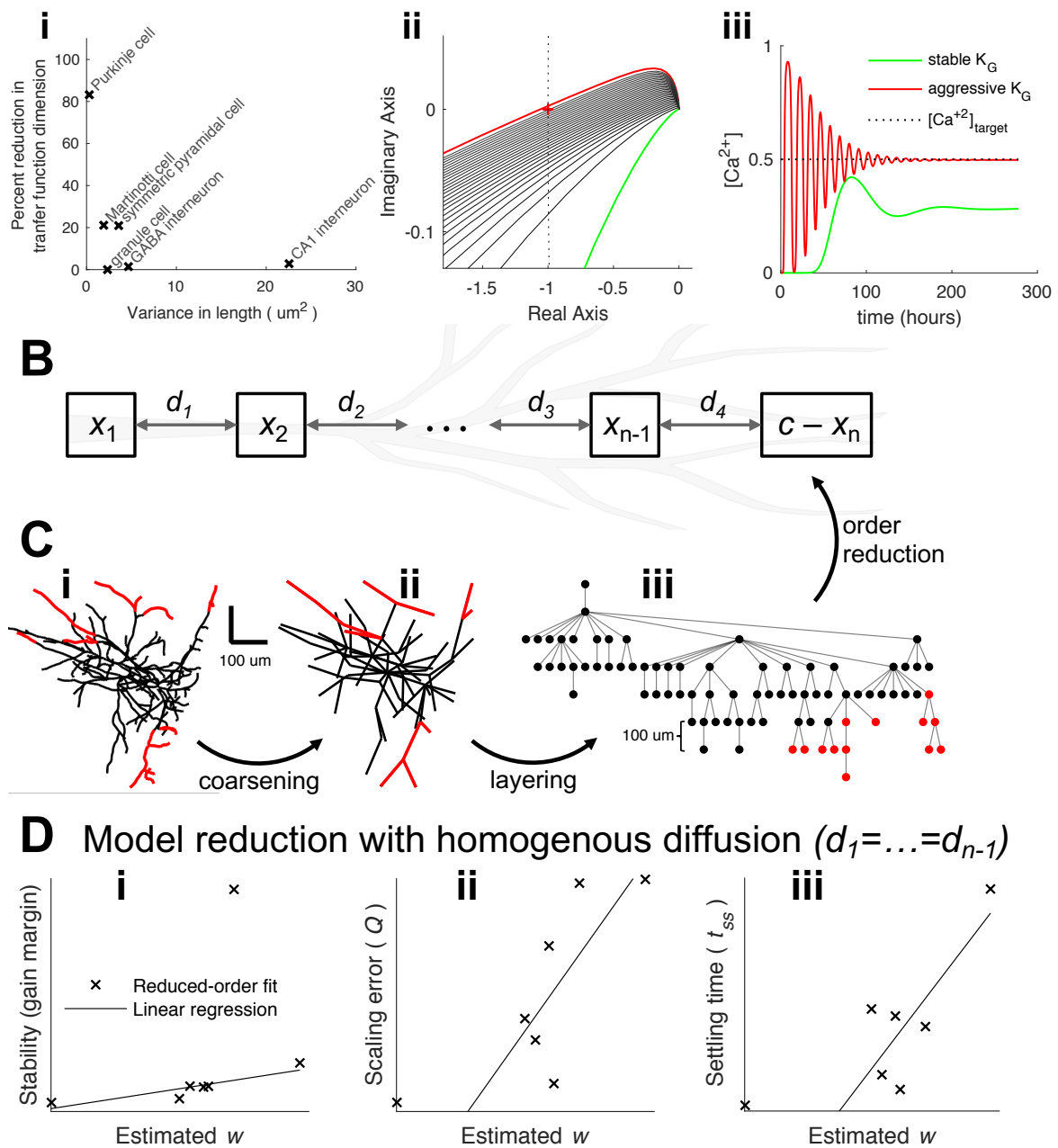


Fig. 6.11 Transfer functions and reduced-order models of neuron morphologies predict scaling performance. (A) Transfer function reductions producing equivalent line models can represent aggressiveness of synaptic scaling. Morphology symmetry, captured by neurite variances, strongly affects the number of observable states and transfer function reduction (i). A family of Nyquist plots in an equivalent line with varying K_G accurately predicts the response time for global regulation (ii-iii). (B): The generalized ball-stick representation has parameters for diffusion d , capacity c , number of compartments n , and degradation w . (C): Fitting to ball-stick models begins with a raw neuron morphology (i), which is coarsened to some discretization (ii), and then layered (iii) before constraining to parameters. (D): The estimated w from the ball-stick model best captures scaling performance, depicted with metrics for stability (i), scaling error (ii), and settling time (iii).

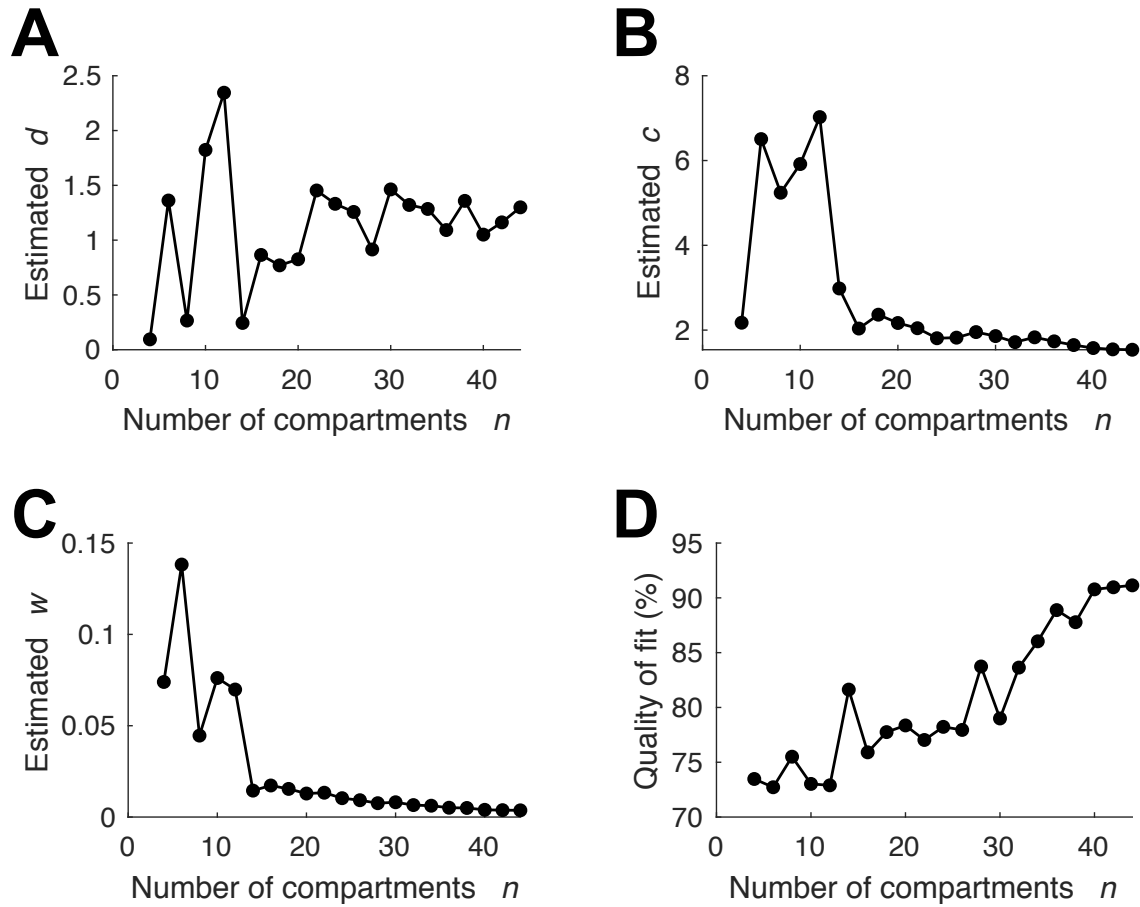


Fig. 6.12 Ball-stick parameters for Martinotti cell converge with increasing n (A-C). Quality of fit improves with increasing n (D).

Table 6.2 - Size and symmetry metrics of neuron morphologies. Total length is the sum longitudinal length of all dendrites and branches. The longest path of cargo transport is the max soma-tip distance. Branch order is the number of bifurcations to reach a dendrite tip. For each morphology, the number of tips n_1 and n_2 in each bifurcation $i = 1 \dots B$ is used to compute partition asymmetry as follows: Partition asymmetry = $\sum_{i=1}^B \left| \frac{n_1 - n_2}{n_1 + n_2 - 2} \right| / B$.

Cell type	Total length (μm)	Max soma-tip distance (μm)	Max branch order	Partition asymmetry	NeuroMorpho ID
CA1 interneuron	11819.2	1671.66	41	0.87	NMO_124538
granule cell	271.31	155.22	2	0	NMO_80458
L3 pyramidal, asymmetric	12422.1	1503.44	13	0.46	NMO_86997
L3 pyramidal, symmetric	8172.44	948.43	14	0.48	NMO_86957
Martinotti cell	8514.45	573.99	17	0.57	NMO_06140
Purkinje cell	6964.66	254.44	36	0.55	NMO_99860

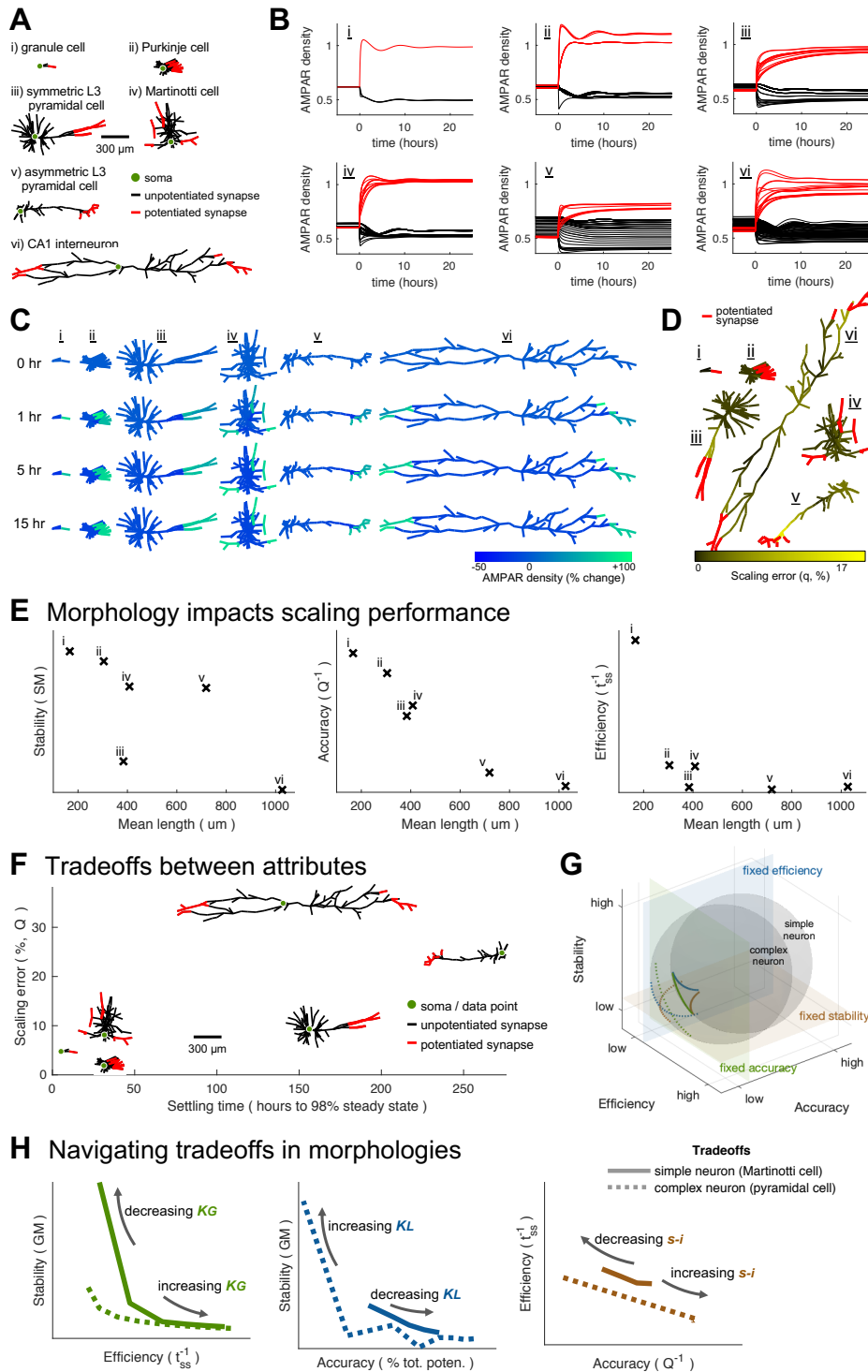


Fig. 6.13 Neuron size and symmetry significantly impact scaling performance. (A): Six distinct neuron structures with varying size and symmetry are examined. (B): Simulations of LTP results in stable simulations. (C): Synaptic scaling settles throughout each morphology, depicted at four time points. (D): Scaling error at steady state following LTP reveals increased error in distal compartments and bottleneck regions. (E): Mean length affects scaling performance (efficiency, accuracy, and stability). (F): Smaller, more symmetric morphologies have better scaling performance. (G): A conceptual depiction of the tradeoffs across all three attributes is navigated by varying free parameters K_G , K_L , and s_{-i} . Spheres represent scaling performance data for hypothetical simple and complex cells. 2D tradeoff plots are visualized by fixing one scaling attribute, as in (H). (H): Martinotti and pyramidal cells navigate the tradeoff between scaling attributes.

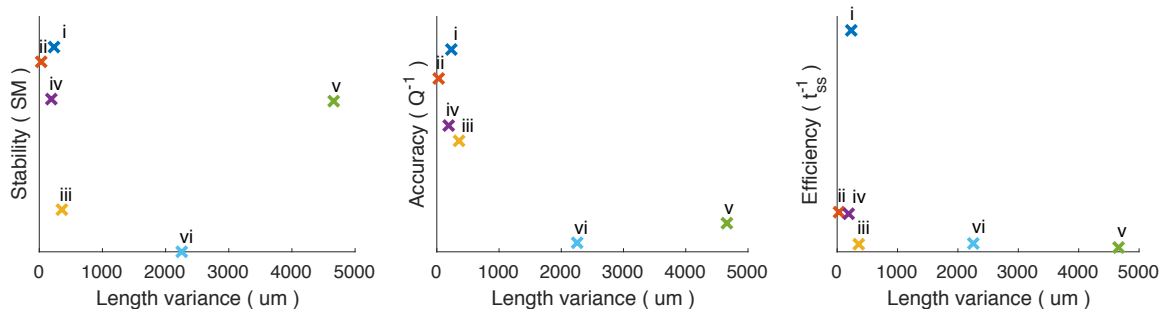


Fig. 6.14 Variance in neuron length (which corresponds to asymmetry) strongly correlates with scaling performance, depicted with stability, accuracy, and efficiency.

We first examine scaling performance across the spatial dimension. The progression of AMPAR distribution over time is depicted in Fig. 6.13C. Granule cells have small morphologies and settle within 1 hour (Fig. 6.13Ci). Martinotti and Purkinje cells are larger and fairly symmetric and settle within 5 hours (Fig. 6.13Cii,iv). The CA1 interneuron and pyramidal cells require up to 15 hours for complete synaptic scaling (Fig. 6.13Ciii,v,vi). This is likely a result of bottleneck effects, which cause transport delays and increased convergence time [247].

The scaling error for individual synaptic compartments (q , see Eq. 6.1) is depicted over each morphology in Fig. 6.13D. Regions of poor accuracy have high AMPAR demand or low cargo supply. This includes regions far from the AMPAR source (soma) and adjacent to potentiated synapses, evident in the pyramidal cells (Fig. 6.13Diii,v). High densities of bifurcations also increase scaling error, evident in the CA1 interneuron (Fig. 6.13Dvi). Bottleneck effects might also play a role in limiting AMPAR supply (Fig. 6.13Dv,vi).

We next consolidate measures of neuron morphology (from Table 6.2) to predict scaling performance. For each morphology, we average all soma-tip path lengths to estimate an effective neural mean length. In Fig. 6.13E, metrics of scaling performance are plotted against effective length. In general, cells with low effective lengths have improved scaling performance. Neurons with the highest effective length (the CA1 interneuron and asymmetric L3 pyramidal cell) have the lowest efficiency, accuracy, and stability. The variance in soma-tip lengths also correlates with scaling attributes (Fig. 6.14), which is consistent with observations and conclusions from toy neuron models (Fig. 6.8).

In Fig. 6.13F, K_G was tuned such that each morphology has a similar stability margin for a fair comparison of scaling efficiency and accuracy. All morphologies have a stability margin in the range $[0.2791, 0.344]$. Smaller neurons scale synapses with better performance. The settling times for all neurons vary significantly, with the granule cell reaching 98% of steady-state in under 5.5 hours, while large neurons like CA1 interneuron require 141 hours.

We lastly present a conceptual diagram of the tradeoffs across all three attributes (Fig. 6.13G). A neuron morphology undergoes synaptic scaling while varying free parameters K_G , K_L , and s_{-i} . By sweeping through these parameters, we create a density cloud of scaling performance, plotted as a sphere on 3D axes for stability, accuracy, and efficiency. Two such clouds are depicted for hypothetical simple and complex cells. The complex cell is expected to have poorer scaling stability, efficiency, and accuracy, and is thus closer to the origin. 2D tradeoff plots are visualized by fixing one scaling attribute, represented by a plane in Fig. 6.13G. Two neuron morphologies are compared within a fixed scaling attribute, as indicated by lines representing the intersection of spheres and planes. We perform such simulations for more simple (Martinotti) and complex (pyramidal) neurons in Fig. 6.13H. We simulate with varying K_G , K_L , and s_{-i} in Fig. 6.13H. In all three tradeoffs, the more complex (asymmetric) neuron—the pyramidal cell—has worse scaling performance. The trends here—negative relationships—match those obtained in a single-compartment model in Fig. 6.9.

6.11 Discussion

Our results here uncovered that intraneuronal distribution necessitates tradeoffs between stability, accuracy, and efficiency for transport performance. We study this balance in the context of synaptic scaling with transport of AMPA receptors, but these conclusions are generalizable to intracellular trafficking for other functions. We showed that global regulation, local regulation, and local internal cargo pools mediate between attributes of this tradeoff. We report numerous disadvantages for highly sensitive regulation, which might account for why we observed no immediate regulation of cargo trafficking in previous chapters (Sec. 3.6). Our results culminate with a demonstration of ion channel distribution and regulation in numerous neuron morphologies.

In this chapter, we again examined the regulation of cargo distribution. Neurons face the challenge of distributing millions of protein subunits throughout large and complex morphologies. Synaptic scaling is a highly relevant manifestation of protein distribution and regulation. Homeostatic synaptic scaling is critical for the function of neurons and therefore for higher cognitive functions including learning and memory. Dysfunction of homeostatic plasticity are increasingly revealed to be of importance in fields of biomedicine. For instance, deficits in synaptic scaling have been associated with age and onset of epileptic seizures [81]. Other forms of plasticity that are also activity-dependent, such as structural plasticity, have been analyzed in a similar framework [4].

Chapter 7

Summary and implications

This thesis concerns the distribution and regulation of ion channels in full neuron morphologies. We began with an overview of ion channels, cargo transport, and neuronal regulation (Chapter 1). We then established the experimental, analytical, and theoretical methods as well as validated preliminary results (Chapter 2). We next explored potassium channel Kv4.2 (Chapters 3-5), which was of particular interest given its distinct localization and expression profile. Although we thoroughly characterized Kv4.2 active transport (Chapter 3), diffusion (Chapter 5), and established a unified model of global transport (Chapter 4), we did not observe global regulation of this cargo. We therefore studied AMPA receptors in the context of synaptic scaling, a well-established phenomenon of neural homeostasis and regulation.

In this chapter, we summarize the principle findings from this dissertation. We further discuss the implications of the results, in the context of each individual chapter and of cellular/molecular biology (across cargo and neuron type).

7.1 Summary of contributions

This thesis sets forth a number of advances in neurobiology and physiology. Most evident are the substantial data sets and analyses of ion channel kinetics and neuronal dynamics. More important are the implications of these results in the broader context of neural function.

In Chapter 1, the relevant topics were introduced, with a literature review and overviews specific the subsequent results. Chapter 2 reiterates and verifies preliminary methods and results in pyramidal cells of hippocampal cultures. These early chapters guide the author and readers to a mutual understanding and appreciation of previous work and protocols in this field. They served to establish the premises and methodological competencies for the remaining chapters.

Chapter 3 introduced a sizable data set of neurite recordings from which numerous basic conclusions are revealed. Kv4.2 primarily localizes along the somatodendritic axis, with minimal but non-negligible static densities in axons. In pyramidal hippocampal cells, Kv4.2 is actively trafficked on microtubules in puncta, which are more prevalent in axons than in dendrites. Actively-trafficked Kv4.2 decreases in density with distance along the somatodendritic axis. This distribution of mobile density is the reverse of the static density. The results thus far motivate the differentiation of these two densities in compartmental modeling (as in Chapter 4). Analysis of trajectory kinetics revealed that transport in axons and dendrites not only differed quantitatively but also qualitatively. Axonal puncta are transported over greater distances with higher average velocity. Dendritic puncta stall for longer, whereas axonal puncta undergo longer unidirectional runs. The analysis of trajectory kinetics suggest distinct biophysical mechanisms in each neurite type (explored further in Chapter 4). Lastly, a negative result: the transport of Kv4.2 is not markedly perturbed with neural excitability (high KCl or AMPA stimulation) over short timescales. This finding, no global neuron regulation over minutes to hours, is later evaluated in Chapter 6.

Chapter 4 contains models of transport and delivery that reconcile the observed densities of static and mobile Kv4.2. Mass-action models with lumped and discretized neurites predict relative densities as observed in Chapter 3. The distinct somatodendritic static distribution of Kv4.2 is derived from mobile densities and velocities observed experimentally. The qualitative kinetic measures (displacement, velocity, stall time, superdiffusivity) between axons and dendrites also reflect the demand in axons and dendrites. However, we infer that these kinetic differences are not explained by cargo demand alone and that an additional inertial or propulsion mechanism likely differs between axons and dendrites. The results of this chapter prompt caution in the interpretation of mobile and static cargo densities in studies of neuron imaging and cargo distribution.

Chapter 5 focuses on the diffusive element of Kv4.2 transport. Using FRAP microscopy, the recovery rate and mobile fraction of Kv4.2 is estimated, from which the diffusion coefficient is derived. Drift is estimated by binning bleach recovery across the length of the dendrites, revealing a slight directional bias distal to the soma. Fluorescence recovery is then used to estimate rates between mobile and immobile fractions. Estimated rates are lastly simulated in a large neuron morphology, revealing settling times consistent with timescales of global regulation.

The results chapters thus far have concerned the distribution, transport, and delivery of Kv4.2. Experimental observations of global Kv4.2 *regulation*, however, were been unsuccessful. To study homeostasis, we shifted focus to AMPA receptors, which have well-established mechanisms of local and global regulation.

Chapter 6 accordingly focuses on AMPA receptors in the context of synaptic scaling. A model of AMPA receptor transport, activation, and regulation is developed, which replicates synaptic scaling. Tradeoffs between scaling attributes—efficiency, accuracy, and stability—are mediated by free parameters—global gain, local gain, and AMPAR pool size. These tradeoffs are consistent throughout an alternate system with scaling factor Arc as well as full neuron morphologies of varying size and symmetry. These results indicate that the neuron morphology itself imposes constraints on the quality of global homeostasis.

7.1.1 Active transit versus passive diffusion

Our results throughout this dissertation encourage the comparison of active versus passive transport in intraneuronal cargo distribution. Our data sets include measurements of both microtubule-based transit and diffusion for one specific cargo—Kv4.2. We also simulated biased and unbiased transport, corresponding to active and passive trafficking, with realistic rates in full neuron morphologies.

The resultant settling times for cargo distribution in pyramidal cells were on the order of days regardless of active versus passive transport. For instance, our results in Sec. 5.6 imply that distribution of cargo throughout a complex morphology with diffusion alone is sufficient to achieve settling times predicted for global regulation. Simulation of active AMPAR transport (Sec. 6.10) with velocities similar to those observed experimentally for Kv4.2 (Fig. 3.9) also produces similar settling times. What, then, is the role of active transport? From a systems-level perspective, the principle feature of active transport is that it provides directed localization. We hypothesize that active transport is suitable for targeted, local regulation of cargo. Passive diffusion broadly disseminates a cargo throughout an arbor (see Chapter 5 and [198]). Active transport, like insertion rates or activation rates, targets cargo to a specific location. These mechanisms are not well-elucidated in the biological literature, and our coarse-grained models do not capture them in detail.

7.1.2 Timescale of global versus local regulation

Chapter 6 explores the interplay between global and local mechanisms of neuronal regulation in the context of synaptic scaling. Global and local gains modulate the quality of synaptic scaling, a global-level homeostatic phenomena. The insights from our theoretical study of synaptic scaling can be extended to other homeostatic mechanisms involving other cargo types. Here, we discuss the interplay of global and local regulation for our other cargo of interest—Kv4.2.

Previous studies have observed local regulation of Kv4.2 with AMPA stimulation [118, 164]. An early motivation for this course of study was to replicate similar neuronal stimulation while observing longitudinal cargo transport. In Sec. 3.6, we found no evidence for activity-dependent regulation of active Kv4.2 transport within a short time frame after perturbation with KCl or AMPA. Why would neuronal stimulation impact local mechanisms as in previous studies [118, 164] but not affect active transport over a similar timescale?

We hypothesize that our results from Chapter 6 are directly relevant here. In our theoretical study of synaptic scaling, we found that fast global regulation of cargo can result in instabilities, particularly in large cells. The efficiency-stability tradeoff relates back to our measurements of Kv4.2. A change in active Kv4.2 transport, such as varying puncta frequency or kinetics, is a global phenomena. Global regulation of Kv4.2, like that of AMPA receptors, is limited by neuron size. We might expect global Kv4.2 regulation to occur over longer timescales of days to weeks, as has been observed for AMPA receptors (Chapter 6) and other ion channels [174, 178]. In conclusion, the same tradeoffs apply to any process that requires global signaling throughout a large and complex morphology where that signal might experience or induce significant time delays. Any such processes must be regulated slowly enough to avoid instability.

7.1.3 Implications for other cargoes and neuron types

Most of the main conclusions from the data, modeling, and theory in this dissertation have been relevant for large complex neurons. In general, the tradeoffs, time delays, and timescales for global regulation discussed here are exacerbated for larger cells and alleviated for smaller cells. In general, a transport network that strains the time delay between a global controller (here, ion channel production in soma) and the variable controlled (active ion channel throughout the arbor) can destabilize global regulation.

The same discussion can be extended to varying cargo type. The conclusions in this dissertation are most relevant for ion channels. For this discussion, we assume a constant demand and lifetime across all cargo types. Smaller cargo might diffuse more quickly or be packed more densely into membrane vesicles, both of which improve delivery, easing the tradeoffs and instabilities of global regulation. Larger cargoes, like organelles, might be trafficked more slowly and worsen the tradeoffs.

In summary, the general tradeoffs discussed in this thesis exist in all neurons and cargo types. However, the severity of the constraints and the degree of biophysically-relevant limitations for neuron physiology are largely dependent on cell size, symmetry, and complexity as well as cargo size, speed, and demand.

7.2 Closing remarks

At a basic level, the topic of ion channel distribution and regulation in neurons involves individual observations of fundamental transport mechanisms. This topic also extends to broad, lumped phenomena and coarse-grained models. The results presented in this thesis examine cargo distribution across these multiple levels of granularity. We discussed the interplay between these types of analyses and their implications for progress in this field.

Throughout the results, we have made physical observations of protein transport. We monitored actively transported ion channels on microtubules (Chapter 3), localization densities of subunits (Chapter 3), and passive dissemination through diffusion (Chapter 5). These experimental observations were focused measurements of singular phenomena, as traditionally studied in molecular and cellular biology. These investigations produced numerous findings, some of which were unexpected from the narrow perspective of those experiments alone.

Those basic experiments also produced some unexpected results, such as discordant distributions of static and transported cargo. In order to explain these findings, we adopted a broader perspective of cargo distribution and regulation. The systems-level viewpoint comprises several molecular- and cellular-level phenomena. With comprehensive, coarse-grained models, we reconcile these seemingly paradoxical results with our current understanding of intracellular distribution (Chapter 4). The combination of microscopic measurements with coarse-grained modeling allows us to draw conclusions that are not apparent from either experimental or theoretical studies alone.

In this thesis, we selected a cargo—ion channel Kv4.2—with a known function, a specific intraneurite distribution, high neurite polarity, and available tools for intracellular tracking. The individual measurements of ion channel localization, passive diffusion, and microtubule-based transport were novel and interesting on their own (Chapters 3 and 5). However, we drew greater insight by incorporating these results into detailed biophysical models of trafficking and global frameworks of cargo distribution (Chapter 4). Both coarse-grained models and precise physical measurements are necessary for explaining how the unique Kv4.2 gradient arises or inferring whether cargo sequestration determines transport kinetics. Data-driven, coarse-grained modeling answers questions that neither data nor modeling can address alone.

We lastly extended this philosophy to study a crucial manifestation of ion channel distribution and regulation: synaptic scaling (Chapter 6). These models are again based in physical measurements, using data from other studies. With a global framework of intraneuronal distribution (now, of AMPA receptors), we replicate synaptic scaling in realistic morphologies and infer the major limitations imposed by large and complex cells. The stability, efficiency, and accuracy of synaptic scaling must be balanced—no attribute can

be improved without worsening the others. Scaling performance is inherently limited by the morphology of cells. These results are therefore generalizable to other phenomena involving global cargo trafficking. This extends to other forms of neuronal plasticity, such as modulation of intrinsic excitability by regulation of voltage-gated ion channels.

In closing, these results address the logistical challenges of continuous and regulated cargo delivery throughout large and complex neurons. Quantitative measurements of ion channel Kv4.2 reveal distribution profiles of delivered cargo and cargo in transit, including the kinetics of microtubule-based and diffusive motion. Coarse-grained models of subunit transport, delivery, and regulation reconcile these distributions for Kv4.2 and provide insight on the limitations of intraneuronal distribution of AMPA receptors.

References

- [1] Abbott, L. F. (1999). Lapicque's introduction of the integrate-and-fire model neuron (1907). *Brain research bulletin*, 50(5-6):303–304.
- [2] Al-Rodhan, N. R. and Fox, J. L. (1986). Al-zahrawi and arabian neurosurgery, 936–1013 ad. *Surgical neurology*, 26(1):92–95.
- [3] Alfaro-Ruíz, R., Aguado, C., Martín-Belmonte, A., Moreno-Martínez, A. E., and Luján, R. (2019). Expression, Cellular and Subcellular Localisation of Kv4.2 and Kv4.3 Channels in the Rodent Hippocampus. *International Journal of Molecular Sciences*, 20(2):246.
- [4] Aljaberi, S., O'Leary, T., and Forni, F. (2020). Dendritic trafficking: synaptic scaling and structural plasticity. *arXiv preprint arXiv:2011.12067*.
- [5] Aljaberi, S., O'Leary, T., and Forni, F. (2019). Qualitative behavior and robustness of dendritic trafficking. In *2019 IEEE 58th Conference on Decision and Control (CDC)*, pages 6628–6633. IEEE.
- [6] Allen, R. D., Metzals, J., Tasaki, I., Brady, S. T., and Gilbert, S. P. (1982). Fast axonal transport in squid giant axon. *Science*, 218(4577):1127–1129.
- [7] Andrei, N. (2006). Modern control theory. *Studies in Informatics and Control*, 15(1):51.
- [8] Andreu, J. M. and Timasheff, S. N. (1982). Tubulin bound to colchicine forms polymers different from microtubules. *Proceedings of the National Academy of Sciences of the United States of America*, 79(22 D):6753–6756.
- [9] Axelrod, D., Koppel, D., Schlessinger, J., Elson, E., and Webb, W. W. (1976). Mobility measurement by analysis of fluorescence photobleaching recovery kinetics. *Biophysical journal*, 16(9):1055.
- [10] Barcroft, J. (1934). Some forms of apparatus for the equilibration of blood. *The Journal of physiology*, 80(4):388.
- [11] Barcroft, J. (2015). *Features in the architecture of physiological function*. Cambridge University Press.
- [12] Bear, M., Connors, B., and Paradiso, M. A. (2020). *Neuroscience: Exploring the brain*. Jones & Bartlett Learning, LLC.
- [13] Bear, M. F. and Malenka, R. C. (1994). Synaptic plasticity: Ltp and ltd. *Current opinion in neurobiology*, 4(3):389–399.

- [14] Benavides-Piccione, R., Regalado-Reyes, M., Fernaud-Espinosa, I., Kastanauskaite, A., Tapia-González, S., León-Espinosa, G., Rojo, C., Insausti, R., Segev, I., and DeFelipe, J. (2020). Differential structure of hippocampal ca1 pyramidal neurons in the human and mouse. *Cerebral Cortex*, 30(2):730–752.
- [15] Berezhkovskii, A. M., Dagdug, L., and Bezrukov, S. M. (2019). Exact solutions for distributions of first-passage, direct-transit, and looping times in symmetric cusp potential barriers and wells. *The Journal of Physical Chemistry B*, 123(17):3786–3796.
- [16] Bernard, C., Anderson, A., Becker, A., Poolos, N. P., Beck, H., and Johnston, D. (2004). Acquired dendritic channelopathy in temporal lobe epilepsy. *Science*, 305(5683):532–535.
- [17] Blobel, G. (2000). Protein targeting (nobel lecture). *Chembiochem*, 1(2):86–102.
- [18] Bock, O. (2013). Cajal, golgi, nansen, schäfer and the neuron doctrine. *Endeavour*, 37(4):228–234.
- [19] Boncompain, G., Divoux, S., Gareil, N., De Forges, H., Lescure, A., Latreche, L., Mercanti, V., Jollivet, F., Raposo, G., and Perez, F. (2012). Synchronization of secretory protein traffic in populations of cells. *Nature methods*, 9(5):493–498.
- [20] Bower, J. and Beeman, D. (1995). The book of genesis. telos, the electronic library of science.
- [21] Branco, T. and Staras, K. (2009). The probability of neurotransmitter release: variability and feedback control at single synapses. *Nature Reviews Neuroscience*, 10(5):373–383.
- [22] Bressloff, P. C. (2014). *Stochastic processes in cell biology*, volume 41. Springer.
- [23] Bressloff, P. C. and Levien, E. (2015). Synaptic democracy and vesicular transport in axons. *Physical review letters*, 114(16):168101.
- [24] Brickley, S. G., Revilla, V., Cull-Candy, S. G., Wisden, W., and Farrant, M. (2001). Adaptive regulation of neuronal excitability by a voltage-independent potassium conductance. *Nature*, 409(6816):88–92.
- [25] Brookes, M. (2006). Voicebox: Speech processing toolbox for matlab {Online}. A vailable: <http://www.ee.imperial.ac.uk/hp/staff/dmb/voicebox/voicebox.html>.
- [26] Brown, T. H., Kairiss, E. W., and Keenan, C. L. (1990). Hebbian synapses: biophysical mechanisms and algorithms. *Annual review of neuroscience*, 13(1):475–511.
- [27] Butz, M., Wörgötter, F., and van Ooyen, A. (2009). Activity-dependent structural plasticity. *Brain research reviews*, 60(2):287–305.
- [28] Buxbaum, A. R., Haimovich, G., and Singer, R. H. (2015a). In the right place at the right time: visualizing and understanding mrna localization. *Nature reviews Molecular cell biology*, 16(2):95–109.
- [29] Buxbaum, A. R., Yoon, Y. J., Singer, R. H., and Park, H. Y. (2015b). Single-molecule insights into mrna dynamics in neurons. *Trends in cell biology*, 25(8):468–475.

- [30] Cai, X., Liang, C. W., Muralidharan, S., Kao, J. P. Y., Tang, C. M., and Thompson, S. M. (2004). Unique roles of SK and Kv4.2 potassium channels in dendritic integration. *Neuron*, 44(2):351–364.
- [31] Cajigas, I. J., Tushev, G., Will, T. J., Tom Dieck, S., Fuerst, N., and Schuman, E. M. (2012). The Local Transcriptome in the Synaptic Neuropil Revealed by Deep Sequencing and High-Resolution Imaging. *Neuron*, 74(3):453–466.
- [32] Cannon, W. B. (1932). Homeostasis. *The wisdom of the body*. Norton, Newyork.
- [33] Cannon, W. B. (1939). The wisdom of the body.
- [34] Canny, J. (1986). A computational approach to edge detection. *IEEE Transactions on pattern analysis and machine intelligence*, (6):679–698.
- [35] Carnevale, N. T. and Hines, M. L. (2006). *The NEURON book*. Cambridge University Press.
- [36] Caroni, P., Donato, F., and Muller, D. (2012). Structural plasticity upon learning: regulation and functions. *Nature Reviews Neuroscience*, 13(7):478–490.
- [37] Caspi, A., Granek, R., and Elbaum, M. (2000). Enhanced Diffusion in Active Intracellular Transport. *Physical Review Letters*, 85(26):5655–5658.
- [38] Caspi, A., Granek, R., and Elbaum, M. (2002). Diffusion and directed motion in cellular transport. *Physical Review E - Statistical Physics, Plasmas, Fluids, and Related Interdisciplinary Topics*, 66(1).
- [39] Chandrasekhar, S. (1943). Stochastic problems in physics and astronomy. *Reviews of modern physics*, 15(1):1.
- [40] Chaphalkar, A. R., Jain, K., Gangan, M. S., and Athale, C. A. (2016). Automated multi-peak tracking kymography (amtrak): a tool to quantify sub-cellular dynamics with sub-pixel accuracy. *PloS one*, 11(12):e0167620.
- [41] Chater, T. E. and Goda, Y. (2014). The role of ampa receptors in postsynaptic mechanisms of synaptic plasticity. *Frontiers in cellular neuroscience*, 8:401.
- [42] Chen, J.-Y., Lonjers, P., Lee, C., Chistiakova, M., Volgushev, M., and Bazhenov, M. (2013). Heterosynaptic plasticity prevents runaway synaptic dynamics. *Journal of Neuroscience*, 33(40):15915–15929.
- [43] Chen, X., Yuan, L.-L., Zhao, C., Birnbaum, S. G., Frick, A., Jung, W. E., Schwarz, T. L., Sweatt, J. D., and Johnston, D. (2006). Deletion of Kv4.2 Gene Eliminates Dendritic A-Type K⁺ Current and Enhances Induction of Long-Term Potentiation in Hippocampal CA1 Pyramidal Neurons. *Journal of Neuroscience*, 26(47):12143–12151.
- [44] Chimileski, S. and Kolter, R. (2017). *Life at the Edge of Sight: A Photographic Exploration of the Microbial World*. Harvard University Press.
- [45] Chistiakova, M., Bannon, N. M., Chen, J.-Y., Bazhenov, M., and Volgushev, M. (2015). Homeostatic role of heterosynaptic plasticity: models and experiments. *Frontiers in computational neuroscience*, 9:89.

- [46] Choi, S. C. and Wette, R. (1969). Maximum likelihood estimation of the parameters of the gamma distribution and their bias. *Technometrics*, 11(4):683–690.
- [47] Chowdhury, S., Shepherd, J. D., Okuno, H., Lyford, G., Petralia, R. S., Plath, N., Kuhl, D., Huganir, R. L., and Worley, P. F. (2006). Arc/arg3.1 interacts with the endocytic machinery to regulate ampa receptor trafficking. *Neuron*, 52(3):445–459.
- [48] Chu, N. (2006). Centennial of the nobel prize for golgi and cajal-founding of modern neuroscience and irony of discovery. *Acta Neurologica Taiwanica*, 15(3):217.
- [49] Chu, P. J., Rivera, J. F., and Arnold, D. B. (2006). A role for Kif17 in transport of Kv4.2. *Journal of Biological Chemistry*, 281(1):365–373.
- [50] Cimino, G. (1999). Reticular theory versus neuron theory in the work of camillo golgi.
- [51] Cobb, M. (2017). 60 years ago, francis crick changed the logic of biology. *PLoS biology*, 15(9).
- [52] Colbert, C. M. and Pan, E. (2002). Ion channel properties underlying axonal action potential initiation in pyramidal neurons. *Nature Neuroscience*, 5(6):533–538.
- [53] Cole, K. S. and Baker, R. F. (1941). Longitudinal impedance of the squid giant axon. *The Journal of general physiology*, 24(6):771–788.
- [54] Cole, K. S. and Curtis, H. J. (1939). Electric impedance of the squid giant axon during activity. *The Journal of general physiology*, 22(5):649–670.
- [55] Cooper, G. M. and Hausman, R. E. (2004). *The cell: Molecular approach*. Medicinska naklada.
- [56] Cope, Z. (1967). Joseph lister, 1827-1912. *British medical journal*, 2(5543):7.
- [57] Cuntz, H., Forstner, F., Borst, A., and Häusser, M. (2010). One rule to grow them all: a general theory of neuronal branching and its practical application. *PLoS Comput Biol*, 6(8):e1000877.
- [58] Dayan, P. and Abbott, L. F. (2001). Theoretical neuroscience: computational and mathematical modeling of neural systems.
- [59] Debanne, D., Campanac, E., Bialowas, A., Carrier, E., and Alcaraz, G. (2011). Axon physiology. *Physiological reviews*, 91(2):555–602.
- [60] Desai, N. S., Rutherford, L. C., and Turrigiano, G. G. (1999). Plasticity in the intrinsic excitability of cortical pyramidal neurons. *Nature Neuroscience*, 2(6):515–520.
- [61] Doyle, M. and Kiebler, M. A. (2011a). Mechanisms of dendritic mrna transport and its role in synaptic tagging. *The EMBO journal*, 30(17):3540–3552.
- [62] Doyle, M. and Kiebler, M. A. (2011b). Mechanisms of dendritic mrna transport and its role in synaptic tagging. *The EMBO journal*, 30(17):3540–3552.

- [63] Duméniéu, M., Oulé, M., Kreutz, M. R., and Lopez-Rojas, J. (2017). The Segregated Expression of Voltage-Gated Potassium and Sodium Channels in Neuronal Membranes: Functional Implications and Regulatory Mechanisms. *Frontiers in Cellular Neuroscience*, 11:115.
- [64] Earnshaw, B. A. and Bressloff, P. C. (2006). Biophysical model of ampa receptor trafficking and its regulation during long-term potentiation/long-term depression. *Journal of Neuroscience*, 26(47):12362–12373.
- [65] Eden, E., Geva-Zatorsky, N., Issaeva, I., Cohen, A., Dekel, E., Danon, T., Cohen, L., Mayo, A., and Alon, U. (2011). Proteome half-life dynamics in living human cells. *Science (New York, N.Y.)*, 331(6018):764–8.
- [66] Einstein, A. (1905). Über die von der molekularkinetischen theorie der wärme geforderte bewegung von in ruhenden flüssigkeiten suspendierten teilchen. *Annalen der physik*, 4.
- [67] Feffer, S. M. (1996). ernst abbe, carl zeiss, and the transformation of microscopical optics. In *Scientific Credibility and Technical Standards in 19th and early 20th century Germany and Britain*, pages 23–66. Springer.
- [68] Fernández Cara, E. and Zuazua Iriondo, E. (2003). Control theory: History, mathematical achievements and perspectives. *Boletín de la Sociedad Española de Matemática Aplicada*, 26, 79-140.
- [69] Fick, A. (1855). Ueber diffusion. *Annalen der Physik*, 170(1):59–86.
- [70] Finger, S. (2001). *Origins of neuroscience: a history of explorations into brain function*. Oxford University Press, USA.
- [71] Fink, B. R., Byers, M. R., and Middaugh, M. E. (1973). Dynamics of colchicine effects on rapid axonal transport and axonal morphology. *Brain Research*, 56(C):299–311.
- [72] Finkelstein, G. (2013). *Emil du Bois-Reymond: neuroscience, self, and society in nineteenth-century Germany*. MIT Press.
- [73] Fisher, M. E. and Kolomeisky, A. B. (1999). The force exerted by a molecular motor. *Proceedings of the National Academy of Sciences*, 96(12):6597–6602.
- [74] Fisher, M. E. and Kolomeisky, A. B. (2001). Simple mechanochemistry describes the dynamics of kinesin molecules. *Proceedings of the National Academy of Sciences*, 98(14):7748–7753.
- [75] Fossati, G., Morini, R., Corradini, I., Antonucci, F., Trepte, P., Edry, E., Sharma, V., Papale, A., Pozzi, D., Defilippi, P., et al. (2015). Reduced snap-25 increases psd-95 mobility and impairs spine morphogenesis. *Cell Death & Differentiation*, 22(9):1425–1436.
- [76] Frick, A. and Johnston, D. (2005). Plasticity of dendritic excitability.
- [77] García-López, V., Chen, F., Nilewski, L. G., Duret, G., Aliyan, A., Kolomeisky, A. B., Robinson, J. T., Wang, G., Pal, R., and Tour, J. M. (2017). Molecular machines open cell membranes. *Nature*, 548(7669):567–572.

- [78] Gasselin, C., Inglebert, Y., and Debanne, D. (2015). Homeostatic regulation of h-conductance controls intrinsic excitability and stabilizes the threshold for synaptic modification in CA1 neurons. *Journal of Physiology*, 593(22):4855–4869.
- [79] Gest, H. (2004). The discovery of microorganisms by robert hooke and antoni van leeuwenhoek, fellows of the royal society. *Notes and records of the Royal Society of London*, 58(2):187–201.
- [80] Glock, C., Heumüller, M., and Schuman, E. M. (2017). mRNA transport & local translation in neurons. *Current Opinion in Neurobiology*, 45:169–177.
- [81] González, O. C., Krishnan, G. P., Chauvette, S., Timofeev, I., Sejnowski, T., and Bazhenov, M. (2015). Modeling of age-dependent epileptogenesis by differential homeostatic synaptic scaling. *Journal of Neuroscience*, 35(39):13448–13462.
- [82] Gross, C., Yao, X., Pong, D. L., Jeromin, A., and Bassell, G. J. (2011). Fragile x mental retardation protein regulates protein expression and mrna translation of the potassium channel kv4. 2. *Journal of Neuroscience*, 31(15):5693–5698.
- [83] Gross, C. G. (1987). Neuroscience, early history of. *Journal of Encyclopedia of Neuroscience* pp. 843, 847.
- [84] Guglielmi, L., Servettini, I., Caramia, M., Catacuzzeno, L., Franciolini, F., D’Adamo, M. C., and Pessia, M. (2015). Update on the implication of potassium channels in autism: K+ channelautism spectrum disorder. *Frontiers in cellular neuroscience*, 9:34.
- [85] Guo, W., Kamiya, K., and Toyama, J. (1997). Differential effects of chronic membrane depolarization on the k+ channel activities in cultured rat ventricular cells. *Cardiovascular research*, 33(1):139–146.
- [86] Hahn, G. J. and Shapiro, S. S. (1967). Statistical models in engineering. Technical report.
- [87] Hall, A. M., Throesch, B. T., Buckingham, S. C., Markwardt, S. J., Peng, Y., Wang, Q., Hoffman, D. A., and Roberson, E. D. (2015). Tau-dependent kv4. 2 depletion and dendritic hyperexcitability in a mouse model of alzheimer’s disease. *Journal of Neuroscience*, 35(15):6221–6230.
- [88] Hammond, R. S., Lin, L., Sidorov, M. S., Wikenheiser, A. M., and Hoffman, D. A. (2008). Protein Kinase A Mediates Activity-Dependent Kv4.2 Channel Trafficking. *Journal of Neuroscience*, 28(30):7513–7519.
- [89] Han, W., Li, J., Pelkey, K. A., Pandey, S., Chen, X., Wang, Y. X., Wu, K., Ge, L., Li, T., Castellano, D., Liu, C., Wu, L. G., Petralia, R. S., Lynch, J. W., McBain, C. J., and Lu, W. (2019). Shisa7 is a GABAA receptor auxiliary subunit controlling benzodiazepine actions. *Science*, 366(6462):246–250.
- [90] Hancock, W. O. (2014). Bidirectional cargo transport: moving beyond tug of war. *Nature reviews Molecular cell biology*, 15(9):615–628.
- [91] Harris, K. M. (1999). Calcium from internal stores modifies dendritic spine shape. *Proceedings of the National Academy of Sciences*, 96(22):12213–12215.

- [92] Häusser, M. (2001). Synaptic function: dendritic democracy. *Current Biology*, 11(1):R10–R12.
- [93] Hebb, D. O. (1949). *The organization of behavior: a neuropsychological theory*. J. Wiley; Chapman & Hall.
- [94] Hehny, H. and Stamnes, M. (2007). Regulating cytoskeleton-based vesicle motility. *FEBS letters*, 581(11):2112–2118.
- [95] Henley, J. M. and Wilkinson, K. A. (2016). Synaptic ampa receptor composition in development, plasticity and disease. *Nature Reviews Neuroscience*, 17(6):337–350.
- [96] Ho, B., Baryshnikova, A., and Brown, G. W. (2018). Unification of protein abundance datasets yields a quantitative *saccharomyces cerevisiae* proteome. *Cell systems*, 6(2):192–205.
- [97] Ho, V. M., Lee, J.-A., and Martin, K. C. (2011). The cell biology of synaptic plasticity. *Science*, 334(6056):623–628.
- [98] Hodgkin, A. L. and Huxley, A. F. (1952a). The components of membrane conductance in the giant axon of loligo. *The Journal of physiology*, 116(4):473–496.
- [99] Hodgkin, A. L. and Huxley, A. F. (1952b). Currents carried by sodium and potassium ions through the membrane of the giant axon of loligo. *The Journal of physiology*, 116(4):449–472.
- [100] Hodgkin, A. L. and Huxley, A. F. (1952c). The dual effect of membrane potential on sodium conductance in the giant axon of loligo. *The Journal of physiology*, 116(4):497–506.
- [101] Hodgkin, A. L. and Huxley, A. F. (1952d). A quantitative description of membrane current and its application to conduction and excitation in nerve. *The Journal of physiology*, 117(4):500–544.
- [102] Hodgkin, A. L., Huxley, A. F., and Katz, B. (1952). Measurement of current-voltage relations in the membrane of the giant axon of loligo. *The Journal of physiology*, 116(4):424–448.
- [103] Hodgkin, A. L. and Katz, B. (1949). The effect of sodium ions on the electrical activity of the giant axon of the squid. *The Journal of physiology*, 108(1):37–77.
- [104] Höfflin, F., Jack, A., Riedel, C., Mack-Bucher, J., Roos, J., Corcelli, C., Schultz, C., Wahle, P., and Engelhardt, M. (2017). Heterogeneity of the axon initial segment in interneurons and pyramidal cells of rodent visual cortex. *Frontiers in Cellular Neuroscience*, 11:332.
- [105] Hoffman, D. A., Johnston, D., Koester, H., Migliore, M., Johnston, D., Jung, W. E., Schwarz, T. L., Sweatt, J. D., and Johnston, D. (1998). Downregulation of transient K⁺ channels in dendrites of hippocampal CA1 pyramidal neurons by activation of PKA and PKC. *The Journal of neuroscience : the official journal of the Society for Neuroscience*, 18(10):3521–8.

- [106] Hoffman, D. A., Magee, J. C., Colbert, C. M., and Johnston, D. (1997). K⁺ channel regulation of signal propagation in dendrites of hippocampal pyramidal neurons. *Nature*, 387(6636):869–875.
- [107] Holt, C. E. and Schuman, E. M. (2013). The central dogma decentralized: New perspectives on RNA function and local translation in neurons.
- [108] Hooven, F. J. (1978). The wright brothers' flight-control system. *Scientific American*, 239(5):166–185.
- [109] Jacobson, K., Sheets, E. D., and Simson, R. (1995). Revisiting the fluid mosaic model of membranes. *Science*, 268(5216):1441–1443.
- [110] Jakobs, M. A., Dimitracopoulos, A., and Franze, K. (2019). Kymobutler, a deep learning software for automated kymograph analysis. *Elife*, 8:e42288.
- [111] Jensen, C. S. and Misonou, H. (2014). Live-cell Imaging of Post-Golgi Transport Vesicles in Cultured Hippocampal Neurons. *Cellular and Molecular Neurobiology*, 35(1):123–135.
- [112] Jensen, C. S., Watanabe, S., Rasmussen, H. B., Schmitt, N., Olesen, S.-P., Frost, N. A., Blanpied, T. A., and Misonou, H. (2014). Specific sorting and post-Golgi trafficking of dendritic potassium channels in living neurons. *The Journal of biological chemistry*, 289(15):10566–81.
- [113] Jin, E. J., Kiral, F. R., and Hiesinger, P. R. (2018). The where, what, and when of membrane protein degradation in neurons. *Developmental neurobiology*, 78(3):283–297.
- [114] Johnston, D., Hoffman, D. A., Magee, J. C., Poolos, N. P., Watanabe, S., Colbert, C. M., and Migliore, M. (2000). Topical Review Dendritic potassium channels in hippocampal pyramidal neurons. *J Physiol*, 525(1):75–81.
- [115] Kapitein, L. C. and Hoogenraad, C. C. (2011). Which way to go? Cytoskeletal organization and polarized transport in neurons. *Molecular and Cellular Neuroscience*, 46(1):9–20.
- [116] Kapitein, L. C., Schlager, M. A., Kuijpers, M., Wulf, P. S., van Spronsen, M., MacKintosh, F. C., and Hoogenraad, C. C. (2010). Mixed Microtubules Steer Dynein-Driven Cargo Transport into Dendrites. *Current Biology*, 20(4):290–299.
- [117] Kerti, K., Lorincz, A., and Nusser, Z. (2012). Unique somato-dendritic distribution pattern of Kv4.2 channels on hippocampal CA1 pyramidal cells. *European Journal of Neuroscience*, 35(1):66–75.
- [118] Kim, J., Jung, S. C., Clemens, A. M., Petralia, R. S., and Hoffman, D. A. (2007). Regulation of Dendritic Excitability by Activity-Dependent Trafficking of the A-Type K⁺ Channel Subunit Kv4.2 in Hippocampal Neurons. *Neuron*, 54(6):933–947.
- [119] Kim, J., Wei, D. S., and Hoffman, D. A. (2005). Kv4 potassium channel subunits control action potential repolarization and frequency-dependent broadening in rat hippocampal CA1 pyramidal neurons. *Journal of Physiology*, 569(1):41–57.

- [120] Koch, C. (1984). Cable theory in neurons with active, linearized membranes. *Biological cybernetics*, 50(1):15–33.
- [121] Koch, G., Ponzo, V., Di Lorenzo, F., Caltagirone, C., and Veniero, D. (2013). Hebbian and anti-hebbian spike-timing-dependent plasticity of human cortico-cortical connections. *Journal of Neuroscience*, 33(23):9725–9733.
- [122] Kolomeisky, A. B. and Fisher, M. E. (2007). Molecular motors: a theorist’s perspective. *Annu. Rev. Phys. Chem.*, 58:675–695.
- [123] Kremers, G. J., Goedhart, J., Van Den Heuvel, D. J., Gerritsen, H. C., and Gadella, T. W. (2007). Improved green and blue fluorescent proteins for expression in bacteria and mammalian cells. *Biochemistry*, 46(12):3775–3783.
- [124] Kreutzberg, G. W. (1969). Neuronal dynamics and axonal flow. IV. Blockage of intra-axonal enzyme transport by colchicine. *Proceedings of the National Academy of Sciences of the United States of America*, 62(3):722–728.
- [125] Kullmann, D. M. and Lamsa, K. P. (2007). Long-term synaptic plasticity in hippocampal interneurons. *Nature Reviews Neuroscience*, 8(9):687–699.
- [126] Kuznetsov, A. V. (2014). Sorting of cargos between axons and dendrites: modelling of differences in cargo transport in these two types of neurites. *Computer Methods in Biomechanics and Biomedical Engineering*, 17(7):792–799.
- [127] Lai, H. C. and Jan, L. Y. (2006). The distribution and targeting of neuronal voltage-gated ion channels. *Nature Reviews Neuroscience*, 7(7):548–562.
- [128] Lamprecht, R. and LeDoux, J. (2004). Structural plasticity and memory. *Nature Reviews Neuroscience*, 5(1):45–54.
- [129] Lapique, L. (1907). Recherches quantitatives sur l’excitation électrique des nerfs traitée comme une polarisation. *Journal de Physiologie et de Pathologie Generalej*, 9:620–635.
- [130] Laplace, P. S. (1820). *Théorie analytique des probabilités*. Courcier.
- [131] Lee, H.-K. and Kirkwood, A. (2011). Ampa receptor regulation during synaptic plasticity in hippocampus and neocortex. In *Seminars in cell & developmental biology*, volume 22, pages 514–520. Elsevier.
- [132] Levenberg, K. (1944). A method for the solution of certain non-linear problems in least squares. *Quarterly of Applied Mathematics*, 2(2):164–168.
- [133] Lewis, T. L., Mao, T., Svoboda, K., and Arnold, D. B. (2009). Myosin-dependent targeting of transmembrane proteins to neuronal dendrites. *Nature Neuroscience*, 12(5):568–576.
- [134] Lin, L., Long, L. K., Hatch, M. M., and Hoffman, D. A. (2014). DPP6 domains responsible for its localization and function. *Journal of Biological Chemistry*, 289(46):32153–32165.

- [135] Lin, L., Murphy, J. G., Karlsson, R. M., Petralia, R. S., Gutzmann, J. J., Abebe, D., Wang, Y. X., Cameron, H. A., and Hoffman, D. A. (2018). DPP6 loss impacts hippocampal synaptic development and induces behavioral impairments in recognition, learning and memory. *Frontiers in Cellular Neuroscience*, 12.
- [136] Lin, L., Sun, W., Throesch, B., Kung, F., Decoster, J. T., Berner, C. J., Cheney, R. E., Rudy, B., and Hoffman, D. A. (2013). DPP6 regulation of dendritic morphogenesis impacts hippocampal synaptic development. *Nature communications*, 4:2270.
- [137] Liu, L., Wong, T. P., Pozza, M. F., Lingenhoehl, K., Wang, Y., Sheng, M., Auberson, Y. P., and Wang, Y. T. (2004). Role of nmda receptor subtypes in governing the direction of hippocampal synaptic plasticity. *Science*, 304(5673):1021–1024.
- [138] Lodish, H., Berk, A., Zipursky, S. L., Matsudaira, P., Baltimore, D., and Darnell, J. (2000a). Kinesin, Dynein, and Intracellular Transport.
- [139] Lodish, H., Berk, A., Zipursky, S. L., Matsudaira, P., Baltimore, D., and Darnell, J. (2000b). Molecular cell biology 4th edition. *National Center for Biotechnology Information, Bookshelf*, 9.
- [140] López-Muñoz, F., Boya, J., and Alamo, C. (2006). Neuron theory, the cornerstone of neuroscience, on the centenary of the nobel prize award to santiago ramón y cajal. *Brain research bulletin*, 70(4-6):391–405.
- [141] MacKinnon, R., Cohen, S. L., Kuo, A., Lee, A., and Chait, B. T. (1998). Structural conservation in prokaryotic and eukaryotic potassium channels. *Science*, 280(5360):106–109.
- [142] Maday, S., Twelvetrees, A. E., Moughamian, A. J., and Holzbaur, E. L. (2014). Axonal Transport: Cargo-Specific Mechanisms of Motility and Regulation. *Neuron*, 84(2):292–309.
- [143] Maffie, J. and Rudy, B. (2008). Weighing the evidence for a ternary protein complex mediating A-type K⁺ currents in neurons. *The Journal of physiology*, 586(Pt 23):5609–5623.
- [144] Magee, J. C. (1998). Dendritic hyperpolarization-activated currents modify the integrative properties of hippocampal CA1 pyramidal neurons. *The Journal of neuroscience : the official journal of the Society for Neuroscience*, 18(19):7613–24.
- [145] Malenka, R. C. and Bear, M. F. (2004). Ltp and ltd: an embarrassment of riches. *Neuron*, 44(1):5–21.
- [146] Malenka, R. C. and Nicoll, R. A. (1999). Long-term potentiation—a decade of progress? *Science*, 285(5435):1870–1874.
- [147] Malinow, R. and Malenka, R. C. (2002). Ampa receptor trafficking and synaptic plasticity. *Annual review of neuroscience*, 25(1):103–126.
- [148] Marquardt, D. W. (1963). An Algorithm for Least-Squares Estimation of Nonlinear Parameters. *Journal of the Society for Industrial and Applied Mathematics*, 11(2):431–441.

- [149] marquis de Laplace, P. S. (1825). *Essai philosophique sur les probabilités*. Bachelier.
- [150] Maxwell, J. C. (1868). I. on governors. *Proceedings of the Royal Society of London*, (16):270–283.
- [151] McIntosh, J. R. and Hays, T. (2016). A brief history of research on mitotic mechanisms. *Biology*, 5(4):55.
- [152] Mellman, I. and Emr, S. D. (2013). A nobel prize for membrane traffic: Vesicles find their journey's end.
- [153] Meng-chin, A. L., Cannon, S. C., and Papazian, D. M. (2018). Kv4.2 autism and epilepsy mutation enhances inactivation of closed channels but impairs access to inactivated state after opening. *Proceedings of the National Academy of Sciences*, 115(15):E3559–E3568.
- [154] Meyer, F. (1994). Topographic distance and watershed lines. *Signal processing*, 38(1):113–125.
- [155] Migliore, M., Hoffman, D. A., Magee, J. C., and Johnston, D. (1999). Role of an A-type K⁺ conductance in the back-propagation of action potentials in the dendrites of hippocampal pyramidal neurons. *Journal of Computational Neuroscience*, 7(1):5–15.
- [156] Mika, J. T. and Poolman, B. (2011). Macromolecule diffusion and confinement in prokaryotic cells. *Current opinion in biotechnology*, 22(1):117–126.
- [157] Miller, K. D. (1996). Synaptic economics: competition and cooperation in synaptic plasticity. *Neuron*, 17(3):371–374.
- [158] Mohamed, W. M. (2008). Arab and muslim contributions to modern neuroscience. *IBRO History of Neuroscience*, 169(3):255.
- [159] Monici, M. (2005). Cell and tissue autofluorescence research and diagnostic applications. *Biotechnology annual review*, 11:227–256.
- [160] Müller, M. J., Klumpp, S., and Lipowsky, R. (2008). Tug-of-war as a cooperative mechanism for bidirectional cargo transport by molecular motors. *Proceedings of the National Academy of Sciences*, 105(12):4609–4614.
- [161] Nakata, T. and Hirokawa, N. (2003). Microtubules provide directional cues for polarized axonal transport through interaction with kinesin motor head. *Journal of Cell Biology*, 162(6):1045–1055.
- [162] Nauman, J. V., Campbell, P. G., Lanni, F., and Anderson, J. L. (2007). Diffusion of insulin-like growth factor-i and ribonuclease through fibrin gels. *Biophysical journal*, 92(12):4444–4450.
- [163] Neher, E. and Sakmann, B. (1976). Single-channel currents recorded from membrane of denervated frog muscle fibres. *Nature*, 260(5554):799–802.
- [164] Nestor, M. W. and Hoffman, D. A. (2012). Differential cycling rates of Kv4.2 channels in proximal and distal dendrites of hippocampal CA1 pyramidal neurons. *Hippocampus*, 22(5):969–80.

- [165] Newby, J. and Bressloff, P. C. (2010). Local synaptic signaling enhances the stochastic transport of motor-driven cargo in neurons. *Physical biology*, 7(3):036004.
- [166] Newpher, T. M. and Ehlers, M. D. (2008). Glutamate receptor dynamics in dendritic microdomains. *Neuron*, 58(4):472–497.
- [167] Noam, Y., Zha, Q., Phan, L., Wu, R.-L., Chetkovich, D. M., Wadman, W. J., and Baram, T. Z. (2010). Trafficking and surface expression of hyperpolarization-activated cyclic nucleotide-gated channels in hippocampal neurons. *The Journal of biological chemistry*, 285(19):14724–36.
- [168] Nusser, Z. (2012). Differential subcellular distribution of ion channels and the diversity of neuronal function. *Current Opinion in Neurobiology*, 22(3):366–371.
- [169] Nwabuisi-Heath, E., LaDu, M. J., and Yu, C. (2012). Simultaneous analysis of dendritic spine density, morphology and excitatory glutamate receptors during neuron maturation in vitro by quantitative immunocytochemistry. *Journal of neuroscience methods*, 207(2):137–147.
- [170] Nyquist, H. (1932). Regeneration theory. *Bell system technical journal*, 11(1):126–147.
- [171] Ohno, T., Hasegawa, T., Tsuruoka, T., Terabe, K., Gimzewski, J. K., and Aono, M. (2011). Short-term plasticity and long-term potentiation mimicked in single inorganic synapses. *Nature materials*, 10(8):591–595.
- [172] O’Leary, T., Williams, A. H., Caplan, J. S., and Marder, E. (2013). Correlations in ion channel expression emerge from homeostatic tuning rules. *Proceedings of the National Academy of Sciences*, 110(28):E2645–E2654.
- [173] O’Leary, T. S. (2008a). *Homeostatic Regulation of Intrinsic Excitability in Hippocampal Neurons - Timothy Sean O’Leary - A thesis submitted for the degree of Doctor of Philosophy at the University of Edinburgh - December 2008 Neuroinformatics and Computational Neuro*. PhD thesis.
- [174] O’Leary, T. S. (2008b). *Homeostatic Regulation of Intrinsic Excitability in Hippocampal Neurons - Timothy Sean O’Leary - A thesis submitted for the degree of Doctor of Philosophy at the University of Edinburgh - December 2008 Neuroinformatics and Computational Neuro*. PhD thesis.
- [175] Olesko, K. M. and Holmes, F. L. (1993). Experiment, quantification, and discovery: Helmholtz’s early physiological researches, 1843-50.
- [176] Opazo, P., Sainlos, M., and Choquet, D. (2012). Regulation of ampa receptor surface diffusion by psd-95 slots. *Current opinion in neurobiology*, 22(3):453–460.
- [177] Otsu, N. (1979). A threshold selection method from gray-level histograms. *IEEE transactions on systems, man, and cybernetics*, 9(1):62–66.
- [178] O’Leary, T., van Rossum, M. C., and Wyllie, D. J. (2010a). Homeostasis of intrinsic excitability in hippocampal neurones: dynamics and mechanism of the response to chronic depolarization. *The Journal of physiology*, 588(1):157–170.

- [179] O’Leary, T., van Rossum, M. C. W., and Wyllie, D. J. A. (2010b). Homeostasis of intrinsic excitability in hippocampal neurones: dynamics and mechanism of the response to chronic depolarization. *The Journal of Physiology*, 588(1):157–170.
- [180] O’Leary, T., Williams, A. H., Franci, A., and Marder, E. (2014). Cell types, network homeostasis, and pathological compensation from a biologically plausible ion channel expression model. *Neuron*, 82(4):809–821.
- [181] Pawley, J. (2006). *Handbook of biological confocal microscopy*, volume 236. Springer Science & Business Media.
- [182] Petralia, R., Wang, Y., Hua, F., Yi, Z., Zhou, A., Ge, L., Stephenson, F., and Wenthold, R. (2010). Organization of NMDA receptors at extrasynaptic locations. *Neuroscience*, 167(1):68–87.
- [183] Philibert, J. (2006). One and a half century of diffusion: Fick, einstein before and beyond.
- [184] Piccolino, M. (1997). Luigi galvani and animal electricity: two centuries after the foundation of electrophysiology. *Trends in neurosciences*, 20(10):443–448.
- [185] Piccolino, M. (2000). The bicentennial of the voltaic battery (1800–2000): the artificial electric organ. *Trends in neurosciences*, 23(4):147–151.
- [186] Potma, E. O., de Boeij, W. P., Bosgraaf, L., Roelofs, J., van Haastert, P. J., and Wiersma, D. A. (2001). Reduced protein diffusion rate by cytoskeleton in vegetative and polarized dictyostelium cells. *Biophysical Journal*, 81(4):2010–2019.
- [187] Ragazzini, J. R. and Zadeh, L. A. (1952). The analysis of sampled-data systems. *Transactions of the American Institute of Electrical Engineers, Part II: Applications and Industry*, 71(5):225–234.
- [188] Rajewsky, N., Santen, L., Schadschneider, A., and Schreckenberg, M. (1998). The asymmetric exclusion process: Comparison of update procedures. *Journal of statistical physics*, 92(1-2):151–194.
- [189] Raju, T. (1999). The nobel chronicles. 1974: Albert claude (1899-1983), george emil palade (b 1912), and christian réne de duve (b 1917). *Lancet (London, England)*, 354(9185):1219.
- [190] Rall, W. (1957). Membrane time constant of motoneurons. *Science*, 126(3271):454–454.
- [191] Rall, W. (1959). Branching dendritic trees and motoneuron membrane resistivity. *Experimental neurology*, 1(5):491–527.
- [192] Rall, W. (1960). Membrane potential transients and membrane time constant of motoneurons. *Experimental neurology*, 2(5):503–532.
- [193] Regner, B. M., Tartakovsky, D. M., and Sejnowski, T. J. (2014). Identifying transport behavior of single-molecule trajectories. *Biophysical Journal*, 107(10):2345–2351.

- [194] Rivera, J. F., Ahmad, S., Quick, M. W., Liman, E. R., and Arnold, D. B. (2003). An evolutionarily conserved dileucine motif in Shal K⁺channels mediates dendritic targeting. *Nature Neuroscience*, 6(3):243–250.
- [195] Royer, S. and Paré, D. (2003). Conservation of total synaptic weight through balanced synaptic depression and potentiation. *Nature*, 422(6931):518–522.
- [196] Ruiz-Gomez, A., Mellström, B., Tornero, D., Morato, E., Savignac, M., Holguín, H., Aurrekoetxea, K., González, P., González-García, C., Ceña, V., Mayor, F., and Naranjo, J. R. (2007). G protein-coupled receptor kinase 2-mediated phosphorylation of downstream regulatory element antagonist modulator regulates membrane trafficking of Kv4.2 potassium channel. *Journal of Biological Chemistry*, 282(2):1205–1215.
- [197] Sajikumar, S., Morris, R. G., and Korte, M. (2014). Competition between recently potentiated synaptic inputs reveals a winner-take-all phase of synaptic tagging and capture. *Proceedings of the National Academy of Sciences*, 111(33):12217–12221.
- [198] Sartori, F., Hafner, A.-S., Karimi, A., Nold, A., Fonkeu, Y., Schuman, E. M., and Tchumatchenko, T. (2020). Statistical laws of protein motion in neuronal dendritic trees. *Cell reports*, 33(7):108391.
- [199] Schnell, E., Sizemore, M., Karimzadegan, S., Chen, L., Brecht, D. S., and Nicoll, R. A. (2002). Direct interactions between psd-95 and stargazin control synaptic ampa receptor number. *Proceedings of the National Academy of Sciences*, 99(21):13902–13907.
- [200] Schulz, P. E. and Fitzgibbons, J. C. (1997). Differing mechanisms of expression for short-and long-term potentiation. *Journal of Neurophysiology*, 78(1):321–334.
- [201] Schwalb, B., Michel, M., Zacher, B., Hauf, K. F., Demel, C., Tresch, A., Gagneur, J., and Cramer, P. (2016). TT-seq maps the human transient transcriptome. *Science*, 352(6290):1225–1228.
- [202] Scott, L., Zelenin, S., Malmersjö, S., Kowalewski, J. M., Markus, E. Z., Nairn, A. C., Greengard, P., Brismar, H., and Aperia, A. (2006). Allosteric changes of the nmda receptor trap diffusible dopamine 1 receptors in spines. *Proceedings of the National Academy of Sciences*, 103(3):762–767.
- [203] Setou, M., Hayasaka, T., and Yao, I. (2004). Axonal Transport versus Dendritic Transport. *J Neurobiol*, 58:201–206.
- [204] Seyfarth, E.-A. (2006). Julius bernstein (1839–1917): pioneer neurobiologist and biophysicist. *Biological cybernetics*, 94(1):2–8.
- [205] Shah, M. M., Hammond, R. S., and Hoffman, D. A. (2010). Dendritic Ion Channel Trafficking and Plasticity. *Trends in neurosciences*, 33(7):307–16.
- [206] Shaner, N. C., Steinbach, P. A., and Tsien, R. Y. (2005). A guide to choosing fluorescent proteins. *Nature methods*, 2(12):905–909.
- [207] Sheng, M. and Pak, D. T. S. (2000). Ligand-Gated Ion Channel Interactions with Cytoskeletal and Signaling Proteins. *Annual Review of Physiology*, 62(1):755–778.

- [208] Sheng, M., Tsaur, M. L., Nung Jan, Y., and Yeh Jan, L. (1992). Subcellular segregation of two A-type K⁺ channel proteins in rat central neurons. *Neuron*, 9(2):271–284.
- [209] Shibata, R., Misonou, H., Campomanes, C. R., Anderson, A. E., Schrader, L. A., Doliveira, L. C., Carroll, K. I., Sweatt, J. D., Rhodes, K. J., and Trimmer, J. S. (2003a). A fundamental role for KChIPs in determining the molecular properties and trafficking of Kv4.2 potassium channels. *Journal of Biological Chemistry*, 278(38):36445–36454.
- [210] Shibata, R., Misonou, H., Campomanes, C. R., Anderson, A. E., Schrader, L. A., Doliveira, L. C., Carroll, K. I., Sweatt, J. D., Rhodes, K. J., and Trimmer, J. S. (2003b). A fundamental role for kchips in determining the molecular properties and trafficking of kv4. 2 potassium channels. *Journal of Biological Chemistry*, 278(38):36445–36454.
- [211] Shimomura, O., Johnson, F. H., and Saiga, Y. (1962). Extraction, purification and properties of aequorin, a bioluminescent protein from the luminous hydromedusan, aequorea. *Journal of cellular and comparative physiology*, 59(3):223–239.
- [212] Singer, S. J. and Nicolson, G. L. (1972). The fluid mosaic model of the structure of cell membranes. *Science*, 175(4023):720–731.
- [213] Singh, B., Ogiwara, I., Kaneda, M., Tokonami, N., Mazaki, E., Baba, K., Matsuda, K., Inoue, Y., and Yamakawa, K. (2006). A kv4. 2 truncation mutation in a patient with temporal lobe epilepsy. *Neurobiology of disease*, 24(2):245–253.
- [214] Smith, D. A. and Simmons, R. M. (2001). Models of motor-assisted transport of intracellular particles. *Biophysical Journal*, 80(1):45–68.
- [215] Smith, G. P. (2008). Unacknowledged contributions of pavlov and barcroft to cannon's theory of homeostasis. *Appetite*, 51(3):428–432.
- [216] Smoluchowski, M. v. (1906). Zur kinetischen theorie der brownschen molekular bewegung und der suspensionen. *Ann. d. Phys.*, 21:756–780.
- [217] Song, I. and Huganir, R. L. (2002). Regulation of ampa receptors during synaptic plasticity. *Trends in neurosciences*, 25(11):578–588.
- [218] Spring, K. R. and Davidson, M. W. (2013). Nikon microscopy: Introduction to fluorescence microscopy.
- [219] Spruston, N., Stuart, G., Häusser, M., Spruston, N., Häusser, M., Stuart, and Spruston (2016a). *Dendrites*. Oxford University Press.
- [220] Spruston, N., Stuart, G., Häusser, M., Spruston, N., Häusser, M., Stuart, and Spruston (2016b). *Dendrites*. Oxford University Press.
- [221] Steward, O., Farris, S., Pirbhoy, P. S., Darnell, J., and Driesche, S. J. V. (2015). Localization and local translation of arc/arg3. 1 mrna at synapses: some observations and paradoxes. *Frontiers in Molecular Neuroscience*, 7:101.
- [222] Steward, O., Wallace, C. S., Lyford, G. L., and Worley, P. F. (1998). Synaptic activation causes the mrna for the ieg arc to localize selectively near activated postsynaptic sites on dendrites. *Neuron*, 21(4):741–751.

- [223] Stockert, J. C. and Blázquez-Castro, A. (2017). *Fluorescence Microscopy in Life Sciences*. Bentham Science Publishers.
- [224] Sun, W., Maffie, J. K., Lin, L., Petralia, R. S., Rudy, B., and Hoffman, D. A. (2011). DPP6 Establishes the A-Type K⁺ Current Gradient Critical for the Regulation of Dendritic Excitability in CA1 Hippocampal Neurons. *Neuron*, 71(6):1102–1115.
- [225] Suszkiw, J., O’leary, M., Murawsky, M., and Wang, T. (1986). Presynaptic calcium channels in rat cortical synaptosomes: fast-kinetics of phasic calcium influx, channel inactivation, and relationship to nitrendipine receptors. *Journal of Neuroscience*, 6(5):1349–1357.
- [226] Swaminathan, R., Hoang, C. P., and Verkman, A. (1997). Photobleaching recovery and anisotropy decay of green fluorescent protein gfp-s65t in solution and cells: cytoplasmic viscosity probed by green fluorescent protein translational and rotational diffusion. *Biophysical journal*, 72(4):1900–1907.
- [227] Takano, T., Funahashi, Y., and Kaibuchi, K. (2019). Neuronal polarity: positive and negative feedback signals. *Frontiers in cell and developmental biology*, 7:69.
- [228] Tanaka, J.-i., Matsuzaki, M., Tarusawa, E., Momiyama, A., Molnar, E., Kasai, H., and Shigemoto, R. (2005). Number and density of ampa receptors in single synapses in immature cerebellum. *Journal of Neuroscience*, 25(4):799–807.
- [229] Tominaga, M. and Ito, K. (2015). The molecular mechanism and physiological role of cytoplasmic streaming. *Current opinion in plant biology*, 27:104–110.
- [230] Triantafilou, M., Morath, S., Mackie, A., Hartung, T., and Triantafilou, K. (2004). Lateral diffusion of toll-like receptors reveals that they are transiently confined within lipid rafts on the plasma membrane. *Journal of cell science*, 117(17):4007–4014.
- [231] Triesch, J., Vo, A. D., and Hafner, A.-S. (2018). Competition for synaptic building blocks shapes synaptic plasticity. *Elife*, 7:e37836.
- [232] Trimmer, J. S. (2015). Subcellular localization of K⁺channels in mammalian brain neurons: Remarkable precision in the midst of extraordinary complexity.
- [233] Turrigiano, G. (2012). Homeostatic synaptic plasticity: Local and global mechanisms for stabilizing neuronal function. *Cold Spring Harbor Perspectives in Biology*, 4(1).
- [234] Turrigiano, G. G. (1999). Homeostatic plasticity in neuronal networks: The more things change, the more they stay the same.
- [235] Turrigiano, G. G. (2008). The self-tuning neuron: synaptic scaling of excitatory synapses. *Cell*, 135(3):422–435.
- [236] Tushev, G., Glock, C., Heumüller, M., Biever, A., Jovanovic, M., and Schuman, E. M. (2018). Alternative 3 UTRs Modify the Localization, Regulatory Potential, Stability, and Plasticity of mRNAs in Neuronal Compartments. *Neuron*, 98(3):495–511.
- [237] Tytell, M., Black, M. M., Garner, J. A., and Lasek, R. J. (1981). Axonal transport: each major rate component reflects the movement of distinct macromolecular complexes. *Science*, 214(4517):179–181.

- [238] Vale, R. D. (2003). The molecular motor toolbox for intracellular transport. *Cell*, 112(4):467–480.
- [239] Van der Pas, P. W. (1971). The discovery of the brownian motion. *Scientiarum Historia: Tijdschrift voor de Geschiedenis van de Wetenschappen en de Geneeskunde*, 13(1):27–35.
- [240] Van Helden, A., Dupré, S., and van Gent, R. (2010). *The origins of the telescope*, volume 12. Amsterdam University Press.
- [241] van Welie, I., van Hooft, J. A., and Wadman, W. J. (2004). Homeostatic scaling of neuronal excitability by synaptic modulation of somatic hyperpolarization-activated Ih channels. *Proceedings of the National Academy of Sciences*, 101(14):5123–5128.
- [242] Varga, A. W., Anderson, A. E., Adams, J. P., Vogel, H., and Sweatt, J. D. (2000). Input-Specific Immunolocalization of Differentially Phosphorylated Kv4.2 in the Mouse Brain. *Learning & Memory*, 7(5):321–332.
- [243] Varga, A. W., Yuan, L.-L., Anderson, A. E., Schrader, L. A., Wu, G.-Y., Gatchel, J. R., Johnston, D., and Sweatt, J. D. (2004a). Calcium-calmodulin-dependent kinase II modulates Kv4.2 channel expression and upregulates neuronal A-type potassium currents. *The Journal of neuroscience : the official journal of the Society for Neuroscience*, 24(14):3643–54.
- [244] Varga, A. W., Yuan, L.-L., Anderson, A. E., Schrader, L. A., Wu, G.-Y., Gatchel, J. R., Johnston, D., and Sweatt, J. D. (2004b). Calcium-calmodulin-dependent kinase II modulates Kv4.2 channel expression and upregulates neuronal A-type potassium currents. *The Journal of neuroscience : the official journal of the Society for Neuroscience*, 24(14):3643–54.
- [245] Voit, E. O., Martens, H. A., and Omholt, S. W. (2015). 150 years of the mass action law. *PLoS Comput Biol*, 11(1):e1004012.
- [246] Wallace, C. S., Lyford, G. L., Worley, P. F., and Steward, O. (1998). Differential intracellular sorting of immediate early gene mrnas depends on signals in the mrna sequence. *Journal of Neuroscience*, 18(1):26–35.
- [247] Williams, A. H., O’Donnell, C., Sejnowski, T. J., and O’Leary, T. (2016). Dendritic trafficking faces physiologically critical speed-precision tradeoffs. *eLife*, 5(DECEMBER2016).
- [248] Zenke, F., Hennequin, G., and Gerstner, W. (2013). Synaptic plasticity in neural networks needs homeostasis with a fast rate detector. *PLoS computational biology*, 9(11).
- [249] Zimorski, V., Ku, C., Martin, W. F., and Gould, S. B. (2014). Endosymbiotic theory for organelle origins. *Current opinion in microbiology*, 22:38–48.

Appendix A

Derivations

A.1 Derivation of advection-diffusion equation

Here we derive the advection-diffusion equation in one dimension from a random walk.

A.1.1 Random walk master equation

We begin with a one dimension line that is discretized in space with index $x = 1, 2, \dots, X$ and in time with index $n = 1, 2, \dots, N$. We are observing a random walk, where a random walker has a probability of f that a step is taken to the right (forwards) and b that a step is taken to the left (backwards). Each step therefore increases or decreases space by one distance unit Δx ($x \rightarrow x - \Delta x$ or $x \rightarrow x + \Delta x$, respectively). Each step also increases time by one time unit ($n \rightarrow n + \Delta n$) where Δn is the duration of one time step.

Let $P_n(x)$ be the probability of finding the walker at position x at some time n . We can now write a master equation for the walker occupying position x at time $n + \Delta n$:

$$P_{n+\Delta n}(x) = fP_n(x - \Delta x) + bP_n(x + \Delta x) + (1 - f - b)P_n(x) \quad (\text{A.1})$$

Notice that we allow for the probability that the walker stays in place with probability $1 - f - b$. If we distribute the last term on the RHS, we have

$$P_{n+\Delta n}(x) = fP_n(x - \Delta x) + bP_n(x + \Delta x) + P_n(x) - fP_n(x) - bP_n(x)$$

Subtract the term $P_n(x)$ from both sides.

$$P_{n+\Delta n}(x) - P_n(x) = fP_n(x - \Delta x) + bP_n(x + \Delta x) - bP_n(x) - fP_n(x) \quad (\text{A.2})$$

We leave the LHS of Equation A.2 as it is now before converting to continuous time and space after working on the RHS.

The RHS of Equation A.2 is algebraically modified to a form related to the finite difference approximations of the first and second spatial derivatives. In order to do this, the first and second terms of the RHS of Equation A.2 are expanded as follows:

$$pP_n(x - \Delta x) = \frac{1}{2}fP_n(x - \Delta x) - \frac{1}{2}pP_n(x - \Delta x)$$

$$bP_n(x + \Delta x) = \frac{1}{2}bP_n(x + \Delta x) - \frac{1}{2}bP_n(x + \Delta x)$$

Additionally, the following terms summing to zero are added to the RHS of Equation A.2

$$\frac{1}{2}fP_n(x + \Delta x) - \frac{1}{2}fP_n(x + \Delta x) + \frac{1}{2}bP_n(x - \Delta x) - \frac{1}{2}bP_n(x - \Delta x)$$

All terms are added to Equation A.2 and expansions are substituted into Equation A.2. Rearrangement of terms and factoring puts the equation in the desired form, as follows:

$$\begin{aligned} P_{n+\Delta n}(x) - P_n(x) &= fP_n(x - \Delta x) + bP_n(x + \Delta x) - fP_n(x) - bP_n(x) \\ &= \frac{1}{2}fP_n(x - \Delta x) - fP_n(x) + \frac{1}{2}pP_n(x + \Delta x) + \frac{1}{2}bP_n(x - \Delta x) - bP_n(x) \\ &\quad + \frac{1}{2}bP_n(x + \Delta x) - \frac{1}{2}fP_n(x + \Delta x) + \frac{1}{2}fP_n(x - \Delta x) + \frac{1}{2}bP_n(x + \Delta x) \\ &\quad - \frac{1}{2}bP_n(x - \Delta x) \\ &= \frac{1}{2} \left(fP_n(x - \Delta x) - 2fP_n(x) + fP_n(x + \Delta x) + bP_n(x - \Delta x) - 2bP_n(x) \right. \\ &\quad \left. + bP_n(x + \Delta x) \right) - \frac{1}{2} \left(fP_n(x + \Delta x) - fP_n(x - \Delta x) - bP_n(x + \Delta x) \right. \\ &\quad \left. + bP_n(x - \Delta x) \right) \\ P_{n+\Delta n}(x) - P_n(x) &= \frac{1}{2}(f + b) \left(P_n(x - \Delta x) - 2P_n(x) + P_n(x + \Delta x) \right) \\ &\quad - \frac{1}{2}(f - b) \left(P_n(x + \Delta x) - P_n(x - \Delta x) \right) \end{aligned} \tag{A.3}$$

The LHS of Equation A.3 will become the time derivative of P , and the first and second terms on the RHS will become second and first spatial derivatives of P , respectively.

A.1.2 Finite difference approximation

As the spatial and temporal step sizes Δx and Δt approach zero, Equation A.3 approaches the continuous advection-diffusion equation. In order to approximate the form of the derivatives in continuous space and time, we can use the finite difference approximations for first and second derivatives. We begin with the forward difference equation for a first derivative of some arbitrary function $f(t)$:

$$\frac{df}{dt} = \frac{f(t + \Delta t) - f(t)}{\Delta t} \quad (\text{A.4})$$

We can also consider the central difference equation for the first derivative of $f(t)$:

$$\frac{df}{dt} = \frac{f(t + \frac{1}{2}\Delta t) - f(t - \frac{1}{2}\Delta t)}{\Delta t}$$

Since the smallest step size in our discrete case was Δt and not $\frac{1}{2}\Delta t$, it might be more helpful to take a central difference approximation over two steps $2\Delta t$:

$$\frac{df}{dt} = \frac{f(t + \Delta t) - f(t - \Delta t)}{2\Delta t} \quad (\text{A.5})$$

The central difference approximation can then be applied to a second derivative using the chain rule:

$$\begin{aligned} \frac{d^2f}{dt^2} &= \frac{\frac{d}{dt}f(t + \frac{1}{2}\Delta t) - \frac{d}{dt}f(t - \frac{1}{2}\Delta t)}{\Delta t} \\ \frac{d^2f}{dt^2} &= \frac{1}{\Delta t} \left(\frac{f(t + \Delta t) - f(t)}{\Delta t} - \frac{f(t) - f(t - \Delta t)}{\Delta t} \right) \\ \frac{d^2f}{dt^2} &= \frac{f(t + \Delta t) - 2f(t) + f(t - \Delta t)}{\Delta t^2} \end{aligned} \quad (\text{A.6})$$

The approximations in Equations A.4, A.5, and A.6 can be used to write discrete difference equations as continuous derivatives.

A.1.3 Discrete to continuous space and time

In order to modify our master equation in Equation A.3 to continuous space and time, all terms must be in the form of Equations A.4, A.5, or A.6. We can multiply the LHS by unit

value $\frac{\Delta n}{\Delta n}$, the first term on the RHS by unit $\frac{\Delta x^2}{\Delta x^2}$, and the second term on the RHS by unit $\frac{\Delta x}{\Delta x}$:

$$\begin{aligned} \left(P_{n+\Delta n}(x) - P_n(x) \right) \frac{\Delta n}{\Delta n} &= \frac{1}{2} \frac{\Delta x^2}{\Delta x^2} (f+b) \left(P_n(x-\Delta x) - 2P_n(x) + P_n(x+\Delta x) \right) \\ &\quad - \frac{1}{2} \frac{\Delta x}{\Delta x} (f-b) \left(P_n(x+\Delta x) - P_n(x-\Delta x) \right) \\ \frac{P_{n+\Delta n}(x) - P_n(x)}{\Delta n} \Delta n &= \frac{\Delta x^2}{2} (f+b) \frac{P_n(x-\Delta x) - 2P_n(x) + P_n(x+\Delta x)}{\Delta x^2} \\ &\quad - \frac{\Delta x}{2} (f-b) \frac{P_n(x+\Delta x) - P_n(x-\Delta x)}{\Delta x} \\ \frac{P_{n+\Delta n}(x) - P_n(x)}{\Delta n} &= \frac{\Delta x^2 (f+b)}{2\Delta n} \frac{P_n(x-\Delta x) - 2P_n(x) + P_n(x+\Delta x)}{\Delta x^2} \\ &\quad - \frac{\Delta x (f-b)}{\Delta n} \frac{P_n(x+\Delta x) - P_n(x-\Delta x)}{2\Delta x} \end{aligned}$$

We can now make derivative approximations using Equations A.4, A.5, and A.6 and replace discrete time n and space x with continuous time t and space x .

$$\frac{\partial P(x,t)}{\partial t} = D \frac{\partial^2 P(x,t)}{\partial x^2} + v \frac{\partial P(x,t)}{\partial x}$$

where $P(x,t)$ is the probability of finding a random walker at position x at time t in continuous space and time. We have also identified $D = \frac{\Delta x^2 (f+b)}{2\Delta n}$ and $v = \frac{\Delta x (f-b)}{\Delta n}$ as $\lim_{\Delta x \rightarrow 0}$ and $\lim_{\Delta n \rightarrow 0}$. For a population that contains a total of T random walkers, the concentration of particles in some segment of line can be defined as $c(x,t) = TP(x,t)/\Delta x$ using the law of large numbers. Substituting this into our equation produces the one-dimensional advection-diffusion equation for a large population of particles in a more recognizable form:

$$\frac{\partial c(x,t)}{\partial t} = D \frac{\partial^2 c(x,t)}{\partial x^2} + v \frac{\partial c(x,t)}{\partial x} \quad (\text{A.7})$$

A.2 Estimation of diffusion coefficient from FRAP

This derivation has been adapted from the Supporting Text of Scott et al, 2006 [202].

The purpose of this derivation is to estimate the diffusion coefficient D from experimental data obtained with fluorescence recovery after photobleaching (FRAP). We begin by defining the problem, depicted in Fig. A.1. A neurite is approximated as a cylinder, and intracellular transport (diffusion) of cargo $c(x,t)$ occurs along the longitudinal axis x of the cylinder over time t . A bleach region of width w is defined, centered about $x = 2l = 0$. At $t = 0$, there is no cargo in this region $c([-l, l], 0) = 0$, corresponding to the moment fluorescence recovery

begins, just after photobleaching. In the adjacent regions ($x > l$ and $x < -l$), the density of cargo is C_0 at $t = 0$.

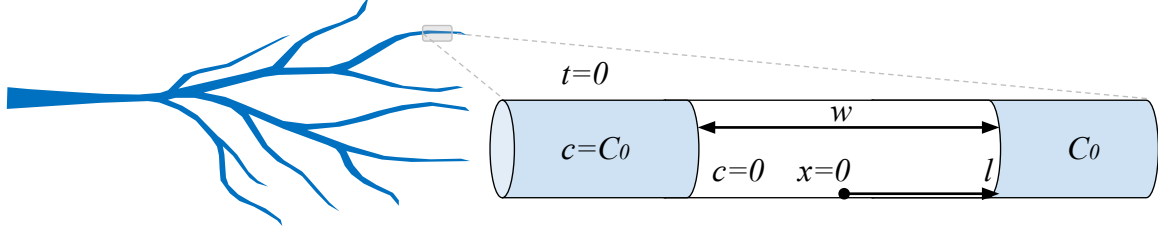


Fig. A.1 A segment of neurite is depicted immediately after photobleaching. Solving the diffusion equation in this 1D system estimates D .

We begin with the diffusion equation with the assumption of no drift:

$$\frac{\partial c(x,t)}{\partial t} = D \frac{\partial^2 c(x,t)}{\partial x^2}$$

The solution to this equation with the aforementioned initial conditions is

$$c(x,t) = \frac{C_0}{2} \left(\operatorname{erfc} \left(\frac{x+l}{2\sqrt{Dt}} \right) + \operatorname{erfc} \left(\frac{-x+l}{2\sqrt{Dt}} \right) \right)$$

where erfc is the complementary error function and all other terms are as previously defined.

We next integrate this function over the bleached area $-l$ to l (see Fig. A.1):

$$\frac{1}{2l} \int_{-l}^{+l} c(x,t) dx = C_0 \left(\sqrt{\frac{Dt}{\pi l^2}} \left(1 - \exp\left(\frac{-l^2}{Dt}\right) \right) + \operatorname{erfc} \left(\frac{l}{\sqrt{Dt}} \right) \right)$$

We then solve for the time at which this expression reaches half maximum $t = t_{1/2}$:

$$\frac{1}{2} = \sqrt{\frac{Dt_{1/2}}{\pi l^2}} \left(1 - \exp\left(\frac{-l^2}{Dt_{1/2}}\right) \right) + \operatorname{erfc} \left(\frac{l}{\sqrt{Dt_{1/2}}} \right)$$

We can solve the preceding equation for $\frac{Dt_{1/2}}{l^2}$ to obtain the numerical solution:

$$\frac{Dt_{1/2}}{l^2} \approx 0.925$$

Rearranging

$$D \approx 0.925 \frac{l^2}{t_{1/2}}$$

Substituting in $w = 2l$, we have:

$$D \approx 0.231 \frac{w^2}{t_{1/2}} \quad (\text{A.8})$$

We use Eq. A.8 to estimate the D for dendrites in our dataset in Chapter 5.

Appendix B

Stochastic model: analysis and inference

B.1 Distributions of kinetic measures in stochastic model

In this section, the stochastic model is analyzed as a modified discrete time random walk. We aim to realize the distributions of the experimental measures of puncta kinetics (Fig. 3.9). Among the distributions derived here are distance traveled and mean speed.

B.1.1 Total distance traveled

Until absorption, a puncta in this stochastic model behaves as in a one-dimensional unbiased random walk. We use this premise to solve for the distributions of the kinetic measures of interest.

We begin with total distance traveled D_{tot} , which is a measure of the puncta's final position relative to its origin. The final position is the site of absorption, which ends the random walk. The expected value of an unbiased random walk is 0, regardless of the number of time steps n . For a biased random walk with rightward (+1) propensity f and leftward (-1) propensity b , the expected value after n time steps is $n(f - b)$. The variability around this expected value scales with \sqrt{n} . As the number of puncta simulated approaches infinity, the distribution of their final positions - by central limit theorem - approximates a bell curve. In a DTRW with no absorption, this is well approximated by a normal distribution. We also find that unidirectional runs (with increasing parameter p_{mem}) increase the the standard deviation σ of the normal distribution approximation [39, 247].

In a DTRW with absorption (also called decay, degradation, sink, etc.), the shape of the distribution changes. To estimate the total distance traveled by puncta on a 1D lattice with absorption, we use a differential equation for diffusion. A random walk with more than a few

steps is well approximated by diffusion [39]. The PDE for diffusion with decay and source is

$$\frac{\partial c}{\partial t} = D \frac{\partial^2 c}{\partial x^2} - K_{\text{off}} c + s \quad (\text{B.1})$$

where $c = c(x, t)$ is the concentration of puncta at some position x at time t , D is the diffusion coefficient, K_{off} is the absorption rate, and s is puncta source at $x = 0$. The distribution of net displacement of puncta is approximated by the steady-state ($\frac{\partial c}{\partial t} = 0$) of Eq. B.1:

$$0 = D \frac{\partial^2 c}{\partial x^2} - K_{\text{off}} c$$

Solving this produces two exponentials of the form:

$$c(x) = A e^{\lambda x} + B e^{-\lambda x} \quad (\text{B.2})$$

where λ is a space constant for spread of puncta before absorption: $\lambda = \sqrt{K_{\text{off}}/D}$. If we next impose the restriction that $c \rightarrow 0$ as $x \rightarrow \pm\infty$, then Eq. B.2 is restricted to

$$\begin{aligned} c(x) &= A e^{\lambda x} && \text{for } x < 0 \\ c(x) &= B e^{-\lambda x} && \text{for } x > 0 \end{aligned}$$

For continuity at $c(0)$, $A = B$. Solving for this single coefficient $A = B$ requires the amount of mass M released at the source at $c = 0$. This quantity M in units of quantity per cross sectional area per time is split into left and right directions, therefore

$$A = B = \frac{M}{2D\lambda} = \frac{M}{2\sqrt{DK_{\text{off}}}}$$

. The full symmetric solution is

$$\begin{aligned} c(x) &= \frac{M}{2\sqrt{DK_{\text{off}}}} \exp \sqrt{K_{\text{off}}/D} x && \text{for } x < 0 \\ c(x) &= \frac{M}{2\sqrt{DK_{\text{off}}}} \exp -\sqrt{K_{\text{off}}/D} x && \text{for } x > 0 \end{aligned}$$

In our experiments, the orientation of axons was not always clear. We therefore report this measure as distance traveled rather than net displacement, since we can only account for magnitude of displacement and not direction. The distribution for this measure of total

distance traveled is thus symmetric about the y-axis:

$$c(x) = \frac{M}{\sqrt{DK_{\text{off}}}} \exp -\sqrt{K_{\text{off}}/D}x \quad \text{for } x > 0 \quad (\text{B.3})$$

For a DTRW, the diffusion coefficient can be approximated as $D = 2(\Delta x)^2 p_+ p_- / \Delta t$, where Δx and Δt are the discrete steps in space and time, and p_+ and p_- are right and left jump probabilities [15]. The total punctal distance traveled as computed in our experimental kinetic measure is follows a distribution with the form of Eq. B.3, a monotonic decreasing function.

B.1.2 Average speed

The next kinetic measure for which we derive a probability distribution is average speed v . As a kinetic measure, v is computed as distance traveled divided by total puncta run time.

As before, we assume that a DTRW with more than a few steps is well approximated by diffusion [39]. We can then solve the diffusion equation

$$\frac{\partial c}{\partial t} = D \frac{\partial^2 c}{\partial x^2}$$

for diffusion propagator $c(x, t)$

$$c(x, t) = \frac{1}{\sqrt{4\pi Dt}} \exp \left(-\frac{x^2}{4Dt} - K_{\text{off}} t \right)$$

We use $c(x, t)$ to compute the probability of puncta at position x at time t : $p(x|t)$.

$$\begin{aligned} p(x|t) &= \frac{K_{\text{off}} c(x, t)}{\int_{-\infty}^{\infty} K_{\text{off}} c(x, t) dx} \\ &= \frac{K_{\text{off}} \frac{1}{\sqrt{4\pi Dt}} \exp \left(-\frac{x^2}{4Dt} - K_{\text{off}} t \right)}{\int_{-\infty}^{\infty} K_{\text{off}} \frac{1}{\sqrt{4\pi Dt}} \exp \left(-\frac{x^2}{4Dt} - K_{\text{off}} t \right) dx} \end{aligned}$$

We cancel terms in the numerator and denominator and solve the integral:

$$\begin{aligned} p(x|t) &= \frac{\exp\left(-\frac{x^2}{4Dt}\right)}{\int_{-\infty}^{\infty} \exp\left(-\frac{x^2}{4Dt}\right) dx} \\ &= \frac{\exp\left(-\frac{x^2}{4Dt}\right)}{\sqrt{4\pi Dt}} \end{aligned}$$

Note that $p(x|t)$ is independent of K_{off}

With $p(x|t)$, we can now compute the probability of a given puncta velocity v at time t : $p(v|t)$

$$p(v|t) = \int_{-\infty}^{\infty} \delta\left(v - \frac{|x|}{t}\right) p(x|t) dx$$

where δ is the Dirac delta function. This integral sweeps through all positions x to find the probability of puncta at least location ($p(x|t)$) that matches each speed ($\delta\left(v - \frac{|x|}{t}\right)$). We proceed using the scaling, symmetry, and translation properties of the Dirac delta function:

$$\begin{aligned} p(v|t) &= \int_{-\infty}^{\infty} \delta\left(v - \frac{|x|}{t}\right) p(x|t) dx \\ &= \int_{-\infty}^{\infty} \delta\left(\frac{1}{t}(vt - |x|)\right) p(x|t) dx \\ &= \int_{-\infty}^{\infty} t \delta(vt - |x|) p(x|t) dx \\ &= t \int_{-\infty}^{\infty} \delta(vt - |x|) p(x|t) dx \\ &= t \left(p(\delta t|t) + p(-\delta t|t) \right) \\ &= \frac{2t}{\sqrt{4\pi Dt}} e^{-(vt)^2/4Dt} \\ p(v|t) &= \frac{t}{\sqrt{\pi D}} e^{-v^2 t/4D} \end{aligned}$$

To check this probability distribution, we integrate it over the entire domain to ensure it sums to 1:

$$\int_0^{\infty} p(v|t) dv = \frac{1}{2} \int_{-\infty}^{\infty} p(v|t) dv = \frac{1}{2} \sqrt{\frac{t}{\pi D}} \int_{-\infty}^{\infty} \exp\left(-\frac{v^2 t}{4D}\right) dv = \frac{1}{2} \sqrt{\frac{t}{\pi D}} \sqrt{\frac{4\pi D}{t}} = 1$$

We next compute the expected time until absorption $\phi(t)$, which is approximated as

$$\phi(t) = K_{\text{off}} e^{-K_{\text{off}} t}$$

With $p(v|t)$ and $\phi(t)$, we can now compute the probability distribution for average speed $F(v)$. We integrate the velocity distribution at a fixed time ($p(v|t)$) multiplied by the fraction of particles ($\phi(t)$) for all time $t > 0$:

$$\begin{aligned}
 F(v) &= \int_0^{\infty} p(v|t)\phi(t)dt \\
 &= \int_0^{\infty} \left(\frac{t}{\sqrt{\pi D}} e^{-v^2 t/4D} \right) \left(K_{\text{off}} e^{-K_{\text{off}} t} \right) dt \\
 &= \frac{K_{\text{off}}}{\sqrt{\pi D}} \int_0^{\infty} \sqrt{t} e^{-(v^2/4D + K_{\text{off}})t} dt \\
 &= \frac{K_{\text{off}}}{\sqrt{\pi D}} \frac{\sqrt{\pi}}{2} \left(\frac{v^2}{4D} + K_{\text{off}} \right)^{-3/2} \\
 &= \frac{K_{\text{off}}}{2\sqrt{D} \left(\frac{v^2}{4D} + K_{\text{off}} \right)^{-3/2}}
 \end{aligned}$$

If we substitute $v_0 = 2\sqrt{DK_{\text{off}}}$,

$$F(v) = \frac{1}{v_0} \left(\frac{v^2}{v_0^2} + 1 \right)^{-3/2} \quad (\text{B.4})$$

To confirm our result, we can compute its integral for all $v \geq 0$:

$$\int_0^{\infty} F(v)dv = 1$$

Like $c(x)$, $F(v)$ is a monotonically decreasing function. Increasing D and/or K_{off} increases the tailedness of the distribution. We can compute the expected value of mean particle speed $\langle v \rangle$ as follows:

$$\langle v \rangle = \int_0^{\infty} vF(v)dv = v_0 = 2\sqrt{DK_{\text{off}}}$$

This shows that $\langle v \rangle$ increases with increasing D and/or K_{off}

B.2 Statistical inference using stochastic model

The heuristic method of statistical inference of puncta behavior based on experimental observations is described here. In broad terms, we estimate parameters p_{off} and p_{mem} from our stochastic model using the observed distributions of kinetic measurements.

We interpret our experimental measures of puncta kinetics (Fig. 3.9) as evidence of puncta behavior. We have developed a stochastic model of puncta transport based on a modified random walk (Fig. 4.5), consistent with observed intracellular transport [37, 38, 193]. Our

model produces simulated data similar to our experiments (compare Fig. 3.8 and 4.6). We aim to infer whether the observed differences between axons and dendrites can result from a difference in p_{off} or p_{mem} . To this end, we perform a model fit to data from axons and dendrites. We then compare a model fit using p_{off} alone as well as with p_{off} and p_{mem} .

B.2.1 Maximum likelihood estimation

Maximum likelihood estimation (MLE) is a standard method of estimating the parameters of a model such that the model's output is the most probable match to some observed data. In this method, a likelihood equation is derived from the joint probability distribution of simulated and observed data as a function of model parameters. The set of parameters that maximizes the likelihood equation produces the best fit between the simulated and observed data.

We first explore the direct estimation of p_{off} and p_{mem} for which our stochastic model most closely reproduces our observed data. We then estimate parameters that reproduce a distribution that estimates our observed data—a less direct but simpler method.

We begin by defining the likelihood function:

$$\mathcal{L}(p_{\text{off}}, p_{\text{mem}} \mid \text{observed data}) = P(\text{transport producing observed data} \mid p_{\text{off}}, p_{\text{mem}}) \quad (\text{B.5})$$

where the likelihood \mathcal{L} of parameters $p_{\text{off}}, p_{\text{mem}}$ producing the observed data is equal to the probability of the actual physical transport mechanism producing the observed data given those parameters $p_{\text{off}}, p_{\text{mem}}$. Defining the probability in Eq. B.5 is difficult for a few reasons. First, the observed data consists of sets of net displacements δ , mean speeds s , stall fractions ε , and diffusivities α for $N_a = 961$ puncta in axons and $N_d = 507$ puncta in dendrites:

$$\delta_1, \delta_2, \dots, \delta_{N_a-1}, \delta_{N_a} \qquad \delta_1, \delta_2, \dots, \delta_{N_d-1}, \delta_{N_d} \quad (\text{B.6})$$

$$s_1, s_2, \dots, s_{N_a-1}, s_{N_a} \qquad s_1, s_2, \dots, s_{N_d-1}, s_{N_d} \quad (\text{B.7})$$

$$\varepsilon_1, \varepsilon_2, \dots, \varepsilon_{N_a-1}, \varepsilon_{N_a} \qquad \varepsilon_1, \varepsilon_2, \dots, \varepsilon_{N_d-1}, \varepsilon_{N_d} \quad (\text{B.8})$$

$$\alpha_1, \alpha_2, \dots, \alpha_{N_a-1}, \alpha_{N_a} \qquad \alpha_1, \alpha_2, \dots, \alpha_{N_d-1}, \alpha_{N_d} \quad (\text{B.9})$$

This observed data is a large combination of variables. Further, these variables (Eqs. B.6-B.9) are not measured directly; they are computed from the physical coordinates of trajectories from individual puncta. Computing s , ε , and α involves the trajectories themselves, not just the final position. The random process in our model is time-dependent (non-stationary) and non-ergodic, so deriving the statistics (expected value and variance) does not reveal the time averages. The expected value itself would only be useful in computing net displacements (Eq.

B.6), since this is the only kinetic measure computed using solely outcome of the random process without the full trajectory. Since a key parameter of our system p_{mem} abruptly ends the random process, the statistics are not as simple as those of a standard random walk. These nontrivial derivations only produce the likelihood function, which then requires differentiation w.r.t. p_{off} and p_{mem} for an analytical solution to this problem. For these reasons, rather than deriving the statistics and time-averages of our model, we opt for a numerical approach to this problem.

Instead of deriving equations for δ , s , ε , and α , we can estimate these probability distributions of these kinetic measures by averaging the behavior of simulated puncta. Simulating a large number of puncta N_s is crucial given the stochasticity of the model. From N_s simulated trajectories with a given p_{off} and p_{mem} , we can then compute:

$$\delta_1, \delta_2, \dots, \delta_{N_s-1}, \delta_{N_s} \quad (\text{B.10})$$

$$s_1, s_2, \dots, s_{N_s-1}, s_{N_s} \quad (\text{B.11})$$

$$\varepsilon_1, \varepsilon_2, \dots, \varepsilon_{N_s-1}, \varepsilon_{N_s} \quad (\text{B.12})$$

$$\alpha_1, \alpha_2, \dots, \alpha_{N_s-1}, \alpha_{N_s} \quad (\text{B.13})$$

With a sufficiently large N_s , we obtain averages of δ , s , ε , and α . This method follows the law of large numbers, whereby the average of a large number of iterations approaches the expected behavior of the random process. We can then compare simulated data (Eqs. B.10-B.13) to observed data (Eqs. B.6-B.9) and optimize for parameter set p_{off} and p_{mem} that minimizes this variation. This semi-empirical approach employs both model simulation to estimate kinetic distributions and optimization to minimize the difference between simulated and observed data.

MLE is still applicable in this approach. Approximating simulated and observed data as probability distributions simplifies the optimization problem. Both observed and simulated sample sets can be approximated as probability distributions, and the distance between distribution parameters is minimized. MLE is a suitable method for fitting observed and simulated data to a distribution with a defined probability density function (pdf).

The pdf of two kinetic measures δ (Eq. B.3) and s (Eq. B.4) are derived in the previous section. Both are monotonically decreasing functions with domain $[0, \infty)$. The pdf of the other measures ε and α are seemingly intractable and beyond the scope of this paper. We therefore approximate the distributions of kinetic measures using an estimate likelihood with the gamma distribution. The gamma distribution can accommodate the monotonic decreasing pdfs derived here and is flexible for all simulated and observed data (Eqs. B.10-B.13 and Eqs. B.6-B.9 depicted in Fig. 4.8). The gamma distribution is appropriate because it is continuous

and covers a semi-infinite $[0, \infty)$ interval. A gamma distribution has shape k and scale θ , which are fit to both observed and simulated data.

To this end, we derive a function for the likelihood of the gamma distribution with parameters k and θ producing observed or simulated data. As an example, we estimate k and θ that best match the observed mean speed s in axons:

$$\mathcal{L}(k, \theta | X = s_1, \dots, s_{N_a}) = P(\text{gamma distribution fits } X | k, \theta)$$

Here, the probability in the RHS is, by definition, the pdf of the gamma distribution:

$$\mathcal{L}(k, \theta | X = s_1, \dots, s_{N_a}) = \frac{1}{\Gamma(k)\theta^k} X^{k-1} e^{x/\theta} \quad (\text{B.14})$$

where vector X is the data to which a gamma distribution is fit. The RHS of Eq. B.14 is the pdf of the gamma distribution, where Γ is the gamma function: $\Gamma(g) = \int_0^\infty z^{g-1} e^{-z} dz$.

The remaining steps for MLE involve calculating the log-likelihood $\ell(k, \theta | X)$, taking partial derivatives w.r.t. each parameter $\partial \ell(k, \theta) / \partial k$ and $\partial \ell(k, \theta) / \partial \theta$, setting to zero, and solving for both k and θ . The solution for MLE using the gamma distribution has no closed-form expression [46, 86]. Rather, a numerical solution is computed. We use MATLAB function `fitdist`, which solves the following system of two equations:

$$\ln k - \psi(k) = \ln \left(\frac{(\sum_{i=1}^{N_a} s_i) / N_a}{(\prod_{i=1}^{N_a} s_i)^{1/N_a}} \right), \quad \theta = \frac{(\sum_{i=1}^{N_a} s_i) / N_a}{k}$$

where ψ is the digamma function: $\psi(g) = \frac{d}{dx} \ln(\Gamma(g))$.

MLE for gamma distribution parameters is performed for each set of observed data (Eqs. B.6-B.9) as well as for N_s trajectories simulated using the stochastic model (Eqs. B.10-B.13) with a given p_{off} and p_{mem} . Observed data for net displacement and average speed are normalized between 0 and 1. All resultant gamma parameters are:

$$k_{\delta,a}, \theta_{\delta,a} \quad k_{s,a}, \theta_{s,a} \quad k_{\epsilon,a}, \theta_{\epsilon,a} \quad k_{\alpha,a}, \theta_{\alpha,a} \quad (\text{B.15})$$

$$k_{\delta,d}, \theta_{\delta,d} \quad k_{s,d}, \theta_{s,d} \quad k_{\epsilon,d}, \theta_{\epsilon,d} \quad k_{\alpha,d}, \theta_{\alpha,d} \quad (\text{B.16})$$

$$k_{\delta,s}, \theta_{\delta,s} \quad k_{s,s}, \theta_{s,s} \quad k_{\epsilon,s}, \theta_{\epsilon,s} \quad k_{\alpha,s}, \theta_{\alpha,s} \quad (\text{B.17})$$

where each variable k or θ denotes gamma shape or scale parameter, the first subscript denotes kinetic measure, and the second subscript denotes source of the distribution (axons, dendrites, or simulation). The gamma distributions of kinetic measures in axons and dendrites (Eqs. B.15 and B.16) are plotted over the raw data in Fig. 3.9. We now have a succinct

description of each distribution using two rather than N_a , N_d , or N_s terms. This framework allows us to compare observed and simulated data. We next use a least squares method fit simulation parameters p_{off} and p_{mem} to the experimental data.

B.2.2 Least squares method of optimization

MLE allows for a representation of data from axons, dendrites, or simulations as a gamma distribution using only two parameters k and θ . We now aim to fit our stochastic model to experimental data. A standard approach in model fitting is the least squares method (LSM) of regression. Here, we describe LSM in the context of our problem. We then outline numerical algorithms for solving nonlinear LSM problems.

We describe a model M with output y as a function of independent variable x and adjustable parameters β :

$$y = M(x, \beta)$$

We substitute an example optimization problem using our data and parameters,

$$[k_{\delta,s}, \theta_{\delta,s}] = M(p_{\text{off}}, p_{\text{mem}}) \quad (\text{B.18})$$

where M is the stochastic model, p_{off} and p_{mem} are the adjustable parameters that are tweaked for an optimal fit with output $y = [k_{\delta,s}, \theta_{\delta,s}]$. Model fitting can be applied to any number of outputs from Eq. B.17. Note that our function for optimization in Eq. B.18 differs from that in curve fitting in that it takes no independent variables x . The model fitting in our example fits only the model parameters. Further, M itself is a complex, nonlinear function. Contained within M is a simulation of the N_s puncta trajectories using the stochastic model (Fig. S8). Also contained within M is computation of kinetic measures (δ , s , ϵ , and α) for each of the N_s trajectories. Lastly contained within M is the MLE of the gamma parameters (k and θ) from the distributions of kinetic measures (Eqs. B.10-B.13). Selection of N_s is therefore a balance between computational cost (run time) and accuracy of expected puncta behavior (by law of large numbers). We choose $N_s = 10,000$ puncta in each iteration of M .

The quality of fit for the output of M is measured by the size of the residuals, or the difference between the observed data and estimated data:

$$\text{residuals} = \text{observed data} - \text{simulated data}$$

In the context of our problem, we will fit the output in Eq. B.18 to observed data in axons:

$$\begin{aligned} r &= [k_{\delta,a}, \theta_{\delta,a}] - M(p_{\text{off}}, p_{\text{mem}}) \\ r &= [k_{\delta,a}, \theta_{\delta,a}] - [k_{\delta,s}, \theta_{\delta,s}] \end{aligned} \quad (\text{B.19})$$

where $[k_{\delta,a}, \theta_{\delta,a}]$ is the axonal data, and r is a vector of residuals, $r = [r_1, r_2]$. The LSM aims to minimize the sum of the squares S of the residuals: $S = \sum r_i^2$. S is minimized by setting its gradient to zero. This involves taking a partial derivative of S w.r.t. each parameter. In our example:

$$\begin{aligned} \frac{\partial S}{\partial p_{\text{off}}} &= \frac{\partial}{\partial p_{\text{off}}} \sum_i r_i^2 = 0 & \frac{\partial S}{\partial p_{\text{mem}}} &= \frac{\partial}{\partial p_{\text{mem}}} \sum_i r_i^2 = 0 \\ &= 2 \sum_i r_i \frac{\partial r_i}{\partial p_{\text{off}}} = 0 & &= 2 \sum_i r_i \frac{\partial r_i}{\partial p_{\text{mem}}} = 0 \end{aligned}$$

Using Eq. B.19 and given that the partial derivatives of $[k_{\delta,a}, \theta_{\delta,a}]$ w.r.t. p_{off} and p_{mem} is zero,

$$\frac{\partial S}{\partial p_{\text{off}}} = -2 \sum_i r_i \frac{\partial M}{\partial p_{\text{off}}} = 0 \quad \frac{\partial S}{\partial p_{\text{mem}}} = -2 \sum_i r_i \frac{\partial M}{\partial p_{\text{mem}}} = 0 \quad (\text{B.20})$$

A closed-form solution for Eq. B.20, as in most non-linear least squares problems, does not exist. A numerical algorithm is instead used to minimize S .

There are several algorithms for nonlinear curve-fitting and data-fitting in the least squares sense. We use MATLAB function `lsqcurvefit`, which employs a damped LSM, also known as the Levenberg–Marquardt algorithm [132, 148]. The damped LSM is a combination of the Gauss–Newton algorithm with a trust region. A broad overview of the damped LSM is presented here.

The damped LSM is an iterative process that begins at a starting point for parameter vector β . For our system, $\beta = [p_{\text{off}}, p_{\text{mem}}]$. The aim is to find the set of β that best fits each of the m data points (x_i, y_i) . Again, in our system, we have no independent variables x_i , and we fit outputs of model M to observed data y_i . In each step of the algorithm, β is updated with a new parameter estimate $\beta + \Delta$. To make a sensible modification Δ to the parameter estimate, the nonlinear function M is approximated by linearization (first-order approximation):

$$M(x_i, \beta + \Delta) \approx M(x_i, \beta) + J_i \Delta \quad , \quad J_i = \frac{\partial M(\beta)}{\partial \beta}$$

where J_i is the gradient of M w.r.t. β . Using this approximation, we can compute the sum of squares S of the residuals:

$$\begin{aligned} S(\beta + \Delta) &\approx \sum_i^m r_i^2 \\ S(\beta + \Delta) &\approx \sum_i^m \left(y_i - M(x_i, \beta) - J_i \Delta \right)^2 \end{aligned} \quad (\text{B.21})$$

As before, Eq. B.21 is minimized where its derivative equals zero. The derivative of Eq. B.21 w.r.t. Δ is

$$(J^T J) \Delta = J^T (y - M(\beta)) \quad (\text{B.22})$$

where J is a Jacobian matrix consisting of rows J_i . Matrix multiplication in Eq. B.22 results in a system of linear equations that is solved for Δ . This procedure of linearization, function approximation, and solving for step Δ repeats to progress toward a minimum S . The algorithm stops when step size Δ falls below some preset threshold. The approach as described thus far is the Gauss-Newton method.

The damped LSM has the addition of damping factor λ , a non-negative scalar, as follows:

$$(J^T J + \lambda I) \Delta = J^T (y - M(\beta)) \quad (\text{B.23})$$

where I is the identity matrix. When λ is small or zero, the method approximates the Gauss-Newton method. When λ is large, the direction of Δ approaches the direction of steepest descent but with magnitude approaching zero. λ adjusts the size of the step, defining a trust region around the current estimate β that is reevaluated at each iteration. If $S(\beta + \Delta) < S(\beta)$, a successful step toward a minima, λ is decreased and the trust region increased. If $S(\beta + \Delta) > S(\beta)$, λ is increased and the trust region decreased. In this regard, a dynamic λ allows for a search that mediates between steepest descent and the Gauss-Newton method. For instance, a limitation of the Gauss-Newton method arises when second-order terms dominant the gradient, since the Gauss-Newton method relies on first-order approximation. Dampening with λ can ensure descent path more efficient than searching for steepest descent.

We use this algorithm in a series of model fits to our experimental data. Given the stochastic nature of M in our system, we increase the lower threshold for the finite difference step size Δ . This ensures continuous progression toward a global minima despite slight variation in output with repeated evaluations of M . Otherwise, with a low minimum Δ , the algorithm greatly reduces the trust region and terminates at a false local minima—an artifact of the randomness in M .

We first fit

$$[k_{\delta,s}, \theta_{\delta,s}, k_{s,s}, \theta_{s,s}] = M(p_{\text{off}}, p_{\text{mem}} = 0)$$

to the corresponding experimental results in axons ($[k_{\delta,a}, \theta_{\delta,a}, k_{s,a}, \theta_{s,a}]$) and dendrites ($[k_{\delta,d}, \theta_{\delta,d}, k_{s,d}, \theta_{s,d}]$). p_{mem} is constrained to zero, and upper and lower bounds for p_{off} are set to 0 and 1, consistent with the range of a probability. The starting value was $p_{\text{off}} = 0.001$. The result of this fit is depicted in Fig. 4.8 (*second column*). We then fit

$$[k_{\delta,s}, \theta_{\delta,s}, k_{s,s}, \theta_{s,s}, k_{\epsilon,s}, \theta_{\epsilon,s}] = M(p_{\text{off}}, p_{\text{mem}})$$

to the corresponding experimental results in axons and dendrites. We now fit both parameters, and both are bounded between 0 and 1 with starting values $p_{\text{off}} = 0.001$ and $p_{\text{mem}} = 0.01$. The result of this fit is depicted in Fig. 4.8 (*third column*). The goodness of these fits and their implications are discussed in Sec. 4.5.4.

Appendix C

Synaptic scaling: full model description

C.1 Unified model of synaptic potentiation, scaling, transport, and regulation

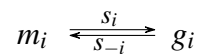
This section contains a thorough descriptions of all components of the unified model.

C.1.1 Model formulation and methods

A mathematical description of our model begins with discussion of the two species in the system: m and g . g is the effective form of AMPA receptors (AMPARs), active and located in their functional sites. g is the form that affects neuron properties (intrinsic excitability, synapse strength, etc.) and is thus the regulated species. m is the precursor to g . m can take the form of pro-protein, pre-pro-protein, protein endocytosed in vesicles, or other internalized pool of the protein. Both fundamentally represent the same cargo, albeit in differing forms.

C.1.2 Cargo insertion (activation and inactivation)

Experimental studies reveal inactive pools of AMPAR receptors located internally or anchored to nanodomains. These inactive AMPARs are available to cycle to and from post-synaptic densities ([95]). We therefore implement a reversible reaction between m and g :



where s_i and s_{-i} are the transfer rates from m_i to g_i , and g_i to m_i , accordingly. The subscript i indexes the spatial compartment of the species. Dendritic compartments are discretized into n compartments. g_i are located in the postsynaptic terminals of dendritic spines.

A dendritic spine consists of a neck that connects the dendritic shaft to a spine head containing ion channels, receptors, and other proteins. Spines are heterogeneous throughout a dendritic tree, with variable size, volume, and number of receptor slots. We assume that spines are significantly smaller than the dendritic shafts. Therefore, g_i have finite capacity which limits g_i concentration. Spine size and number of receptor slots are plastic, which impacts synaptic activity and strength [91]. We capture this property of spines, synapses, and postsynaptic densities in a single term for capacity c_i . With inspiration from [231], we model the interaction between m_i and g_i as follows:

$$\begin{aligned}\dot{m}_i &= f(m_i) - s_i m_i (c_i - g_i) + s_{-i} g_i - \omega_i^m m_i \\ \dot{g}_i &= s_i m_i (c_i - g_i) - s_{-i} g_i - \omega_i^g g_i\end{aligned}\tag{C.1}$$

Parameters ω_i^m and ω_i^g represent degradation rates for m_i and g_i , respectively. $f(m)$ summarizes the transport that occur among the m species, discussed next. The nonlinearity $(c - g_i)$ can be interpreted as a saturation and arise from modeling the transition from m_i to g_i as a mean-field approximation of a partially asymmetric exclusion process (PASEP) [188]. This allows us to model the finite capacity of a spine/synapse, to simulate perturbations in synaptic expression and plasticity, all while maintaining the driving force of mass action.

C.1.3 Cargo trafficking via active transport

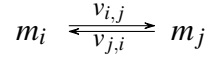
Transport over long distances in a large neurite is a significant limiting factor for feedback regulation and maintenance of homeostasis. We assume that inactive AMPARs m_i are longitudinally transported via an active, motor-based mechanism. Active and passive transport are distinct in a few ways. Motor-based transport is significantly faster and metabolically active, i.e. it requires cellular energy in the form of ATP. Passive transport is diffusive and flows down concentration gradients. We assume that m_i is exclusively transported via motor-based mechanisms, such as with dynein and kinesin on microtubules or with myosin on actin filaments. ([160])

Motor-based transport differs between axons and dendrites. In axons, microtubules are uniformly oriented with plus-ends directed away from the soma. In axons, kinesins and dyneins thus generally move in different directions (anterograde and retrograde, respectively). Kinesins are largely responsible for transporting cargo to the periphery, whereas dyneins carry cargo toward the soma for recycling. ([160, 90])

Dendrites differ in that microtubules have mixed orientation. In dendrites, all motor protein families carry cargo toward or away from the soma. Two distinct hypotheses have been proposed regarding directed transport in dendrites. One hypothesis suggests that motors

act cooperatively, where the motor-cargo complex responds to stimuli for forward movement, backward movement, attachment, and detachment ([160, 90]). The second hypothesis, called the tug-of-war model of bidirectional transport describes both active kinesins and dyneins, and the cargo moves in the direction of the dominant motor type. Net movement thus depends on the number of kinesins and dyneins motors attached to the cargo, and quantitative predictions are based on observations of single motor proteins ([22]). Both hypotheses predict that the motor-cargo complex experiences bidirectional, stochastic movement ([22, 23]).

To capture such motion, we use on a mean-field description and assign to m transport a forward v_f and backward rate v_b . We consider transport parameters where $v_f > v_b$ for net movement away from the soma. This assumption of directionality is consistent with active transport and differs from unbiased diffusion. These rates are depicted as a schematic between two compartments as follows:



where $v_{i,j} > v_{j,i}$ for compartment i closer to the soma than j . The instantaneous change in m_i as a result of evolves according to the following differential equation:

$$f(m_i) = v_{i-1,i}m_{i-1} - (v_{i,i-1} + v_{i,i+1})m_i + v_{i+1,i}m_{i+1} \quad (\text{C.2})$$

We assume that transport between synapse compartments occurs for the cargo precursor m only.

C.1.4 Homeostasis and feedback regulation

Biological cells tend to maintain a number of their intrinsic properties, a process called homeostasis. One such regulated property is the average electrical activity in a neuron. We represent electrical activity using intracellular/somatic calcium levels $[\text{Ca}^{2+}]$ as a function of total active AMPARs g_i throughout the cell. We assume that a neuron compares $[\text{Ca}^{2+}]$ to a global set point $[\text{Ca}^{2+}]_{target}$. The mismatch between the two quantities is $e_G = [\text{Ca}^{2+}]_{target} - [\text{Ca}^{2+}]$. Production of cargo occurs in soma, where most transcription and translation machinery is located. Production is regulated by some signaling molecule u that depends on e_G according to the following differential equation:

$$\dot{u} = K_G e_G - \gamma_G u. \quad (\text{C.3})$$

We assume that a number of regulatory pathways for transcription and translation are $[\text{Ca}^{2+}]$ -dependent ([180, 172]). u represents biosynthesis of AMPARs that increases as $[\text{Ca}^{2+}]$

deviates from $[Ca^{2+}]_{target}$, implemented as integral control in Eq. C.3. Like any signaling molecule, u is not stored perfectly. We therefore implement a leaky integrator, and u degrades with rate γ_G . A non-zero γ_G prevents the neuron from achieving perfect tracking, i.e. achieving $[Ca^{2+}]_{target} = [Ca^{2+}]$.

We can express steady-state AMPAR production as $u_e = \frac{k_{\bar{G}}}{\gamma_G} e_G$. $\frac{k_{\bar{G}}}{\gamma_G}$ represents the ratio of AMPAR production to degradation, also called the turnover rate.

We assume that calcium influx occurs on a substantially faster timescale than cargo production and transport ([225]). We therefore calculate intracellular $[Ca^{2+}]$ as a proxy for neural activity. We compute $[Ca^{2+}]$ at steady state with a static, monotonic relation to V as follows:

$$[Ca^{2+}] = \frac{\alpha}{1 + e^{-V/\beta}} \quad (C.4)$$

where α and β are buffering mechanisms that shape the correlation. We model V as a leaky single-compartment equipotential neuron with

$$C\dot{V} = g_{leak}(E_{leak} - V) + \bar{g}(E_{\bar{g}} - V) \quad (C.5)$$

where C is the membrane capacitance, E_{leak} is the equilibrium potential of the ionic leak conductance, and $E_{\bar{g}}$ is the equilibrium potential of the cargo channel. \bar{g} is the mean active cargo throughout all n compartments of the system:

$$\bar{g} = \frac{\sum g_i}{n}$$

This simple model of conductance averages the fast, computationally-expensive dynamics for electrical signal transmission in a neurite. Rather than simulating EPSP input and initiation/propagation of dendritic spikes, membrane potential in the soma is computed as an average of electrical activity over a timescale closer to that of AMPAR production and trafficking. In this scheme, the global feedback and regulation are dependent on the average amount of AMPARs throughout the neurite: \bar{g} . We assume that these dynamics converge quickly compared to cargo production and transport and occur at a similar timescale to $[Ca^{2+}]$ influx in Eq. C.4. We therefore compute V using a steady state assumption of Eq. C.5, as follows:

$$V = \frac{\bar{g}E_{\bar{g}} + g_{leak}E_{leak}}{\bar{g} + g_{leak}}. \quad (C.6)$$

Eqs. C.3-C.6 physiologically resemble the common calcium ion signaling step in the various signal transduction pathways of cells ([172, 180]). Here, the regulatory signal produced is excitatory AMPARs g . The cell monitors the level of intrinsic excitability via the average membrane potential V over time. An increasing V results an influx of Ca^{2+} ions, likely through voltage-gated calcium channels. Additional enzyme(s) u respond to the perturbation in $[\text{Ca}^{2+}]$. If $[\text{Ca}^{2+}]$ increases, the cell slows production of regulatory cargo. If $[\text{Ca}^{2+}]$ decreases, the cell increases production. Increased production physiologically corresponds to mRNA transcription, protein translation, and the various modification and regulatory processes that occur with these mechanisms in the cell. Negative feedback is used to maintain homeostasis in membrane potential—a surrogate for intrinsic excitability. This regulation is global in the sense that all active cargo g_i are averaged to produce \bar{g} , a measure of total content.

A dendritic tree modeled as a single electrical compartment does not describe the attenuation of distal signals [92]. EPSPs occurring far from the soma attenuate considerably compared to proximal EPSPs. This discrepancy raises the issue of synaptic democracy, in which all synapses have equal impact on neural activity [157, 92]. In our model, synaptic democracy can be achieved by varying synaptic strengths $c^T = [\dots, c_i, \dots]$.

C.1.5 Model interpretation

The described presented model can be interpreted a few different ways in the context of synaptic plasticity. The aforementioned description interprets species m and g as pre-protein and protein, which are inactive and active in synapses, respectively.

The model can also represent gene transcription. AMPAR mRNA m_i is transported through the dendritic tree to regions of increased synaptic activity. m_i is then transcribed to AMPAR protein at sites of synaptic demand. These model interpretations can also represent NMDA receptors, another ionotropic glutamate receptor crucial to synaptic plasticity [137].

Experimental studies have suggested that Arc protein is the global scaling signal dissipated throughout the dendrites in response to changes in neural firing rate ([222, 47, 221, 235]). In our simulations and analysis thus far, we lump the transport of the scaling signal with AMPAR trafficking. Our modeling assumption is reasonable since AMPARs and Arc are trafficked at similar rates (300 $\mu\text{m/hr}$, [246]). As a conservative estimate, we use fast rates for AMPAR transport. To further evaluate this assumption, we also perform simulations with Arc protein as a separate communication channel to validate that lumping the scaling signal with AMPAR trafficking produces similar results (Fig. 6.10A). In this system, the global controller regulates production of both m and a with some bias $m : a$. This system replicates the same tradeoffs of synaptic scaling for a range of $m : a$ (Fig. 6.10B).

In a variant of the model, we assume that Arc protein is a separate communication channel for global signaling (Fig. 6.10). This introduces Arc protein as another species a . In this system, the global controller regulates production of both m and a with some bias $m : a$. This modified system has the following dynamics:

$$\begin{aligned}\dot{m}_i &= \delta u + f(m_i) - k_i m_i a_i - \omega_i^m m_i \\ \dot{a}_i &= (1 - \delta)u + f(a_i) - k_i m_i a_i - \omega_i^a a_i \\ \dot{[ma]}_i &= k_i m_i a_i - s_i [ma]_i (c_i - g) + s_{-i} g - \omega_i^{[ma]} [ma]_i \\ \dot{g} &= s_i [ma]_i (c_i - g) - s_{-i} g - \omega^g g.\end{aligned}$$

where $[ma]$ is a complex containing both m and a . The remaining model dynamics for this variant are unchanged.

C.1.6 Local cargo regulation

Both short- and long-term synaptic plasticity in neurons have been associated with information processing and memory formation [125]. At the molecular level, the presynaptic probability of neurotransmitter release for individual synapses is dynamic [21]. Postsynaptic terminals undergo long-term plasticity, in which AMPARs are inserted or removed from postsynaptic densities. These neural tasks are enabled by the filtering characteristics of synapses, in which synapses with varying release probabilities act as low-pass or high-pass filters. This property can be changed according to the presynaptic action potential. Long-lasting changes allow neurons to form spatiotemporal patterns as a result of activity-dependent changes. In our model, this is achieved by fine-tuning individual g_i while also maintaining overall neuron activity level $[Ca^{+2}]_{target}$. In doing so, a neuron can dynamically vary synaptic strength while maintaining homeostasis of total neuron activity.

We model these postsynaptic changes, where active AMPARs g_i fluctuate with long-term LTP manifested as changes in synaptic capacity c_i . There are several mechanisms of long-term and short-term LTP, both of which can involve structural changes to the postsynaptic terminal. [146, 145]. Local activity-dependent regulation also modifies intraspinal AMPAR trafficking rates, such as with interactions with scaffolding proteins like Stargazin [199]. Further, experiments reveal activity-dependent regulation of AMPAR into and out of the dendritic spines. For instance, phosphorylation or phosphorylation-induced changes in synapses can activate AMPARs [97]. In our model, we lump these complex mechanisms and interactions into synaptic capacity c_i and rates s_i and s_{-i} .

Next, we augment the dendritic trafficking model with local activity-dependent regulation. Local regulation is faster than other model dynamics (cargo production, cargo transport, and cargo insertion). This captures the fine, local biological processes that take place at the synapse level. In contrast to the broad average for global feedback, local feedback finely tunes individual g_i s. This allows for regulation at high spatial resolution, such as homeostatic plasticity of individual compartments or branches. We assume that individual synapses measure a local error signal e_L that compares local activity g_i to the global target activity level $[Ca^{2+}]_{target}$ to modify local AMPAR activation s_i . Mathematically,

$$\begin{aligned}\tau \dot{s}_i &= k_L e_L - \gamma_L (s_i - \bar{s}_i) \\ e_L &= [Ca^{2+}]_{target} - f(g_i) \\ f(g_i) &= \frac{s_{max} g_i^h}{g_i^h + k_A^h}.\end{aligned}\tag{C.7}$$

where τ is a small (< 1) non-dimensional parameter that reflects the fast dynamics of \dot{s}_i , K_L is the sensitivity of the local controller, γ_L is the degradation/dissipation rate of s_i , and \bar{s}_i is the uncontrolled/basal value of s_i . Local regulation takes the form of a Hill equation, where s_{max} defines the upper limit, k_A is the apparent dissociation constant, and h is the Hill coefficient that describes the degree of cooperativity between ligand (calcium) and regulatory enzyme.

Eq. C.7 shows that the g_i negatively regulates s_i ; this also serves as a stabilizing effect on the steady-state value of g_i , which opposes runaway dynamics of unconstrained Hebbian plasticity.

C.2 Transfer functions and Nyquist plots

This section was a collaboration with Saeed Aljaberi and Fulvio Forni in the Control Group, Department of Engineering, University of Cambridge.

We next demonstrate how to obtain an input-output description of our model to compute stability margins. To simplify derivations, we begin with a general nonlinear function. Each biological process—cargo production, cargo trafficking, cargo activation/inactivation, and membrane conductance—is represented by an individual function.

A nonlinear function of the form

$$\begin{aligned}\dot{x} &= f(x, u) \\ y &= h(x)\end{aligned}\tag{C.8}$$

has u , x , and y as input, state, and output, respectively. In each process, the state x represent a quantity that dynamically changes with respect to time; i.e. x can be u , m , or g . We separate each processes and reconnect them as input-output pairs, as shown in Fig. 6.4B. For example, the cargo production block has e_G as its input and u as its output.

We next obtain a linear state-space representation of the functions. To express nonlinear functions in this form, we take the Taylor series expansion around equilibrium point (x_e, u_e) , which can be computed analytically or numerically, and truncate the expression after the first term. This first order approximation is of the form:

$$\begin{aligned}\dot{x} &:= f(x_e, u_e) + \left. \left(\frac{\partial f}{\partial x} \right) \right|_{(x=x_e, u=u_e)} (x - x_e) + \left. \left(\frac{\partial f}{\partial u} \right) \right|_{(x=x_e, u=u_e)} (u - u_e) \\ y &:= h(x_e) + \left. \left(\frac{\partial h}{\partial x} \right) \right|_{(x=x_e, u=u_e)} (x - x_e).\end{aligned}$$

Since (x_e, u_e) is the equilibrium point, $f(x_e, u_e) = 0$. This produces the following state-space representation:

$$\begin{aligned}\dot{\bar{x}} &= A\bar{x} + B\bar{u} \\ \bar{y} &= C\bar{x}\end{aligned}\tag{C.9}$$

where we have made the following coordinate change:

$$\bar{x} := (x - x_e), \quad \bar{u} := (u - u_e), \quad \bar{y} := (y - y_e) = y - h(x_e)$$

and the following substitutions:

$$A := \left. \left(\frac{\partial f}{\partial x} \right) \right|_{(x=x_e, u=u_e)}, \quad B := \left. \left(\frac{\partial f}{\partial u} \right) \right|_{(x=x_e, u=u_e)}, \quad C := \left. \left(\frac{\partial h}{\partial x} \right) \right|_{(x=x_e, u=u_e)}.$$

The system in state-space form is expressed in the frequency domain using the LaPlace transform. The transfer function in the s-plane is obtained by applying following operation:

$$G(s) = C(sI - A)^{-1}B.\tag{C.10}$$

The transfer function as expressed here shows the input-output relationship of the system in the s-plane.

The transfer function can be parameterized into real and imaginary parts plotted on x- and y-axes, respectively. The result is a Nyquist plot, as depicted in Fig. 6.4D. The Nyquist plot results from evaluating the function $H(s) = 1 + G(s)$ around right-half complex plane.

The gain margin (GM) is the reciprocal of the gain at a phase frequency of -180 degrees. The phase margin (PM) is the difference in phase between the system phase and 180 degrees computed at the point of unity gain. Stability margins are computed using the following equations:

$$\text{GM} = 20 \log \frac{1}{|G(j\omega_{cg})|} \quad (\text{in dB}) \quad ; \quad \text{PM} = 180 + \arg\{G(j\omega_{cg})\} \quad (\text{C.11})$$

where ω_{cg} is the gain crossover frequency, and ω_{cp} is phase crossover frequency. ω_{cg} is the frequency at which the magnitude of $G(s)$ is unity, while ω_{cp} is the frequency at which the phase angle of $G(s)$ is -180 . Stability margins geometrically correspond to the distance between the trace of a transfer function on a Nyquist plot (Fig. 6.4D) from the point $(-1 + 0j)$, as shown in Fig. 6.4D. Fig. C.1 shows a generic Nyquist plot with all the relevant quantities.

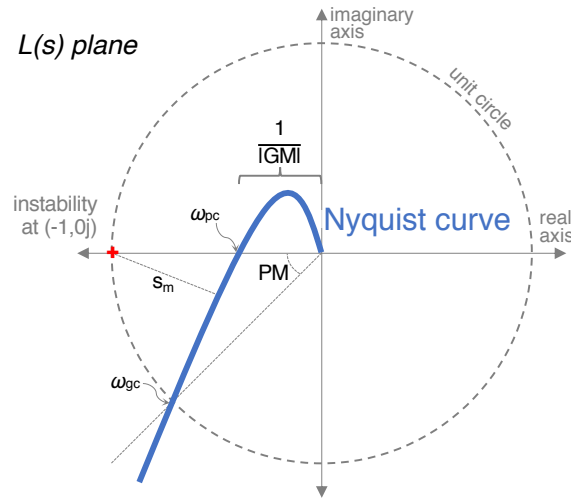


Fig. C.1 A generic Nyquist plot showing the different margins as well as the phase and gain crossover frequencies.

A transfer function is produced for each biological process. The stability of full system is determined with the transfer function of all phenomena, called the loop gain or return ratio $L(s)$, acquired by multiplying individual transfer functions in the loop. For our system, following the loop depicted in Fig. 6.4B, $L(s) = K_{\partial\psi}(s)G_g(s)G_m(s)G_u(s)$, where G_u is the transfer function of the linearized production dynamics, G_m is the transfer function of the linearized transport dynamics, G_g is the transfer function of the linearized activation/inactivation dynamics, and $K_{\partial\psi}$ is the linear approximation of the static map that captures the voltage and calcium relations. Since we previously assumed that voltage and calcium dynamics occur at a fast timescale, they are treated as static nonlinearities here. $L(s)$ now captures the the

interconnected dynamics of the entire system. Lastly, the stability margins are computed using $L(s)$ with Eq. C.11.

The stability margin s_m is another robustness measure. It measures the shortest distance of Nyquist plot from the $(-1, 0j)$, as shown in Fig. C.1. It is computed from the sensitivity function, which is obtained from the loop gain $L(s)$:

$$S(s) = \frac{1}{1 + L(s)} \quad (\text{C.12})$$

then s_m , or the shortest distance between Nyquist plot and $(-1 + 0j)$, is computed from the following relation

$$s_m = \frac{1}{\sup_{\omega} |S(j\omega)|}. \quad (\text{C.13})$$

For single-input-single-output (SISO) systems, the H_∞ norm of a system is simply the $\sup_{\omega} |S(j\omega)|$ or the maximum frequency response of the system (maximal peak value on the Bode magnitude diagram). It can be interpreted as the worst case amplification over the range of frequencies.